THEORY OF ANGLE RESOLVED ELECTRON STIMULATED DESORPTION AND PHOTODESORPTION

Ion Angular Distributions for Desorption of O^+ from the (111) and (100) Surfaces of Tungsten

by

RICHARD H. JANOW

A dissertation submitted to the Graduate Faculty in Physics in partial fulfillment of the requirements for the degree of Doctor of Philosophy, The City University of New York.

1976

This manuscript has been read and accepted for the Graduate Faculty in Physics in satisfaction of the dissertation requirement for the degree of Doctor of Philosophy.

Nov 30, 1976
date

Nachis Tzoar
Chairman of Examining Committee

12/8/76
date

Myriam P. Sarachik
Executive Officer

Arthur C. Damask

Jack Hall

Harold Leich

Norman N. Toth
Supervisory Committee

The City University of New York

ABSTRACT

THEORY OF ANGLE RESOLVED ELECTRON STIMULATED DESORPTION AND PHOTODESORPTION
Ion Angular Distributions for Desorption of O^+ from the (111) and (100) Surfaces of Tungsten

by

RICHARD H. JANOW

Mentor: Professor Narkis Tzoar

A linear response theory in three dimensions for Electron Stimulated Desorption and Photodesorption of chemisorbed species is developed. Cross section expressions which describe angle resolved ESD or Photodesorption phenomena are obtained. A three step picture of the desorption process is employed, with the propagation of desorbing atoms or molecules treated as a classical transport problem, while mechanisms for the excitation and non-radiative decay phases are described quantum mechanically.

ESD Ion Angular Distributions are simulated numerically for O^+ desorption from the Tungsten (111) and (100) surfaces. Simple models incorporating surface plane anisotropy are introduced for the ion-solid interaction potentials. Spatial variation of the excitation and non-radiative decay mechanisms is neglected.

The orientation and number of sharply focussed O^+ emission directions, which have been observed experimentally for W(111) and W(100), may be well understood as a final state effect of O^+ propagation in the anisotropic ion-solid interaction potential. Surface mesh symmetry is utilized to limit the range of oxygen adsorption sites which can produce the observed ESDIAD patterns. Plausible models for β_1 phase oxygen chemisorption on both tungsten surfaces are inferred. These produce calculated ion angular distributions consistent with the experimental results.

Photodesorption cross sections are also calculated for particles chemisorbed on a translationally invariant substrate. One dimensional transport equations are solved analytically for optically excited adparticle emission, and for ground state desorption. A mechanism involving surface plasmon and particle-hole pair excitation is introduced to account for non-radiative decay processes.

Cross sections for the photodesorption process which was

ABSTRACT, continued

examined display strong, peaked dependence on incident photon energy. The desorption kinetic energy distributions are almost monochromatic. Isotope effects analogous to those known in ESD also characterize Photodesorption. The photodesorption cross section for fluorescent particle emission is estimated to be of the order $\sim 10^{-18}$ cm.^{2} for low mass species chemisorbed $\sim$ 2 A.$^{\circ}$ from the surface.

I wish to express the deepest appreciation to Professor Narkis Tzoar, of City College, for his constant guidance and support throughout the research effort which led to this dissertation.

I am indebted as well to Professor Joel Gersten, of City College, for continuous assistance and collaboration.

Also, I wish to thank Dr. T. E. Madey of the National Bureau of Standards for making experimental results available prior to publication.

CONTENTS

TABLES and ILLUSTRATIONS

Note: All figures follow the Chapter in which they are first referenced. Captions are grouped separately, preceding the figures to which they refer.

Chapter I: Introduction

This paper summarizes the results of a continuing project in which desorption phenomena are utilized for the study of surfaces and chemisorption. Increased interest in desorption research has followed improvements over recent years in high vacuum technique and in surface preparation methods. A number of recent review articles have appeared describing progress in chemisorption and desorption studies.[1-5]

Motivations for the study of desorption are both academic and practical. Such studies provide a method for surface characterization and analysis. The physical and chemical processes associated with the adsorption of atoms or molecules may be probed. In principle, one may identify the nature, and measure the density and distribution, of adsorbate films under varying conditions. Angular dependent studies are a new development which should prove especially useful for these purposes[6-9]. The data so obtained provide information complementary to that obtainable by techniques such as LEED or Photoemission studies.[10-12]

As a technological tool, desorption provides a means for surface cleaning and preparation. It may appear as an unwelcome phenomenon whenever sizable particle fluxes bombard surfaces or surface films. Photodesorption from stainless steel has recently been observed[13]. Degradation of the surface and structure of walls may be a matter of practical concern in fission and fusion reactor design. Significant photodesorption may occur from the surfaces of pellets used in laser fusion experiments. Finally, it has been suggested that photodesorption of H and H_2 molecules from the surfaces of interstellar dust

grains may provide an important mechanism coupling the interstellar radiation field to the gas.[14]

In discussions to follow we regard desorption as a collision process in which an incident projectile collides with an atom or molecule and ejects it from the surface to which it is bound. Atoms of the underlying substrate are usually regarded as permanently fixed to the surface. The species, when desorbed, may be an atom or a molecule, either in the ground state, an excited electronic state, or ionized. The desorption of one of these is considered complete when it is far enough from the substrate to neglect all interactions with the surface.

Desorption processes are characterized by the type of incident particle causing the ejection. If the incoming particle is an ion, the process is called 'Sputtering'. When it is an electron, the term 'Electron Stimulated Desorption' (ESD) or 'Electron Induced Desorption' (EID) is applied. The electrons may originate in an external beam, or internally, having been photoemitted, for example, in which case ESD is a secondary process. When the bombardment is with photons, the ejection process is called 'Photodesorption' (PD). 'Thermal Desorption' occurs without the aid of an external particle probe. Ejection follows collisions with phonons, for example, incident from the substrate. Other possible sources of desorbing collisions include any of the elementary excitations of surface or bulk solid.

We limit attention to only two types of desorption phenomena: Electron Stimulated Desorption and Photodesorption. Our efforts result in a three dimen-

sional linear response theory for ESD and PD capable of predicting angular dependent desorption patterns. Attention is given only to desorption from the surfaces of crystalline solids in our three dimensional calculations. These possess the lateral periodicity which can produce structured angular dependence in the desorbing particle beam. Desorption may also occur from the surfaces of amorphous materials; however, the absence of long range order in the surface plane is expected to mask any angular emission effects of interest.

The development of a three dimensional theory for ESD in particular is timely. Experimental investigations of ESD ion currents have been pursued for a number of years.[1-5] However, recent angular dependent studies reveal that O^+ ions emitted from tungsten form desorption patterns which contain sharp cones, whose orientations correlate to the substrate geometry.[6-8] Some of the patterns observed are believed to originate with adsorption phases affecting only a small proportion of the surface atom population.[15-17] The emission directions depend on anisotropies on the scale of the unit surface cell size; hence, the adsorption geometry and ejection dynamics are probed quite directly. Information of this type is not obtainable by surface analytical techniques such as LEED which are sensitive mainly to long range order in the adsorbed layer and substrate.[10,18,19]

The formalism developed here for angular dependent desorption calculations provides a means for testing model surface interactions for consistency with experiment. Information concerning the adsorption geometry and surface parameters will be extracted from the observed patterns. The utility of theoret-

ical simulations of desorption patterns as an adjunct to experiment is demonstrated at a later point when observed ESD patterns are shown via simulation to be explained by anisotropy of the atom-substrate interaction energy.

In Chapter II, the picture of desorption processes and the basic formalism employed throughout this paper are presented. Transport equations are obtained which describe an atom-solid system interacting weakly with an external beam of photons or electrons. Expressions for the total and differential cross sections and desorption rates are defined and expressed in terms of the microscopic distribution functions.

In Chapter III, possible mechanisms for quenching an optically excited particle near the surface are discussed. A model transition rate expression for quenching via surface plasmon emission is obtained, using the semi-infinite free electron gas model for the substrate. Surface plasmon dispersion relations for use in model photodesorption calculations are examined.

Chapter IV applies the linearized transport theory to neutral atom photodesorption. The transport problem is solved analytically in one dimension. The cross section expression for excited state photodesorption at low temperatures is obtained. The solution for the ground state photodesorption cross section is carried out in Appendix I.

In Chapter V we evaluate the photodesorption cross section numerically. We find in order of magnitude calculations that photodesorption of low mass adsorbed particles should occur with cross sections $\sim 10^{-18}\text{cm}^2$. which are well within the limits of observability.

We turn to the study of angular dependence in Chapter VI. Expressions for use in angle-resolved ESD and photodesorption studies are presented, and the method of implementing numerical computations is discussed. Model interactions are presented for use in simulating ESDIAD for O^+ emission from tungsten.

In Chapters VII, VIII we describe detailed ESDIAD simulations of O^+ desorption from the W(111) and W(100) surfaces. These systems were selected for study in response to the recent discovery of interesting angular dependent effects.

Chapter II: Formulation of the Desorption Problem

The formulation of the desorption problem we employ rests on an approximate picture of the process which has proven useful in previous investigations of desorption pheonomena.[1-4,20,21] Molecular vibration and dissociation problems have been treated extensively via similar methods.[22,23] We regard desorption as a three step process, basing the formulation of the theory on the Born-Oppenheimer Approximation and on a Franck-Condon picture of adsorbed particle excitation.

The steps consist of promoting an adsorbed particle to an anti-bonding state from which it may desorb, followed by propagation of the particle in that excited state, and possibly, recapture via quenching back to the ground state through a non-radiative decay mechanism. If a particle is quenched, it may still possess sufficient energy to escape the surface in the ground state. In this case, a fourth step, ground state propagation completes the desorption process. The propagation of desorbing atoms or molecules will be described by classical transport theory. The excitation and decay mechanisms involve electronic interactions which require a quantum mechanical description.

The picture described is useful for treating the response of adparticle-substrate systems which are weakly interacting with an external electron or photon beam. This is the case when either the flux of external particles is small, or the excitation matrix elements have small coupling constants. Throughout this paper, our attention is confined only to response linear in

the strength of the external beam. The strongly coupled response is interesting in its own right; however, we defer these studies to the future.

The formalism for all of the desorption calculations to follow is developed in a three dimensional form suitable for the description of angular dependent desorption effects. At a later point, the one dimensional limit is taken to obtain analytical solutions to the photodesorption problem.

The Surface

Translational invariance in the surface plane which permitted mathematical simplification of previous desorption theories [20,21] is now abandoned. An infinitely extended grid of periodic surface cell structures each of which is anisotropic in the x-y direction now tessellates the surface plane. The observable quantities become the differential ejection rates and cross sections for all desorption channels. Despite the added complexity, a formalism of conceptual simplicity comparable to one dimensional theories is obtained.

The surface mesh structure is regarded as known throughout this analysis. Each bulk lattice type, cleaved along different directions, produces structures with differing periodicity and symmetry properties. We illustrate in later computations the (111) and (100) surfaces of Tungsten. Facetting of the surface or rearrangements of the layer spacing, which are known to occur under certain conditions, [24-27] can be incorporated into the theory later. The surface is taken to be flat, with the surface cell characterized by a pair

of lattice vectors lying in the x-y plane. The case of adsorption on molecular solids presents no problem.

The theory is formulated entirely within a single surface unit cell extended infinitely in the z direction. All of the symmetry properties of the surface mesh are imposed on the functions which describe the stages of desorption. The anisotropies of these quantities within a single cell produce the angular dependent effects of interest. In model calculation performed later, we verify that transverse anisotropies and z dependence in the atom-surface interactions become negligible while the adatom to surface distance is infinitesimal compared to the macroscopic sample size. Asymptotic emission directions and energies are thus reached quickly. At macroscopic separations, each unit cell behaves as a point source of angular dependent intensity.

The Propagation Phase

We will examine the system consisting of a single adsorbed atom or molecule interacting with the surface. In practice, low surface coverages of the order of a monolayer or less are the most interesting cases to consider. The number of adsorbed particles per unit cell is specified by N in discussions to follow. All interactions between neighboring adsorbed particles are neglected for the present. These are re-introduced as part of the atom-solid interaction energy when adsorbed surface molecules are examined.

The Hamiltonian for a single particle residing just outside the surface

may be written:

$$H = -\frac{\nabla_R^2}{2M} + H_e(\vec{R}, \vec{\eta}_i) \qquad (2.1)$$

Here, and frequently in calculations below, we work in the system of atomic units, for which $\hbar = e = m_e = 1$, with m_e the electronic mass. Energies are in Hartrees, where 1 Hartree $= e^2/a_o = 27.211$ ev. The Bohr radius a_o is the length unit. The kinetic energy operator for the surface atom of mass M operates on its mass center coordinates. The electronic Hamiltonian H_e contains all the potentials present in the system, as well as kinetic energy operators for all electrons participating in atom-surface interactions, whose coordinates are the $\vec{\eta}_i$.

Decoupling of the propagation phase of desorption from the electronic interactions in the system is accomplished by means of the Born-Oppenheimer approximation. Definitions of the effective potentials for adparticle propagation are obtained in the separation process. This approximate separation of electronic from atomic coordinates in Eq. (2.1) is facilitated, to order (m_e/M), by the smallness of the electronic to atomic or molecular mass ratio.

One holds the atomic motion fixed while solving the associated electronic eigenvalue problem defined by:

$$H_e \psi_n(\vec{R}, \vec{\eta}_i) = E_n(\vec{R}) \psi_n(\vec{R}, \vec{\eta}_i) \qquad (2.2)$$

Electronic responses to shifts in the atomic coordinate $\vec{r}$ are rapid enough to regard as instantaneous in the analyses to follow. The many particle wave function Ψ_n is required to be recognizable, far from the surface, as the product of an unperturbed atomic or molecular wave function for the n'th state and a wave function for the isolated solid. At intermediate separations, one expects tunnelling to broaden the adparticle states, with H_e almost diagonalized by linear combinations of atomic and substrate wave functions. Close to the surface, a self-consistent description of the adparticle + solid system may be mandated.[28] This case is not treated. We assume that the intermediate coupling case holds at worst. We view internal states of the adsorbed particle, indexed by n, as long lived excitations of the system.

The functions $E_n(r)$ serve as effective potentials approximately governing the state n atomic or molecular mass center motion via the following:

$$\left[-\frac{\nabla_r^2}{2M} + E_n(\vec{r})\right]\phi_n(\vec{r}) = \mathcal{E}\,\phi_n(\vec{r}) \qquad (2.3)$$

We take $E_n(\vec{r})$ to be real; however, an imaginary component may appropriately be added to $E_n(\vec{r})$ when interactions between adparticle and surface dissipate energy for particles propagating in the n'th state. Due to the rapidity of electronic relaxations, the potentials $E_n(\vec{r})$ describing the state n dynamics

are time averages, created jointly by the atomic or molecular electron distribution and the charge density on the solid. The difference $[E_n(\vec{r}) - E_1(\vec{r})]$ is regarded as the internal excitation energy of the adsorbed particle, and is identical to the free atomic value at large atom to surface separations.

To order (m_e/M), the same effective potentials $E_n(\vec{r})$ obtained by solution of the Schrodinger problem in Eq. (2.3) result from a classical computation of the electrostatic interaction energy between an adsorbed particle at $\vec{r}$ and the charge density given by $|\psi_n|^2$. We shall resort to the use of this Hellman-Feynman Theorem at a later point for simplified model calculation of $E_2(\vec{r})$.[22,29]

The problem of calculating the potentials E_n is a difficult one in general, and it has attracted much attention from theorists. To date, we know of only one surface charge density calculation including three dimensional variations. This was done for the (111) face of Silicon.[29] Most work has been focussed on the ground state potential surface near an equilibrium point. This is the region of interest in the chemisorption problem. The Anderson-Newns formalism[30] has met with qualitative success in describing chemisorption as have more recent efforts.[31] However, the details of adsorption on solid surfaces are mostly not known either theoretically or experimentally.

Little effort has been expended in describing the excited states, which govern the desorption dynamics in the processes we consider. The diffi-

culty of this problem implies that statements made in discussions to follow about the nature of the potential surfaces E_n are likely to be crude.

We have shown in Fig. (2.1) the qualitative behavior to be expected of the z dependence in the atom-solid potentials E_n. Similar behavior is expected of effective potentials used in molecular problems. A schematic representation of the three step picture of desorption is also shown in Fig. (2.1). For simplicity, we restrict consideration throughout further discussions to a two level system consisting of a ground state ($n = 1$), in which chemisorption takes place, and an anti-bonding state ($n = 2$) which has the generally repulsive behavior shown. The theory can be extended to include multiple excited states with some complexity added. Inasmuch as Fig. (2.1) is one dimensional, variations of E_n in the plane of the surface should be kept in mind.

The depth of the ground state potential well represents the adatom binding or chemisorption energy. The length 'b' fixes the adsorption site location relative to the surface. Adsorbed ground state particles will be taken to be neutral, although states of partial negative or positive ionization have been found useful for describing chemisorption in some situations.
One expects a repulsive barrier at small z preventing entry into the solid. Asymptotically, the long range attraction approaches $E_1(\infty) = 0$.

The excitation mechanism which operates fixes the character of E_2. We restrict consideration to only those simple cases where state 2 may be

described as neutral or ionic. In the neutral case, state 2 is taken to be one with perturbed internal optical excitation. When the state 2 desorption product is ionic, as is frequently the case in ESD, the propagating core is a compact object, which we approximate in later computations by a point charge. Excited states involving negative ions or neutrals are considerably less compact. In addition to added internal complexity due to correlation and exchange, one expects sizable widths and level shifts to be imposed on the free atomic states via these mechanisms.

We illustrate the form of E_2 appropriate to photodesorption of neutral atoms or molecules by a solid line in Fig. (2.1). Desorption in the excited state can occur only when E_2 is basically repulsive as shown. In the limit $z \to \infty$, the difference $[E_2(\vec{r}) - E_1(\vec{r})]$ approaches $\hbar\omega_{opt}$, the free atomic fluorescence frequency. The monotonically repulsive shape assumed for E_2 prohibits trapping of excited particles, which would be indicated by the presence of local minima of E_2. Trapped particles rejoin the ground state through non-radiative decay, and may possibly desorb.

The dashed curve in Fig. (2.1) sketches the behavior expected of E_2 when the desorption product is ionic. When ions desorb from metal surfaces, one expects trapping at long range by attraction to an image charge density residing near the surface. A photodesorption process analogous to molecular photoionization may occur, whose propagation and decay phases mimic those of ionic ESD.

The propagation of the massive atoms or molecules interacting with the surface will be described classically. Hence we replace Eq. (2.3) by the classical equations of motion for state n:

$$\frac{d\vec{V}}{dt} = -\frac{1}{M}\vec{\nabla}_r E_n(r) \qquad (2.4)$$

We assume below that the solutions $\vec{v}(t)$, $\vec{r}(t)$ are known parametrically as functions of time and a set of initial conditions for each trajectory.

Classical dynamics apply best to the unbound, desorbing states, which form a continuum of travelling wave solutions to Eq. (2.3). Particles propagating in state 2 are quickly accelerated to substantial kinetic energies after excitation by the large gradient of E_2. Except near the point of excitation, the wavelength implied by $\hbar^2K^2/2M$ is small compared to other lengths near the surface, justifying the neglect of diffraction effects. The same argument applies to atoms or molecules desorbing in the ground state after quenching. These generally acquire large kinetic energies due to their history in the excited state.

A classical description is also acceptable for bound states when $\hbar\omega_0 \ll KT$. Here ω_0 is the harmonic oscillator level spacing for a parabolic potential which approximates E_1 near its minima. At high temperatures the Bose distribution of vibrational levels approximates a Maxwellian distribution. Anharmonicity of E_1 compresses the level spacing between higher vibra-

tional states, forming a quasi-continuum. Classical dynamics may be confidently applied to large mass particles desorbing at high temperatures from ground state minima whose profile is shallow.

The formulation of desorption theory presented here provides a qualitatively correct description even in unfavorable cases for which $\hbar\omega_0 \approx KT$. The classical picture of bound state propagation is then invalid. We find that linearizing the theory in the photon or electron flux results in desorption cross sections which necessitate following the propagation of only the desorbing particles. The chemisorbed state propagation dynamics then become irrelevant. A quantum mechanical description of the excitation process is then required, the principal effect of which is to replace the Maxwellian shape of the classical ground state distribution over the Franck-Condon transition region.

Excitation and Quenching

The mechanisms involved in excitation or quenching are primarily electronic transitions. A simplified treatment of these transitions is accorded by the Born-Oppenheimer picture. On the time scale for adparticle propagation, excitation and decay are viewed as sudden inelastic events, during which the motion of an atom or molecule is frozen. Its internal state, its momentum, and the dynamical equations governing its propagation undergo discontinuous change. Transition rates for excitation and decay will be taken to be ensemble averages over all initial and final states of substrate and probe particle which are consistent with a given change of internal and translational state. In effect,

we assume that the density matrix and partition function for the entire atom substrate system factor to order (m_e/M), permitting averages to be performed separately over the electronic states and over the classical phase coordinate which describe atomic or molecular propagation.

The solid at low temperatures will be taken to be in its ground state as the initial condition during excitation or decay. Electrons or photons impinging on the system are assumed to belong to a monochromatic flux.

In the case of ESD, the electronic energies employed experimentally generally lie in the range 100-200 ev.[1,2] So long as incident electrons are of high, but non-relativistic energy, the excitation phase of ESD may be described in the Born Approximation. We assume that the first order transition rate per atom may be written after ensemble averaging as $\langle R_e (\vec{r}, \vec{v}_2 - \vec{v}_1) \rangle$. Here the momentum transfer to an atom or molecule is explicitly written. $\langle R_e \rangle$ is proportional to the incoming flux. When excitation involves ionization, the coordinates of two final state electrons are present in the averaging process, while, when state 2 is neutral, one final state electron is present.

The fate of final state electrons is not of interest. We assume that they exit quickly from the excitation region and are either absorbed by the solid or emitted as Auger electrons. So long as final state electrons are present, a large portion of the ground state distribution is probed. In ESD, where incident electron energies are large compared to $(E_2 - E_1)$, excitation can occur at virtually any point on the energy hypersurfaces of Fig. (2.1).

The photodesorption excitation phase is simpler than that for ESD. We assume that dipole transitions link atomic and molecular states 1 and 2. When the excited state is neutral an exact resonance is required for excitation. The photon momentum is negligible. Photodesorption of neutrals is thus a selective process which probes a thin shell of the energy hypersurfaces where $(E_2 - E_1) = \hbar\omega$. When the excited state is ionic, on the other hand, photodesorption may not display this selectivity. A final state electron is then emitted either as a free particle, or into a bound state of the solid. We take the average transition rate per atom describing the excitation phase of photodesorption to be $\langle R_\gamma (\vec{r}, \vec{v}_2 - \vec{v}_1) \rangle$, as before.

Transitions back to the ground state are assumed to occur primarily via non-radiative decay channels. Lifetimes for optical radiation are long[32,33] compared to times spent by desorbing particles near the surface. For ionic excited states, quenching occurs by reneutralization processes involving electron capture from the solid. When the excited state is neutral, as in the photodesorption calculations to be performed below, quenching involves the creation of a final state surface excitation. We expect non-radiative decay processes to be efficient when atom to surface separations are small, and to weaken rapidly with increasing z. The average quenching rate, per adsorbed atom or ion, is given by $\langle Q (\vec{r}, \vec{v}_2 - \vec{v}_1) \rangle$.

The recoil of an atom or molecule during excitation or decay is negligible and will be neglected. Substantial simplification of the transport theory results. The dominant impulse to adsorbed or desorbing particles is provided

by large gradients of E_n.

Spatial dependence of the transition rates for excitation or quenching is likely to be strong, and to mirror spatial variations in E_n. We denote by $R(\vec{r})$ and $Q(\vec{r})$ the excitation and quenching rates per adsorbed particle, ensemble averaged as described, and summed over all momentum transfers.

Transport Equations

Now a transport theory description of classical adparticles in three dimensions is formulated. Decoupling of the quantum mechanical interactions from classical propagation permits us to regard the transition rates and propagation dynamics as known.

The coupling of state 2 to state 1 by quenching will be presumed to be strong. We take Q to be a zero order quantity, including it to all orders in final expressions for the desorption cross sections. This dependence is found to be exponential in later computation. As noted above, the theory will be linearized in the excitation rate R, which is under experimental control. Hence, R is treated as a first order quantity.

We take $P_n(\vec{r}, \vec{v}, t)\, d^3\vec{r} d^3\vec{v}$ to be the probability of finding a surface atom or molecule, in the n'th state at time t, within the phase space volume element $d^3\vec{r}\, d^3\vec{v}$ centered on $\vec{r}, \vec{v}$. These distribution functions must possess the surface unit cell symmetries. The following normalization is imposed on the P_n:

$$\sum_{n=1,2} \int d^3\vec{r} \int d^3\vec{v}\; P_n(\vec{r}, \vec{v}, t) = 1 \qquad (2.5)$$

The spatial integration is restricted to a single surface cell, extended infinitely in the direction normal to the surface. The normalization is relaxed at a later point when transients are neglected in the course of linearizing the transport equations in R.

Approximate thermal equilibrium may hold for the atom-solid system when it is free of external bombardment. This may not be the case, however, particularly at elevated temperatures, inasmuch as spontaneous desorption may occur. This process occurs via collisions between adsorbed particles and excitations of the solid which provide the large momentum transfers required to desorb particles from the ground state.[34] Desorption through spontaneous excitation to the anti-bonding state is expected to be negligible even at elevated temperatures. The population of high energy excitations of the solid required for initial states contributing to such processes is negligible. A Boltzmann Equation describing spontaneous ground state desorption is the following:

$$\frac{\partial P_i}{\partial t} + \vec{V} \cdot \vec{\nabla}_r P_i + \vec{a} \cdot \vec{\nabla}_v P_i = \left(\frac{dP_i}{dt}\right)_{SURF}$$

The term on the right incorporates interactions between ground state particles and substrate excitations.

We neglect all spontaneous desorption processes throughout develop-

ments which follow. For the systems under consideration, at the experimentally interesting temperatures, the chemisorption energies may be assumed to be large compared to the thermal energy (3/2)kT. Numerous descriptions of spontaneous (flash) desorption appear in the literature.[34] In some situations, ground state thermal desorption may be observed as a by-product of ESD or PD experiments. Local heating of the surface may occur either by direct interaction of the external probe with the surface, or via quenching. We assume below that photon or electron fluxes are weak enough to disregard these effects.

In the absence of external perturbation by electrons or photons, the atom solid system is regarded as a gas of non-interacting particles in thermal equilibrium with the solid. The Boltzmann equation which applies is:[35]

$$\vec{v}\cdot\vec{\nabla}_r P_n^0(\vec{r},\vec{v}) - \frac{1}{M}\vec{\nabla}_r E_n(\vec{r})\cdot\vec{\nabla}_v P_n^0(\vec{r},\vec{v}) = \left(\frac{dP_i}{dt}\right)_{SURF} \simeq 0 \tag{2.6}$$

The zero superscripts henceforth mark quantities pertaining to the equilibrium state. Boltzmann distributions satisfying the above are:

$$P_n^0(\vec{r},\vec{v}) = \eta_n\left(\frac{M\beta}{2\pi}\right)^{3/2} \frac{e^{-\beta\left[\frac{Mv^2}{2}+E_n(\vec{r})\right]}}{\int d^3\vec{r}\, e^{-\beta E_n(\vec{r})}} \tag{2.7}$$

Here $\beta = 1/kT$. M is the adsorbed particle mass. The arbitrary coefficients η_n required to satisfy the normalization implied by Eq. (2.5) are assumed to be $\eta_2 = 0$, $\eta_1 = 1$. The equilibrium state 2 population is negligible, hence:

$$P_2^{\circ}(\vec{r}, \vec{v}) \approx 0$$

Now we examine the case in which the system is driven off equilibrium by an external photon or electron beam, causing upward transitions in Fig. (2.1) into state 2. Both non-radiative decays, and collisions with surface excitations provide relaxation mechanisms which tend to restore equilibrium. Competition between the transition mechanisms which act on the density distributions is summarized by the following set of transport equations:

(2.8a)

$$\frac{\partial P_2}{\partial t} + \vec{v} \circ \vec{\nabla}_r P_2 - \frac{1}{M} \vec{\nabla}_r E_2 \circ \vec{\nabla}_v P_2 = \left(\frac{dP_2}{dt}\right)_{SURF} + \left(\frac{dP_2}{dt}\right)_E - \left(\frac{dP_2}{dt}\right)_Q$$

(2.8b)

$$\frac{\partial P_1}{\partial t} + \vec{v} \circ \vec{\nabla}_r P_1 - \frac{1}{M} \vec{\nabla}_r E_1 \circ \vec{\nabla}_v P_1 = \left(\frac{dP_1}{dt}\right)_{SURF} - \left(\frac{dP_1}{dt}\right)_E + \left(\frac{dP_1}{dt}\right)_Q$$

Each term on the right in Eqs. (2.8a, b) is now examined. The surface interaction term will be neglected, and simple forms found for the excitation (E) and quenching (Q) terms.

The source of excited particles entering state 2 at the phase point $\vec{r}, \vec{v}$ is described by $(dP_2/dt)_E$. This quantity is proportional to both the upward transition rate and to the ground state population. In principle, one should sum over momentum transfers which lead to a final state found excited with $\vec{r}, \vec{v}$. Inasmuch as the recoil is neglected, we approximate:

$$\left(\frac{d P_2(\vec{r},\vec{v},t)}{dt}\right)_E \approx P_1(\vec{r},\vec{v},t) R(\vec{r}) \tag{2.9a}$$

Ground state depletion occurs as a result of the excitation process. The loss term for each region of phase space about r, v is given by:

$$\left(\frac{dP_1}{dt}\right)_E = P_1(\vec{r},\vec{v},t) R(\vec{r}) \approx \left(\frac{dR(\vec{r},\vec{v},t)}{dt}\right)_E \tag{2.9b}$$

In the perturbed system, the state 2 population may no longer be neglected. P_2 must be proportional, in dominant order, to the excitation

rate, and it is thus a first order quantity when coupling to R is weak. The depletion of the excited state through non-radiative decay is given by:

$$\left(\frac{dP_2(\vec{r},\vec{v},t)}{dt}\right)_Q = P_2(\vec{r},\vec{v},t)\,Q(\vec{r}) \qquad (2.9c)$$

Quenched particles repopulating the ground state are the only ones which can desorb in state 1. The distinctly non-thermal component of P_1 containing this probability must be, to dominant order, proportional to both P_2 and to Q; hence it is of order R^1Q^1. The momentum transfer on quenching is neglected, and the following approximation is made:

$$\left(\frac{dP_1}{dt}\right)_Q \approx P_2(\vec{r},\vec{v},t)\,Q(\vec{r}) \approx \left(\frac{dP_2}{dt}\right)_Q \qquad (2.9d)$$

The surface interaction terms $(dP_n/dt)_{SURF}$ describe scattering mechanisms which produce no inter-state transitions. We neglect all such interactions in state 2; hence, $(dP_2/dt)_{SURF} \approx 0$. Ground state collisions provide primarily a relaxation mechanism for state 1 toward equilibrium, which competes with the depletion of P_1 implied by $(dP_1/dt)_E$.

One may neglect $(dP_1/dt)_{SURF}$ in Eq. (2.8b) in the limit of either strong or weak coupling to the electron or photon flux. In the weak

coupling case, which corresponds to the linear response theory of interest, one must also neglect depletion of the ground state by excitation. We do not examine the intermediate coupling regime, where one must specify a value for the ground state collision time τ_c. For convenience, we also designate by τ_E the mean survival time for adsorbed atoms or molecules in the ground state against excitation.

The transport equations are linearized and arguments for neglecting $(dR/dt)_{SURF}$ are clarified by defining P_1^A to be the solution of the following:

$$\frac{\partial P_1^A}{\partial t} + \vec{V} \cdot \vec{\nabla}_r P_1^A - \frac{1}{M} \vec{\nabla} E_0 \cdot \vec{\nabla}_v P_1^A = \left(\frac{dP_1}{dt}\right)_{SURF} - \left(\frac{dP_1}{dt}\right)_E \tag{2.10}$$

Here P_1^A contains terms of lowest order R^0Q^0 and R^1Q^0, either of which may dominate. We write the ground state distribution as

$$P_1 \equiv P_1^A + P_1'$$

where P_1' is the solution of:

$$\frac{\partial P_1'}{\partial t} + \vec{V} \cdot \vec{\nabla}_r P_1' - \frac{1}{M} \vec{\nabla}_r E_0 \cdot \vec{\nabla}_v P_1' = \left(\frac{dP_1}{dt}\right)_Q \tag{2.11}$$

To lowest order, P_1' is dependent on R^1Q^1, hence it contains the contribution to ground state desorption.

We restrict attention to the weakly coupled case, which implies validity of the condition $T_E >> T_c$. In this regime, depletion of the ground state is negligible; thus, surface interactions dominate in Eq. (2.8b) and (2.10), in which the following condition holds:

$$\left(\frac{dP_1}{dt}\right)_{SURF} >> \left(\frac{dP_1}{dt}\right)_E$$

Making use of Eq. (2.6), we take the unquenched part of the ground state distribution, P_1^A to be:

$$P_1^A \approx P_1^0$$

to lowest order.

The linearization is completed with the use of Eqs. (2.9a) - (2.9d). The linearized version of Eq. (2.8a) is:

$$\vec{V}\circ\vec{\nabla}_r P_2'(\vec{r},\vec{v}) - M\,\vec{\nabla}_r E_2(r)\circ\vec{\nabla}_v P_2'(\vec{r},\vec{v}) = \\ = P_1^0(\vec{r},\vec{v})\,R(r) - P_2'(\vec{r},\vec{v})\,Q(r) \qquad (2.12a)$$

Here all terms are of order R^1. We took $P_2 = P_2^0 + P_2'$, recalling that $P_2^0 \approx 0$. We also noted that $P_1 = P_1^0 + P_1'$, where P_1' is of order R^1, hence

its contribution to Eq. (2.8a) is of higher order in R.

Ground state desorption is described by P_1', for which Eq. (2.11) is applicable. Making use of Eq. (2.9d) the result is:

$$\vec{V}_0 \cdot \vec{\nabla}_r P_1'(\vec{r},\vec{v}) - \frac{1}{M} \vec{\nabla}_r E_1(\vec{r}) \cdot \vec{\nabla}_v P_1'(\vec{r},\vec{v}) = P_2'(\vec{r},\vec{v}) Q(\vec{r}) \qquad (2.12b)$$

All terms here are of order R^1, as required.

Equations (2.12a, b) form a set of linearized transport equations which provide the solution to the ESD and photodesorption problem. The one-dimensional analogs of these equations are solved explicitly in Chapter IV and in Appendix I for the photodesorption of neutrals in a one-dimensional system.

A set of transport equations describing the response in both strong and weak coupling regimes may also be written, based on Eqs. (2.8a, b). These are:

$$\frac{\partial P_2}{\partial t} + \vec{V}_0 \cdot \vec{\nabla}_r P_2 - \frac{1}{M} \vec{\nabla}_r E_2 \cdot \vec{\nabla}_v P_2 = P_1 R - P_2 Q \qquad (2.13a)$$

$$\frac{\partial P_1}{\partial t} + \vec{V}_0 \cdot \vec{\nabla}_r P_1 - \frac{1}{M} \vec{\nabla}_r E_1 \cdot \vec{\nabla}_v P_1 = P_2 Q - P_1 R \qquad (2.13b)$$

These equations are not linearized. Their non-linear solutions involve propagation in bound states, for which classical dynamics hold approximately only at high temperatures and for large mass adsorbed particles. In applying them to the weak coupling regime, one must neglect the depletion of state 1, in addition to performing the linearization. This is the procedure followed in Appendix II, where the solution of the angular dependent desorption problem is obtained by expanding the formal solutions of Eqs. (2.13a, b) as a perturbation series in R.

Expressions for the Cross Sections

The objective of the desorption calculations is a description of the current of neutral or ionized particles leaving the surface in each state. We next define the total and differential cross sections and desorption rates which provide this information. The connection between these macroscopic quantities and the distribution functions P_n is specified.

We define $\dot{N}_n(z,t)$ to be the net number of atoms in state n crossing the plane parallel to the surface at z, per unit time, per unit cell. All directions and speeds are contained in this current. When $z \rightarrow L \gg a_o$, there is no incoming component; thus we identify $\dot{N}_n(t)$ as the desorption rate in state n, at time t, per unit cell. One multiplies $\dot{N}_n(t)$ by the number of unit cells in the sample to obtain the total number of state n particles ejected per second. $\dot{N}_n(t)$ is proportional to both the flux F of bombarding particles and to N(t), the number of adsorbed particles per unit cell on the surface at t.

The total desorption cross section for state n is defined to be the desorption rate per unit flux, per adsorbed particle:

$$\sigma_n \equiv \frac{\dot{N}_n(t)}{F N(t)} \qquad (2.14)$$

When the response is linear, σ_n is independent of F. It is time independent also, inasmuch as depletion of the surface coverage, and the decay in the ejection rate display the same time dependence via the factor:

$$\exp[-F\sigma\Delta t]$$

The total desorption cross section σ is summed over all competing desorption channels.[1,2]

The ejection rate should not be observed to decay when desorption is from a clean surface, or from one covered by several monolayers of adsorbed particles, assuming F is constant. The most interesting experimental cases involve coverages of a monolayer or less, for which coverage depletion during a desorption experiment may be significant. In experiments where impacts are counted over Δt to establish $\dot{N}_n(t)$, one should ensure that coverage depletion is small by requiring $F\sigma\Delta t \ll 1$.

For angular dependent studies the quantities of interest are the differential desorption rates $\dot{N}_n(\theta,\phi,t)$ and differential cross sections

$\sigma_n(\theta,\phi)$ related by:

$$\sigma_n(\theta,\phi) = \frac{\dot{N}_n(\theta,\phi,t)}{F\,N(t)} \qquad (2.15)$$

The angles θ, ϕ specify the direction of the ejection velocity. These quantities are integrated over the asymptotic speeds. One integrates over a hemisphere with $0 < \theta < \pi/2$ to obtain the total cross sections and ejection rates:

$$\sigma_n = \int d\Omega\, \sigma_n(\theta,\phi) \qquad (2.16)$$

$$\dot{N}_n(t) = \int d\Omega\, \dot{N}_n(\theta,\phi,t) \qquad (2.17)$$

Next we follow the microscopic particle current in the unit cell to connect $P_n(\vec{r}, \vec{v}, t)$ with the macroscopic quantities. The average density of atoms or molecules in state n in each unit cell is:

$$\rho_n(\vec{r},\vec{v},t) = N(t)\,P_n(\vec{r},\vec{v})\,d^3\vec{v}$$

while the current density associated with that point in phase space is:

$$\vec{j}_n(\vec{r},\vec{v},t) = \rho_n(\vec{r},\vec{v},t)\,\vec{v}$$

Now $\vec{j}(\vec{r}, \vec{v}, t)$ is evaluated in the asymptotic plane at $z = L >> a_0$. Note that $\vec{v} = (v, \theta, \phi)$, $\vec{r} = (\vec{r}_\perp, z)$, where $\vec{r}_\perp$ lies parallel to the surface. One sums $\vec{j}_n(z = L, \vec{r}_\perp, \vec{v}, t)$ over the asymptotic speeds, and integrates over the surface cell area A_c to obtain the ejected current into $d\Omega$ per unit cell. The magnitude of that current divided by $d\Omega$ yields the differential desorption rate which is given by:

$$\dot{N}_n(\theta, \phi, t) = N(t) \int_0^\infty dv\, v^3 \int_{A_c} d^2\vec{r}_\perp\, P_n(\vec{r}_\perp, z = L, v, \theta, \phi) \qquad (2.18)$$

The differential cross sections are:

$$\sigma_n(\theta, \phi) = \frac{1}{F} \int_0^\infty dv\, v^3 \int_{A_c} d^2\vec{r}_\perp\, P_n(\vec{r}_\perp, z = L, v, \theta, \phi) \qquad (2.19)$$

The one-dimensional limit of these expressions is evaluated directly in photodesorption calculations to follow, where analytic solutions to the transport problem are found. In angular dependence studies, we find it most convenient to numerically simulate the total cross section by following particle propagation, then to numerically differentiate, thus recovering the angular dependence. It is found convenient to transfer ensemble averaging and simultaneity to the excitation point in those calculations; hence a reformulated set of expressions for σ_n is obtained in Appendix II.

Chapter II: Figure Caption

Fig. 2.1: Effective potential diagrams for ESD and Photodesorption. The qualitative behavior of the ground and excited states for both processes are represented as functions of the z coordinate. Arrows schematically represent the excitation (R), propagation (P), and quenching (Q) phases of ESD or PD. V_o is the chemisorption energy. The z coordinate of the adsorption site is 'b'. $E_1(r)$, representing the metal + adsorbate system in the ground state, is designated (M + A). Here we chose $E_1(\infty) = 0$. An optically excited state of the system $(M + A)^*$ leads to photodesorption via propagation along the solid E_2 curve. Asymptotically, the excitation energy approaches the free atomic fluorescence frequency $\hbar\omega_{OPT}$. Trapping in the excited $(M + A)^*$ state is excluded in the sketch. $E_2^+(r)$ for an excited state leading to ionic ESD is represented by the dashed line $(M^- + A^+)$. If both incident and ejected electrons are Auger emitted to the vacuum, the asymptotic energy difference between the $(M^- + A^+)$ and the (M + A) states is the atomic ionization potential V_I. If one or both electrons finish in the Fermi sea of the solid, the threshold $V_I - \phi$ or $V_I - 2\phi$ applies, where ϕ is the work function of the substrate. Ionic desorption energies are measured with respect to the horizontal dashed line.

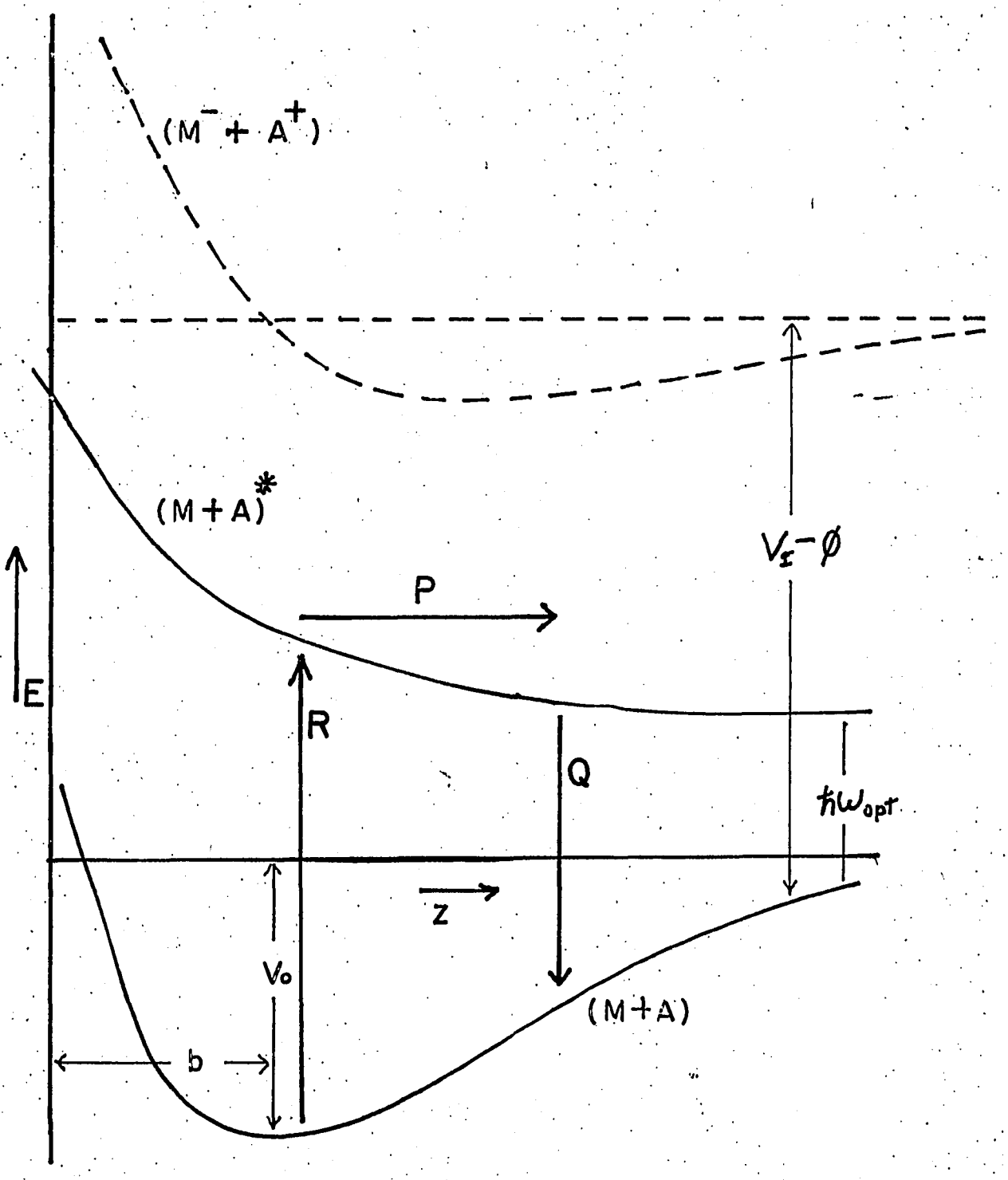

FIG. 2.1

Chapter III: Quenching via Surface Plasmon Excitation

This section is devoted to developing a model for the non-radiative decay of an optically excited neutral particle in the vicinity of the surface. Knowledge of the decay function, Q(z) is required for later use in numerical computation.of the cross sections for photodesorption of neutral atoms or molecules. We adopt a quenching model based on surface plasmon excitation accompanied by the decay of an excited atom to the ground state. The decay rate expression found does not possess lateral anisotropy, inasmuch as the model is based on a semi-infinite free electron gas.

Mechanisms for Non-Radiative Decay

Several possibilities for the dominant decay mode are ruled out. We are treating only neutral excited states; hence, we do not consider reneutralization processes which dominate the quenching in Electron Stimulated Desorption of ions.[1,2] We neglect here excitation modes involving photo-ionization, although desorption through this channel is possible, as in molecular photo-dissociation. Radiative decay processes are inefficient due to their long lifetimes, compared to the flight time to the detector.[32,33] Among non-radiative processes, decay of the neutral excited particle through an ionic intermediate set of states may occur. These are higher order processes which are not expected to contribute unless rapid tunnelling prevails.

The most plausible decay modes involve excitation of electron density fluctuations on the solid. In Fig. (3.1a, b) we illustrate the lowest order diagrams portraying electron-hole pair excitation as a decay mode. Here $|1_g\rangle$ ($|1_e\rangle$) represent occupation of the atomic ground (excited) states, while $|\vec{K}_i\rangle$ ($|\vec{K}_f\rangle$) denote the wavevectors of occupied initial (final) states in the bulk solid. Fig. (3.1a) is the 'direct' and Fig. (3.1b) is the 'exchange' contribution. Throughout our calculations the solid is taken to be a free electron-like metal occupying the semi-infinite region $z < 0$. This model has the merit of simplicity, and has proven to yield reasonable descriptions of several metals. Using the Fermi Golden Rule, we write down a prototype decay rate for the processes depicted:

$$Q = \frac{2\pi}{\hbar} \sum_{\vec{K}_i, \vec{K}_f} |\langle 1_{K_f}, 1_g | \frac{e^2}{|r-r'|} | 1_{K_i}, 1_e \rangle - \langle 1_{K_f}, 1_g | \frac{e^2}{|r-r'|} | 1_e, 1_{K_i} \rangle|^2 \times$$
$$\times f^0_{\vec{K}_i} (1 - f^0_{\vec{K}_f}) \delta(\hbar\omega_{\vec{K}_i, \vec{K}_f} - \hbar\omega)$$

Here f^0 is the Fermi distribution in the metal. The energy $\omega_{\vec{K}_i, \vec{K}_f}$ of the electron-hole pair, and the atomic energy loss ω appear in the delta function.

The computation of such a decay function is quite complex, due to the presence of Coulomb matrix elements. Moreover, it is well known that in bulk materials, the elementary excitations, plasma oscillations, compete at long wavelengths with pair excitation.[36-38] The plasma frequency $\omega_p = \left[\frac{4\pi e^2 n}{m}\right]^{\frac{1}{2}}$ sets the threshold for bulk plasmon excitation, with this mode dominating over pair excitation above threshold. For short wavelengths, i.e. $k > k_{FT}$, the plasmon spectrum merges into electron hole pair excitations, with damping of the collective plasma waves. Such modes are absent in the expression above for Q(z).

We assume that the pre-eminent loss mechanism for optically excited atoms outside a semi-infinite dielectric is coupling to the elementary surface excitations. Numerous theoretical and experimental investigations over several years have revealed the existence of travelling wave solutions called surface plasmons, whose excitation threshold is $\sigma_0 = \omega_p/\sqrt{2}$.[39-41] Thus a non-radiative decay channel is accessible whenever the atomic energy loss upon decay exceeds $\hbar\sigma_0$. As in the bulk plasmon case, the surface plasmon is expected to dominate the decay above threshold. In this analysis, we neglect other contributions to decay.

The Surface Quasi-Mode Formalism

An analytic expression for Q(z) is most convenient for use in computation. We turn to an approximate formalism for the surface plasmon which

has been developed recently for use in Photoemission studies.[42,43] One introduces an anzatz known as the Surface Quasi-Mode (SQM). This is a hybrid excitation resembling the surface plasmon at long wavelengths, and incorporating particle-hole excitations at short wavelengths by replacing them with a single simple pole.

The evaluation of the decay rate starts with Fermi's Golden Rule:

$$Q(Z) = \left\langle \frac{2\pi}{\hbar} |\langle f|H'|i\rangle|^2 \delta(E_f - E_i) \right\rangle$$

Here H' is the atom-solid interaction Hamiltonian. The matrix element is taken between occupation number states of the system. The brackets indicate that ensemble averaging over initial and final states of the solid is to be performed. It is sufficient to take the solid initially in the ground state at zero temperature. We assume $|i\rangle = |1_e, VAC\rangle$. Here the atomic excited state is occupied, with the solid free of excitation. For $|f\rangle$ we have $|1_g, 1_{K_\perp}\rangle$. The atom decays to state 1 creating a final state surface quasi-mode with wavevector $\hat{K}_\perp$ lying in the plane parallel to the surface. These final states are summed over.

Surface excitations do not propagate in the z direction; hence, there is no coupling to the atomic motion normal to the surface. Note that our neglect of momentum transfer in assuming recoilless transitions in the transport equations is justified with this model interaction. The transverse recoil

has negligible effect on the angular dependence of the desorption pattern.

We apply the formalism of Reference (42) to the problem at hand, introducing $\underline{a}^{\dagger}_{\vec{K}_\perp}$, $\underline{a}_{\vec{K}_\perp}$ as creation and annihilation operators for the SQM excitation. These obey commutation relations appropriate to bosons. We denote by $\sigma_{\vec{K}_\perp}$ the SQM dispersion relation; that is, the frequency of an excitation with wavevector $\vec{K}_\perp$ in the surface plane. The quantized electrostatic potential is given by:

$$\underline{\phi}(\vec{r}) = \sum_{\vec{K}_\perp} g(\vec{K}_\perp)\, e^{-K_\perp |z|} \left[e^{-i\vec{K}_\perp \cdot \vec{r}}\, \underline{a}_{\vec{K}_\perp} + e^{+i\vec{K}_\perp \cdot \vec{r}}\, \underline{a}^{\dagger}_{\vec{K}_\perp} \right] \tag{3.1}$$

Here the position $\vec{r} = (\vec{r}_\perp, z)$. The coupling constant is:

$$g(\vec{K}_\perp) = \left[\frac{\pi \hbar \sigma_0^2}{|K_\perp| \sigma_{\vec{K}_\perp}} \right]^{\frac{1}{2}} \tag{3.2}$$

where $\sigma_0 = \omega_p/\sqrt{2}$. The quantization area has been taken to be unity. The potential decays exponentially with z both inside and outside the surface.

We assume that the strongest coupling occurs for excitations whose wavelengths are large compared to the atomic size. The long wavelength variation in $\underline{\phi}(\vec{r})$ over atomic dimensions is small enough for us to treat the atom-surface interaction Hamiltonian in the dipole approximation.

For short wavelength excitations, this approximation becomes cruder, but still permits us to estimate the magnitude of the decay rate. The Hamiltonian for the system is:

$$\underline{H} = \underline{H}_0 + \sum_{K_\perp} \hbar \omega_{K_\perp} \left(\underline{a}^\dagger_{K_\perp} \underline{a}_{K_\perp} + \tfrac{1}{2} \right) + \underline{H}'$$

where

$$\underline{H}' = \underline{\mu} \circ \vec{\nabla} \underline{\phi}(\vec{r})$$

Here H_0 is the atom-solid Hamiltonian neglecting the decay inducing terms. The second term is the SQM self-energy, which plays no further role. The electric dipole moment operator for the perturbed atom is $\underline{\vec{\mu}}$. The decay rate which it is our task to evaluate is given by:

$$Q(z) = \frac{2\pi}{\hbar} \sum_{K_\perp} \left| \langle 1_g, 1_{K_\perp} | \underline{\vec{\mu}} \circ \vec{\nabla} \underline{\phi}(\vec{r}) | 1_e, \text{VAC} \rangle \right|^2 \times \delta(E_2 - E_1 - \hbar \omega_{K_\perp}) \tag{3.3}$$

Here E_1, E_2 are the atomic energies before and after quenching. All higher prder processes, with the exception of those contributing to the surface plasmon, are neglected.

The spacial operators are separated into components along the z and transverse directions:

$$\underline{\vec{\mu}} = \underline{\mu}_z \hat{z} + \underline{\vec{\mu}}_\perp$$

$$\vec{\nabla} = \hat{z} \frac{\partial}{\partial z} + \vec{\nabla}_\perp$$

Now we calculate the operator $\vec{\mu} \cdot \vec{\nabla}\Phi(\vec{r})$. Here $\vec{r} = (\vec{r}_\perp, z)$ are the atomic mass center coordinates. The desorbing particle is treated as a point dipole. Normally, our interest lies in decays at $z > 0$, but the SQM matrix elements inside the solid are kept track of. Wherever double signs occur, the upper denotes the region $z > 0$. We find:

$$\vec{\mu} \cdot \vec{\nabla}\Phi(\vec{r}) = \sum_{\vec{K}_\perp} g(\vec{K}_\perp) e^{-K_\perp |z|} \left\{ [-i\vec{K}_\perp \cdot \vec{\mu}_\perp \mp K_\perp \mu_z] e^{-i\vec{K}_\perp \cdot \vec{r}} a_{\vec{K}_\perp} + [i\vec{K}_\perp \cdot \vec{\mu}_\perp \mp K_\perp \mu_z] e^{+i\vec{K}_\perp \cdot \vec{r}} a^+_{\vec{K}_\perp} \right\}$$

The matrix element appearing in Eq. (3.3) is now taken. We neglect interferences between states of the atom and solid in both initial and final states, thus:

$$|1e, vac\rangle = |1e\rangle |vac\rangle$$

$$|1g, 1_{\vec{q}_\perp}\rangle = |1g\rangle |1_{\vec{q}_\perp}\rangle$$

The second factor in each state describes the surface plasmon occupation on the surface. The states $|1e\rangle, |1g\rangle$ describe the desorbing particle, thus they depend on the mass center coordinate $\vec{r}$ and on $\vec{\zeta}$, the electronic wave function coordinate relative to $\vec{r}$. The matrix

element is:

$$\langle 1_g, 1_{\vec{q}_\perp} | \vec{\mu}_0 \cdot \vec{\nabla} \mathcal{Q}(r) | 1_e, VAC \rangle =$$

$$= \sum_{\vec{K}_\perp} g(K_\perp) e^{-K_\perp |z|} \Big\{ \langle 1_{q_\perp} | a_{K_\perp} | VAC \rangle \langle 1_g | -i \vec{K}_\perp \cdot \vec{\mu}_\perp \mp K_\perp \mu_z | 1_e \rangle \times e^{-i \vec{K}_\perp \cdot \vec{r}_\perp}$$

$$+ \langle 1_{q_\perp} | a^\dagger_{K_\perp} | VAC \rangle \langle 1_g | i \vec{K}_\perp \cdot \vec{\mu}_\perp \mp K_\perp \mu_z | 1_e \rangle \times e^{+i \vec{K}_\perp \cdot \vec{r}_\perp} \Big\}$$

Only the second term in the bracket can contribute, since

$$\langle 1_{\vec{q}_\perp} | a_{\vec{K}_\perp} | VAC \rangle = 0$$

while

$$\langle 1_{\vec{q}_\perp} | a^\dagger_{\vec{K}_\perp} | VAC \rangle = \delta_{\vec{K}_\perp, \vec{q}_\perp}$$

The summation is thus contracted and the matrix element becomes:

$$\langle 1_g, 1_{\vec{q}_\perp} | \vec{\mu}_0 \cdot \vec{\nabla} \mathcal{Q}(r) | 1_e, VAC \rangle =$$

$$= g(\vec{q}_\perp) e^{-q_\perp |z|} e^{i \vec{q}_\perp \cdot \vec{r}_\perp} \langle 1_g | \mp q_\perp \mu_z + i \vec{q}_\perp \cdot \vec{\mu}_\perp | 1_e \rangle \quad (3.4)$$

The remaining matrix element on the right hand side is a spacial integration over coordinates within the atomic mass center system. One expects $\vec{r}$ dependence to remain after integration due to perturbation of the free atomic

wave functions by the solid. The transition moments in Eq. (3.4) above are written as the sum:

$$\langle g | \mp q_\perp \mu_z + i\vec{q}_\perp \cdot \vec{\mu}_\perp | e \rangle =$$

$$= \mp q_\perp \langle g | \mu_z | e \rangle + i\vec{q}_\perp \cdot \langle g | \vec{\mu}_\perp | e \rangle$$

We square Eq. (3.4) above, then substitute it into the expression for the decay rate Q(z) given in Eq. (3.3). The notation given just above is incorporated into the resulting equation for Q(z), which is:

$$Q(z) = \frac{2\pi}{\hbar} \sum_{\vec{q}_\perp} |g(\vec{q}_\perp)|^2 e^{-2q_\perp |z|} \delta(E_2(z) - E_1(z) - \hbar\omega_{\vec{q}_\perp}) \times$$

$$\times \left\{ q_\perp^2 |\langle g | \mu_z | e \rangle|^2 + |\vec{q}_\perp \cdot \langle g | \vec{\mu}_\perp | e \rangle|^2 \mp \left[i q_\perp \vec{q}_\perp \cdot \langle g | \vec{\mu}_\perp | e \rangle \langle g | \mu_z | e \rangle^* + \text{H.C.} \right] \right\}$$

(3.5)

The only term which depends on the sign of z is the cross term, which will shortly be seen to vanish in the course of angular integration. We normalized

to unit volume, thus the prescription for converting the $\vec{q}_\perp$ summation to an integration is:

$$\sum_{\vec{q}_\perp} \longrightarrow \frac{1}{(2\pi)^2}\int_0^{2\pi}\int_0^{\infty} q_\perp \, dq_\perp \, d\phi$$

Here ϕ is the azimuthal angle in the surface plane. We choose $\phi = 0$ to be along the direction of $\langle g | \vec{\mu}_\perp | e \rangle$. The angular integration can be done with the aid of a simplifying assumption about the plasmon dispersion relation $\omega_{\vec{q}_\perp}$, which appears in both the delta function and in $g(\vec{q}_\perp)$. Our model is translationally invariant in the surface plane, so there should be no preferred azimuthal direction either. We take SQM propagation to be isotropic, with $\omega_{q_\perp}$ independent of the angle ϕ. With this simplification, $\delta(E_2 - E_1 - \hbar\omega_{q_\perp})$ and $g(q_\perp)$ factor from the ϕ integration leaving only the terms in brackets in Eq. (3.5). The first of these has no ϕ dependence. The second we write as:

$$|\vec{q}_\perp \cdot \langle g | \vec{\mu}_\perp | e \rangle|^2 = q_\perp^2 \cos^2\phi \, |\langle g | \vec{\mu}_\perp | e \rangle|^2$$

We make the replacement:

$$|\langle g | \vec{\mu}_\perp | e \rangle|^2 = 2\,|\langle g | \mu_x | e \rangle|^2$$

Here one should note that both the x and y transition moments are the same apart from a phase factor. The sum of the cross terms in Eq. (3.5) is rewritten as:

$$-2q_\perp^2 \cos\phi \, \mathrm{Im}\left[\langle g|\mu_\perp|e\rangle\langle g|\mu_z|e\rangle^*\right]$$

Here one makes use of the identity $A - A^* = 2i\,\mathrm{Im}\{A\}$.

The decay rate expression is now the following:

$$Q(z) = \frac{1}{2\pi\hbar}\int_0^\infty dq_\perp \, q_\perp [g(q_\perp)]^2 e^{-2q_\perp|z|} \times I(q_\perp)\,\delta(E_2(z) - E_1(z) - \hbar\omega_{q_\perp})$$

where $I(q_\perp)$ is defined to be:

$$I(q_\perp) \equiv \int_0^{2\pi} d\phi \left\{ q_\perp^2 |\langle g|\mu_z|e\rangle|^2 + 2\cos^2\phi \, q_\perp^2 |\langle g|\mu_x|e\rangle|^2 \mp 2q_\perp^2 \cos\phi \, \mathrm{Im}\{\langle g|\mu_\perp|e\rangle^* \times \langle g|\mu_z|e\rangle^*\} \right\}$$

All of the azimuthal integrations are now trivial. We note that

$$\int_0^{2\pi} d\phi \cos^2\phi = \pi$$

and

$$\int_0^{2\pi} d\phi \cos\phi = 0$$

Thus the cross terms drop out.

Expression for the Non-Radiative Decay Rate

The results are now collected, making use of Eq. (3.2) for the form of g ($q_\perp$). The decay rate expression we now quote as:

$$\Gamma(z) = \sigma_0^2 \pi \theta(E_2 - E_1 - \hbar\omega_0) \left[|\langle g|\mu_z|e\rangle|^2 + |\langle g|\mu_x|e\rangle|^2 \right] \times$$
$$\times \int_0^\infty dq_\perp \frac{q_\perp^2 e^{-2q_\perp|z|}}{\omega_{q_\perp}} \delta(E_2(z) - E_1(z) - \hbar\omega_{q_\perp}) \qquad (3.6)$$

We have inserted the step function as a reminder that no SQM emission is possible below the threshold $\hbar\omega_0$. We denote by $q_0(z)$ the unique root of the resonance condition

$$E_2(z) - E_1(z) - \hbar\omega_{q_0} = 0 \qquad (3.7)$$

Here monotonicity of the energy difference is assumed. In systems where this condition is not fulfilled, one would generalize the result to a summation. Below the threshold the delta function does not contribute: there is no solution for the wavevector q_0. When $[E_2(z) - E_1(z)] \gg \hbar\omega_0$, q_0 is large. In this case we do not expect more than qualitative accuracy for this model. Short wavelength surface plasmons decay to electron-hole pairs. We have treated them as a single mode in the SQM formalism. Moreover, the dipole approximation requires q_0^{-1} to be large relative to atomic dimensions.

These reservations are ameliorated by the presence of the rapidly decaying exponential in the integrand of Q(z). The largest amplitudes occur when $q_\perp |z| \ll 1$, which is the case if $|z| \approx 0$, or $q_\perp a_0 \leq 1$. Here a_0 is the Bohr radius. The quenching effect of short wavelength components is thus important only in the immediate vicinity of the surface. The use of the one mode ansatz in the SQM formalism and the dipole approximation will not introduce serious error except when $z \approx 0$. For systems in which $[E_2(z=0) - E_1(z=0)] \approx \hbar\omega_0$, this model for Q(z) is a good description of the quenching as well.

In calculations to follow, the validity criteria for the decay rate expression are fulfilled. We take the adsorption site to lie at $z_0 > a_0$. Particles in the excited state cannot penetrate to small z, inasmuch as the

surface barrier is large compared to their thermal kinetic energy on excitation.

We note that the z dependence in Eq. (3.6) is not simply exponential. Additional z dependence enters through the transition matrix elements, and via energy dependence which remains after the final integration. Only for $z \gg a_0$ do the transition moments approach their free atomic values. The x and z matrix elements are not simply related in the surface region, but are related by Clebsch-Gordan coefficients in the asymptotic limit. The difference $[E_2(z) - E_1(z)]$ approaches in this limit the free atomic fluorescence energy. Thus Q(z) asymptotically tends to exponential decay. We remark that the states will be broadened due to tunnelling effects; hence the delta function might be replaced with a Lorentzian, whose width is the imaginary part of the self-energy. We neglect such effects here.

The final integration on $q_\perp$ is performed using the delta function. First we replace

$$\delta(E_2(z) - E_1(z) - \hbar\sigma_{q_\perp}) \rightarrow \frac{\delta(q_\perp - q_0)}{\hbar \left| \frac{d\sigma_{q_\perp}}{dq_\perp} \right|_{q_0}}$$

One should also note that

$$\omega_{q_0} \Big/ \frac{d\omega_{q_\perp}}{dq_\perp}\Big|_{q_0} = \frac{1}{2} \Big/ \frac{d\omega_{q_\perp}^2}{dq_\perp}\Big|_{q_0}$$

The non-radiative decay rate expression is:

$$Q(z) = \frac{2\pi}{\hbar}\omega_0^2\,\theta(E_2(z)-E_1(z)-\hbar\omega_0)\,e^{-2|z|q_0(z)} \times$$

$$\times \frac{[q_0(z)]^2\left[|\langle 1|\mu_z|e\rangle|^2+|\langle 1|\mu_x|e\rangle|^2\right]_{q_0}}{\left|\frac{d\omega_{q_\perp}^2}{dq_\perp}\right|_{q_0(z)}} \qquad (3.8)$$

Surface Plasmon Dispersion Relations

Now appropriate models for the SQM dispersion relation are examined for use in the decay rate. We shall express $\omega_{q_\perp}$ as a power series in $q_\perp$ of the form $\omega_{q_\perp} = \omega_0(1+\alpha_1 q_\perp+\alpha_2 q_\perp^2+\dots)$ It is apparent in Eq. (3.8) that the decay rate at threshold ω_0 will be finite so long as the leading $q_\perp$ dependence in $\omega_{q_\perp}$ is of no higher than the third power. This presents no problem.

A prescription leading to the dispersion relation has been given in the literature.[42,43] One makes use of the frequency and wavevector dependent dielectric function $\epsilon(K,\omega)$ of the bulk metal. First, the surface dielectric function is defined:

$$\bar{\epsilon}(\vec{K}_\perp,\omega) \equiv \frac{K_\perp}{\pi}\int_{-\infty}^{+\infty} dK_z \frac{1}{\epsilon(\vec{K},\omega)(K_\perp^2+K_z^2)} \quad (3.9)$$

The dispersion relation has been found to be given by :

$$\sigma_{K_\perp} = \sigma_0\left[\frac{1+\bar{\epsilon}(\vec{K}_\perp,0)}{1-\bar{\epsilon}(K_\perp,0)}\right]^{\frac{1}{2}} \quad (3.10)$$

Thus, $\sigma_{K_\perp}$ is connected to the bulk dielectric properties. For the static dielectric function, it will be convenient to employ the Linhard (RPA) result:[37,44]

$$\epsilon(\vec{K},0) =$$

$$= 1+\frac{q_{FT}^2}{4K_F^2}\frac{1}{x^2}\left[\frac{1}{2}+\frac{1-x^2}{4x}\ln\left|\frac{1-x}{1+x}\right|\right] \quad (3.11)$$

Here $x = k/2k_f$, where k_f is the Fermi wavevector. The Fermi-Thomas screening wavevector is defined to be $q_{ft} = \sqrt{3}\,\omega_p/v_F$. The ratio $(q_{FT}/2K_F)^2$ may be written as $\propto r_s/\pi$. Here r_s

is the plasma parameter expressing the average inter-electronic spacing in atomic units, while $\alpha = (4/9\pi)^{\frac{1}{3}}$.

In general, the procedure we have outlined does not readily yield analytic forms for $\sigma_{q_\perp}$, which are highly desirable in the present inquiry. The model for $\sigma_{q_\perp}$ which has found most use in the literature includes linear dispersion. We find this to be the simplest dispersion relation which yields qualitatively correct rendition of the properties of Q(z).[45-47]

First the effect of completely neglecting the plasmon dispersion is considered, letting $\sigma_{q_\perp} \to \sigma_0$. The formalism described abovereduces to this form by taking $K_\perp \to \epsilon = 0^+$ in Eq. (3.9). The surface dielectric function $\bar{\epsilon}(K_\perp, 0)$ vanishes after the long wavelength limit of the static Linhard Dielectric Function is substituted into Eq. (3.9).

The corresponding expression for the decay rate is found from Eq. (3.6). The delta function has no $q_\perp$ dependence; hence it factors from the integration. Non-radiative decay can occur in this model only at the surface plasmon threshold, which occurs at z_1. Here z_1 is the unique root of the condition $E_2(z_1) - E_1(z_1) = \hbar\sigma_0$. We note that

$$\int_0^\infty dq_\perp \, e^{-2q_\perp |z|} \, q_\perp^2 = \frac{1}{4|z|^3}$$

Thus the quenching rate neglecting dispersion is:

$$Q^{o}(z) = \frac{\sigma_o \pi}{4}\left[|\langle g|\mu_z|e\rangle|^2 + |\langle g|\mu_x|e\rangle|^2\right]_{z_1} \times \frac{\delta(z-z_1)}{|z_1|^3\,|d(E_e-E_g)/dz|_{z_1}} \qquad (3.12)$$

Here we used the identity $\delta(f(x)) = \delta(x-x_0)/|df/dx|_{x_0}$ with $f(x_0) = 0$.

The delta function which remains in $Q^{o}(z)$ above permits analytic solutions for σ_1 and σ_2 in one-dimensional calculations to be performed below. The quenching integral in the survival probabilities is replaced with a single pole. This may be a reasonable approximation when the dispersion is flat. Despite the simplicity of the dispersionless result, a more sophisticated model incorporating dispersion is required. For adsorption sites close to the surface, one expects quenching of the desorbing particles to be strong. In Eq. (3.12) the amplitude of $Q^{o}(z)$ depends only on the location z_1 of the plasma resonance. In fact for z_1 fixed, the attenuation falls off as $z_o \longrightarrow 0$, as examination of expressions which appear below for the survival probability will verify.

The formalism described above may be made to yield a linear dispersion relation, along with a rough estimate of the linear dispersion coefficient. This has been taken [46] to have an imaginary part, describing surface plasmon damping, which we neglect.

One takes the long wavelength limit in Eq. (3.11) for the static dielectric function, which yields the familiar result:

$$\epsilon_{RPA}(K,0) = 1 + q_{FT}^2/K^2$$

The surface dielectric function $\bar{\epsilon}(q_\perp,0)$ may be evaluated analytically using contour integration. After substitution of the above in Eq. (3.9) one analytically continues K_z to the entire complex plane. We denote $\gamma = K_z + i K_z$. The integration contour consists of the real axis plus the infinite semicircle in the upper half plane. There is one simple pole in the upper half plane, which resides at $\gamma = i\sqrt{K_\perp^2 + q_{FT}^2}$. Thus:

$$\bar{\epsilon}(K_\perp,0) = \frac{K_\perp}{\pi}\oint \frac{d\gamma}{(\gamma + i\sqrt{K_\perp^2+q_{FT}^2})(\gamma - i\sqrt{K_\perp^2+q_{FT}^2})}$$

Taking the residue:

$$\bar{\epsilon}(K_\perp,0) = \frac{K_\perp}{(K_\perp^2+q_{FT}^2)^{\frac{1}{2}}}$$

Note that $\bar{\epsilon}(q_\perp,0)$ is always < 1, and it is small when $K_\perp << q_{FT}$, which is the case of interest here.

The plasmon dispersion relation is generated by expanding Eq. (3.10)

to dominant order in the small parameter $\bar{\epsilon}$, viz:

$$\sigma_{K_\perp} = \sigma_0 \left[1 + \bar{\epsilon}/(1-\bar{\epsilon})\right]^{\frac{1}{2}}$$

$$\simeq \sigma_0 \left[1 + 2\bar{\epsilon}\right]^{\frac{1}{2}}$$

Expanding the square root,

$$\sigma_{K_\perp} \simeq \sigma_0 \left[1 + \bar{\epsilon}(K_\perp, 0)\right]$$

Inasmuch as $K_\perp$ is small, we further approximate

$$\bar{\epsilon}(K_\perp, 0) \simeq \frac{|K_\perp}{q_{FT}}$$

The final form of the linear dispersion relation we adopt is:

$$\hbar\sigma_{K_\perp} = \hbar\sigma_0 + \hbar s K_\perp \qquad (3.13)$$

the parameter s is the surface plasmon group velocity, which is constant in this model for excitations of all wavevectors. An explicit expression for s is found in terms of the velocity associated with the Fermi wavevector. Noting that $v_F = \hbar K_F/m$ we find:

$$s = \frac{v_F}{\sqrt{6}} \qquad (3.14a)$$

We used here the definitions of σ_0 and of the screening lenght q_{FT}.

It is useful to write the result in terms of the plasma parameter r_s, and the Hartree (double Rydberg) $\mathcal{E}_0 = 27.211$ ev, as follows:

$$\hbar s = \mathcal{E}_0 a_0 \frac{1}{\sqrt{6}\,\alpha\, r_s} \qquad (3.14b)$$

We show in Fig. (3.2) a variety of values of $\hbar\sigma_0$, and $\hbar s$ for values of r_s in the range of metallic densities.

The quasi-mode dispersion coefficient $\hbar s$ which was calculated above provides an order of magnitude estimate of the group velocity. We do not take the values in Fig. (3.2) as quantitatively correct ones in computations to follow, but we scan values of $\hbar s$ in the neighborhood predicted by our model. An experimental study of surface plasmon dispersion on the Aluminum (111) face has been done recently via inelastic LEED.[45] The value $\hbar s = 2 \pm 1 \times 10^{-8}$ ev-cm. was found. The corresponding value of $\hbar s$ predicted by our theory, using 14.2ev. for the Aluminum bulk plasma frequency, is 5×10^{-8} ev-cm. The agreement is thus only approximate. Moreover, Feibelman[46] has evaluated the RPA surface plasmon linear dispersion coefficients exactly for r_s values in the range 2 to 6. He found $\hbar s$ to be quite sensitive to the shape of the surface, which we approximate crudely in the semi-infinite free-electron

gas model used in developing the SQM formalism.

The quenching rate is now written in a form suitable for use in one-dimensional model calculations incorporating linear dispersion. First we have:

$$q_\perp(z) = \frac{E_2(z) - E_1(z) - \hbar\sigma_0}{\hbar S} \qquad (3.15)$$

Here use of Eq. (3.7) and Eq. (3.13) was made. After substitution the decay rate derived from Eq. (3.8) becomes:

$$Q(z) = \frac{\sigma_0^2 \pi}{\hbar^2}\Theta(E_2(z) - E_1(z) - \hbar\sigma_0) \times$$
$$\times \left[|\langle g|\mu_z|e\rangle|^2 + |\langle g|\mu_x|e\rangle|^2\right]_{\bar{z}} \times$$
$$\times \frac{(E_2(z) - E_1(z) - \hbar\sigma_0)^2}{S^3 (E_2(z) - E_1(z))} e^{-2\frac{|z|(E_2(z) - E_1(z) - \hbar\sigma_0)}{\hbar S}}$$

(3.16)

We have written the energy dependence explicitly. In a later section, this expression is evaluated using model energy functions and trial parameters.

Fig. 3.1a

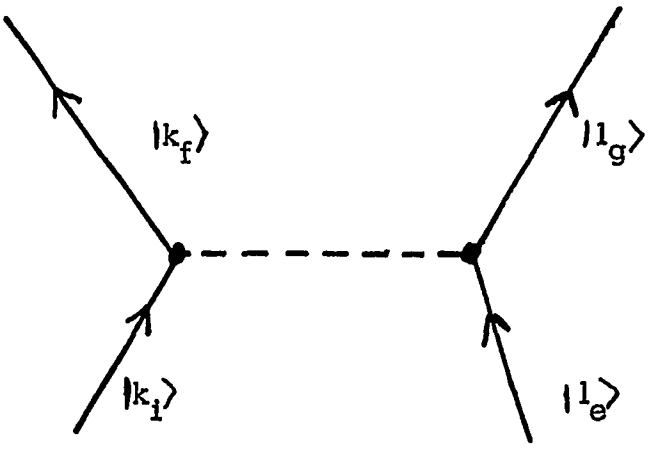

Fig. 3.1b

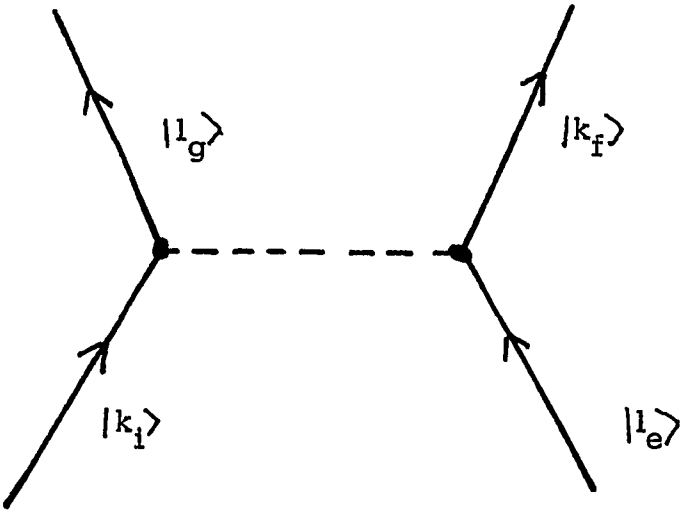

Figure 3.1 Lowest order diagrams for coulomb deexcitation of an excited adatom near a surface. Fig. (3.1a) is the 'direct' and Fig. (3.1b) is the 'exchange' contribution. Solid lines are electron propagators, while dashed lines represent coulomb matrix elements. The states $|1_g\rangle$, $|1_e\rangle$ are the 'ground' and 'excited' states of the atom-substrate system. The initial and final occupations of the solid are represented by $|k_i\rangle$ and $|k_f\rangle$.

r_s	$\hbar\sigma_0$ (ev.)	$\hbar\omega_p$ (ev.)	$\hbar S$ (ev-cm.)
1.0	33.3	47.1	1.13×10^{-7}
1.5	18.1	25.7	7.52×10^{-8}
2.0	11.8	16.7	5.64×10^{-8}
2.5	8.43	11.9	4.51×10^{-8}
3.0	6.41	9.07	3.76×10^{-8}
3.5	5.09	7.20	3.22×10^{-8}
4.0	4.17	5.89	2.82×10^{-8}
4.5	3.49	4.94	2.51×10^{-8}
5.0	2.98	4.22	2.26×10^{-8}
5.5	2.58	3.65	2.05×10^{-8}
6.0	2.27	3.21	1.88×10^{-8}

Figure 3.2 Representitive values of the SQM linear dispersion coefficient $\hbar S$ for r_s values in the range of metallic densities. The predicted group velocities lie in the range 10^{-8} to 10^{-7} ev-cm. Corresponding values of the surface plasma frequency $\hbar\sigma_0$, and the bulk plasma frequency $\hbar\omega_p$ are also shown.

Chapter IV: Theory of Photodesorption in One Dimension

This section initiates a study of photodesorption of neutral atoms or molecules from a substrate which is translationally invariant in the plane parallel to the surface. A thorough understanding of desorption in this simple system is useful before examining the more complicated dynamics encountered in angular dependent desorption studies. The excitation and quenching phases of neutral particle photodesorption are more susceptible to analytic solution than they are for ESD.

In this chapter we derive analytic expressions approximating the photodesorption cross sections for both states 1 and 2, after solving the transport equations in one dimension. In Chapter V the analysis continues with the presentation of detailed model calculations illustrating the qualitative features of photodesorption. Order of magnitude estimates of the excited state cross section are then performed, utilizing the quenching model developed in Chapter III.

The ability of photons to desorb chemisorbed or physiadsorbed species from solids has been known for some time.[48-53] More recently,[13,54-56] photodesorption has been distinguished under experimental conditions from a related process which involves local heating of the surface by incident photons. Photon stimulated thermal desorption then results.[57,58] The use of stainless steel in high vacuum apparatus has slowed progress in photodesorption research,[13] inasmuch as strong photodesorption from this material has been shown to occur.

Experimental interest in photodesorption has recently increased sharply. The cross section for photodesorption of neutral CO_2 from ZnO was

recently measured to be 4×10^{-19} cm^2. [56] This cross section includes all channels inasmuch as it was inferred from exponentially decaying desorbing particle currents. Utility for photodesorption as a surface cleaning and preparation technique is suggested strongly by this result, as carbon was believed to be present on the surface as a trace impurity.

Prior to our publication of some of the results to be presented below,[59] theoretical investigations of photodesorption appeared to be lacking. One dimensional desorption theories previously published have been phenomenological and applicable only to ESD. Our published results are significantly extended in the treatment to follow. Attention is given to the temperature and frequency dependence of neutral atom photodesorption, which selectively probes the Franck-Condon transition region of Fig. (2.1). By contrast ESD probes the entire ground state at once.

The Excitation Phase

The excitation phase is described by $R_\gamma(\vec{r})$. A model for this function is incorporated into the solution of the transport equations below. The substrate is assumed to remain in its ground state before and after excitation. The upward transition rate is approximated, using the Golden Rule, by:

$$R_\gamma(\vec{r}) = \left\langle \frac{2\pi}{\hbar} |\langle 2|H'|1\rangle|^2 \delta(E_2(\vec{r}) - E_1(\vec{r}) - \hbar\omega) \right\rangle$$

Here H' is the perturbing field Hamiltonian. The states $|n\rangle$, $n = 1, 2$, depend on $\vec{r}$. They describe perturbed atomic states of the adsorbed atom or

molecule. Only a single excitation channel is considered. Our attention is directed to the case where excitation occurs via simple atomic dipole transitions, hence the perturbing Hamiltonian is given semi-classically by:

$$H' = -\vec{\mu} \cdot \vec{E} = \mu_x E_0 \cos(\omega t)$$

Here $\vec{\mu}$ is the atomic dipole moment operator. We assume that a monochromatic photon beam falls on the surface at normal incidence. The photon flux F is given by:

$$F = \frac{c}{8\pi} \frac{E_0^2}{\hbar\omega}$$

A quantity analogous to the free atomic excitation cross section σ_A is given by the transition rate per atom per unit photon flux:

$$\chi_\gamma(\vec{r}) \equiv \frac{8\pi\omega}{c} |\langle 2|\mu_x|1\rangle|^2 \delta(E_2(\vec{r}) - E_1(\vec{r}) - \hbar\omega) \qquad (4.1)$$

As defined above $\chi_\gamma \to \sigma_A$ in the limit $z \to \infty$, where the wavefunctions and the resonance condition approach limiting values. We have averaged over the time, eliminating $(\cos^2 \omega t)$ dependence from $|\langle 2|H'|1\rangle|^2$

Note that :

$$R_\gamma(\vec{r}) = F \chi_\gamma(\vec{r}) \qquad (4.2)$$

More complex excitation processes involving intermediate states of the substrate have been proposed to explain recent experiments in which CO_2 was photodesorbed from ZnO.[55,56] Such processes are describable within this theory by substitution of appropriate matrix elements for $|\langle 2|H'|1\rangle|^2$.

Transport Equations

Cylindrical coordinates defined by $\vec{r} \equiv (\vec{r}_\perp, z)$, $\vec{v} \equiv (\vec{v}_\perp, z)$ are adopted, where $\vec{r}_\perp$, $\vec{v}_\perp$ lie parallel to the surface. The functions R, Q, E_n, P_n are independent of $\vec{r}_\perp$ in this translationally invariant system. The state 1 equilibrium distribution defined by Eq. (2.7) becomes:

$$P_1^0(\vec{r}, \vec{v}) \equiv P_1^0(z, v_z)\, A(v_\perp^2)$$

Where the z dependent distribution is:

$$P_1^0(z, v_z) = \left(\frac{M\beta}{2\pi}\right)^{\frac{1}{2}} \frac{\exp[-\beta E_z]}{\int dz' \exp[-\beta E_1(z')]} \qquad (4.3)$$

Here $E_z = \frac{1}{2}Mv_z^2 + E_1(z)$ is the energy associated with propagation normal to the surface.

For the translationally invariant substrate surface, the desorption problem is one dimensional on the microscopic scale. The function $A(v_\perp^2)$ is a gaussian normalized to the surface cell area, which is now arbitrary. The solutions P_1^1, P_2^1 are also found to be modulated by $A(v_\perp^2)$. The differential

cross sections defined by Eq. (2.18) will not display significant colatitude dependence; hence, we shall examine the total cross sections only. Emission will be directed primarily in the z direction, inasmuch as kT, the thermal kinetic energy associated with transverse propagation, is small compared to realistic values of $[E_2(z_o) - E_2(\infty)]$. Here z_o is the excitation coordinate.

The linearized transport equations to be solved are the following:

$$v\frac{\partial P_2'(z,v)}{\partial z} - \frac{1}{M}\frac{dE_2(z)}{dz}\frac{\partial P_2'(z,v)}{\partial v} = P_1^0(z,v)R(z) - P_2'(z,v)Q(z) \qquad (4.4a)$$

$$v\frac{\partial P_1'(z,v)}{\partial z} - \frac{1}{M}\frac{dE_1(z)}{dz}\frac{\partial P_1'(z,v)}{\partial v} = P_2'(z,v)Q(z) \qquad (4.4b)$$

A separation of variables was easily carried out in the transport equations (2.12a, b) for linear response, obtaining the above for the steady state description.

The total desorption cross sections follow integration of Eq. (2.16a) and (2.18) over $\vec{r}_\perp$ and over the gaussian $\vec{v}_\perp$ dependence. The result, for $L >> a_o$ is:

$$\sigma_n = \frac{1}{F}\int_0^\infty dv\, v\, P_n(z=L) \qquad (4.5)$$

The total ejection rate per unit sample area is:

$$\dot{N}_n(t) = N(t)\int_0^\infty dv\, v\, P_n(z=L) \qquad (4.6)$$

Here N(t) is the number of adsorbed particles per unit area on the surface at time t. The number of state n atoms ejected from the surface per unit time is obtained by multiplying $\dot{N}_n(t)$ by the sample area.

Experimentally, the ejection rate $\dot{N}$ including all channels, and $\dot{N}_2$ are of interest. The latter is monitored by detecting the free atomic fluorescent radiation at the frequency $\hbar\omega_{opt} = E_2(\infty) - E_1(\infty)$, which has energy of the order of one to several electron volts.

The solid line representing E_2 in Fig. (2.1) indicates the qualitatively reasonable behavior for $E_2(z)$, which is monotonically decreasing. Trapping in state 2 is neglected. The adsorption site coordinate indicated by b_o in Fig. (2.1) lies in the range 1 - 4 A^o in realistic systems.

It is also assumed that $[E_2(z) - E_1(z)]$ decreases monotonically with z. There is thus a unique solution to the resonance condition:

$$\hbar\omega = E_2(z_o) - E_1(z_o) \tag{4.7}$$

which appears in the delta function of Eq. (4.2) specifying R(z). This assumption may be relaxed at a later point if necessary. The excitation term in transport equation (4.4a) may now be simplified. We note that:

$$\delta(E_2(z_o) - E_1(z_o) - \hbar\omega) = \frac{\delta(z - z_o)}{\left|\frac{d(E_2 - E_1)}{dz}\right|_{z_o}}$$

For convenience we make use of the expressions for R(z), P_1^o (z v) to define:

$$g(z_o) \equiv \frac{\pi E_o^2}{\hbar} \frac{|\langle 2|\mu_x|1\rangle|^2_{z_o} \left(\frac{M\beta}{2\pi}\right)^{\frac{1}{2}} e^{-\beta E_1(z_o)}}{\left|\frac{d(E_2-E_1)}{dz}\right|_{z_o} \int dz' e^{-\beta E_1(z')}} \tag{4.8}$$

The delta function was used to evaluate all quantities at the resonance point z_o.

The state 2 transport equation is now written with a point excitation source as follows:

$$V\frac{\partial P_2'}{\partial z} - \frac{1}{M}\frac{dE_2}{dz}\frac{\partial P_2'}{\partial V} + P_2'Q = g(z_o)\, e^{-\frac{\beta M V^2}{2}} \delta(z-z_o) \tag{4.4c}$$

Solution for P_2'

Expressions for the photodesorption cross sections are now derived. First, the transport equation (4.4c) is integrated to find P_2' (z, v), after which the state 2 desorption cross section σ_2 is obtained. The result for $P_2'(z, v)$ is then substituted into Eq. (4.4a) to obtain $P_1'(z, v)$, and subsequently the ground state photodesorption cross section. The monotonically repulsive shape we assume for $E_2(z)$ ensures that the condition $\theta(E_2(z) - E_2(\infty)) = 1$ is always satisfied. Here $\theta(x)$ is the step function.

The coordinates at excitation are z_0, v_0. We define the thermal speed carried over from the ground state $S \equiv |V_0|$, and the speed at an arbitrary point $u = |V|$. No frictional forces affect propagation in this model, hence the total energy is a constant of the motion given by:

$$E = \frac{1}{2} M S^2 + E_z(z_0)$$

A lower bound on the z excursion of the atomic motion is set by the classical turning point z_{min} where the speed u vanishes. This point is the root of $E = E_z(z_{MIN})$. Barring deexcitation, a desorbing particle moves directly from z_0 to $z = \infty$ when v_0 is positive. A reflection at z_{min} occurs when v_0 is toward the surface.

We separate $P_2'(z, v)$ into outgoing and incoming components, distinguished by + or - superscripts. The substitution:

$$P_2'(z,V) = \Theta(V) P_2^+(z,u) + \Theta(-V) P_2^-(z,u) \tag{4.9}$$

allows us to separate the transport equation (4.4c) into separate equations for P_2^+ and P_2^- plus a boundary condition for $u = 0$. Making use of the identity $\delta(x) = \frac{d\Theta(x)}{dx}$ the transport equation becomes:

$$\begin{aligned} &\Theta(V)\left[u \frac{\partial P_2^+}{\partial z} - \frac{1}{M}\frac{dE_2}{dz}\frac{\partial P_2^+}{\partial u} + Q P_2^+\right] \\ &- \Theta(-V)\left[u \frac{\partial P_2^-}{\partial z} - \frac{1}{M}\frac{dE_2}{dz}\frac{\partial P_2^-}{\partial u} - Q P_2^-\right] = g(z_0)\delta(z-z_0) e^{-\frac{\beta M u^2}{2}} \\ &- \delta(u)\frac{1}{M}\frac{dE_2}{dz}\left[P_2^+ - P_2^-\right] \end{aligned} \tag{4.10}$$

Away from the turning point at u = 0, the new set of transport equations is now:

$$u\frac{\partial P_2^{\pm}}{\partial z} - \frac{1}{M}\frac{dE_2}{dz}\frac{\partial P_2^{\pm}}{\partial u} \pm Q P_2^{\pm} = \pm g(z_0)\,\delta(z-z_0)\,e^{-\frac{\beta M u^2}{2}} \tag{4.11a}$$

At the turning point we obtain the boundary condition:

$$\lim_{u\to 0} P_2^{+}(z,u) = \lim_{u\to 0} P_2^{-}(z,u) \tag{4.11b}$$

Here equation (4.10) was integrated over v on the range $v \in [-\eta, +\eta]$ where $\eta = 0^{+}$. After performing the trivial integrations, the limit $\eta \to 0$ was taken. We assumed that gradients of P_2^{+} and P_2^{-} both either remain finite or approach the same infinite limit as $u \longrightarrow 0$.

The next objective is to transform equation (4.11a) to a new set of variables in which the differentiation on the speed is eliminated. The variables ϕ and $\xi = \frac{1}{2}Ms^2$ accomplish this. Here ξ is the thermal kinetic energy at excitation. The required transformation is:

$$\phi = z$$

$$\xi = \frac{1}{2}Mu^2 + E_2(z) - E_2(z_0)$$

$$P_2^{\pm}(z,u) \longrightarrow P_2^{\pm}(\phi,\xi) \tag{4.12}$$

The physically intuitive solutions satisfy

$$\Theta\left(\tfrac{1}{2}\pm M u^2\right) = 1$$

where the speed is now given by the function:

$$u(\phi,\xi) = \sqrt{\frac{2}{M}\left[\xi + E_2(z_0) - E_2(\phi)\right]} \tag{4.13}$$

Under the transformation indicated, the derivatives in Eq. (4.11a) transform as follows:

$$\frac{\partial P_2^{\pm}(z,u)}{\partial z} \longrightarrow \frac{\partial P_2^{\pm}(\phi,\xi)}{\partial \phi} + \frac{d E_2(\phi)}{d\phi}\frac{\partial P_2^{\pm}(\phi,\xi)}{\partial \xi}$$

$$\frac{\partial P_2^{\pm}(z,u)}{\partial u} \longrightarrow M u(\phi,\xi)\frac{\partial P_2^{\pm}(\phi,\xi)}{\partial \xi} \tag{4.14}$$

We find that Eq. (4.11a) assumes the form:

$$u(\phi,\xi)\frac{\partial P_2^{\pm}(\phi,\xi)}{\partial \phi} \pm Q(\phi) P_2^{\pm}(\phi,\xi) = \pm g(z_0)\delta(\phi - z_0) e^{-\frac{\beta M u^2}{2}}$$

Further simplification results from dividing by $u(\phi,\xi)$ and using the delta function to substitute $\xi = u(\phi,\xi)$ on the right, with the result:

$$\frac{\partial \rho_2^{\pm}}{\partial \phi} \pm \frac{Q \rho_2^{\pm}}{u} = \pm \frac{g(z_0)}{\left(\frac{2\xi}{M}\right)^{\frac{1}{2}}} \delta(\phi - z_0)\, e^{-\beta \xi} \tag{4.15}$$

The solution of the transport equation continues with the adoption of a trial solution having the form:

$$\rho_2^{\pm}(\phi, \xi) \equiv \frac{e^{-\beta \xi}}{\left(\frac{2\xi}{M}\right)^{\frac{1}{2}}} \rho_2^{\pm}(\phi, \xi) \tag{4.16}$$

After cancelling some factors in Eq. (4.15) we obtain the final form of the transport equation suitable for solution when $u \neq 0$:

$$\frac{\partial \rho_2^{\pm}}{\partial \phi} \pm \frac{Q \rho_2^{\pm}}{u} = \pm g(z_0)\, \delta(\phi - z_0) \tag{4.17}$$

The solution at $\phi = z_{min}$ will satisfy the boundary condition derived from Eq. (4.11b), namely:

$$\lim_{\phi \to z_{min}} \rho_2^{+}(\phi, \xi) = \lim_{\phi \to z_{min}} \rho_2^{-}(\phi, \xi) \tag{4.18}$$

The integration of Eq. (4.17) is accomplished trivially. We integrate separately over the ranges of ϕ defined by the inequalities $z_0 + \epsilon \leq \phi \leq z_1$, $z_{min} < z \leq \phi \leq z_0 - \epsilon$, for which the delta function causes the right hand

side of Eq. (4.17) to vanish, and finally over the range $z_0-\epsilon < \phi < z_0+\epsilon$

Here $\epsilon = 0^+$. For the first case we have:

$$\int_{z_0+\epsilon}^{z} \frac{d\rho_2^{\pm}}{\rho_2^{\pm}} = \mp \int_{z_0+\epsilon}^{z} d\phi \, \frac{Q(\phi)}{\mathcal{U}(\phi,\zeta)}$$

This yields the following solution, valid at $z \geq z_0+\epsilon$:

$$\rho_2^{\pm}(z,\zeta) = \rho_2^{\pm}(z_0+\epsilon,\zeta) \exp\left[\mp \int_{z_0}^{z} d\phi \, \frac{Q(\phi)}{\mathcal{U}(\phi,\zeta)}\right] \tag{4.19a}$$

Integrating over the second interval, one similarly finds a solution in the range $z_{min} < z \leq z_0-\epsilon$:

$$\rho_2^{\pm}(z,\zeta) = \rho_2^{\pm}(z_0-\epsilon,\zeta) \exp\left[\pm \int_{z}^{z_0} d\phi \, \frac{Q(\phi)}{\mathcal{U}(\phi,\zeta)}\right] \tag{4.19b}$$

Finally, we integrate in the neighborhood of z_0, defined by the interval

$z_0-\epsilon < \phi < z_0+\epsilon$. The delta function contributes here and we find:

$$\int_{z_0-\epsilon}^{z_0+\epsilon} d\phi \, \frac{\partial \rho_2^{\pm}(\phi,\zeta)}{\partial \phi} = \mp \int_{z_0-\epsilon}^{z_0+\epsilon} d\phi \, \frac{Q(\phi)\rho_2^{\pm}(\phi,\zeta)}{\mathcal{U}(\phi,\zeta)} \pm g(z_0)$$

The integral on the right vanishes, as it may be reduced to a form in which it is proportional to ϵ, namely:

$$\mp \epsilon \, \frac{Q(z_0)}{\left(\frac{2\zeta}{M}\right)^{\frac{1}{2}}} \left[\rho_2^{\pm}(z_0+\epsilon,\zeta) - \rho_2^{\pm}(z_0-\epsilon,\zeta)\right]$$

There is thus a discontinuity in the solution at z_o given by:

$$\rho_2^{\pm}(z_0+\epsilon,\xi) - \rho_2^{\pm}(z_0-\epsilon,\xi) = \pm g(z_0) \qquad (4.19c)$$

The discontinuity at z_o should be expected, inasmuch as a source of incoming particles resides there.

The solution for P_2' follows after matching the boundary conditions. For economy we abbreviate the exponents appearing in the solutions for $\rho_2^{\pm}$ by the following common form:

$$K(z_1,z_2) \equiv \int_{z_1}^{z_2} \frac{d\phi\, Q(\phi)}{\alpha(\phi,\xi)} \qquad (4.20)$$

The dependence of $K(z_1,z_2)$ on ξ is suppressed for the moment.

The boundary condition at z_{min}, Eq. (4.18), is used along with the solution for $\rho_2^{\pm}$ in Eq. (4.19b) to obtain:

$$\rho_2^{+}(z_0-\epsilon,\xi) = \rho_2^{-}(z_0-\epsilon,\xi)\, e^{-2K(z_{min},z_0)} \qquad (4.21)$$

Next, we assume that there is no incoming particle flux in the region where $z > z_o$. $E_2(z)$ is monotonically decreasing; hence no trapping of desorbing particles results. We impose the condition:

$$\rho_2^{-}(z_0+\epsilon,\xi) = 0$$

The remaining coefficients at $z_o \pm \epsilon$ were found with the use of Eqs. (4.21),

(4.19a, b, c) and the above. These are:

$$\rho_2^-(z_0-\epsilon,\xi) = g(z_0)$$

$$\rho_2^+(z_0-\epsilon,\xi) = g(z_0)\, e^{-2K(z_{min},z_0)}$$

$$\rho_2^+(z_0+\epsilon,\xi) = g(z_0)\left[1 + e^{-2K(z_{min},z_0)}\right]$$

The form of the solution for the probability density in terms of $\rho_2^{\pm}$ is given by the following, where we have used Eqs. (4.9), (4.12), (4.16):

$$\rho_2'(z,\xi) = \frac{e^{-\beta\xi}}{\left(\frac{2\xi}{M}\right)^{\frac{1}{2}}}\left[\theta(v)\rho_2^+(z,\xi) + \theta(-v)\rho_2^-(z,\xi)\right]$$

Now all the results are collected to write the solution to the transport equation for the excited state. At arbitrary z, ξ the solution is:

$$\rho_2'(z,\xi) = \frac{e^{-\beta\xi}\, g(z_0)}{\left(\frac{2\xi}{M}\right)^{\frac{1}{2}}}\Big\{\theta(z-z_0)\,\theta(v)\left[1+e^{-2K(z_{min},z_0)}\right]e^{-K(z_0,z)}$$
$$+\theta(z-z_{min})\,\theta(z_0-z)\,\theta(v)\,e^{-K(z_{min},z_0)}\,e^{-K(z_{min},z)}$$
$$+\theta(z-z_{min})\,\theta(z_0-z)\,\theta(-v)\,e^{-K(z,z_0)}\Big\} \qquad (4.22)$$

We inserted the step function $\theta(z-z_{min})$ to cut off the solution automatically at the turning point z_{min}, which depends on ξ and z_o. Only the large z limit of this result is required to evaluate the excited state desorption cross section. The full solution for arbitrary z is required in finding the transport solution for the ground state, P_1'.

All terms in the Eq. (4.22) have clear physical interpretations. First, one should note that the quenching integrals of the form $K(z_1, z_2)$ yield the decay probability along the particle trajectory from z_1 to z_2. Entities of this form in Eq. (4.22) appear with the lower integration limit closest to the surface, hence they are positive. The exponentials in which the quenching integrals appear are thus attenuating the emission probability. Quantities of the form:

$$S_2(z_1, z_2, \xi) \equiv \exp\left[-K(z_1, z_2, \xi)\right]$$

represent the probability for a desorbing particle to survive from z_1 to z_2 along its path without undergoing decay. Survival probabilities related to these appear in discussions of desorption which have appeared previously.[1,2] We recast the result into a more convenient form for discussion, displaying the survival probabilities:

$$P_2'(z,\xi) = \frac{e^{-\beta\xi} q(z_o)}{\left(\frac{2\xi}{M}\right)^{\frac{1}{2}}} \Big\{ \theta(V)\theta(z-z_o)\left[1+S_2^2(z_{min}, z_o)\right] S_2(z_o, z) + \theta(V)\theta(z-z_{min})\,\theta(z_o-z)\, S_2(z_{min}, z_o)\, S_2(z_{min}, z) + \theta(-V)\,\theta(z-z_{min})\,\theta(z_o-z)\, S_2(z, z_o) \Big\} \tag{4.23}$$

The first term in our result for P_2' Eq. (4.23) represents the outward desorbing particle flux at $z > z_o$. This is the term which survives when the cross section σ_2 is evaluated below. The factor $S_2^2(z_{min}, z_o)$ is the probability of surviving the round trip from z_o to the turning point z_{min} and back in the excited state. The quantity in brackets, namely $[1 + S_2^2(z_{min}, z_o)]$, is thus the sum of contributions from particles excited with outgoing velocities at z_o, which produce the '1', plus those directed toward the surface upon excitation. The overall factor of $S_2(z_o, z)$ further attenuates the outward flux in transit to z. Similarly, the second term in P_2' contains the outbound contribution at $z < z_o$. These particles have been reflected by the potential barrier at z_{min}. The interpretation of the third term representing inbound flux is analogous.

Photodesorption Cross Section, State 2

Next the photodesorption cross section for state 2 is obtained. The non-radiative decay rate Q(z) depends on coupling to the solid, and therefore vanishes at large z. The result for $P_2'(z, \xi)$ approaches an asymptotic value independent of z in the detection plane, located at $L \gg z_o$. The survival probability $S_2(z_o, z, \xi)$ approaches a constant as $z \to \infty$. The limiting form of the probability density is:

$$P_2'(z=\infty, \xi) = \frac{e^{-\beta\xi} g(z_0)}{\left(\frac{2\xi}{M}\right)^{\frac{1}{2}}} \Theta(v)\,\Theta(\xi + E_2(z_0) - E_2(\infty)) \times \left[1 + S_2^2(z_{min}, z_0, \xi)\right] S_2(z_0, \infty) \tag{4.24}$$

The step functions inserted here emphasize the point that only those trajectories satisfying their conditions lead to particle desorption from the surface. Trapped excited states eventually decay to the ground state, possibly possessing enough energy to desorb.

The cross section is defined by Eq. (4.5). We take $P_2(z,v) \simeq P_2'(z,v)$ as we did previously in linearizing the transport equations, inasmuch as $P_2^0(z,v) \simeq 0$. The expression which results after the substitution of Eq. (4.24) is:

$$\sigma_2 = \frac{g(z_0)}{F} \int_0^\infty dV \frac{V e^{-\beta\xi}}{\left(\frac{2\xi}{M}\right)^{\frac{1}{2}}} \Theta(\xi + E_2(z_0) - E_2(\infty)) \times \left[1 + S_2^2(z_{MIN}, z_0, \xi)\right] S_2(z_0, \infty, \xi)$$

The integration on the ejection speed V may be converted to one on the thermal energy ξ. Recall that the thermal energy is uniquely connected to the asymptotic speed through energy conservation by

$$\xi = \frac{1}{2} M V^2 + E_2(\infty) - E_2(z_0)$$

Under the permissible change $V dV \rightarrow d\xi/M$ the lower limit on the resulting integral is zero; ξ is necessarily positive definite. The photon flux F is $\frac{cE_0^2}{8\pi\hbar\omega}$. Eq. (4.8) defines $g(z_0)$. The resulting cross section for free atomic fluorescence upon photodesorbing is:

$$\sigma_2(z_0,\beta) = A(z_0,\beta) \int_0^\infty \frac{d\xi\, e^{-\beta\xi}}{\xi^{\frac{1}{2}}} \Theta(\xi + E_2(z_0) - E_2(\infty)) \times \left[1 + S_2^2(z_{MIN}, z_0, \xi)\right] S_2(z_0, \infty, \xi) \qquad (4.25a)$$

The coefficient $A(z_0,\beta)$ is independent of the perturbing photon flux as expected. It is given by:

$$A(z_0\beta) = \frac{4\pi\omega}{c}\frac{(\beta\pi)^{\frac{1}{2}} e^{-\beta E_1(z_0)}}{\int d\xi' e^{-\beta E_1(\xi')}} \frac{|\langle 2|\mu_x|1\rangle|^2_{z_0}}{\left|\frac{d(E_2-E_1)}{dz}\right|_{z_0}} \qquad (4.25b)$$

The final integration on ξ in Eq. (4.25a) for σ_z is difficult to perform analytically. The survival probabilities depend on ξ as does the step function. However, the boltzmann factor $\exp[-\beta\xi]$ heavily weights the integrand so that small ξ satisfying $\xi \leq kT$ contribute most of the intensity.

Only a small error is introduced into the result by neglecting the weak ξ dependence in the survival probabilities and step function which appear in Eq. (4.25a). The overall factor of $\xi^{-\frac{1}{2}}\exp(-\beta\xi)$ is retained. The temperatures of interest for desorption studies lie in the range where kT $\approx$ .025 ev., while the desorption energies $[E_2(z_0) - E_2(\infty)]$ are from one to several electron volts when z_0 is up to several angstroms. The scale of variation in E_2 is such that we may neglect energies of order kT in computing the speed, except in the immediate vicinity of z_0. The step function in Eq. (4.25a) may be removed from the integration, inasmuch as $\xi \leq \frac{1}{\beta} << [E_2(z_0) - E_2(\infty)]$. The only effect of neglecting $1/\beta$ here is a slight shift of the threshold. We replace the thermal energy ξ by its average value in the survival probabilities. That is, we replace $S_2(z_{min}, z_0, \xi)$

and $S_2(z_o, \infty, \xi)$ by their values for $\xi = 1/\beta$. The turning point at z_{min} is now approximated by the solution of $1/\beta = E_2(z_{min}) - E_2(z_o)$. In the low temperature limit, $z_{min} \longrightarrow z_o$. The width of the integration in $K(z_{min}, z_o, 1/\beta)$ is small. We have verified by expansion that for low temperatures, one may approximate:

$$S_2(z_{min}, z_o, 1/\beta) \simeq 1$$

Finally, the factor $S_2(z_o, \infty, 1/\beta)$ is removed from the integration. The remaining trivial integral is:

$$\int_0^\infty d\xi \frac{e^{-\beta\xi}}{\xi^{1/2}} = \frac{\Gamma(\frac{1}{2})}{\beta^{1/2}} = \left(\frac{\pi}{\beta}\right)^{\frac{1}{2}}$$

As a final step, the usage prevalent in the desorption literature is adopted. We identify the coefficient of σ_z as the optical excitation cross section from state 1 at temperature β and frequency ω. It is given by:

$$\sigma_{EX}(\beta, z_o) \equiv \frac{8\pi^2\omega}{c} \frac{e^{-\beta E_1(z_o)}}{\int dz' e^{-\beta E_1(z')}} \frac{|\langle 2|\mu_x|1\rangle|^2_{z_o}}{\left|\frac{d(E_2 - E_1)}{dz}\right|_{z_o}} \qquad (4.26a)$$

Here, there is a unique correspondence between z_o and ω by previous assumption. The single atom excitation cross sections have been ensemble averaged over all initial state 2 velocities resulting from Franck-Condon excitation. The resonances implied by the optical transition rate contracted

the spacial ensemble, whose width is set by E_1 and β, to a single point at z_0. The frequency dependence of $\sigma_{EX}(\beta, z_0)$ thus directly probes the energy differences for vertical transitions on Fig. (2.1).

The photodesorption cross section for optically excited particles is given in this approximation by:

$$\sigma_2(\beta, z_0) = \sigma_{EX}(\beta, z_0)\,\Theta(E_2(z_0) - E_2(\infty))\,S_2(z_0, \infty, \beta) \qquad (4.26b)$$

Here, the survival probability $S_2(z_0, \infty)$ attenuates the outgoing beam via a non-radiative decay process. Written explicitly:

$$S_2(z_0, \infty, \beta) = e^{-\left(\frac{M}{2}\right)^{\frac{1}{2}} \int_{z_0}^{\infty} \frac{dz\, Q(z)}{\left[\frac{1}{\beta} + E_2(z_0) - E_2(z)\right]^{\frac{1}{2}}}} \qquad (4.26c)$$

Ground State Desorption Cross Section

Methods similar to those employed in obtaining σ_2 yield the cross section for particles photodesorbing in the ground state. The full solution for σ_2 for large β is given in Appendix I. The result is:

$$\sigma_1(z_0, \beta) = \left(\frac{M}{2}\right)^{\frac{1}{2}} \sigma_{EX}(z_0, \beta) \int_{z_0}^{\infty} \frac{dz\, Q(z)\, S_2(z_0, z, \beta)}{\left[\frac{1}{\beta} + E_2(z_0) - E_2(z)\right]^{\frac{1}{2}}} \times \Theta\left[E_2(z_0) - E_2(z) + E_1(z) - E_1(\infty)\right] \qquad (4.27)$$

The denominator in Eq. (4.26c) and (4.27) is the approximate speed u(z) at the decay point z in either state.

One should expect this result intuitively. $\sigma_{EX} S_2(z_0,z)$ is the cross section associated with a particle excited to state 2 at z_0 attenuated by propagation to the point z. The probability of a decay over dz is $\frac{Q(z)\,dz}{u(z)}$. The step function ensures that the kinetic energy at z is sufficient to permit desorption. One integrates over all intermediate points along the desorption trajectory where decay can occur. The total photodesorption cross section in this model is simply the sum $\sigma_1+\sigma_2$. Particles desorbing in the excited state may be experimentally distinguished from those emitted in the ground state if one monitors their fluorescent radiation at the frequency $\hbar\omega = E_2(\infty) - E_1(\infty)$.

We shall explore the features of the final results of this section in the next chapter, where models for the unknown decay function Q(z) and for $E_1(z)$, $E_2(z)$ are adopted.

Chapter V: Evaluation of the Photodesorption Cross Section

The cross section for photodesorption of neutral particles in the excited state is now evaluated numerically. The systematics of variation in the expressions for σ_2, ν_{ex} obtained in the last chapter is examined. Our one dimensional analysis is facilitated by the adoption of effective potentials for $E_2(z)$, $E_1(z)$. The dominant decay mode for excited atoms or molecules is taken to be surface plasmon excitation, for which a decay rate was obtained in Chapter III. In order of magnitude calculations, we find that excited state photodesorption cross sections for low mass adsorbed species are large enough to encourage experimental studies.

Model Effective Potentials

The qualitative behavior required of E_1, E_2 for neutral atom desorption was outlined in the discussion of Fig. (2.1). In addition, we require $[E_2(z) - E_1(z)]$ to be monotonically decreasing with z. A variety of functions possessing the required properties are well known in molecular physics, among them the Lennard-Jones [60] and the Morse [23] potentials. The choice of form for E_n is not critical in this investigation, as we explore qualitative features and trends. The following form for $E_1(z)$ serves our purpose:

$$E_1(z) \simeq \frac{V_1 a^6}{(z+a)^6} - \frac{V_2 a^3}{(z+a)^3}$$

Here a long range dipole interaction and a short range London interaction are assumed. We model the excited state energy E_2 as a purely repulsive London interaction, omitting the long range attraction to prohibit trapping:

$$E_1(z) = \frac{A_2}{(1+a_2 z)^6} + E_2(\infty) \qquad (5.1)$$

In the above, $E_2(\infty)$ is the free atomic fluorescent frequency. A Born-Mayer potential for E_2 was used with similar results in preliminary computation.[61,21]

It is convenient to write $E_1(z)$ in terms of the chemisorption energy V_0, the adsorption site coordinate b, and a spring constant k, which defines the width of the harmonic part of E_1. We define:

$$\gamma \equiv \frac{1}{3}\left[\frac{K}{2V_0}\right]^{\frac{1}{2}}$$

for which

$$E_1(z) = V_0\left\{\frac{1}{(1+\gamma[z-b])^6} - \frac{2}{(1+\gamma[z-b])^3}\right\} \qquad (5.2)$$

The harmonic expansion which approximates E_1 near the minimum at $z = b$ is:

$$E_1(z) = -V_0 + \frac{1}{2}K(z-b)^2 \qquad (5.3)$$

Typical numerical values for the parameters which determine the cross section are displayed in Fig. (5.1). We shall not scan their full range of possible values. In Fig. (5.2), the functions $E_2(z)$ and $E_1(z)$ are plotted, with the parameter choice guaranteeing the monotonicity of $\hbar\omega(z) = E_2(z) - E_1(z)$. The dashed line is the plot of $\hbar\omega(z)$. Optical excitation at $z = b$ requires a 6 ev. photon. This energy lies in the ultra-violet where photodesorption fre-

quencies have been found.[13,62]

Excitation Cross Section

We now infer some of the qualitative features of photodesorption from the structure of $\sigma_{ex}, \sigma_2, \sigma_1$ as given in Chapter IV. Several approximations facilitating numerical computation will be made.

The excitation cross section $\sigma_{ex}(\omega,\beta)$ was given in Eq. (4.26a). It is an upper bound on the total cross section, viz:

$$\sigma_1(\omega,\beta) + \sigma_2(\omega,\beta) \leq \sigma_{ex}(\omega,\beta)$$

The dominant frequency dependence of the σ_2, σ_1 spectra mirrors the frequency dependence of σ_{ex}. The excitation cross section depends on the in the region near the adsorption site at $z = b$. The spectra of $\sigma_{ex}, \sigma_2, \sigma_1$ in the region near the adsorption site at $z = b$. The spectra of $\sigma_{ex}, \sigma_2, \sigma_1$ thus replicate the ground state distribution P_1^o, modulated by more slowly varying functions of the photon frequency. Scanning $\hbar\omega$ above the excitation threshold at $\hbar\omega_{opt} = [E_2(\infty) - E_1(\infty)]$ probes values of z_o progressively closer to the surface.

The most interesting temperatures lie in the range $kT \sim .025$ ev., for which thermal desorption will be negligible. The ground state population is sharply localized near the chemisorption site; hence, the behavior of $E_1(z)$ only in the region $z \sim b$ significantly affects σ_{ex}. Anharmonic terms in E_1 are important only where σ_{ex} has negligible amplitude. We therefore expect the excitation threshold at $\hbar\omega_{opt}$ to occur where the cross section is unobservably small.

For numerical evaluation, we make the harmonic approximation, Eq. (5.3), for E_1 in the excitation cross section. The partition function in Eq.(4.26a) is readily evaluated, with the result:

$$\int dz \exp[-\beta E_1(z)] = e^{\beta V_0}\left[\frac{2\pi}{\beta\kappa}\right]^{\frac{1}{2}}$$

The excitation cross section now has gaussian dependence on the atomic coordinate z_0 at excitation:

$$\sigma_{EX}(z_0,\beta) = (8\pi^2\alpha a_0^2)\frac{e^{-\frac{1}{2}\left(\frac{z_0-b}{\Gamma}\right)^2}}{\sqrt{2\pi}\Gamma}\frac{\omega(z_0)\,|\langle 2|x|1\rangle|^2_{z_0}}{\left|\frac{d\omega(z)}{dz}\right|_{z_0}} \qquad (5.4)$$

Here, a_0 is the Bohr radius, with all other quantities in atomic units. The coefficient has the value $8\pi^2\alpha a_0^2 = 1.6 \times 10^{-17}$ cm^2., which establishes that appreciable coupling exists to the excitation phase. The gaussian width $\Gamma \equiv (\beta\kappa)^{-\frac{1}{2}}$. We choose $\beta = 40$ ev.$^{-1}$ initially, for which $\Gamma \approx .5\, a_0$; hence, the ground state is localized. The region between $z_0 = b \pm \Gamma$, where the amplitude of σ_{EX} is large, is cross-hatched in Fig. (5.2). The peak amplitude of σ_{EX} decays as $(kT)^{-1/2}$, while the width Γ increases at elevated desorption temperature. One might modify the spectrum of σ_{EX} by quantizing the ground state, for low mass particles or low temperatures, replacing the normalized gaussian of Eq. (5.4) with a bose distribution of harmonic oscillator states. Temperature dependent effects on the quenching are discussed below.

The Condon Approximation [63] is used to evaluate the frequency dependent transition moment in σ_{EX} ; that is, we neglect the spacial variation in $|\langle 2|\mu_x|1\rangle|_{z_0}$, which is slowly varying compared to the sharp peaked structure in σ_{EX} . The variation of $|\langle \mu_x \rangle|$ from its free atomic value is taken to be a small perturbation. The numerical value $|\mu_x| \sim 10^{-18}$ esu-cm. is chosen for use in computation. This value corresponds to the 1s → 2p excitation of hydrogen. The factor $\omega(z_0)/|\omega'(z_0)|$ in σ_{EX} is also slowly varying for the energy functions chosen, as examination of Fig. (5.2) will verify.

In computation, we substitute Eq. (5.4) into the expression for the excited state photodesorption cross section given by:

$$\sigma_2(\omega,\beta) = \sigma_{EX}(\omega,\beta) S_2(z_0,\infty,\beta)\,\theta(E_2(z_0)-E_2(\infty)) \tag{5.5}$$

The survival probability $S_2(z_0, \infty, \beta)$ defined by Eq. (4.26c) is now written in the form:

$$S_2(z_0,\infty,\beta) = \exp\left[-\left(\frac{M}{2}\right)^{\frac{1}{2}} D(z_0,\infty,\beta)\right] \tag{5.6}$$

where

$$D(z_0,\infty,\beta) \equiv \int_{z_0}^{\infty} \frac{dz\, Q(z)}{\left[\frac{1}{\beta} + E_2(z_0) - E_2(z)\right]^{\frac{1}{2}}} \tag{5.7}$$

Here we note that an isotope effect is expected in photodesorption. Similar mass dependence has been noted experimentally and in the theory of ESD. [1,2]

The function $D(z_0, \infty, \beta)$ depends on the electronic states, hence, it is independent of isotopic mass. We are neglecting mass dependence in ν_{ex} as the ground state is represented as classical.

Quenching

We assume that the dominant decay channel involves creation of a final state surface plasmon with energy $\hbar\omega_{q_\perp} = \omega(z)$. Here, $\omega(z)$ is the loss $[E_2(z) - E_1(z)]$ in the internal energy of an adsorbate particle decaying at z. We examined this decay mode in Chapter III, where a quenching rate expression assuming linear plasmon dispersion was given in Eq. (3.16). Now we write Q as a function of energy loss ω, using the system of atomic units:

$$Q(\omega) = Q_0 \theta(\omega - \omega_0) \frac{\omega_0^2}{s^3} \left(\frac{\omega - \omega_0}{\omega}\right)^2 |\mu_{x1}|^2 e^{-2|z|/\left(\frac{\omega - \omega_0}{s}\right)} \tag{5.8}$$

We did not make the harmonic approximation for E_1 in computing Q. This function appears in the exponent in S_2, hence, its sensitivity to the detailed behavior of $[E_2 - E_1]$ away from $z_0 = b$ is taken into account. The coupling constant Q_0 is defined by:

$$Q_0 = \frac{2\pi R_\infty}{\hbar} \approx 1.3 \times 10^{17} \text{ sec}^{-1}$$

with $R_\infty = 13.6$ ev. We made the Condon approximation for the dipole transition moment in $Q(\omega)$ as in ν_{ex}, taking $|\langle 2|\mu_z|1\rangle| \approx 0$, $|\langle 2|\mu_x|1\rangle| \simeq .4$ atomic units. The initial and final states involved in excitation are merely interchanged for quenching.

The plasmon wavevector required for a decay at z is:

$$q_\perp(z) = \frac{\omega(z) - \sigma_0}{s}$$

The behavior of this function mirrors $\omega(z)$, plotted in Fig. (5.2). When the group velocity s is small and $\omega(z=0) > \sigma_0$, large wavevectors $q_\perp a_0 >> 1$ are required to create surface excitations in decays. The dipole approximation requires $q_\perp a_0 << 1$. However, one may estimate to order of magnitude in Eq. (5.8) that heavy damping of excited atoms or molecules should be expected near the surface.

The substrate properties in quenching are characterized by its mobile electron density n, or equivalently, by the plasma parameter $r_s \equiv [3/4\pi n]^{1/3}$. The plasmon threshold energy is:

$$\sigma_0 = \sqrt{\frac{3}{2}}\, r_s^{-\frac{3}{2}} \qquad (5.9a)$$

and the group velocity was estimated in Chapter III by:

$$s \approx v_F/\sqrt{6} = [\sqrt{6}\,\alpha\, r_s]^{-1} \qquad (5.9b)$$

where $\alpha = .521$. We write the decay rate displaying its dominant r_s dependence as follows:

$$Q(\omega, r_s) = \frac{4\sqrt{6}}{\pi} Q_0\, \Theta(\omega - \sigma_0)\, \frac{(\omega - \sigma_0)^2}{\omega} |\mu_x|^2 \times e^{-2\sqrt{6}\,\alpha |z| (\omega - \sigma_0) r_s}$$

For a low density substrate ($r_s >> 1$), ω_0 is small; hence, quenching can contribute, in principle, up to large spearations from the surface. However, the exponential r_s dependence implies that Q is non-negligible only quite near the surface. In a high density substrate, the effective quenching range extends to $\omega(z) = \omega_0$.

Photodesorption in the excited state only is possible when the photon frequency lies below ω_0. One should observe in Eq. (5.8) and (5.7) that S_2 is then 1. One may verify in Eq. (4.27) that the ground state desorption is then zero. Naively, we expect to observe a drop in σ_2, accompanied by the onset of ground state desorption, when the photon frequency is scanned upward past ω_0. The sharpness of this threshold is a measure of $\hbar s$, inasmuch as $Q \propto \beta_\perp^2$, to dominant order, just above threshold. The threshold effect will be observable, in practice, only if $\omega_0 \approx \omega(b)$, due to the sharp drop in the magnitude of σ_{ex} away from the adsorption site. This condition is fulfilled, with the parameters we chose, when $\omega_0 = 6$ ev., which corresponds to $r_s = 3.12$. If $\omega_0 > \omega(b)$, as in a high electron density substrate, one expects to observe a large unquenched photodesorption cross section σ_2 equal to σ_{ex}. We neglect here the effect of substrate electron density on the effective potentials $E_n(z)$.

The most interesting systems for study are those for which $\omega_0 < \omega(b)$. We select $r_s = 3.45$ for initial computation. This lies in the range of metallic densities, and corresponds to $\hbar\omega_0 = 5.2$ ev. The quenching mechanism cuts off for $z \geq 4.8$ A°, at which point $\hbar\omega(z) = \hbar\omega_0$. σ_{ex} is negligible here, so the threshold will not be observed. The plasmon group velocity

for this r_s value is estimated, by Eq. (5.9b), to be $\hbar s = 3.27 \times 10^{-8}$ ev-cm. Inasmuch as this is a rough approximation to the dispersion, we also vary $\hbar s$ independently of $\hbar \sigma_0$, bracketting values in the range 10^{-9} to 10^{-7} ev-cm. We also approximated the case where the amplitude of σ_{ex} at its peak suffers the heaviest attenuation. We maximized Q, by setting $dQ/ds = 0$ at $z = b$. This provided the value $\hbar s = 1.13 \times 10^{-8}$ ev-cm. for study.

In Fig. (5.3) the nonradiative decay rate Q is plotted as a function of energy loss $\hbar\omega$. In Fig. (5.4), we incorporate the models for E_2, and E_1 to plot Q as a function of the z coordinate at decay. The plasmon pole expected with a dispersionless surface plasmon model is evident for the small group velocities. Close to the surface, large wavevector excitations contribute to Q. The physically reasonable group velocities lie in the range 10^{-8} to 10^{-7}, for which Q declines monotonically with z. One expects the survival probability S_2 to rapidly decrease as the photon frequency is scanned to higher energy.

In Fig. (5.5), the effect of various substrates on the decay rate amplitude at $z = b$ is examined. $Q(z=b)$ is a measure of the attenuation that σ_{ex} should suffer at its peak amplitude. An almost exact resonance between the substrate plasma frequency and the energy gap is required to quench with appreciable strength, when the dispersion is small. In realistic systems, $\hbar\sigma_0$ and $\hbar s$ are coupled, hence, we plot the dashed curve, on which $\hbar\sigma_0$ and $\hbar s$ are varied together, in accord with Eq. (5.9a), (5.9b), The strongest quenching at $z = b$ is found for $r_s = 3.67$, for which $\hbar\sigma_0 = 4.75$ ev. It is likely that we considerably overestimate quenching effects below, when we study a system with $\hbar s = 10^{-8}$ ev-cm. and $\hbar\sigma_0 = 5.2$ ev.

Results and Discussion

Now the excited state photodesorption cross section $\sigma_2(\omega, \beta)$ is evaluated numerically for a number of hypothetical adsorbate-substrate combinations.

First, photodesorption of hydrogen chemisorbed at 300°K. on a substrate with $r_s = 3.45$ is portrayed in Fig. (5.6). Here the gaussian shape predicted for σ_{EX}, the dashed line, is seen, with peak amplitude $\sim 6 \times 10^{-17}$ cm.^{2} at $z_0 =$ b. Similar amplitudes for the excitation cross section have been deduced for ESD in experimental studies, although the excitation mechanism is quite different.[64,65] For H^+, the ESD excitation cross section is $\sim 10^{-17}$ cm.^{2}, while for O^+, $\sigma_{EX} \sim 10^{-16}$ cm.^{2}. The photodesorption cross section we calculate, $\sim 2 \times 10^{-18}$ cm.^{2} at its peak, should be readily measurable.[1] Smaller or larger dispersion coefficients produce spectra of σ_2 lying between those plotted, as we have deliberately maximized the quenching.

Fig. (5.7) shows the comparison of σ_2 for adsorbates of mass 1, 2, and 16 amu. on the same substrate as in the previous illustration. The isotope effect implied by Eq.(5.6) reduces the deuterium cross section to roughly 1/3 of its value for hydrogen. For oxygen, the flux is quenched by about six orders of magnitude in Fig. (5.7), to $\sim 1.6 \times 10^{-22}$ cm.^{2} in the neighborhood of the σ_{EX} peak. The frequency spectrum for 16 amu. is shifted downward in energy by about 1 ev. One expects reduced survival probability at high frequencies. Thus, skewing of the σ_2 spectrum to lower energy occurs when quenching couples effectively. Clearly, wherever there is strong quenching, desorption

cross sections for massive adsorbed atoms or molecules will be small.

For an isotopic mixture present on a surface, one should quite generally expect preferential ejection of the lighter species in the excited state, inasmuch as the exponent of S_2 has $[M]^{1/2}$ dependence. Isotope separation is negligible if quenching is weak, and absent when $\hbar\Gamma_0 > \hbar\omega$. Enrichment of the heavier species remaining on the surface and of the ground state desorbing flux is expected. Experimentally, the isotope effect may be used to deduce Γ_{EX} and to estimate the quenching integral $D(z_0, \infty, \beta)$, if photodesorption cross sections for isotopic species are separately known. One finds:

$$D(z_0,\infty,\beta) = \frac{Ln\left[\Gamma_2^{(1)}(\omega,\beta)/\Gamma_2^{(2)}(\omega,\beta)\right]}{\left[\frac{M_1}{2}\right]^{\frac{1}{2}}\left[\left(\frac{M_2}{M_1}\right)^{\frac{1}{2}}-1\right]}$$

Here, $M_2(M_1)$ and $\Gamma_2^{(2)}(\Gamma_2^{(1)})$ correspond to the mass and known experimental photodesorption cross section for the more (less) massive species residing on the surface. The isotopic bonding and anti-bonding E_n curves and their excitation cross sections are taken to be indistinguishable.

Isotope effects analogous to those described are well known in the ESD literature.[1,2,64-67] The ratio $\Gamma_2(H^+)/\Gamma_2(D^+) \sim$ 100-150 has been found for ESD of H^+ from tungsten. The survival probability $S_2 \sim 5 \times 10^{-6}$ is implied. For O^+ desorption from tungsten, $\Gamma_2(O^{16})/\Gamma_2(O^{18}) =$ 1.6 was found, implying that $S_2 \sim 4 \times 10^{-4}$.

In Fig. (5.8) we examine the dependence of the survival probability on the substrate electron density, and on the dispersion coefficient $\hbar S$. The treatment is crude, inasmuch as $E_2(z)$, $E_1(z)$ are taken to be the same for all

cases. Differences in the chemisorption parameters are thus neglected. We plot S_2 for a 1 amu. particle excited by a photon with $\hbar\omega = 6.05$ ev, corresponding to the peak of the excitation cross section. Substrates with $\hbar\sigma_0 \geq 4.5$ ev. ($r_s \leq 3.8$) are included. When $\hbar\sigma_0 > \hbar\omega$, $S_2 = 1$. In the dashed curve $\hbar\sigma_0$ and $\hbar s$ are varied together as suggested by Eq. (5.9a, b).

In general, S_2 is quite sensitive to the surface plasmon dispersion. However, the dashed curve in Fig. (5.8) indicates that one should expect survival probabilities in the range $[.25 - 1]$ for a 1 amu. adsorbed particle on a wide variety of substrates. One may obtain S_2 for massive adsorbates by scaling by the square root of the mass. Thus, for CO (M=28), we would estimate S_2 to lie in the range $[7.4 \times 10^{-4} - 1]$, while for CO_2 desorption, survival probabilities from $[1.2 \times 10^{-4} - 1]$ are suggested via surface plasmon decay over the same class of substrates. Setting aside differences in the chemisorption parameters, Fig. (5.8) suggests that photodesorption cross sections for light atoms are of similar order of magnitude for many combinations of solid and adsorbed atom or molecule. The cross section will be strongly substrate dependent for massive adsorbed species. Real combinations of surface and adsorbate frequently possess several adsorption geometries, for which quenching effectiveness will be drastically different.

We examine the frequency and temperature dependence of the survival rate for a 16 amu. particle in Fig. (5.9). A decrease in quenching effectiveness with temperature is expected from Eq. (5.7). We see that variation in S_2 over 100-600°K., the range of interest in desorption experiments, has little impact

on the quenching. The frequency dependence of S_2 is strong. The heavier quenching for excitation sites close to the surface originates in the rapid increase of Q(z). This behavior is apparent in Fig. (5.3), (5.4). We are led to hypothesize, in this simple model, that when several adsorption phases coexist on a surface, the ones closest to the surface are the most heavily quenched.

Finally, we look at the temperature dependence of the excited particle photodesorption cross section, in Fig. (5.10). The oxygenic combination of atom and substrate of the previous plot is examined. The excitation cross section broadens and declines in amplitude with increased temperature, as discussed earlier. Qualitatively similar behavior is expected if the ground state is quantized. There is little temperature dependence in the desorption cross sections, which stabilize at $\sigma_2 \sim 10^{-18}$ cm.^{2}. This lack of apparent temperature dependence in the peak value of σ_2 originates in competition between reduced excitation cross section, and increased survival probability. The near cancellation of these effects in this model calculation should not be expected in general.

Our picture of desorption predicts an almost monochromatic energy distribution for atoms emitted as fluorescent particles. This is in sharp contrast to the desorption energy spectra in ESD, where the shape of P_1 and E_2 are in effect integrated over, producing a broader distribution. The desorption kinetic energy E_D is simply:

$$\begin{aligned} E_D &= E_2(z_0) - E_2(\infty) \\ &= E_1(z_0) + \hbar\omega - E_1(\infty) - \hbar\omega_{opt} \end{aligned}$$

for the process we study. The selectivity of excitation should permit inference of the shape of E_2 and E_1 in the vicinity of a chemisorption site.

Systematic consideration of the ground state photodesorption cross section, given by Eq. (4.27), is deferred to the future. The step function appearing in the integrand of σ_j prohibits the escape of particles excited at $z_o \gtrsim .75\ A^o$, with our choice of potential curves. The ground state desorption threshold thus lies at $\hbar\omega \approx 6.7$ ev., where the excitation cross section is several orders of magnitude smaller than its peak value. When the adsorption site is quite close to the surface, large ground state photodesorption cross sections are expected.

Photodesorption can occur via a variety of indirect processes which should be experimentally distinguishable from the direct optical excitation mechanism assumed in this paper. Photon-induced thermal desorption occurs via heating of the surface by the photon beam. Thermal desorption then takes place. The photon energy dependence of such a process will be weak. Another possibility is photoemission followed by electron stimulated desorption. An upper limit on these cross sections may be obtained via:

$$\sigma_{PHOTO-ESD} \leq Y \sigma_{ESD}$$

where Y is the photoemission yield of electrons above the ESD threshold. σ_{ESD} generally lies in the range $< 10^{-19} cm.^2$ for neutrals,[1] while Y is typically $\ll 1$. Such processes should be small, and are characterized by broader desorption energy spectra than photodesorption. Recent experiments have re-

vealed photodesorption of CO_2 from ZnO powder and crystals.[55,56] A substrate interaction mechanism is hypothesized to explain the formation of CO_2^- on a carbon contaminated surface. Illumination above the ZnO band gap is assumed to generate holes, permitting formation of neutral physiadsorbed CO_2, which then thermally desorbs.

The popular adsorption systems consisting of oxygen or hydrogen adsorbed on tungsten may be interesting subjects for photodesorption studies. The tungsten surface plasmon threshold lies at $\sim$17 ev., based on the bulk plasma frequency $\hbar\omega_p \sim 23.5$ ev.[68] The sums of the chemisorption energy and the atomic ionization energy lie in the same range. Taking this as an upper limit on the excitation energies to be expected in the neighborhood of adsorption sites, it is quite possible that unquenched emission may occur from some of the adsorption phases.

Summary

The direct dipole excitation mechanism we propose yields readily measurable estimated cross sections for fluorescent particle emission. Cross sections of the order 10^{-18} - 10^{-17} cm.^{2} are indicated for low mass species adsorbed $\sim$ 2 A^o from the surface. This photodesorption mechanism is characterized by sharply peaked frequency dependence of σ_2, and an almost monochromatic emission energy distribution. In ESD, for comparison, cross sections are weakly dependent on the incident electron energy, which is usually $\sim 10^2$ ev. The σ_2 spectrum sharpens somewhat for low desorption temperatures. When the substrate plasma frequency is high, quenching may be inoperative, and

large cross sections may be found even for massive adsorbate particles. On lower electron density substrates, quenching produces isotope selection in the outgoing beam, analogous to that observed in ESD. Linearity of the desorption rate with the photon flux should be observed.

More exact calculations, including predictions for specific adsorbate-substrate combinations are not feasible at present. This is principally due to the absence of detailed knowledge of the effective potentials. Photodesorption experiments should make it possible to probe these curves in the region of an adsorption site.

Chapter V: Figure Captions

Fig. 5.1: Typical numerical values for parameters determining the photodesorption cross section. Departures from these choices are indicated in the text.

Fig. 5.2: Model Effective Potential curves for photodesorption calculations. The parameter choices for $E_2(z)$, $E_1(z)$ are as specified in Fig. (5.1). The dashed line is the energy difference $\hbar\omega = E_2(z) - E_1(z)$.

Fig. 5.3: The Non-radiative Decay Rate $Q(\omega)$ via Surface Plasmon emission, plotted as a function of the atomic energy loss $\hbar\omega$. The threshold lies at $\hbar\sigma_o = 5.2$ ev. Values of $\hbar s$ corresponding to each $Q(\omega)$ curve are indicated, in ev-cm. The dashed line corresponds to $\hbar s$ estimated via Eq. (5.9b). The substrate is assumed to have $r_s = 3.45$.

Fig. 5.4: The Non-radiative Decay Rate $Q(z)$, plotted as a function of the z coordinate at decay. The model effective potentials portrayed in Fig. (5.2) were used in evaluating $Q(z)$. The cutoff for plasmon emission occurs at $z_1 = 4.82$ A.^{o}, corresponding to the surface plasma frequency $\hbar\sigma_o$. Other parameters are as in Fig. (5.3).

Fig. 5.5: The Non-radiative decay rate as a function of surface plasmon threshold energy $\hbar\sigma_o$, evaluated at the chemisorption site at $z = b = 2$ Angstroms. Several values of the group velocity $\hbar s$ are considered. For the dashed line, $\hbar s$ was

Chapter V: Figure Captions, continued

varied with $\hbar\sigma_0$ in accordance with the prescription given in Eqns. (5.9a,b), namely; $s = .6844\sigma_o^{2/3}$. When $\hbar\sigma_0 > 6.05$ ev., with the chosen parameters, no plasmon emission is possible. Circles plotted at $\hbar\sigma_0 = 5.2$ ev. correspond to points on Fig. (5.3).

Fig. 5.6: Excited State Photodesorption Cross Section and Excitation cross section for a 1 amu. particle chemisorbed at 300°K. on a substrate with $\hbar\sigma_0 = 5.2$ ev. The dashed line represents $\sigma_{EX}(\omega)$. The solid line is $\sigma_2(\omega)$. The location of the E_1 minimum at z = 2 A.° is marked. Quenching effectiveness was maximized at this point by choosing $\hbar S = 1.13 \times 10^{-8}$ ev-cm. Slight skewing of the σ_2 peak to smaller photon energies is evident.

Fig. 5.7: Mass Dependence of the Excited State Photodesorption Cross Section σ_2. Adsorbed particles at 300°K. representing $_1H^1$, $_1D^2$, and $_8O^{16}$ are portrayed, chemisorbed on the same substrate as in Fig. (5.6). The dashed line depicting σ_{EX} is independent of adsorbate mass. The same effective potentials were used for all atomic species.

Fig. 5.8: The Survival Probability S_2 as a function of substrate plasma frequency $\hbar\sigma_0$. S_2 evaluated at the chemisorption site, corresponding to $\hbar\omega = 6.05$ ev., is plotted for a 1 amu. particle at 300°K. Several group velocities $\hbar S$ in the range 10^{-9} to 10^{-7} ev-cm. are examined. For the

Chapter V: Figure Captions, continued

dashed curve, $\hbar s$ was varied with $\hbar\sigma_0$ as in Fig.(5.5). The vertical scale is logarithmic. Differences which one should realistically expect in the chemisorption parameters and antibonding effective potentials on different substrates are neglected.

Fig. 5.9: The survival probability $S_2(\omega,\beta)$ as a function of photon energy and temperature for a 16 amu. adsorbate. Here, $\hbar\sigma_0$ = 5.2 ev., and $\hbar s = 3.27 \times 10^{-8}$ ev-cm.

Fig 5.10: Temperature dependence of the Excited State Photodesorption Cross Section (solid line). Dashed lines denote σ_{ex} for T = 300,100, and 600 degrees K. The adsorbate mass is 16 amu. As before, $\hbar\sigma_0$ = 5.2 ev., and $\hbar s = 3.27 \times 10^{-8}$ ev-cm.

Fig. 5.1 Typical numerical values for parameters determining the photodesorption cross section. Departures from these choices are indicated in the text.

V_o	2 ev.	.074 atomic units
b	2 A.^{o}	3.78 "
k	6.14×10^3 gm/sec^2	.004 "
$E_2(\infty)$	3.75 ev.	.138 "
A_2	5.0 ev.	.184 "
a_2	3×10^7 cm.$^{-1}$	.159 "
kT	.025 ev.	9.2×10^{-4} "
$\lvert\langle\mu\rangle\rvert$	10^{-18} esu-cm.	.39 "
$\hbar\sigma_o$	5.2 ev.	.191 "
z_1	4.82 A.^{o}	9.11 "
$\hbar s$:	3.27×10^{-8} ev-cm	.227 "
	10^{-9} ev-cm.	.0069 "
	5×10^{-9} ev-cm.	.035 "
	10^{-8} ev-cm.	.069 "
	1.13×10^{-8} ev-cm.	.078 "

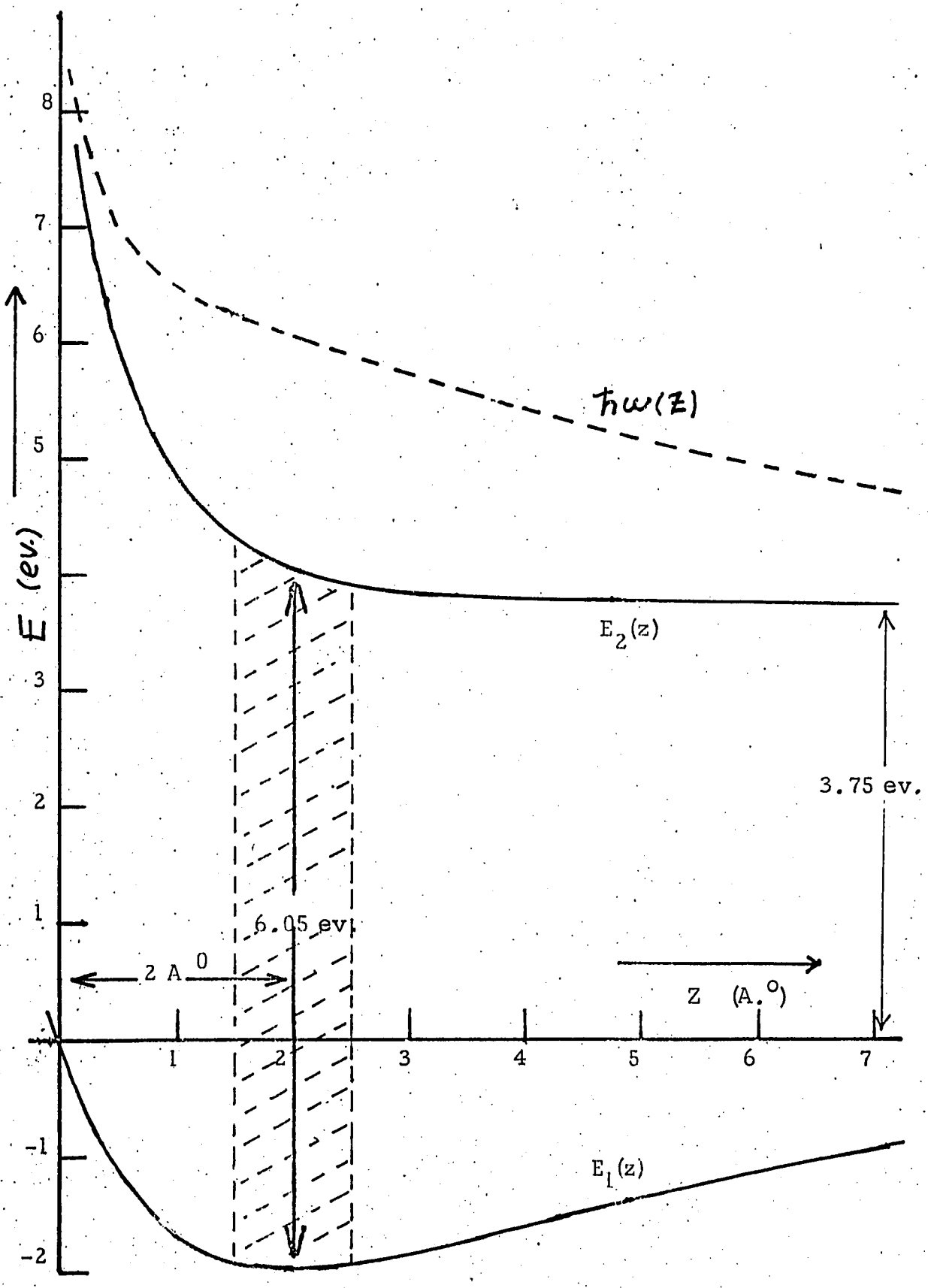
8
7
6
5
3
2
1
-1
-2
E (ev.)
$\hbar\omega(z)$
$E_2(z)$
$E_1(z)$
3.75 ev.
6.05 ev.
2 A 0
Z (A.°)
1
2
3
4
5
6
7

FIG. 5.2

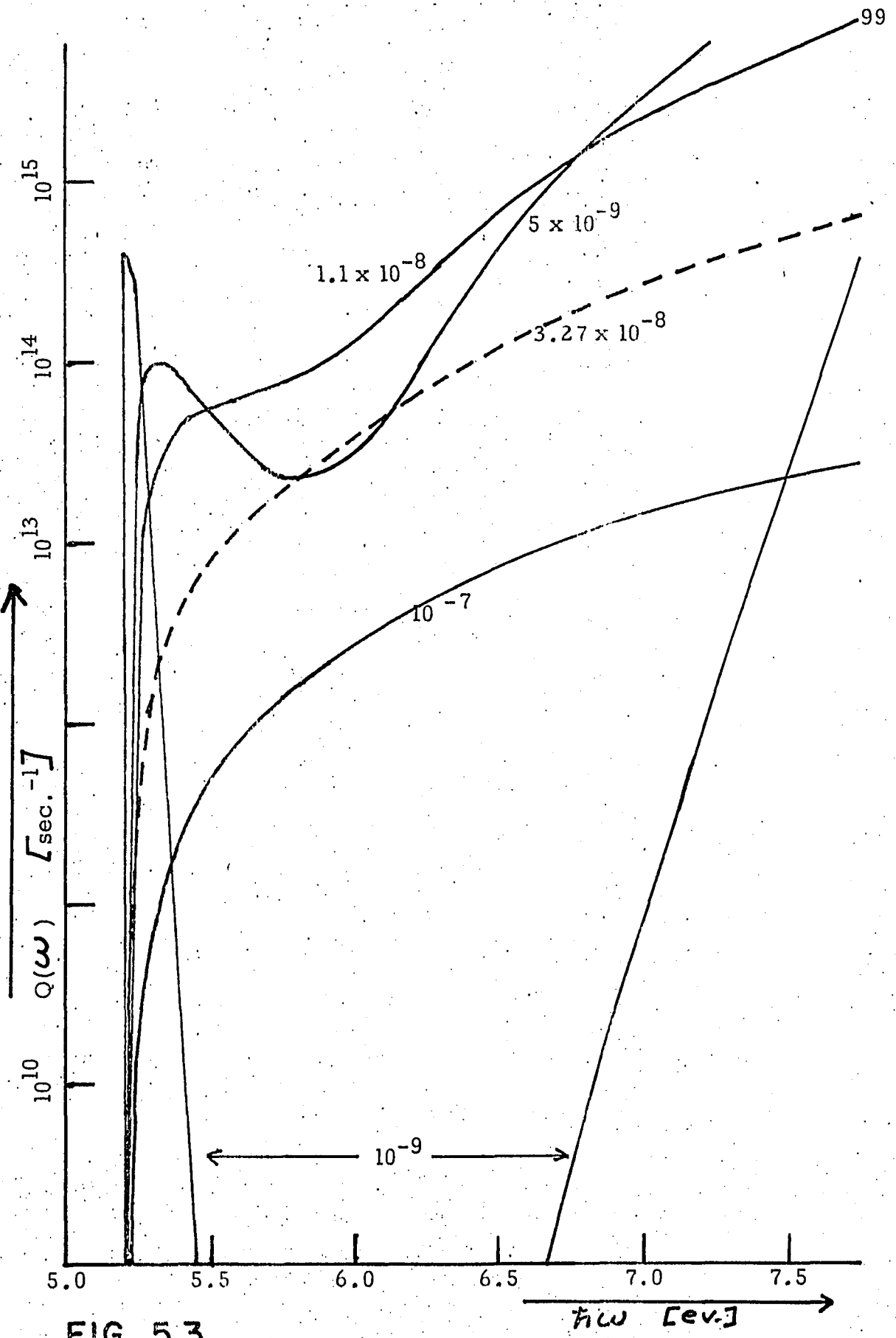
99
10^{15}
10^{14}
10^{13}
10^{10}
5×10^{-9}
1.1×10^{-8}
3.27×10^{-8}
10^{-7}
10^{-9}
$Q(\omega)$ [sec.$^{-1}$]
5.0
5.5
6.0
6.5
7.0
7.5
$\hbar\omega$ [ev.]

FIG. 5.3

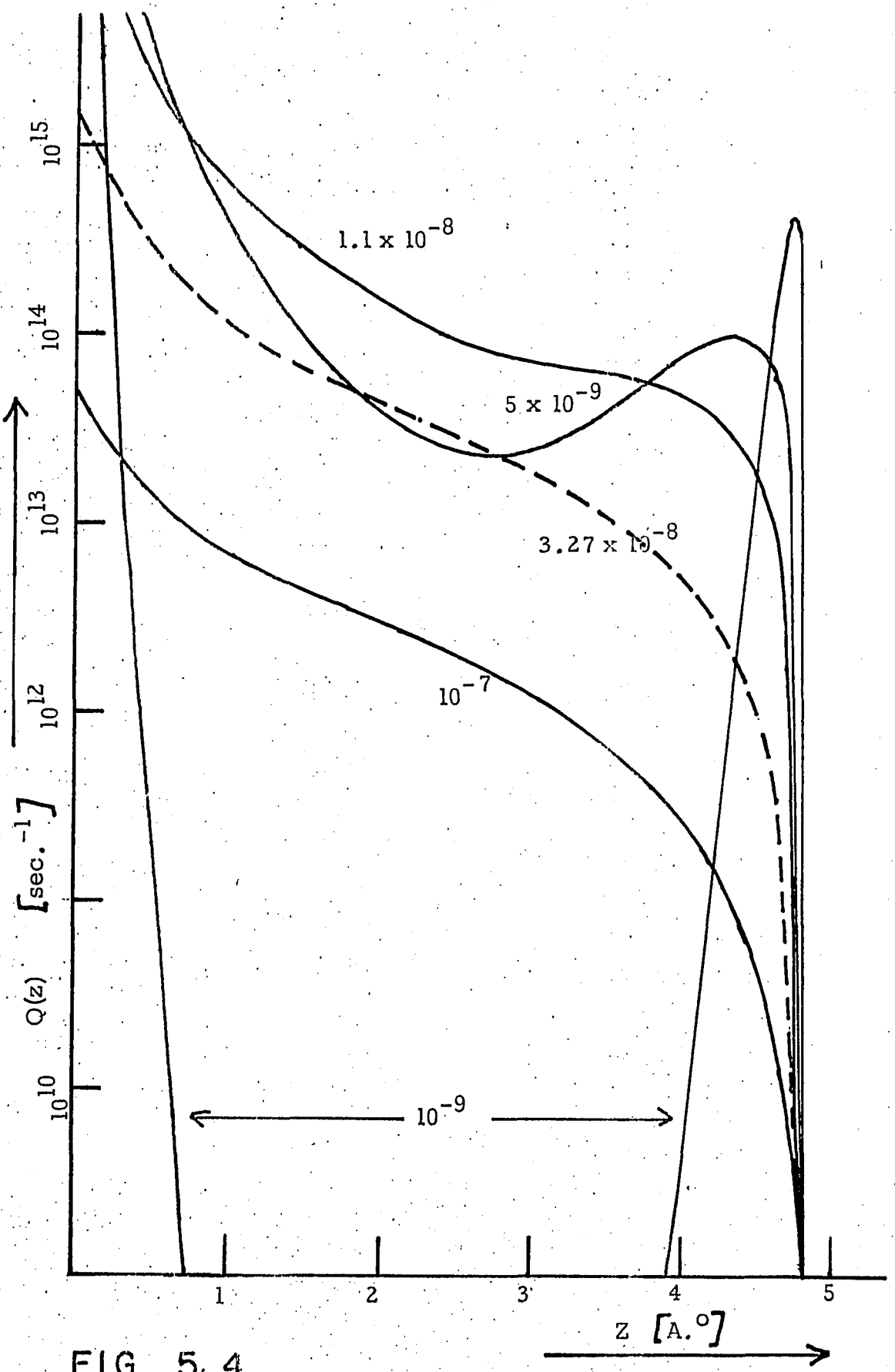
10^{15}
10^{14}
10^{13}
10^{12}
10^{10}
Q(z) [sec.$^{-1}$]
1.1×10^{-8}
5×10^{-9}
3.27×10^{-8}
10^{-7}
10^{-9}
1
2
3
4
5
Z [A.°]

FIG. 5.4

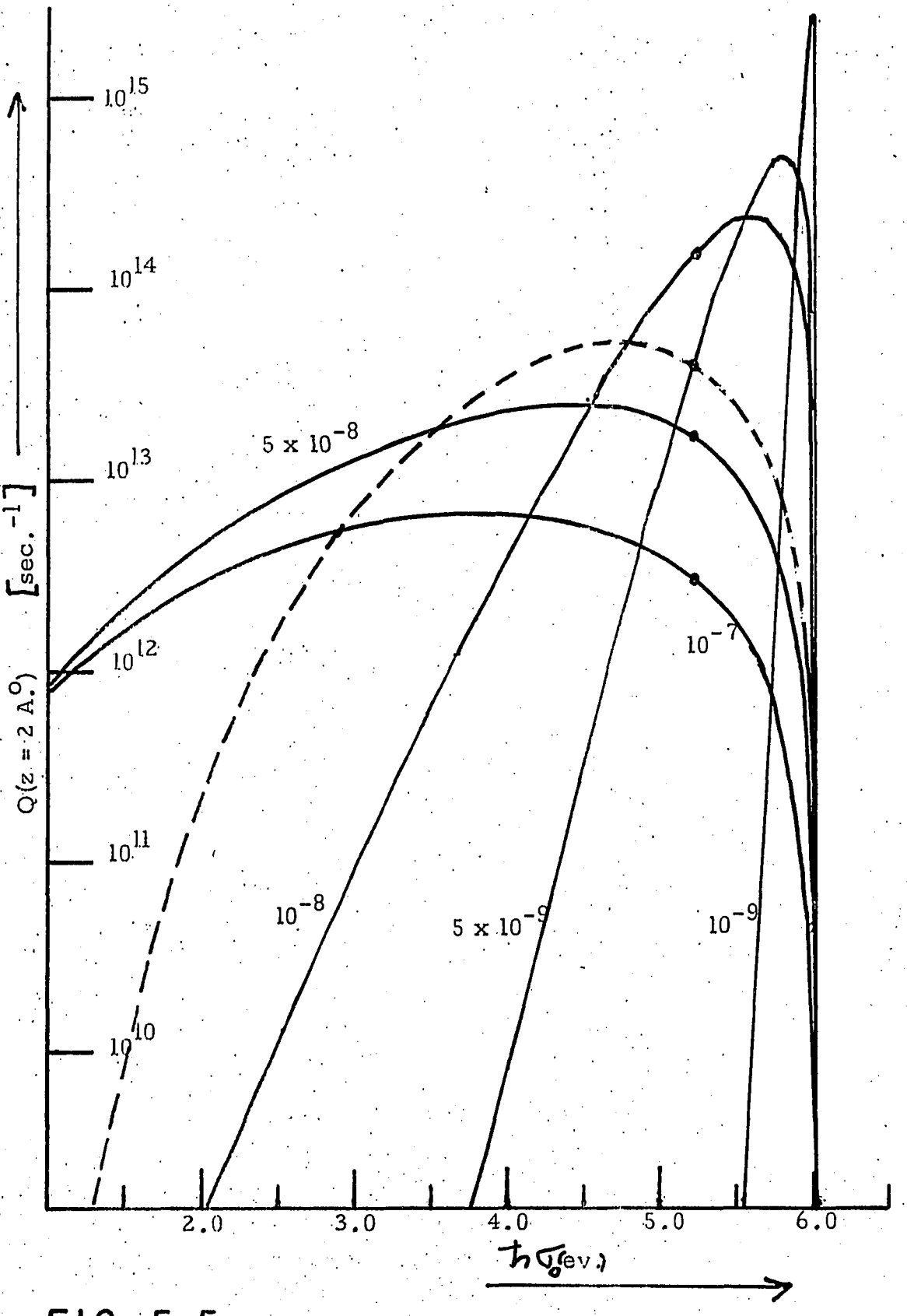
10^{15}
10^{14}
10^{13}
10^{12}
10^{11}
10^{10}
Q(z = 2 A.°) [sec.$^{-1}$]
5×10^{-8}
10^{-7}
10^{-8}
5×10^{-9}
10^{-9}
2.0
3.0
4.0
5.0
6.0
$h\sigma_0$(ev.)

FIG. 5.5

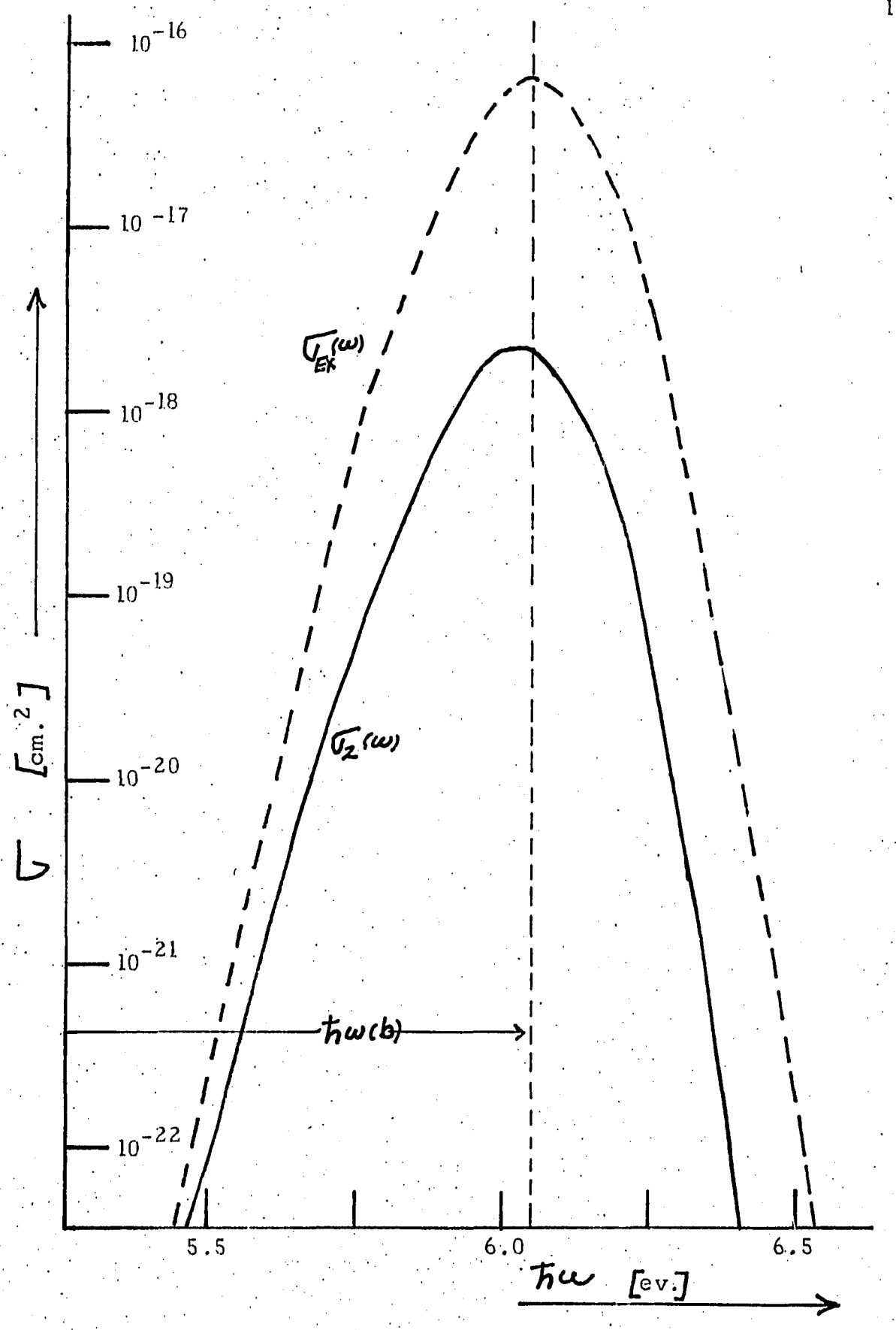
10^{-16}
10^{-17}
10^{-18}
10^{-19}
10^{-20}
10^{-21}
10^{-22}
σ [cm.^{2}]
$\sigma_{EX}(\omega)$
$\sigma_2(\omega)$
$\hbar\omega(b)$
5.5
6.0
6.5
$\hbar\omega$ [ev.]

FIG. 5.6

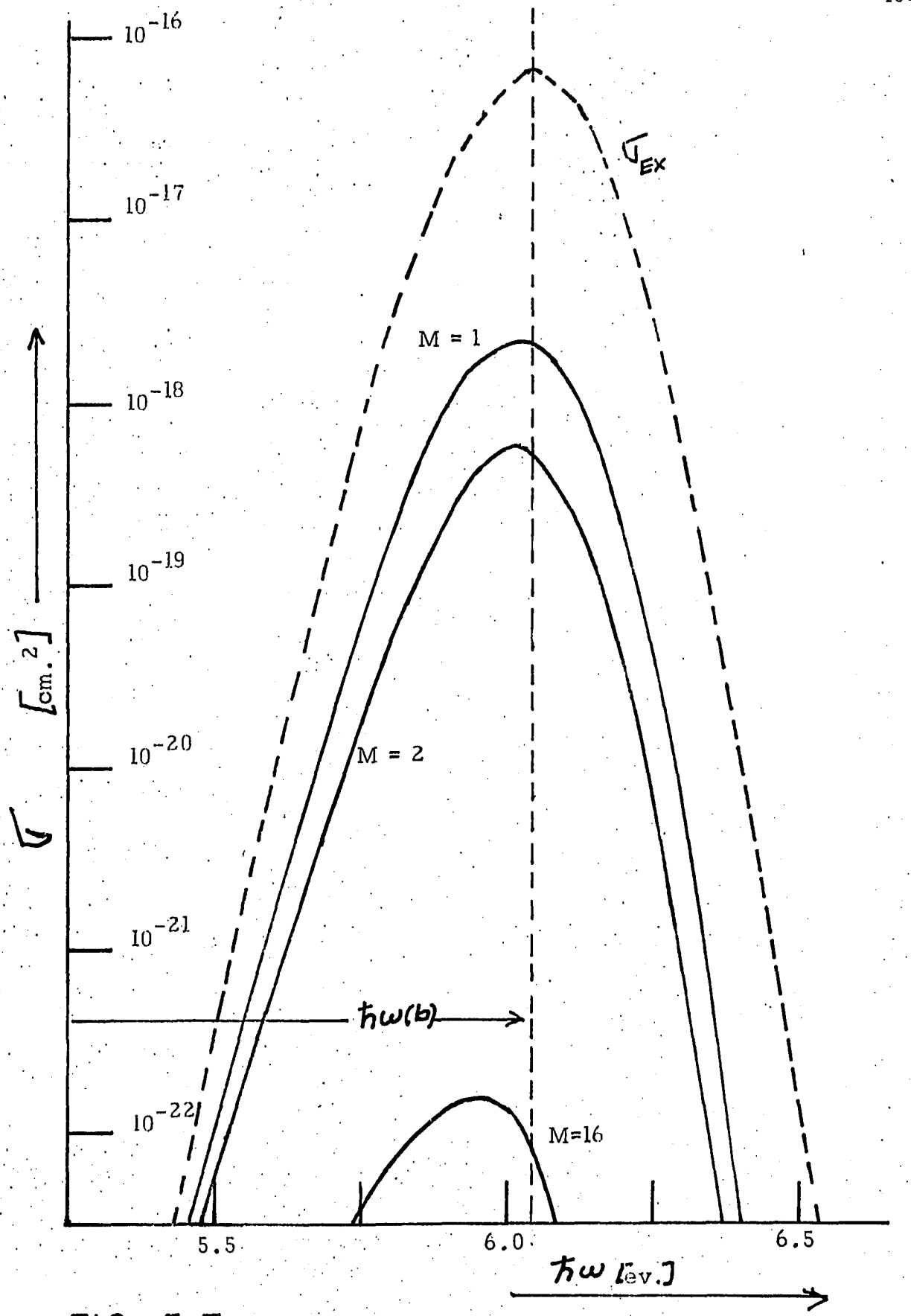
10^{-16}
10^{-17}
10^{-18}
10^{-19}
10^{-20}
10^{-21}
10^{-22}
σ [cm.^{2}]
σ_{EX}
M = 1
M = 2
M=16
$\hbar\omega(b)$
5.5
6.0
6.5
$\hbar\omega$ [ev.]

FIG. 5.7

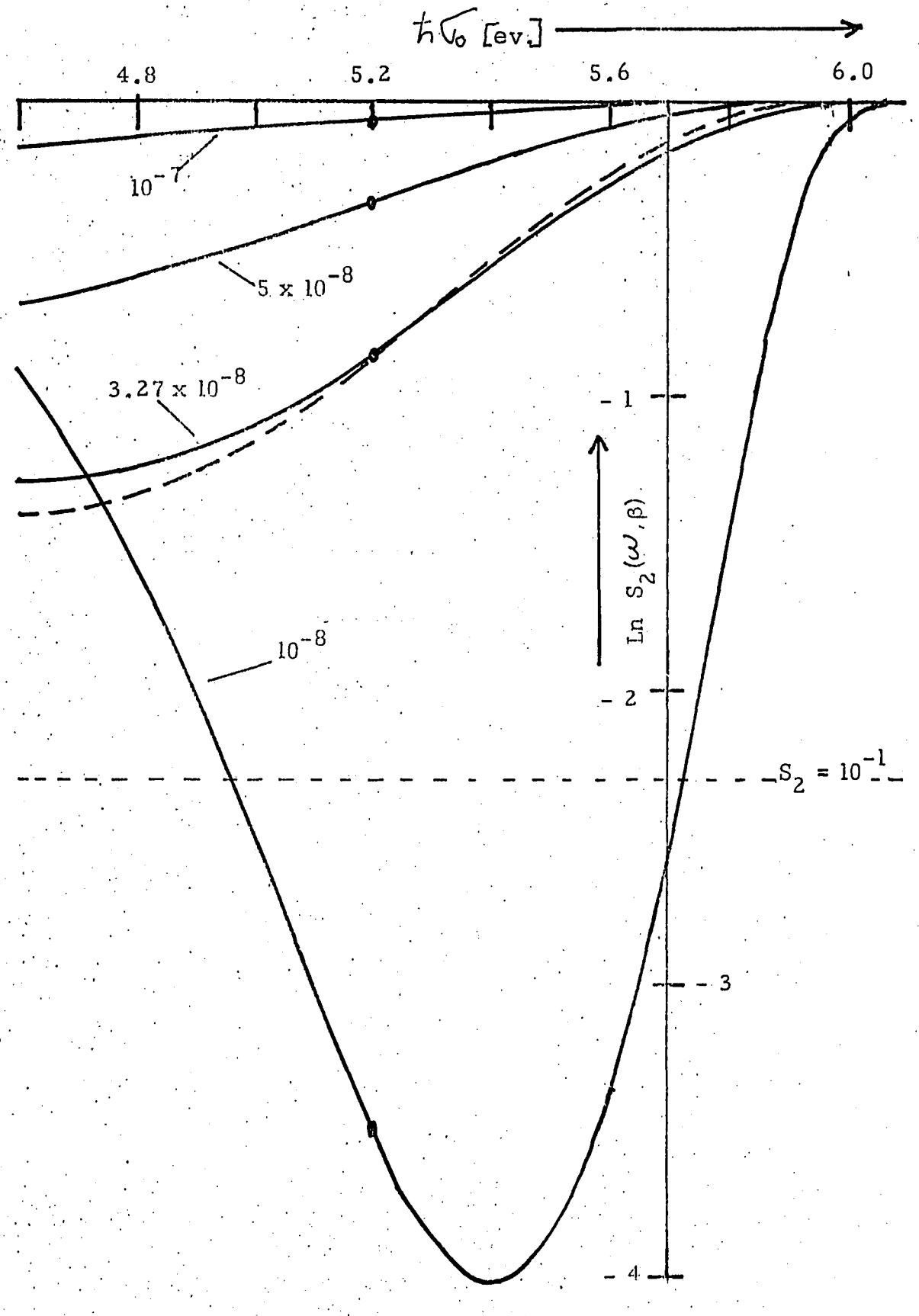
$\hbar\omega_0$ [ev.]
4.8
5.2
5.6
6.0
10^{-7}
5×10^{-8}
3.27×10^{-8}
10^{-8}
- 1
- 2
- 3
- 4
Ln $S_2(\omega, \beta)$
$S_2 = 10^{-1}$

FIG. 5.8

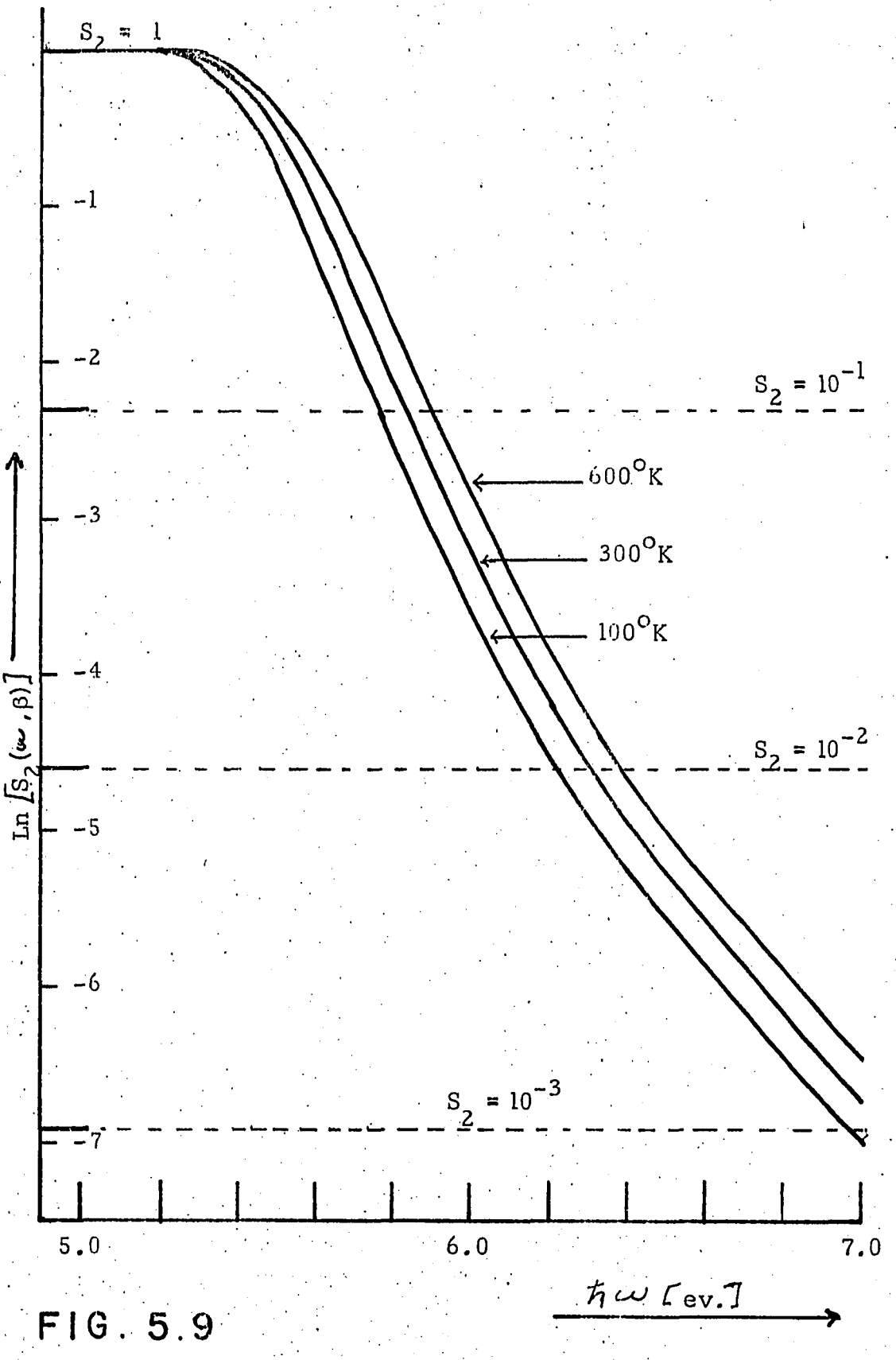
$S_2 = 1$
-1
-2
$S_2 = 10^{-1}$
600°K
300°K
100°K
-3
-4
$S_2 = 10^{-2}$
-5
-6
$S_2 = 10^{-3}$
-7
$\ln [S_2(\omega, \beta)]$
5.0
6.0
7.0
$\hbar\omega$ [ev.]

FIG. 5.9

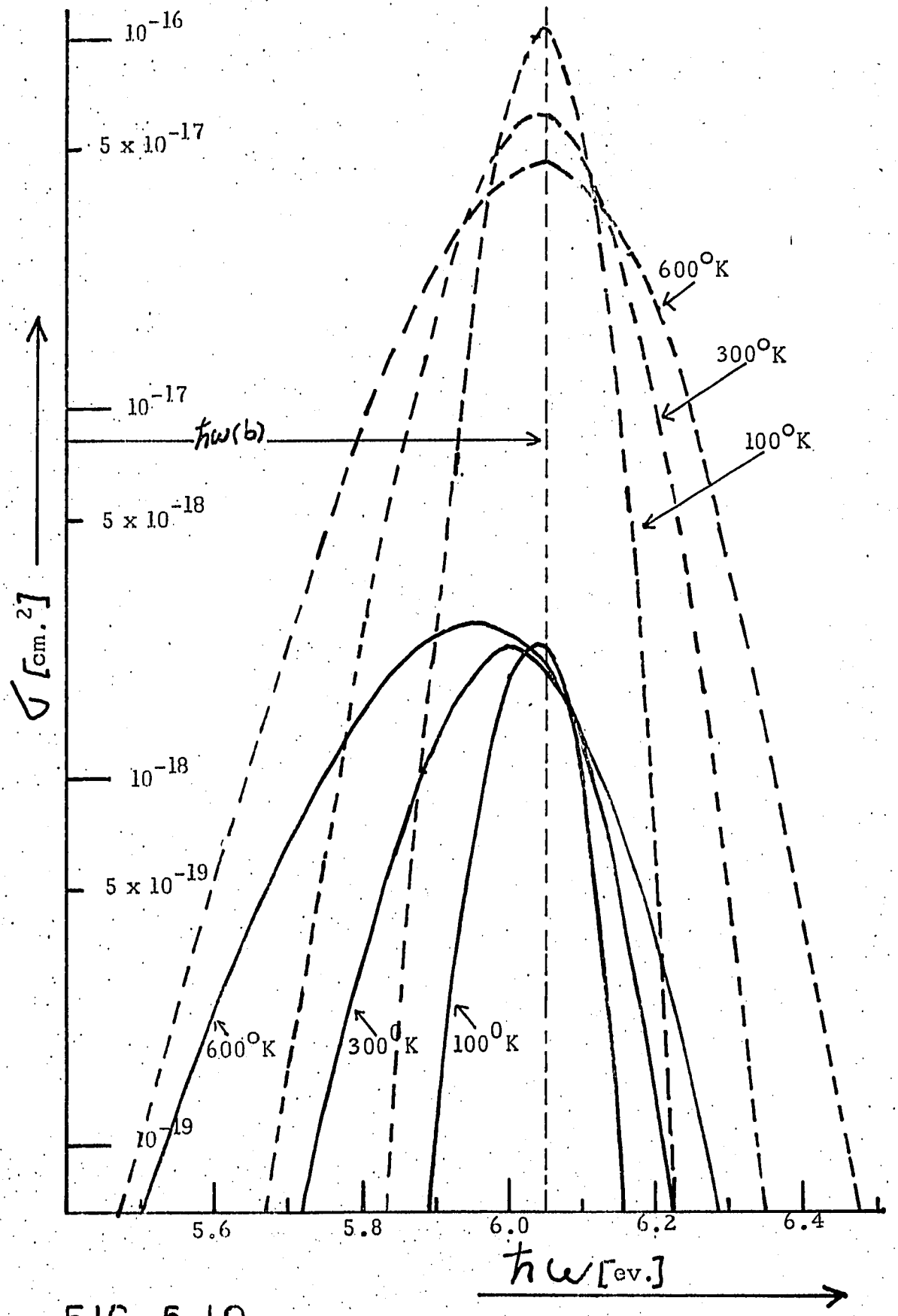
10^{-16}
5×10^{-17}
10^{-17}
$\hbar\omega(b)$
5×10^{-18}
10^{-18}
5×10^{-19}
10^{-19}
σ [cm.^{2}]
600°K
300°K
100°K
600°K
300°K
100°K
5.6
5.8
6.0
6.2
6.4
$\hbar\omega$ [ev.]

FIG. 5.10

Chapter VI: Angular Dependent Theory of ESD and Photodesorption

The first theoretical study of angular dependence in ESD and Photodesorption is initiated in this section. Expressions for the desorption cross sections are presented, and the method for implementing numerical calculations is discussed. We also introduce model interactions for O^+ desorption from tungsten which are utilized in detailed numerical ESD calculations which comprise the following chapters.

As remarked earlier, recent experimental studies of angular dependence in ionic ESD [6,7,8] have prompted interest in theoretical descriptions of angular dependent desorption.[1,2] Our approach is necessarily directed toward numerical computation. The simplest models for the functions $E_n(\vec{r})$, $Q(\vec{r})$, $R(\vec{r})$ which lack translational invariance in the surface plane still involve sufficiently complicated dynamics to prohibit analytical solution of the problem.

A set of formulas for the ESD and PD cross sections is presented below via an heuristic derivation based on the linear response picture of desorption introduced in Chapter II. It is also straightforward to generalize the one dimensional photodesorption cross sections derived in Chapter IV, by replacing the translationally invariant surface with a spatially anisotropic mesh of unit cells. The reader interested in a more complete derivation of σ_2, σ_1 is referred to Appendix II. There the formal solutions of the un-linearized transport equations are expanded in the upward transition rate R. The perturbation series are then linearized and used to construct σ_2, σ_1.

Desorption Cross Sections

The computational strategy follows the time ordered three step picture of desorption, which is applicable to the linear response approximation. The entire flux of ejected ground or excited state particles is simulated; hence, the total desorption cross sections are the ones of interest. An external photon or electron beam promotes an ensemble of adsorbed atoms or molecules to state 2. Excitations all occur simultaneously at t_o, with each particle occupying phase coordinates $\vec{r}_o$, $\vec{v}_o$ upon entering the excited state. The forward evolution of the system is then followed, without further interaction with the external beam, to a time t large enough for all desorbing atoms or molecules to cross the detection plane. Emission intensities for all asymptotic directions θ, ϕ are thus generated. The angular dependence may be recovered simply, by numerical differentiation; the intensities associated with individual particle impacts on the detector are assigned to 'bins', each enclosing a small solid angle.

The particles excited into state 2 must be individually followed as they evolve to their asymptotic emission directions, and their contributions to the cross sections evaluated, including attenuation due to quenching. The classical equations of motion describe the desorbing particle dynamics in either state. The functions $\vec{r}(\vec{r}_o, \vec{v}_o, t)$, $\vec{v}(\vec{r}_o, \vec{v}_o, t)$ are assumed to be known parametrically as functions of the initial coordinates and the time. In practice, Newton's Second Law is numerically integrated along each path from the excitation time t_o to the time t when detection occurs. The simulated

desorbing particles do not cross the detection plane simultaneously; however, their arrivals are treated as simultaneous inasmuch as the cross sections are time independent for steady state response. The differential cross sections, given explicitly in Eqs. (2.19) are cumbersome to implement efficiently on the computer. In order to evaluate them at asymptotic directions where σ_n is negligible, one must still perform inward trajectory integration toward the surface.

First we represent the total cross sections as ensemble averages over the phase space coordinates at t_o. Let the quantity $\sigma_n^{EJ}(t_o,t)$ denote the cross section for the entire process resulting in ejection of a single atom or molecule in the n th state. $\sigma_n^{EJ}(t_o,t)$ is proportional to the upward transition rate $R(\vec{r}_o)$, as the atom is promoted to state 2 at t_o. Quenching must occur during the interval $[t_o, t]$ if a particle is ejected in the ground state; hence, σ_1^{EJ} is proportional to the decay rate Q as well. We form the total cross sections by weighting σ_n^{EJ} with the probability that $d^3\vec{r}_o\, d^3\vec{v}_o$ is occupied, given by $P_1^0(\vec{r}_o, \vec{v}_o) d^3\vec{r}_o d^3\vec{v}_o$. Hence the expression is:

$$\sigma_n(t_o,t) = \int d^3\vec{r}_o\, d^3\vec{v}_o\, P_1^0(\vec{r}_o,\vec{v}_o)\, \sigma_n^{EJ}(t_o,t) \qquad (6.1)$$

The spatial integration here extends over the unit surface cell and $-\infty < z < +\infty$

The equilibrium distribution P_1^0 approximates the ground state ensemble at t_o. We have neglected spontaneous desorption, hence the departure of the

ground state from equilibrium is to dominant order $\sim R^1$. This non-thermal term in P_1 can contribute only to the non-linear response inasmuch as σ_n^{EJ} is already of order R^1. Throughout this study, in which the detailed profiles of emission lobes are not predicted, it is adequate to represent P_1^0 as a Boltzmann distribution, normalized as in Eq. (2.7). There is no obstacle to extending this approach to quantitatively accurate intensity calculations. One may then resort to a Franck-Condon excitation model, quantizing the vibrational states of the adsorbed particle.

We define $\chi(\omega, \vec{r}_0, \vec{v}_0)$ to be the cross section for excitation of an atom or molecule at t_0. This function must approach the free atomic or molecular excitation cross section in the limit where $\vec{r}_0$ lies far from the surface. Here, ω is the energy lost by the exciting photon or electron. χ is proportional to the transition rate R_e (for ESD) or R_γ (for PD) defined in Chapter II. For ESD there is no resonant delta function in R_e, hence

$$\chi_e = \frac{R_e}{F_e} \tag{6.2}$$

where F_e is the electron flux. For photo-excitation in which no final state electrons are present, R_γ contains a delta function and an amplitude $M(r_0, \omega)$, as in Eq. (4.1). Inasmuch as we numerically integrate using a finite number of points, it is necessary to allow the photon flux F_γ to possess a small arbitrary width Γ. Then χ_γ, after averaging over

the frequency interval $[\omega - \Gamma/2, \omega + \Gamma/2]$ is given by:

$$\chi_\gamma(\vec{r}_0) = \frac{M(\vec{r}_0)\,\Theta(\omega + \frac{\Gamma}{2} - \Delta(t_0))\,\Theta(\Delta(t_0) - \omega + \frac{\Gamma}{2})}{F_\gamma \Gamma} \qquad (6.3)$$

Here, $\Delta(t_0) = E_2(\vec{r}_0) - E_1(\vec{r}_0)$. This cross section permits excitation only on a thin shell of the E_1 - E_2 hypersurface where $E_2(\vec{r}_0) - E_1(\vec{r}_0) \approx \hbar\omega$.

We also define the probability $S_2(t_0, t)$ for a desorbing particle to survive without being quenched from t_0 to t. Quenching is an efficient process in many real systems. ESD cross sections are found experimentally to generally be several orders of magnitude small than those for related atomic or molecular dissociations.[1,2] Hence, we include quenching to all orders in the survival probability S_2, which has the form:

$$S_2(t_0, t) \equiv \exp\left[-\int_{t_0}^{t} dt'\, Q(t')\right] \qquad (6.4)$$

The exponent is the integrated non-radiative decay probability, evaluated along the excited particle path from $\vec{r}(t_0)$ to $\vec{r}(t)$. Q(t) is the downward transition rate, displaying its parametric time dependence. One may also adopt notation in which the exponent in Eq. (6.4) displays the path integration explicitly, viz:

$$-\int_{\vec{r}_0}^{\vec{r}(t)} Q(\vec{r}')\,\frac{\vec{V}(\vec{r}')\cdot d\vec{r}'}{|V(\vec{r}')|^2}$$

Here $v(\vec{r}')$ is the velocity of an atom or molecule at $\vec{r}'$.

The form for S_2 displayed in Eq. (6.4) is most simply deduced by solving either of the transport equations (2.12a) or (2.13a) for P_2, with the excitation terms neglected. Making use of Liouvilles Theorem[69] and displaying parametric time dependence explicitly, either transport equation may be reduced to:

$$\frac{dP_2}{P_2} = -\Phi(t)\,dt$$

Integrating formally from t_0 to t produces the result $P_2(t) = P_2(t_0) S_2(t_0,t)$ with S_2 as in Eq. (6.4). It is useful to interpret S_2 as an evolution operator for excited atoms or molecules, analogous to the quantum mechanical evolution operators of the interaction picture.

The excited state ejection cross section $\sigma_2^{EJ}(t_0,t)$ is evaluated by mapping $\chi(\omega,\vec{r}_0,\vec{v}_0)$ to the asymptotic region via the survival probability. Hence:

$$\sigma_2^{EJ}(t_0,t,\omega) = \chi(\omega,t_0)\, S_2(t_0,t)\,\Theta\left(\tfrac{1}{2}Mv_0^2 + E_2(\vec{r}_0) - E_2(\infty)\right) \tag{6.5}$$

The step function is inserted to eliminate following trajectories for which desorption is energetically prohibited. In numerical computation, σ_2^{EJ} is to be treated as a single-fold integration. The decay probability is integrated from point to point as the trajectory is followed.

The ground state ejection cross section $\sigma_1^{EJ}(t_0,t)$ is proportional to the decay rate $Q(t')$. Decay is a random process which can in principle

occur at any intermediate time t' between excitation and detection. Integration on t' is thus implied. One follows the evolution and attenuation of a particle by evaluating $\chi(t_0,\omega) S_2(t_0,t')$ up to t', governed by the excited state dynamics. After quenching at t' the survival probability $S_1(t', t)$ against re-excitation from the quenched state prescribes the evolution. We take $S_1(t', t) \approx 1$, inasmuch as ground state depletion is neglected. If one refers to the unlinearized transport equation (2.13b) for P_1, neglecting the repopulation, one finds:

$$S_1(t', t) = \exp\left[-\int_{t'}^{t} dt'' R(t'')\right]$$

after formal integration, which we take to be ≈ 1 in the linear response approximation.

Our observations above imply that the ground state ejection cross section is represented by the following:

$$\sigma_1^{EJ}(t_0, t) = \chi(\omega, t_0) \int_{t_0}^{t} dt' Q(t') S_2(t_0, t') \times \Theta\left(\tfrac{1}{2}MV_0^2 + E_2(\vec{r}_0) - E_2(\vec{r}') + E_1(\vec{r}') - E_1(\infty)\right) \tag{6.6}$$

Here we inserted the step function at the decay point $\vec{r}' = \vec{r}(t')$ to prevent following trapped trajectories numerically. The ground state energy $E_1(\vec{r})$ determines the propagation dynamics subsequent to t' for recovering the angular dependence. Numerical evaluation of this quantity is time consuming due to the presence of two-fold integration.

Now we summarize the expressions which will be employed in numerical simulations of the angular dependent desorption cross sections:

$$\sigma_2(\omega) = \int d^3\vec{r}_0\, d^3\vec{v}_0\, P_1^0(\vec{r}_0,\vec{v}_0)\, \chi(\omega,t_0)\, S_2(t_0,t) \times \times \Theta\left(\tfrac{1}{2}MV_0^2 + E_2(\vec{r}_0) - E_2(\infty)\right) \tag{6.7a}$$

$$\sigma_1(\omega) = \int d^3\vec{r}_0\, d^3\vec{v}_0\, P_1^0(\vec{r}_0,\vec{v}_0)\, \chi(\omega,t_0) \times \times \int_{t_0}^{t} dt'\, Q(t')\, S_2(t_0,t') \times \times \Theta\left(\tfrac{1}{2}MV_0^2 + E_2(\vec{r}_0) - E_2(\vec{r}') + E_1(\vec{r}') - E_1(\infty)\right) \tag{6.7b}$$

The structure of these is a generalization of the one dimensional forms for σ_2 , σ_1 in Eq. (4.26b) and (4.27), which were deduced for photodesorption. Equations (6.7a, b) are model independent, except for the general restrictions imposed earlier on R, Q, E_n, and P_1^0 . One may use them to predict accurate angular intensities and desorption energy distributions provided realistic models for the surface interactions are available.

The six-fold integration in Equations (6.7a,b) over the phase coordinates at t_0 is cumbersome to implement on the computer. We adopt an equivalent but more economical alternative to straightforward integration provided by the Monte Carlo method. A procedure is devised to select $\vec{r}_0$, $\vec{v}_0$ randomly, according to the distribution $P_1^0(\vec{r}_0, \vec{v}_0)$. The phase integration is in effect performed to any desired degree of accuracy by sampling an appropriate number, n, of points. This feature is useful in calculations to follow, where a small

number of trajectories is found sufficient to simulate the qualitative features of angular emission patterns. Operationally, one accumulates the asymptotic intensities and directions associated with ∇_n^{ET} for each Monte Carlo coordinate choice. The sums of intensities in each asymptotic solid angle sector are normalized to n.

It is appropriate to mention that the trajectory integrations were accomplished step-wise with the use of a predictor-corrector method.[70] Each step in time consisted of estimating $\vec{r}$, $\vec{v}$ at the end of the interval by Taylor series. The result is substituted into an integral form of the equations of motion, and iterated until consistency to full machine accuracy is achieved. The advantage of this method lies in its flexibility in varying the density of integration points. Closely spaced steps are required near the surface, where E_n, Q, and the accelerations are rapidly varying functions of position. For economy, the density of integration points was made small wherever accelerations were roughly constant. The computer program adjusted the step size continuously to keep the total energy of a desorbing particle constant to within a small tolerance.

Model for ESD of O^+ from Tungsten

From this point, we examine only ESD of positive oxygen ions from a tungsten surface. Equation (6.7a) is adapted to the specific cases for which angular dependent desorption data are presently available: O^+ emission from W(111) and W (100).[6-8] Appropriate models for the propagation dynamics, excitation and quenching to be used in later numerical computation are now introduced.

Detailed studies of O^+ - W(111) and O^+ - W(100) comprise chapters VII and VIII.

Consideration of ESD emission of ground state or excited neutral particles is deferred to the future, when experimental angular dependence data are expected to become available.[71] It is known that neutrals are the dominant ESD product in many systems.[2,3] Detailed models for the reneutralization rate and ground state dynamics are required in applying our computational method to ground state desorption. Such models may require approximate solution of the chemisorption problem; hence, they are beyond the scope of this inquiry. We speculate that only diffuse emission cones for desorbing ground state particles should be observed if quenching is efficient over a large portion of the surface cell.

Simplified model interactions may be adopted for the ionic desorption problem at hand. The state of angular dependent desorption studies up to this point is preliminary. Hence, we decline to predict those intensity variations in the desorption cross sections which arise from spatial variation of the excitation and decay rates. We focus attention on the excited state propagation phase of ESD, which we assume, subject to a posteriori verification, to give rise to the qualitative structure of ion distribution patterns. We investigate the ion optics of particles propagating in the anisotropic potential $E_2(\vec{r})$, finding in Chaps. VII, VIII that sharply focussed emission spots are produced by surface cell variations of the ion-solid interaction energy.

The Excitation Phase

First we examine an expression for the cross section $\chi_e(\frac{k^2}{2}, \vec{r}_0)$

describing excitation of a particle to the ionic state. The incident electron flux, F_e, is taken to be an almost monochromatic beam of particles with energy $k^2/2$, in atomic units. A simple ionization process is examined in which the incident electron suffers momentum transfer $\vec{q}$, and ejects an electron which was bound to the adsorbed atom or molecule. The emitted free electron has energy $q^2/2$, inasmuch as the ionic recoil is neglected. An expression for the cross section may be written as:

$$\chi_e(K^2/2, \vec{r}) = \frac{2\pi}{F_e} \sum_{\vec{q}} [1 - f_{\vec{q}}] \, |\langle 2| \frac{1}{r + \vec{r}' - \vec{r}_1'} |1\rangle|^2 \times$$

$$\times \delta(E_2(\vec{r}) - E_1(\vec{r}) - \vec{q} \circ (\vec{K} - \vec{q}))$$

Here the factor $[1 - f_{\vec{q}}]$, with $f_{\vec{q}}$ the fermi distribution, ensures that the final state is unoccupied. The initial state $|1\rangle$ of the system represents the occupation $|1_0, \text{vac}, 1_k\rangle$ while $|2\rangle = |1_+, 1_q, 1_{(k-q)}\rangle$ is the final state. In the coulomb interaction, $\vec{r}'$ is the incident electron coordinate, while $\vec{\rho}$ describes the bound state electron relative to the ionic mass center at $\vec{r}$.

We take the excitation cross section χ_e to be a constant in calculations which follow. The effect of this approximation is to neglect spatial variations which remain principally in the coulomb matrix elements after the final state degrees of freedom are averaged over. The delta function in the expression for χ_e is consumed by the $\vec{q}$ integration; hence, this ESD process is not a resonant one confined to a restricted portion of the surface cell, as was found to be the case for neutral particle photodesorption. The electron probe energies are generally $\sim$ 100-200 ev.,[7,8] which is large

compared to $[E_2 - E_1]$ over the unit cell. Ionization is therefore possible from the entire ground state particle distribution. One expects χ_e and σ_2 to display only weak dependence on the probe energy $k^2/2$. Experimental study has confirmed this observation for probe energies far above the ESD threshold.[7,72] Approximating χ by a constant introduces only small error into later calculations when we localize P_1^0 to a small region of the zone.

The Quenching Phase

The quenching process is now examined. This proceeds for a positive ionic excited state via reneutralizations in which electrons are induced to tunnel from the substrate into quasi-atomic or molecular bound levels. A reneutralized ion then either desorbs as a de-excited particle or rejoins the P_1^0 distribution. We briefly examine a simple reneutralization mechanism represented by the transition rate:

$$Q(\vec{r}) = 2\pi \sum_{\vec{k}} f_{\vec{k}} \left| \langle 1_0, 0_k | \frac{1}{\vec{r} - \vec{r}_e} | 1_+, 1_k \rangle \right|^2 \times \delta(\omega_k + E_1(\vec{r}) - E_2(\vec{r}))$$

We sum above over the initial electronic states in the solid, whose occupation is ensured by the Fermi distribution. The substrate is left with a vacancy below the Fermi surface, whose energy is ω_k. $Q(\vec{r})$ should display rapid decay in its z dependence, due to the presence of overlap integrals in the coulomb matrix element between quasi-atomic and substrate wave functions.

The delta function, however, will be consumed by the initial state summation. Hence, the variations in Q over the zone are due principally to anisotropy of the matrix element. Quenching should be expected to occur over much of the surface cell with significant intensity.

In numerical computation, the survival probability S_2 against quenching was replaced by a constant. Numerical values for the cross sections were not calculated; hence, we took $S_2 = 1$. The consequences of this approximation are more severe for quenching than for the excitation cross section. In practice, however, only localized sources of adsorbed particles were studied. The interesting cases are those in which sharp O^+ emission cones arise. For these, quenching does not drastically modulate relative intensities within an emission spot. For diffuse patterns, spatial variation in S_2 is more significant. This model for S_2 makes comparison of emission intensities between widely separated adsorption sites difficult. We discuss the constant quenching approximation further in connection with our results in Chapter VII.

The Ground State Energy

Now the ground state energy $E_1(\vec{r})$ is examined. The chemisorption or physiadsorption sites correspond to minima of E_1. As noted above, E_1 and hence the chemisorption site locations may be deduced from knowledge of the surface charge density using the Hellmann-Feynman Theorem. At present this problem has been solved only for the Si(111) and Si(100) surfaces.[29,73] At the low temperatures of interest, however, only the lowest ground state vibrational levels are occupied. Hence, the shape of E_1 only in the region near its minima has a significant effect on the desorption.

In computation we approximated $E_1(\vec{r})$ by a three dimensional harmonic potential near each chemisorption site. Our objective in these computations was to infer plausible locations for the unknown oxygen adsorption sites on tungsten by comparison of the experimental ESD patterns to those calculated.

Near a site at $\vec{b}$ we replace:

$$E_1(\vec{r}) \approx -V_0 + \tfrac{1}{2}(\vec{r}-\vec{b})\cdot\overleftrightarrow{K}\cdot(\vec{r}-\vec{b})$$

Here V_0 is the chemisorption energy for the site examined. Knowledge of V_0 was not required in this study, as χ_e was taken to be constant. $\overleftrightarrow{K}$ is a spring constant tensor describing anisotropic vibrational states at an adsorption site. We assume that principal axes diagonalizing $\overleftrightarrow{K}$ at each site may be found. Numerical values for the spring constants were estimated phenomenologically.

The equilibrium distribution P_1^0 to be simulated by the Monte Carlo method was assumed to factor into the product of six gaussians having the form:

$$P(\xi) = \frac{1}{\sqrt{2\pi}\sigma_\xi} e^{-\frac{1}{2}\left(\frac{\xi-\bar{\xi}}{\sigma_\xi}\right)^2}$$

In the above $\sigma_{x_n} = (\beta K_n)^{-\frac{1}{2}}$ is the spatial width, and $\sigma_{v_n} = (M\beta)^{-\frac{1}{2}}$ is the thermal velocity spread for each component. Standard subroutines were used to implement the numerical simulation of P_1^0. It was a simple matter, using this approximation, to examine a large variety of possible

chemisorption sites by shifting $\vec{b}$, without the need for detailed re-modelling of the ground state energy. A more precise model for E_1 must be incorporated into the non-radiative decay rate, when detailed quantitative cross sections are calculated.

Model O^+-W Interaction Energy

The key to angular dependent ion distributions is knowledge of the interaction energy $E_2(\vec{r})$ between oxygen ions and the tungsten surface. A realistic model is required for this function, including anisotropy in the direction parallel to the surface. Most attention in the literature has been directed away from excited state energies toward the chemisorption problem. It is fortunately not as difficult to model E_2 for positive ions as for neutral particles or negative ions. Correlation, exchange, and Pauli repulsive effects are greatly reduced for the positive ion. The positive ion is a compact object which responds to the local electrostatic potential produced by the surface.

We treated O^+ ions propagating near the surface as point charges, in computing interactions with the surface. The effects considered a priori likely to be dominant were included in E_2; namely, the unperturbed Hartree potential of the solid V_H plus averaged electron density fluctuations which produce the image potential V_{IM}, viz:

$$E_2(\vec{r}) = Q V_H + Q V_{IM}$$

Here Q is the ionic charge and $QV_{IM} \equiv \langle H_{IM} \rangle$ is the thermal average of an interaction Hamiltonian H_{IM}, chosen to represent the electron density fluctuations.

The Hartree potential is in principle obtained by solving Poissons equation: [74]

$$\nabla^2 V_H(\vec{r}) = -4\pi \sum_{\vec{R}_i} \delta(\vec{r}-\vec{R}_i) + 4\pi \sum_{\vec{K},\sigma} f_K |\psi_{\vec{K},\sigma}(\vec{r})|^2$$

Here one sums over the locations $\vec{R}_i$ of all the tungsten ions in the semi-infinite solid. The electronic contribution is summed over all occupied electronic states $\psi_{\vec{K}\sigma}(\vec{r})$ of the solid. One must solve the band structure problem for a semi-infinite solid to obtain the electronic states ψ, and hence the charge density. This problem is distinctly non-trivial.

The tungsten surface charge density has not been calculated although progress in such calculations has been made for Silicon. Self-consistent atomic structure calculations have, however, provided tungsten wave functions from which the free atomic charge density may be inferred. [75, 76] In tungsten, six unfilled shell electrons participate significantly in the binding. The band structure of transition metals, and tungsten in particular, has been extensively discussed in the literature. [77] Superpositions of atomic tungsten wave functions have proven to be a reasonable starting point for self-consistent band structure calculations in bulk tungsten. [78, 79] We assume that they will fulfill the same role when detailed surface charge density computations are performed.

We elect to approximate the surface charge density contributing to V_H

by a sum of unperturbed atomic charge distributions. The Hartree potential becomes the sum of free atomic Hartree potentials, displaced so that their origins reside on the lattice sites. One might argue that neglecting the bonding effects is not as serious for the atomic layers near the surface as in the interior of the solid. The formal solution to Poissons equation provides a prescription for evaluating $V_A(r)$, the atomic Hartree potential:

$$V_A(\vec{r}) = \frac{Z}{r} - \sum_{j=1,Z} \int d^3\vec{r}' \frac{|\psi_j(\vec{r}')|^2}{|\vec{r}-\vec{r}'|}$$

For tungsten, the ionic charge $Z = 6$. The Herman-Skillman wave functions [75] were used to evaluate $V_A(r)$ numerically. The result was fitted to an exponential decay at oxygen-tungsten atom separations larger than the sum of the atomic radii. The result, used below in numerical computations is:

$$V_A(r) \approx 7.719 \exp[-1.29 r] \qquad (6.8)$$

All quantities are in atomic units.

Interaction with the positive ions produces surface charge density fluctuations which we associate with the image potential V_{IM}. For the present, we neglect delocalization effects, and lateral anisotropy in V_{IM} due to surface cell structure, picturing the image charge to reside in a plane called the 'dielectric surface'. We argue that Hartree repulsion is likely to dominate over attractive image forces at close range. Thus, we assume that neglecting

lateral anisotropy in V_{IM} introduces errors which are perturbations on this model. In effect, by modelling V_{IM} for a translationally invariant surface we average over the transverse direction.

Classical electrostatics using the method of images yields the interaction energy QV^{o}_{IM} given by:

$$Q V^{o}_{IM} = - Q^2 / 4z$$

We recognize that in quantum mechanical computation the relation $\langle H_{IM} \rangle \sim Q^2$ must be found. We expect V^{o}_{IM} to be the asymptotic limit in the model calculation below.

The surface density fluctuations resulting in V_{IM} are regarded as the consequence of coupling between the ionic charge and virtual surface plasmons. These are the normal modes whose superposition creates the fluctuation in the Hartree field. We find QV_{IM} by diagonalizing a model interaction Hamiltonian given by:

$$H_{IM} = Q \Phi(\vec{r}) + \sum_{\vec{q}_\perp} \sigma_{\vec{q}_\perp} a^{\dagger}_{\vec{q}_\perp} a_{\vec{q}_\perp}$$

Here, $\Phi(\vec{r})$ is the ion-plasmon interaction operator describing fluctuations induced in the Hartree field via surface plasmon creation and annihilation. The creation operator is $a^{\dagger}_{\vec{q}_\perp}$, where $\vec{q}_\perp$ is a wavevector describing propagation on the surface. $\sigma_{\vec{q}_\perp}$ is the energy of a plasmon with wavelength $[q_\perp]^{-1}$. We included the plasmon self-energy in H_{IM}.

We shall make use of the Surface Quasi-Mode formalism to provide an approximate description of surface plasmon properties. This construct was developed recently for use in Photoemission studies.[42,43] We discussed the SQM method in some detail in Chapter III. The ion-plasmon interaction Hamiltonian may be written as an expansion in the operators $a^{\dagger}$, a by referring to Eq. (3.1):

$$Q\bar{\Phi}(\vec{r}) = Q\sum_{\vec{q}_\perp} g(q_\perp) e^{-q_\perp |z|} \times \left[e^{i\vec{q}_\perp \cdot \vec{r}} a^{\dagger}_{\vec{q}_\perp} + e^{-i\vec{q}_\perp \cdot \vec{r}} a_{\vec{q}_\perp} \right] \tag{6.10}$$

The coupling constant $g(q_\perp)$ was given by:

$$g(q_\perp) = \left[\frac{\pi \sigma_0^2}{q_\perp \sigma_{q_\perp}} \right]^{\frac{1}{2}} \tag{3.2}$$

where $\sigma_0 = \omega_p/\sqrt{2}$. Φ is manifestly not diagonal with respect to the plasmon occupation states $|1_+, 1_{K_\perp}\rangle$. We observe that

$$\langle 1_+, 1_{K_\perp} | Q\Phi | 1_+, \text{VAC} \rangle = Q g(K_\perp) e^{-K_\perp |z|} e^{i\vec{K}_\perp \cdot \vec{r}}$$

We are motivated to diagonalize H_{IM} by means of a reduced oscillator transformation to a new set of bosons. The transformed self energy term becomes decoupled from the ionic interaction, and will be neglected. The

substitution which accomplishes this is defined by:

$$a^{\dagger}_{\vec{q}_\perp} = A^{\dagger}_{\vec{q}_\perp} - \frac{Q}{\sqrt{q_\perp}} g(\vec{q}_\perp) e^{-q_\perp |z|} e^{-i\vec{q}_\perp \cdot \vec{r}}$$

where $A^{\dagger}_{\vec{q}_\perp}$ creates the new excitation. After some algebraic manipulation we find that:

$$H_{IM} = \sum_{\vec{q}_\perp} \omega_{\vec{q}_\perp} A^{\dagger}_{\vec{q}_\perp} A_{\vec{q}_\perp} - Q^2 \sum_{q_\perp} \frac{\pi \omega_0^2}{q_\perp \omega_{q_\perp}^2} e^{-2q_\perp |z|} \qquad (6.11)$$

This transformed Hamiltonian is diagonal with respect to the new plasmon occupation states. Now we ensemble average over the surface plasmon states using the prescription:

$$\langle \mathcal{O} \rangle = \text{trace}\,(\rho \mathcal{O})$$

Here, ρ is a Bose distribution normalized to $\sum_{\vec{q}_\perp} \rho_{\vec{q}_\perp} = 1$. The first term of Eq. (6.11) becomes the energy contained in surface excitations, which we discard. The second term is the image potential. After converting the sum to an integration and integrating over the azimuthal angle we equate:

$$Q V_{IM} = -\frac{Q^2}{2} \int_0^{\infty} dq_\perp \frac{\omega_0^2}{\omega_{q_\perp}^2} e^{-2q_\perp |z|} \qquad (6.12)$$

This quantity may be evaluated numerically for quantitative image potential calculations, provided the plasmon dispersion relation is known. Note that the image interaction is $\propto Q^2$, as expected.

It is trivial to recover the classical result from Eq. (6.12) when plasmon dispersion is neglected by taking $\omega_{q_\perp} \to \omega_0$. Now we take $Q = 1$, for singly ionized oxygen atoms. Surface plasmon dispersion eliminates the classical divergence at $Z = 0$ caused by high $q_\perp$ components of V_{IM} . It is convenient to employ the static RPA (Linhard) dielectric function, Eq. (3.11), in evaluating V_{IM} numerically. One uses the prescription for $\omega_{q_\perp}$ given by Eqs. (3.9), (3.10). The resulting expression depends parametrically on the plasma parameter r_s. V_{IM} was evaluated for a number of values of r_s and z, and was found to be a good fit to the following formula:

$$V_{IM}(r_s, z) \approx -\frac{1}{4z + 1.16 + 1.34 r_s - .04 r_s^2} \qquad (6.13)$$

The divergence has been shifted to the region interior to the dielectric surface. This cusp will be rounded in a treatment where the dielectric surface is delocalized over the charge distribution radius of the tungsten atoms. The choice of origin for the dielectric surface is a compromise in this model, which we make later for each system studied.

The r_s value of bulk tungsten is determined by means of the known plasma frequency of 23.5 ev. (.864 Hartrees).[68] The bulk tungsten structure is body centered cubic; hence, the electron density n in the metal is given by $n = r_s^{-3}$. There are two atoms per unit cell; hence the number of electrons per atom participating in the dielectric properties of tungsten is $Z = nV_c/2$. Here the unit cell volume $V_c = a^3$, with the lattice

constant a = 5.97 a_0. Taking the effective mass to be approximately 1, the plasma parameter is:

$$r_s = \left[\frac{4\pi}{\omega_p^2}\right]^{\frac{1}{3}} = 2.56$$

Also, one finds Z = 6.3 ≈ 6 electrons/atom. Thus, all six unfilled shell electrons will be assumed to participate in the plasma response and screening.

Chapter VII: ESD of O^+ from the (111) Surface of Tungsten

In this section we present a detailed study of the Electron Stimulated Desorption of oxygen ions from the (111) face of tungsten. The ion angular distributions to be expected for emission of chemisorbed oxygen atoms have been simulated for a variety of adsorption sites in the (111) tungsten surface unit cell. We find that adsorption of oxygen in atomic form provides a plausible description of the observed features of angular distribution patterns for this system.

In calculations below, compact O^+ emission spot patterns are found associated with atomic oxygen adsorption sites located in the recesses of the surface unit cell. Their strongly focussed forms and emission directions are attributable to the ion-solid interaction potential $E_2(\vec{r})$. Cones of O^+ emission non-normal to the surface are found for oxygen adsorbed at the low symmetry points within the surface cell. Surface complexes involving several oxygen atoms are briefly discussed, but detailed calculations were not performed for the wide variety of such systems which can be hypothesized.

Our findings are compared with the experimental results obtained recently for O^+ on W(111) by Madey, et al.[8] The experimental findings include the discovery of collimated emission cones for O^+ ions both normal and non-normal to the surface. The centers of the observed lobes corresponding to non-normal emission are aligned with the atomic rows in the substrate. We will introduce experimental details into the discussions

to follow as needed. The main findings are briefly summarized below.

Two important classes of desorption patterns were observed. One sequence was obtained with oxygen adsorption temperatures $T \leq 100^{o}K$. A series of patterns was formed by heat treating the oxygen covered sample for a specified period of time to each of several temperatures before cooling the sample back to $100^{o}K.$, at which temperature the ESD experiments were performed. For heat treatments to $665^{o}K.$ and above, no desorption normal to the surface was observed. Instead, trios of lobes, or collimated cones of O^{+} emission, were found centered on the apexes of equilateral triangles. The 'primary' set of lobes are oriented with respect to the substrate as shown in Fig. (7.1). A second, apparently less intense trio becomes observable at the higher heat treatment temperatures in conjunction with the 'primary' set, rotated from the 'primary' orientation by 180^{o}. These are termed the 'secondary' lobes. For low heat treatment temperatures, O^{+} emission normal to the surface is observed in combination with the 'primary' lobes. These lobes become more sharply resolved with increased heat treatment temperatures, and the normal emission spot declines in relative intensity.

In the first part of our investigation, we infer limitations on the range of plausible oxygen adsorption sites from the number and orientation of the lobe distributions in the observed patterns. Our results here confirm the conclusion drawn earlier from our work on the desorption of O^{+} from W(100), [80] which is amplified elsewhere in this paper; namely, the number and emission directions of the desorption cones may be well understood

in terms of anisotropies in the ion-solid interaction energy. In the second phase of investigation, we identify a number of sites which are consistent with the observed ion distributions and energies, within the limitations imposed by our modelling of the interactions present on the surface.

The W(111) Surface

First we introduce the geometry of the Tungsten (111) surface.[81] The bulk lattice is Body Centered Cubic, with the lattice content a = 5.97 atomic units.[82] We show a single unit cube of this structure in Fig. (7.2). The surface is created by slicing the bulk lattice with a plane normal to the main diagonal of Fig. (7.2), passing through a tungsten atom. A planar net of equilateral triangles with side a_s given by $a\sqrt{2}$, and with a tungsten atom at each corner, thus forms the surface layer. Each additional slice with a plane parallel to the first produces an identical net with the tungsten sites shifted cyclically, from layer to layer, to the geometrical centers of the previous net. We show in Fig. (7.3) a view of the surface looking along the (-1,-1,-1) direction. Here the tungsten sites in the surface layer are labelled 'A', those in the second and third layer into the solid are labelled 'B' and 'C' respectively. The interplanar spacing, d, is $a\sqrt{3}/6$. Small shifts in d for the topmost layer, which have been observed on Tungsten,[24] are inconsequential in our analysis. From the perspective of Fig. (7.3), the layer at z = -3d and the surface layer are superimposed. There are thus three distinct shifted orientations of tungsten planes in a full cycle, which

then repeats to form the solid. We have displayed the numerical values of many of the pertinent lengths in the Tungsten-Oxygen system in tabular form in Fig. (7.4).

The surface has sixfold symmetry in the following sense. Axes normal to the surface through any of the inequivalent symmetry points 'A', 'B', or 'C' are threefold rotation axes, thus the lines containing all of 'A', 'B', and 'C' are present in three orientations, rotated by 120^{o}. Each such line is also a mirror axis. The lines defined by A-A, B-B, C-C, however, do not possess this last property.

For use in further analysis, we have chosen the smallest surface unit cell structure as shown in Fig. (7.1). We adhere henceforth to the choice of x and y axes shown in that figure when referring to the surface geometry. The z axis is normal to the surface. The structure shown can cover the surface plane by means of lattice translation vectors alone. An appropriate choice of these is $a_n = a_s \hat{\alpha}_n$, where $\hat{\alpha}_1 = (\frac{1}{2}, \frac{\sqrt{3}}{2})$ and $\hat{\alpha}_2 = (\frac{1}{2}, -\frac{\sqrt{3}}{2})$. Several points of interest, in addition to A, B, and C, to be discussed later, are designated D-O on Fig. (7.1). The low symmetry points $'\alpha'$ are all equivalent, as are all those labelled $'\beta', 'P', 'E'$. Thus, in general, there is sixfold degeneracy. However, any location in the zone lying along the mirror axes ABCA is only threefold degenerate. The symmetry points occur only once.

Excitation and Quenching

We have dealt with the modelling problem for the excitation and decay phases of ESD in the same manner used in our earlier work.[80]

An adsorbed atom is suddenly converted to a positive ion at some point in the zone of Fig. (7.1). We neglect all spacial variation in the excitation and decay rates. Each desorbing ion is thus viewed as carrying the same intensity contribution to the cross-section. The distortion introduced into the calculated emission patterns by this approximation is not expected to be serious when excitation occurs within a well localized region in the vicinity of an adsorption site. In view of the sharp emission cones seen experimentally, this is the most interesting case to consider. It is reasonable to expect sharp cones to result from adsorbed oxygen atoms which are bound in localized sites. Quenching will be most effective for ions which spend comparatively long times in the vicinity of the surface. As a result, one should expect ions desorbing at low kinetic energies to be over-represented in our simulated spectra of ion energies. Low energy desorption cones generally originate where the ion-solid force is small. We leave open, in this approach, the question of relative intensities between patterns produced by well separated adsorption sites. The experimental data do not as yet contain estimates of such relative intensities; hence this feature of our procedure produces adequate results.

Ion-Solid Interaction Energy

We focus attention in this investigation on the propagation phase of desorption. The angle at which an atom desorbs is strongly correlated to the point where ionization occurs. The key to understanding angular dis-

tributions is knowledge of the ion-solid interaction energy.

We construct $E_2(\vec{r})$ in accordance with the prescription set forth in an earlier section:

$$E_2(\vec{r}) = \sum_{\vec{R}_j} V_H(\vec{r}-\vec{R}_j) + V_{IM}(\vec{r}) + E_2(\infty)$$

Here we sum individual Hartree potentials for each tungsten atom, which have been fitted to:

$$V_H(\vec{r}-\vec{R}_j) = 7.719 \exp\left[-1.291\cdot|\vec{r}-\vec{R}_j|\right]$$

The tungsten locations are at $\vec{R}_j$. In principle, we must sum over all sites within the solid at $z \leq 0$; in practice, a small number of the nearest tungsten potentials yields sufficiently accurate values of $E_2(\vec{r})$ within the unit cell to which our trajectory calculations are confined. At large z, more distant tungstens contribute to the Hartree component of E_2, but the total Hartree contribution is negligible compared to the image potential, given by $V_{Im}(\vec{r})$.

As discussed previously in an earlier section $V_{Im}(\vec{r})$, before taking delocalization into account, is a good fit to:

$$V_{IM}(\vec{r}, r_s) \simeq -\frac{1}{4z + 1.16 + 1.34 r_s - .04 r_s^2}$$

Here r_s is the plasma parameter, which goes as $n^{-1/3}$, with n the density of mobile electrons in the solid. Transverse anisotropies, which are

undoubtedly present in the image potential, have been averaged over in this treatment. The image surface charge density is imagined to lie on a plane termed the 'dielectric surface', which is parallel to the outermost tungsten atom net.

We have chosen the origin for the image potential so that the dielectric surface resides at $z = -d$. The image attraction is overestimated if one chooses the dielectric surface to lie at $z = 0$, inasmuch as the average electron density in this region is low. We have found our conclusions in this section to be insensitive to the precise choice of origin for the dielectric surface.

We show in Fig. (7.5) the z dependence of E_2 constructed as we have discussed. Here the energies are plotted for points above the symmetry sites A, B, C. The image contribution is also displayed separately.

At small separation from the surface the repulsive Hartree potential dominates. As an ion approaches a tungsten site the repulsion becomes quite strong; both E_2 and the magnitude and direction of the force approach the values for an isolated $W\text{-}O^+$ pair. The attractive image force dominates when z is large. We expect that atoms which move slowly throughout their trajectories will experience significant deflection due to the image force, despite its relative weakness at intermediate values of z. Anisotropies in the transverse direction are negligible for $z \gtrsim 7a_0$. Desorption of an ion is energetically forbidden unless its total energy exceeds $E_2(\infty)$ whose value is about $-.007$. The implied cutoffs on the ionization sites z

coordinates which can lead to desorption are thus $\sim$ 4.1, 2.6, 1.4 a_0 above the sites A, B, C respectively. The thermal velocity spread, which is of the order of $KT \approx$ .01-.02 slightly extends these cutoffs.

Contour plots of E_2 are presented in Figs. (7.6a, b, c), for the planes at z =.5, 2.0 , 3.5. Here we observe that the potential directly over the symmetry sites has near cylindrical symmetry. Within any given plane, A is always a local maximum and also the largest value of E_2 in the zone. B is a local maximum as well. Above C, one finds a local minimum for all positive values of z less than the desorption cutoff. The following observation is important in the discussions to follow: for any location on the mirror axis of the cell, only the y component of the transverse force is non-zero. This is not the case at general points in the zone; in particular, for sites on the x axis the y directed force component is positive, decreasing in magnitude from the zone center to either edge.

It is our intention to explore ion emission patterns produced by various adsorbed oxygen locations throughout the zone. Freedom in the locations of ground state energy minima is retained by modelling the ground state energy near its minima as a parabolic potential of the form:

$$E_1(\vec{r}) = -V_0 + \frac{1}{2}(\vec{r}-\vec{b})\cdot\overleftrightarrow{K}\cdot(\vec{r}-\vec{b})$$

The point $\vec{b}$ is some point in the zone representing an adsorption site.

V_0 is the chemisorption energy, which plays no explicit role in our calculations, since we approximate the excitation cross section by an unspecified constant. The principal axes for which we expect the spring constant tensor $\overleftrightarrow{K}$ to be diagonal are related to the direction between $\vec{b}$ and the nearest tungsten atom, when chemisorption occurs via a single bond similar to those in molecules. If the atom is adsorbed, over a symmetry site, the principal axes of the surface mesh should also diagonalize $\overleftrightarrow{K}$.

The vibrational frequencies related to the components of $\overleftrightarrow{K}$ are unfortunately not known for oxygen adsorbed on tungsten. Definite knowledge about the assymmetries to be expected in the ground state distribution is absent. Thus, we choose $\overleftrightarrow{K}$ diagonal along the principal axes of the cell. Three spring constants K_n, with $n = 1, 2, 3$ set the width Δr_n of the ground state, with $\Delta r_n = (\beta K_n)^{-1/2}$. For the time being, we assume an isotropic ground state. We estimate the order of magnitude of the K_n by scaling the known vibrational frequency of hydrogen on tungsten by the square root of the oxygen-hydrogen mass ratio; thus $K_n \approx .01$ Atomic units for $n = 1, 2, 3$.[83,84]

At room temperature, $\Delta r_n \approx .3 a_0$, which is small compared to the dimensions of the surface cell. The ground state we are using is thus well localized about any adsorption site. We expect the mean asymptotic direction of emission velocities within the pattern produced by each site to be fairly insensitive to the precise values of K_n chosen. However, the energy distributions within a lobe, and the angular width of the emission cone will be

sensitive to both K_n and to the temperature β. The curvature of the E_2 hypersurface is steep, at most places in the zone, compared, for example, to the thermal energy. Both Δr_n and the width of the thermal velocity distribution go as $\beta^{-1/2}$. Thus the effect of widening the ground state spacial potential well, either thermally, or through changing the spring constants, is generally an increase in the mean ejection energy and in the width of the ejected energy distribution. Widening of the ground state results also in admitting a wider cone of directions for the acceleration in the excitation region; hence the solid angle subtended by the desorption spots increases. We assume here that the asymptotic velocity for an ion is strongly correlated to its acceleration integrated over the short segment of the ionic path in the immediate region of the excitation point. Anticipating our findings, we remark that this is true for most of the sites studied. Thus, ions generally reach their asymptotic directions quickly. Their subsequent motion is dominated by the image attraction, whose integrated effect should be expected to be significant only on slowly moving ions. These have their impact colatitudes shifted to larger values. We remark, in passing, that measurements fixing the vibration energies of oxygen on tungsten are expected to be available soon.

Surface cell symmetry is the key to understanding the numbers of lobes observed. If adsorption is possible at any site in the zone, it is equally probable at all equivalent zone sites. Thus, each of the observed angular distribution patterns must be understood to be the superposition of six single site patterns related to each other by the covering operations of the surface.

Desorption patterns displaying lobes, such as those observed, will result only when a strong focussing mechanism operates. In the absence of such a mechanism, the thermal velocity spread will produce patterns which are diffuse, and which exhibit no tendency to form discrete emission spots. The attractive image force causes defocussing at intermediate distances, thus when focussing occurs it is close to the region where ionization takes place. We use the magnitude of the force at an adsorption site as a predictor of the degree of focussing to be expected. We use the colatitude $\theta_a = \tan^{-1}(F_\perp/F_z)$ and azimuth $\phi = \tan^{-1}(F_y/F_x)$ as an indication of the anticipated emission direction. We shall see later, when we discuss the results of calculation, that this rule of thumb holds. We neglect to discuss the role of the thermal velocity spread for the moment, as the gradients of E_2 are generally large.

When ionization occurs at or near one of the symmetry sites A, B, C, the ion trajectories will be normal, or nearly so to the surface, inasmuch as the transverse gradients of E_2 vanish. Excitation from a narrow spatial range centered around such a point will produce patterns having the same symmetry as E_2 about this point, and in which the predominant emission occurs normal to the surface if there is significant focussing. These patterns map into themselves under the symmetry pperations of the surface; hence, the points A, B, C, should produce cones of emission normal to the surface.

Away from the high symmetry sites, the transverse force on an ion is not negligible. When excitation occurs from a point located along the mirror

axis of Fig. (7.1), however, F_x will vanish. The ion emission directions will then conform to the 'primary' lobe orientation when F_y is negative, and the 'secondary' orientation when F_y is positive. Ionizing the surface atoms within a narrow region centered on such a point will produce a pattern with bilateral symmetry about the y axis. Thus three rotated replicas of such a pattern, will be observed, exhibiting the observed lobe structure whenever focussing is strong enough and the emission colatitude θ_v is large enough for them to be resolved. Patterns associated with a single low symmetry site, such as 'P', 'E' in Fig. (7.1) will be replicated six times. Inasmuch as the transverse component of F is not parallel to the mirror axes, at such sites, one expects six lobed patterns rotated from both the 'primary' and 'secondary' orientations.

Preliminary Calculations

In simulating the ion distributions, we have the option of using all equivalent sites in the zone, or considering the zone to be present on the surface in the three rotated orientations, plus their reflections. We adopt the second, more economical procedure, replicating each single site pattern in accordance with the six covering operations before displaying it. We chose scatter plots as the most convenient mode of display for the angular information. Each ion carries the same intensity in our approximation; hence we simply plot a symbol to simulate each desorbing ion impacting upon a screen. The position assigned to each impact corresponds to the colatitude and azimuth of the asymptotic velocity.

The qualitative conclusions which we will present regarding O^+

desorption from the W(111) surface are based both on a preliminary study and on more recent computations using quantitatively more realistic parameters. In preliminary computations we simulated angular distributions for the series of adsorption sites labelled A to O in Fig. (7.1), scanning these positions within a series of planes at fixed z coordinate wherever the energetics permitted desorption. Planes located from 0 to 3 atomic units from the surface were covered. Generally, one should restrict the tungsten-oxygen separation to exceed the sum of atomic radii, or the sum of covalent radii. In some cases, unrealistically small separations were chosen in these scans; however, all results cohere well with our later study in which quantitatively more correct separations were used. We chose 100^{o}K. as the desorption temperature, echoing the choice in most of the experimental runs. Scans at 700^{o}K. were also done to observe the temperature dependence. Three hundred trajectories originating on each adsorption site proved sufficient to establish the spot contours. In an independent set of computations, to be described below, we scanned adsorption site candidates at fixed values of the tungsten-oxygen separation.

Discussion of Results

The qualitative features of our results show marked independence of the choice for the dielectric surface. Computations done with this plane placed at $z = 0$ were compared with results obtained with the dielectric surface placed at $z = -d$. Increasing the image attraction diffused the emission cones and increased the colatitudes of the projected lobe centers. Excessive trapping of the ion trajectories at reasonable tungsten-oxygen separations

was observed with the $z = 0$ choice.

The image potential thus provides a mechanism which defocusses the desorption pattern of each localized adsorption site. Its effect should be expected to be most pronounced for small kinetic energies. The refractive effect of the image force on the spot pattern colatitudes is amplified when emission angles relative to the surface normal are large. Some of the quantitative identifications of adsorption site candidates with spot center angles, which we make later, are thus sensitive to our image potential model.

We found that the model surface potential which we have constructed for O^+ on W(111) produces sufficiently strong focussing of a distributed ion source, localized around an adsorption site, to form compact desorption spot patterns at most positions in the surface cell. The most diffuse spots were found near the trapping cutoff contours of E_2. Here the potential energies are the lowest. The image force and thermal velocity defocussing mechanisms compete successfully with the repulsive focussing mechanism. In general, wherever the surface potential is large, the magnitude of its gradient is large as well. In our model, focussing is caused by the impulse imparted to an ion in the neighborhood where it is excited. The detailed ion optics of E_2 are complicated, and we thus do not discuss them at length here. Each individual adsorption site is responsible for contributing a single lobe to the desorption pattern, wherever the emission direction is away from the surface normal.

It is impractical to present a sufficient number of angular distribution patterns to illustrate all of our observations. We have selected those

using plausible values of the adsorbed oxygen-tungsten distance only. We take 2.08A^{o} and 1.95A^{o} as indicators of the proper range for this parameter, for reasons discussed below.

As expected, we found that the number of distinct emission spots seen in the desorption pattern for an adsorption site candidate equals the number of points in the surface cell structure equivalent to the chosen site. This rule is essentially a truism imposed by the surface symmetry; we have verified that the potential we constructed does in fact possess the required property. This rule should be applicable to other surface geometries.

Directly over the symmetry points A, B, or C, central spot patterns are invariably found. The width of the spot above a particular point on the surface tends to increase with the bond length. In general, patterns obtained at the same bond length over the symmetry sites are significantly more diffuse for 'A' than for 'B' or 'C'. We have marked the points corresponding to the bond length 2.08A^{o} on the E_2 curves in Fig. (7.5). The potential decreases in the order C-B-A. These differences in compactness we attribute to the joint effect of image defocussing and the relative importance of transverse thermal momenta for the weakly accelerated ions at point 'A'.

The central spots generally exhibit some noticeable degree of axial assymmetry. One should anticipate this since E_2 is approximately axially symmetric only in the immediate vicinity of 'A', 'B', or 'C'. The departure from axial symmetry increases with widening of the excitation region. The spot patterns above 'B' or 'C' tend to assume roughly triangular shapes. Those associated with 'C' consistently assume the downward position for one

apex, relative to Fig. (7.1), reminiscent of the substrate registry of the primary lobes. Patterns for site 'B' consistently appear with apex up. We display in Figs. (7.7a, b, c) the spot patterns for adsorption sites 2.08 A^{o} above tungsten atoms at 'A', 'B', 'C' respectively. These positions correspond to $z \simeq 3.93$, 2.21, and .48 atomic units. The desorption temperature is $300^{o}K$. Similar, slightly compacted patterns were obtained with the bond length 1.95 A^{o}. Similar behavior was observed with less realistic values of the tungsten-oxygen separation with the anisotropies amplified in some cases.

Sites off the symmetry axis produce ion distributions quite unlike those observed experimentally. We illustrate in Fig. (7.8) a six lobed pattern produced by site 'P' on the x axis of Fig. (7.1). Here we chose $z \simeq 3.0a_0$, with $x \simeq -3.0a_0$. The image of this point lies on the right half of the asymptotic x-axis in Fig. (7.8), with superpositions producing the six lobed arrangement as expected. As one scans the desorption site from 'P' through 'E' toward 'D', the single lobe rotates counterclockwise about the origin toward the 'secondary' orientation. At site 'E', the off axis lobe has elongated sufficiently in its axial extent to produce a doughnut after superposition. Although patterns containing six lobes were observed experimentally, those produced in our simulation by off-axis sites cannot reproduce the observed orientations.

Sites anywhere along the cell symmetry axis except near A, B, or C, produce only trios of lobes having either the primary or secondary orientation. We display sets of such patterns in Appendix III. The adsorption sites

involved are identified in Fig. (7.12a, b).

We neither find, nor should we expect to find, a single adsorption site anywhere in the vicinity of the surface which produces all six lobes with the orientation observed by Madey, et al.

As one scans adsorption sites above the y-axis of Fig. (7.1), at fixed values of z, one finds that sites located between 'A' (at the top of the figure), and 'C' produce lobed distributions having the primary orientation only, while sites between C and B, or between B and A (at the bottom of the figure), produce only the secondary spots. A large increase or decrease in the strength of the O^{+}—tungsten atom potential would be required to cause E_2 to possess maxima at both 'C' and 'B', or minima at both points. As one scans from one symmetry point to the next, the lobe center colatitude grows in magnitude, reaches a maximum, and declines to zero as the next symmetry site is reached.

We have already stated that one may infer the calculated lobe orientation relative to the substrate, in a qualitative sense, by constructing the normal to the potential surface. Here one might refer to the contour maps in Fig. (7.6a, b, c) for verification. From A to C, the potential surface slopes downward into the paper in all the maps. From C to B, the slope is monotonically uphill. In Fig. (7.6a), for $z = .5$ A.U., the local maximum near B is pronounced, and it appears that a reversion to the primary orientation should occur, followed by an additional reversal to the secondary orientation toward the bottom of the map. This feature will not be observable, inasmuch as the

tungsten-oxygen separation in the $z = .5\, a_o$ plane is unreasonably small. The closest plane respecting the proper minimum bond length lies approximately at $z = 2.0\, a_o$ Here the potential surface is a plateau in the neighborhood below B, with a cliff between B and the x axis.

The effect of increasing the desorption temperature in our simulations was simply an increase in the width of emission cones or central spot patterns. We attribute this loss of definition to two mechanisms. The first is associated with the kinetic energy of the transverse thermal motion. The second is due to broadening of the ground state spacial distribution with temperature. Imagine the gradient vectors to E_2 to be constructed at each point in a volume of space corresponding to an ionization region. If the volume is widened, the cone of solid angles occupied by these vectors widens, since the curvature of a planar slice of the E_2 hypersurface is non-zero. This temperature effect in our simulation conforms to the experimental observations.

Qualitative Conclusions

The following conclusions concerning the adsorption of atomic oxygen on the tungsten (111) surface appear to be warranted, after comparing the results of our simulation to experimental findings.

1. Adsorption of oxygen on W(111) is confined to sites directly above the bilateral symmetry axis of the zone, and its degenerate rotations.

2. Emission patterns peaked in intensity normal to the surface are evidence of adsorption above one of the high symmetry sites 'A', 'B', or 'C'.

3. Adsorption sites located between 'B' and 'C' are the origin of

the trios of resolved emission spots observed with the primary orientation. The trios of secondary lobes are caused by oxygen atoms adsorbed between 'B' and 'C', or between 'A' and 'B'.

4. The ion distribution obtained experimentally via adsorption at $100^{o}K.$, with intermediate heat treatment to high temperatures (those displaying the six spot pattern), are superpositions formed by two oxygen adsorption phases coexisting on the surface, one producing each trio of spots.

It also appears reasonable to hypothesize that the remainder of the low adsorption temperature sequence, i.e. those patterns obtained with heat treatment to temperatures $\leq 235^{o}K$, may be superpositions of two oxygen adsorption phases, one at a high symmetry site A, B, or C, plus a site producing the downward facing apexes of the triangle, which evolve into well resolved primary lobes with heat treatment to progressively higher temperatures. This model involves the assumption that migration of oxygen atoms adsorbed on the surface away from a symmetry site into a bonding configuration which produces the primary lobe set is permitted. Presumably, a threshold is reached at higher temperature permitting significant migration to a third adsorption site, producing the secondary lobe set, and completing the depletion of the source of the normal emission spot. The observed changes in emission geometry do not arise simply from excitation of higher vibrational states in state 1. Such changes would be expected to show thermal reversibility.

We do not adopt this speculative evolutionary picture too readily, as other models involving the formation of surface complexes containing

several oxygen atoms may be able to account for the observed lobe pattern sequence.[8,85]

Identification of Adsorption Sites

Now we present quantitative findings obtained for O^+ on W(111) by consistently respecting realistic values of the oxygen-tungsten bond length. The objective has now become the following: we locate a series of plausible adsorption sites whose simulated ESD patterns match those observed experimentally as closely as possible. The range of sites to scan has already been narrowed to the y-z plane of Fig. (7.1) by symmetry, hence only this region will be considered.

Our strategy is the following: We survey the desorption patterns produced by scanning two series of adsorption sites in the y-z plane. Each series consists of points which are a fixed bond length from the nearest tungsten atom. In addition to examining ion distribution plots, we make quantitative determinations of the lobe center locations for each site.

At the outset, one should observe that the quantitative results of this section depend on the specific model surface potential we are using. Our conclusions up to this point remain stable over a wide range of potential models. We have taken the liberty of neglecting spatial variations in the quenching and excitation rate; however, these approximations are expected to lead to serious error only in intensity calculations. A computation such as this one, provides a rough guide to limit the tenable adsorption geometries, as well as exemplifying the use of angular desorption simulations for discriminating them.

The primary lobe center colatitude $\langle \theta_v \rangle$ has been estimated for one of the six spot ESD patterns observed by Madey, et al. The reader is referred to Fig. (2c) of reference (8) which displays that pattern obtained by oxygen adsorption at 100°K., heat treatment to 665°K., and cooling to 100°K. for the desorption experiment. The estimate $\langle \theta_v \rangle \approx 34° \pm 4°$ was made. No determination of $\langle \theta_v \rangle$ for the secondary trio of lobes was given. The geometry of the figure prompts us to estimate $|\langle \theta_v \rangle| \leq 38°$ Henceforth, we consistently assign $\langle \theta_v \rangle > 0$ to the primary lobe geometry, $\langle \theta_v \rangle < 0$ to the secondary, for the remainder of this paper. Our $\langle \theta_v \rangle$ estimate for the secondary trio may be speculative for reasons cited by the authors of reference (8).

We assume that oxygen adsorption on tungsten results in the formation of entities on the surface resembling molecules, in that at most several nearest tungsten atoms participate in the oxygen binding. We do not rule out the possibility of O_2 molecules adsorbed on the surface, or surface complexes involving several oxygen atoms. For the present we restrict consideration to adsorbed oxygen in atomic form.

More than one tungsten-oxygen bond length may be required in this system. We have already inferred from the ion distribution data the presence here of at least two adsorption phases, whose bond lengths may differ. Hence, we bracket the bond length in these calculations between two plausibly chosen values, performing one complete scan of adsorption sites with each value.

One trial value for the bond length was based on the work of Van Hove and Tong,[25] who recently found the W-O bond length on the W(110) surface

via LEED. They find atomic oxygen bound principally to three nearest tungsten atoms in the surface layer, equidistant from each. The bond length found is 2.08 A^{o}, which is close to the sum of covalent radii. We accepted this value despite the fact that the W(111) geometry does not permit this adsorption geometry along the mirror symmetry axis. Points on the mirror axis equidistant from three or more tungsten atoms can be found only with long bond lengths, placing the oxygen center in the region where image attraction prohibits desorption. We also adopt for use in this calculation the sum of Slaters empirical atomic radii. This has the value 1.95 A^{o}.

In Fig. (7.9) we show a scale cross sectional view of the W(111) surface cell sliced by the y-z plane. Tungsten atoms are shown as circles. Their radii are proportional to the empirical atomic radius of tungsten, the sum of which agrees well with the known interatomic spacing in the solid. Other dimensions shown may be deduced from the data given in Fig. (7.4). Not shown are the two surface layer tungsten atoms, which would appear above and below the point $x = 0$, $y = 0$ in this projection. The angles 19.5^{o} and 35.3^{o} are those formed by the surface normal with the (112) and (110) surface facets respectively.

We show by the curves labelled 's' and 't' in Fig. (7.9) the range of adsorption sites candidates covered in our scans. Each is the locus of points either 2.08 or 1.95 A^{o} from the nearest tungsten center. The cusps denote points equidistant from two nearest tungsten atoms. Computations were performed at the points marked by triangles. Their zone coordinates

may be inferred from Fig. (7.9). The angles α, β, γ defined as shown specify the relation of an oxygen atom to the nearest 'A', 'B', or 'C' type tungsten. They are positive counterclockwise from the surface normals. The angles $\alpha_{max}, \beta_{max}, \gamma_{max}$ are slightly different for the two bond lengths. Their values are shown on Fig. (7.9).

We performed two series of computer calculations as described. For computational economy only 100 trajectories originating on each site were selected by our Monte Carlo simulator and integrated to $z = 50\ A^{o}$. We chose the spring constants $K_n = .04$ atomic units, departing from the value used previously. This combination of K_n and 100 points was sufficient to establish lobe centers which agreed to within 1-2 degrees with those generated by 500 points and $K_n = .01$ in initial testing. This compromise facilitated accumulating simulated data for enough sites to allow interpolation as described below. Somewhat higher vibrational energies may be physically justified near the sites at $\alpha_{max}, \beta_{max}$ and γ_{max} where double bonding may exist.

We recorded simulated ion distribution data consisting of the asymptotic velocity components, the desorption energy, and the time of flight for each ion trajectory. The desorption energy we took to be $E_2(\vec{r}_0) + \frac{1}{2}Mv_0^2 - E_2(\infty)$ where $\vec{r}_0$, $\vec{v}_0$ are the initial coordinates. Errors in following the trajectory were estimated by comparing this value with the exit kinetic energy computed from the final velocity components. This discrepancy was kept below 2%. We also retained the acceleration components at the excitation point for each ion. These play an important role in our analysis.

The lobe center positions were established by vector averaging the asymptotic velocities emerging from each adsorption site. The colatitudes of these quantities we denote $\langle \theta_v \rangle$, the azimuths $\langle \phi_v \rangle$. Some distortion was introduced by projecting our ion distribution plots on either a flat or hemispherical screen, simulating the experimental viewing arrangement. Significant differences in the apparent lobe shapes result. However discrepancies between the projected central colatitudes and $\langle \theta_v \rangle$ were insignificant. We also vector averaged the initial accelerations for ions excited at each site, denoting their colatitudes and azimuths $\langle \theta_a \rangle$ and $\langle \phi_a \rangle$ respectively. Both $\langle \phi_v \rangle$ and $\langle \phi_a \rangle$ were either 90° or 270° as required, hence we consider them no further. The positive sense for $\langle \theta_a \rangle$ is in the primary lobe orientation. Each site thus produced a trio of lobes with one of the two observed experimental orientations, confirming earlier results. Ion distribution plots were prepared for each site.

Discussion of Results

In Fig. (7.10a, b) and (7.11a, b) we plot the variation of lobe center with bond angle. Here we add for comparison the acceleration colatitude. Mean ion desorption energies were also calculated, as were the times of flight to the $z = 50\text{A}^\circ$ plane, where desorption is considered complete. This information is displayed as functions of α, β and γ in Figs. (7.10c) and (7.11c). Inasmuch as the information contained in these graphs yields important clues to the ion dynamics we examine them in some detail.

The results for both bond lengths show consistency in their trends, with some quantitative differences. First we note in Figs. (7.10a) and (7.11a) that the primary lobe directions are produced only for $\alpha > 0$ and $\beta < 0$. This range corresponds to adsorption in the region from A to C along the mirror axes, with all other sites producing secondaries or central spots. Our earlier conclusion is thus supported. Moreover, this conclusion is resistant to errors in modelling E_2 unless they are serious enough to convert both $\beta = 0$ and $\gamma = 0$ into strong maxima or minima.

For all of the atomic positions studied, there is good qualitative agreement between $\langle \theta_a \rangle$ and $\langle \theta_v \rangle$, confirming expectations that the initial impulse direction is a useful indicator of lobe orientation. For both bond lengths there is excellent quantitative agreement between $\langle \theta_a \rangle$ and $\langle \theta_v \rangle$ as well, in the neighborhood flanking the 'B' and 'C' tungsten atoms; that is, throughout the β and γ angular range. Also, there is near coincidence of Fig. (7.10b) and Fig. (7.11b) for the β, γ range of sites. We take this as an indicator that our predictions throughout these regions for $\langle \theta_v \rangle$ are independent of small errors in the bond length. The in-flight ion dynamics appear to be simple in these regions. Ionized oxygen atoms propagate in essentially a straight line away from the surface, with no significant image refraction.

Next we examine chemisorption sites in the region directly over a surface tungsten atom. For these the quantitative agreement of $\langle \theta_v \rangle$ with $\langle \theta_a \rangle$ is poor. Emission spots form significantly further from the surface

normal than $\langle\theta_a\rangle$ would indicate. We attribute this effect to refraction of the ion trajectories by the image force, with the most effective refraction occurring in the range $\alpha \approx 55^\circ$, $\alpha \approx -40^\circ$ for both bond lengths studied. In general, image refraction and defocussing effects are amplified for the longer bond length. Our predictions for $\langle\theta_v\rangle$ for adsorption sites over the surface tungsten atoms thus display considerable bond length dependence. In actuality, most of the interesting sites considered below lie where bond length dependence is not strong enough to shift the result appreciably.

The region on both Fig. (7.11a) and Fig. (7.10a) between $\alpha \approx 70^\circ$ and $\beta \approx -10^\circ$ displays behavior quite different from that described above. Here $\langle\theta_a\rangle$ lies above $\langle\theta_v\rangle$, implying that deflection of the ions toward the surface normal occurs in flight. Repulsion dominated behavior such as this can arise only from the atomic tungsten potentials, with the deflection occurring before the ions have left the surface cell. The sharp switch in Fig. (7.10a) and Fig. (7.11a) to repulsion dominated behavior, accompanied by a sharp drop in $\langle\theta_v\rangle$, is no doubt attributable to repulsion by the tungsten atom at 'C', and by those not shown in Fig. (7.9) in the surface layer.

In the region $-30 \leq \alpha \leq +40^\circ$, a single tungsten atom in the $z = 0$ layer provides the dominant initial impulse to an ion, as one should expect. The acceleration colatitudes are an excellent fit to the 45° line $\langle\theta_a\rangle = \alpha$. The lobe centers $\langle\theta_v\rangle$ also fit a straight line, which is rotated however due to image refraction. Here the directions one would impute to the chemisorption bonds agree well with $\langle\theta_a\rangle$.

In the range $-50 \leq \gamma \leq 0$ there is also fair agreement with $\langle \theta_a \rangle = \alpha$, except for a constant shift of about 7°. Here ionized oxygen atoms exit approximately radially away from the 'B' tungsten atom.

Elsewhere in the zone, several surface tungsten atoms combine to produce the initial impulse. The direction radially away from the nearest tungsten atom, which one would tend to associate with the bond direction, is not a reliable indicator of oxygen emission directions. In our model, ionization is a recoilless event, with the emission direction set by the properties of $E_2(r)$. Hence, speculations about the strengths and direction of the ground state chemisorption bonds are superfluous.

Ion distribution plots for each adsorption site and bond length were examined. The most diffuse lobes were found where image refraction effects dominate most strongly; that is, in the range $\alpha \approx 50^{\circ}$, $\alpha \approx -40^{\circ}$ in our model calculation. The compact structure observed in the experimental ion patterns is preserved throughout the β and γ range of sites, with the densest structures found with the largest desorption energies $\langle E \rangle$. These points are found at α_{max}, β_{max} and γ_{max} on Fig. (7.10c) and Fig. (7.11c) equidistant from a pair of tungsten atoms. Desorption energies in the β, γ range of sites are significantly larger than those in the image dominated region $-40 \leq \alpha \leq +60$, throughout which $\langle E \rangle$ is flat. One expects this flat region if an ion interacts here principally with a single surface atom.

Our picture of the ion dynamics prompts us to associate well focussed emission spots with high average desorption energies, while diffuse lobes with poor definition result when energies are low. Here, there is an implied comparison of repulsion and image contributions specific to the system we consider. This picture may need modification if $E_2(\vec{r})$ is highly anisotropic over the width of the ground state, in which case there may be defocussing of high energy cones. Longer bonds lengths tend to lower the desorption energies, magnifying image effects. Minima of $\langle E \rangle$ occur directly over the symmetry sites A, B, C, with the value of $\langle E \rangle$ at the minimum increasing in that order. The compactness of central spot pattern increases in the same order.

The flight times are interesting as an indicator of the effectiveness of reneutralization processes, which we discuss further at a later point. The times remain roughly constant on Figs. (7.10c) and (7.11c) throughout the β, γ range of adsorption sites. However, $\langle t \rangle$ increases sharply for adsorption over the surface tungsten layer, becoming quite sensitive to variations in α and in $\langle E \rangle$. The assymmetry in $\langle t \rangle$ about $\alpha = 0$ is evident also in Fig. (7.10a), (7.11a) portraying $\langle \theta \rangle$. It is no doubt caused by proximity to a 'B' layer tungsten atom for $\alpha < 0$ as opposed to a deeper 'C' layer tungsten atom for $\alpha > 0$. In the region about $\alpha = 0$ where $\langle E \rangle$ is constant, $\langle t \rangle$ would increase as $1/\cos(\alpha)$ even if the image potential were neglected. Our graphs do not fit such behavior, indicating that the ion paths are curved.

Two series of adsorption site candidates were obtained by interpolation from Fig. (7.10a,b) and Fig. (7.11a,b). Values of α, β, and γ consistent with the primary lobes having $\langle\theta_v\rangle \simeq 34^\circ$, or secondary lobes at $\langle\theta_v\rangle \simeq 38^\circ$ were selected. One such series was interpolated for each of the bond lengths we are using. The locations of the chosen points are displayed in Fig. (7.12a,b). For each site an ESD pattern at 100°K. was calculated in the manner previously described. The original estimate $K_n \approx .01$ atomic units was retained, setting the width of the ground state distribution at .18 atomic units for 100°K. In each case 500 ion paths were selected by the Monte Carlo method. Simulated central spot patterns were also obtained for sites above A, B, C, under the same conditions. Several of the sites we interpolated are almost equidistant from a pair of tungsten atoms. We thus calculated ion distributions also for the sites at α_{max}, β_{max}, and γ_{max}.

The calculated values of $\langle\theta_v\rangle$, $\langle\theta_a\rangle$, $\langle E\rangle$ and σ_E are displayed in tabular form in Figs. (7.12a,b). The widths of the desorption energy distributions, σ_E, and the range of flight times, were estimated by calculating the standard deviations of data for single ion paths. Ion distribution plots for each site were prepared.

Potential Oxygen adsorption sites we have identified fall naturally into three grouping according to desorption energy and flight time. These clustering mirror their spacial distribution in the surface cell. The 'surface' group, consisting of the sites in the neighborhood of the symmetry point at 'A', includes those at $\alpha = 0$, $\alpha \approx \pm 20$. The 'interior' group, consisting

of those locations most deeply embedded in the surface, includes locations above 'C', and those flanking it near α_{max} , β_{max} . The desorption energies in each group show considerable dependence on bond length, as evidenced by comparison of Fig. (7.10c) to Fig. (7.11c). However, the energy clusterings are preserved for each of the bond lengths in this study. Those sites within the 'surface' group emit ions with significantly lower energies than those in the 'interior' group.

Conclusions

The simulation of ESD for O^+ from W(111) described above suggests the following conclusions: The ionic desorption spots in the experimental ESD pattern sequence under consideration [8] are consistent with the adsorption of atomic oxygen. All of the sites listed in Fig. (7.12a,b) match the lobe orientation and number, as well as the colatitudes of the observed normal and non-normal emission spots. Either the 'surface' group or the 'interior' group of sites alone can plausibly account for the gross features observed experimentally. One assumes that adsorption phases within each group coexist on the surface, producing ESD intensities which are superpositions of the patterns from individual sites. In the discussions to follow, we discuss the clusters of sites collectively, assuming that either adsorption over the surface tungsten layer, or adsorption within the recesses of the surface cell is favored.

The apparent differences between simulated angular distribution patterns of a given emission spot type are ones of compactness and shape. Comparisons with experiment based primarily on visual similarity are thus subjective.

The ion distributions which we display as illustrations do not by themselves provide an adequate basis for selecting that superposition of patterns most consistent with experiment. The experimental ion optics and display apparatus introduce unknown contrast compressions which may be quite different from those of our simulation. Moreover, reneutralization may significantly modulate the lobe shape predicted by our constant quenching model. Relative intensities and widths of lobes depend on quenching effectiveness and on the unknown populations of the sites involved.

We have recently been informed that the desorption energies for O^+ ions in this system lie in the range ~ 8 ev.[86] The calculated desorption energies displayed in Fig. (7.12a, b) lead us to favor those sites with the largest values of $\langle E \rangle$ as possible sources of the experimental ESD patterns. Here we are suggesting that adsorption at or near the points α_{max}, β_{max}, and above site 'C' on Fig. (7.9) produces the primary, secondary, and normal emission spots respectively. Adsorption over the surface tungsten layer is most strongly ruled out by our simulation. Adsorption in the vicinity of the tungsten layer at 'B' is less plausible, inasmuch as lower desorption energies are produced here than at the sites selected.

We review below the arguments supporting these conclusions. In addition to appraising the desorption energy data and visual agreement of the simulated patterns, some of the qualitative effects expected due to reneutralization are anticipated in the following discussion. The dependence of the results on the model ion-solid potential is considered.

Reneutralization mechanisms are known to be effective in this system. The average ion survival probability has been estimated to be [86] $\langle S_2 \rangle \sim 10^{-4}$. This estimate is made by comparison of the total O^+ desorption cross section on W(111) with that for O_2 molecular dissociation by electrons.

We gain qualitative insight into the role of quenching for the sites under study by approximating the reneutralization rate Q(z) by an average value $\langle Q \rangle$ neglecting all spatial variation. In general, Q decays rapidly with distance from the surface inasmuch as it involves overlap matrix elements. Transverse anisotropies may be important as well. In the W(111) cell, spaces between tungsten atoms exposed to the vacuum are large. It may be reasonable to speculate that contours of constant Q parallel the loci of adsorption sites in this study at constant distance from the atomic centers. The average ionic survival probability for desorption from a particular site might be taken to be:

$$\langle S_2 \rangle \approx \exp\left[-\langle Q \rangle \langle t \rangle\right]$$

with $\langle t \rangle$ the mean flight time. Here the inferred value of $\langle Q \rangle$ grossly underestimates the reneutralization rate near the surface, whose decay is neglected. This picture is useful for comparative discussion only. Estimation of the quantitative importance of quenching requires independent determination of Q, including spatial variation. Based on the flight times in Figs. (7.10c),

(7.11c), an estimate of $\langle Q \rangle$ is obtained. For the surface sites $\langle Q \rangle \sim 5 \times 10^{+12}$ sec^{-1} is indicated, while if the 'interior' sites are the emission source, Q 8x10 ^{12}sec^{-1}. Inasmuch as times of flight to z $\approx$100 a_o are given, the average amplitude near the surface should be $\sim 10^2$ larger.

Within this model, lobes with small desorption energies are heavily quenched. Heavy attenuation for the surface site group should be expected, compared to those near 'C'. Modulation of the intensities within a single lobe is related to the compactness of the spot. Wherever emission patterns are highly collimated, the ions follow similar paths; S_2 then attenuates each ion comparably, with only slight modification of lobe contour resulting. Large values of $\langle E \rangle$ are associated with such emission; thus the overall intensity reduction of compact emission cones is minor compared to the attenuation of diffuse patterns. These are found in our simulation to occur with evident image refraction and dispersion. A model calculation incorporating quenching would preferentially extinguish low energy ions, which are assumed to exit at high colatitudes when image effects are dominant, compacting the emission cones and shifting $\langle \theta_v \rangle$ inward.

Attenuation of the low energy part of the desorption spectrum via reneutralization will shift upward the mean ejection energy. It would be useful to know the experimental ion energy spectrum for each lobe and normal emission cone. This form of spectroscopy can be used to discriminate between alternative adsorption phases and to probe interactions with the surface. Ex-

perimental information on ion desorption spectra is not, however, available at present.

We illustrate in Fig. (7.13) a pair of typical emission energy spectra resulting from our simulation. Here we compare the primary lobe sources whose bond lengths are 1.95 A^o: one at $\alpha \approx 23^o$, the other at $\alpha \approx 85^o$. The spectra for these adsorption phases should be distinguishable. The spectra become harder to resolve if the 'surface' site is quenched most heavily, as constant $\langle Q \rangle$ would suggest. Its spectrum will shift further upward in energy than the spectrum for $\alpha = 85^o$. We find that desorption spectra for sites within the same cluster of Fig. (7.12a, b) may be difficult to resolve spectroscopically as they overlap.

This model calculation predicts desorption energies which are low for all sites considered compared to the experimental estimate of ~8 ev. Final judgement of the quantitative correctness of our model for E_2 is reserved pending additional spectroscopic data. The best agreement occurs for sites with the 1.95 A^o tungsten-oxygen separation at $\alpha = 85^o$, $\gamma = -53^o$. Their energy spectra peak at ~ 2 ev., with widths of ~ .5 ev. The corresponding central spot source has $\langle E \rangle \approx 1.3$ ev. and is slightly narrower. A crude estimate of the upward mean desorption energy shift due to quenching was made. With the energy distributions taken to be gaussian, the peak is shifted upward by 1-2 times the width σ_E .

Examination of Figs. (7.10a), (7.11a) reveals that $\langle \theta \rangle$ is insensitive to small shifts of adsorption site location near α_{MAX}, β_{MAX}, while

$\langle E \rangle$ varies sensitively with shifts in the same range. Adsorption on the sites at α_{MAX}, β_{MAX}, with larger desorption energies, is therefore plausible as a prediction of this model. Adsorption near γ_{MAX} is sensitive to small locations shifts; however, agreement of $\langle \theta_v \rangle$ at the point γ_{MAX} with the observed secondary lobe colatitude is poor.

We observe that the site at α_{MAX} lies along the direction normal to that taken by (110) facets which might form on the surface, while β_{MAX}, γ_{MAX} lie normal to the (112) facet direction. An explanation of O^+ emission based on desorption normal to such facets has been considered [8] but rejected. Desorption normal to a (112) facet predicts secondary lobes at $\langle \theta_v \rangle \sim 20^\circ$, as does desorption from the site at γ_{MAX} in our study. Evidence has not established the formation of actual facets in the experimental temperature range. Sites near β_{MAX} produce secondary emission lobes in our study at $\langle \theta_v \rangle \geq 30^\circ$, rather than $\langle \theta_v \rangle \sim 20^\circ$, due to the effect of V_{IM} on $\langle \theta_a \rangle$.

Mean energies for the surface site group are an order of magnitude smaller than the experimental energy estimate of 8 ev. Small changes in the dielectric surface location alter the detailed results, but leave the choice of preferred adsorption locations invariant. An outward shift lowers the desorption energies for all sites, while bringing $\langle \theta_v \rangle$ for α_{MAX}, β_{MAX} closer to the observed value. An inward relocation raises the desorption energies for the surface sites only slightly. Our conclusion is most sensitive to the model Hartree potential. We approximated V_H as the sum of individual

tungsten potentials for neutral, unperturbed atoms interacting with a point charge O^+ ion. Our rejection of adsorption sites over the surface tungsten layer would require revision if, for example, tungsten atoms in the surface layer were found to carry partial ionization sufficient to produce an order of magnitude change in the interaction energy.

Ion Distribution Plots

Now we present ion distribution plots obtained by superposing emission patterns from some of the adsorption site candidates in Fig. (7.12a,b). The visual trends in these confirm conclusions reached in the discussion of ion desorption energies. For completeness, the ion distribution patterns calculated for each of the sites listed in Figs. (7.12a,b) are presented for inspection as Appendix III.

In Fig. (7.14a) and (7.14b) we show the pair of superpositions least favorable to adsorption at the 'interior' sites. Ion distributions for sites at $\alpha = 23^\circ$ and $\alpha = -27^\circ$, 1.95 A° from the surface tungsten atom were merged to form Fig. (7.14a), showing primary and secondary lobes. The trios of spots originating at $\alpha = 80^\circ$, $\gamma = -49^\circ$, W-O distance 2.08 A° are displayed in Fig. (7.14b).

The 'surface' sites produce the expected diffuse lobes, with well developed cometary tails. Those formed by the 'interior' group are densely packed. The primary lobes possess a distinct cigar shape. Compactness and definition deteriorate in order of decreasing $\langle E \rangle$. The projection scheme in use magnifies the cometary aspect of Fig. (7.14a). However, the authors of reference (8) imply that the actual ion paths through their

apparatus justify this projection. We cannot estimate reliably the degree to which the lobes of Fig. (7.14a) will be compacted by quenching. One should expect some reduction in the cometary aspect, accompanied by an inward shift of $\langle \Theta_v \rangle$. The lobes for sites near γ_{MAX} are intermediate in density between those displayed for 'surface' and 'interior' oxygen locations. Our previous dynamical picture involving image effects explains the structural differences. We note that in-flight repulsion of the ions is implied, for the primary lobes only, by Fig. (7.10a) and (7.11a). This produces the cigar shape. The secondary lobes are roughly circular as the flight dynamics are simple.

Now superpositions of primary and secondary lobes most favorable to our conclusion are shown. Fig. (7.14c) shows emission of oxygen adsorbed 1.95 A^o from the nearest tungsten atom, at $\alpha = 85^o$, $\gamma = -53^o$. Here the spots are almost indistinguishable from those in Fig. (7.14b), although slightly sharpened. Fig. (7.14d) shows the low energy lobes for adsorption 2.08 A^o over a surface tungsten atom. Here the lobes are poorly resolved in the azimuthal direction. Except for variations in $\langle \Theta_v \rangle$, ion distribution lobes for oxygen adsorbed at α_{MAX}, β_{MAX}, γ_{MAX} are barely distinguishable from those shown in the preceding figures. In Figs. (7.15a) to (7.15d) we show superpositions of primary lobes with normal emission spots. These simulate the low heat treatment patterns of Ref. (8), Fig. (2a), (2b). When comparing central spot vs. primary lobe intensities in these patterns, to the experimental sequence, one should recall that variations in site population and quenching effects have not been incorporated into the

simulation.

Summary

Models of oxygen chemisorption on W(111) involving surface complexes containing several oxygen atoms in close association have been proposed by several authors [8,85] These we expect to produce low desorption energies or very high emission angles when repulsion between O^+ ions and neighboring neutral oxygen atoms is included.

Many observed features of the ESD of O^+ from W(111) have been left unexplained in this initial calculation. The original three primary lobes are observed to diverge with heating of the crystal. Such behavior may be related to as yet unobserved thermal changes in the interplanar spacing. The origin of the high adsorption temperature emission sequence observed by Madey, et al is unknown. Despite superficial similarities to the previous sequence, these patterns disappear on heating to $T \approx 600^{\circ}K$. without the formation of a secondary lobe set. Hence, other adsorption phases may be present.

In summary, this investigation has identified several adsorption sites for atomic oxygen on W(111) which provide a reasonable explanation of some of the limited ion distribution and energy data presently available. The symmetrical features of the experimental patterns have been shown to result from anisotropies of the ion-solid potential imposed by surface cell geometry. These features were used to limit the range of plausible atomic oxygen adsorption sites. A method by means of which model ion-solid potentials may be used to produce quantitative simulations of observed ESD ion angular distributions has been illustrated. The utility of desorption energy spectroscopy has been suggested.

Chapter VII: Figure Captions

Fig. 7.1: Unit cell of the W(111) surface. Large circles represent billiard ball tungsten atoms. The orientation of 'primary' ESD emission lobes relative to the substrate is indicated by the trio of heavy circles. The 'secondary' lobe orientation is rotated by 180^{o}. The choice of cartesian axes on the surface is indicated. Dashed lines through points 'B','C' are bilateral symmetry axes. The A - A distance $a_s = a\sqrt{2} = 8.44\ a_o$. Various points of interest where computations were performed are marked by roman letters. The 'A' tungsten atoms lie in the surface layer at the points $(\pm 4.22, 0, 0)$ and $(0, \pm 7.31, 0)$. The 'B' and 'C' tungsten atoms reside in the second and third planes down, at the points (0,-2.44,-1.72) and (0,2.44,-3.44) respectively.

Fig. 7.2: The Unit cube of the Body Centered Cubic bulk lattice of Tungsten. The triangles shown define planes normal to the (111) direction.

Fig. 7.3: View of the W(111) surface. Tungsten atoms are represented as spheres whose radius is $2.55\ a_o$. Sites in the surface layer are marked 'A'. Those in the second and third layers into the solid are denoted 'B' and 'C' respectively. The surface unit cell is outlined, in the orientation of Fig.(7.1).

Fig. 7.4: Table of some characteristic lengths pertaining to the Tungsten-Oxygen system.

Fig. 7.5: The Ion-Solid Interaction Energy $E_2(r)$, as a function of z coordinate, above the W(111) zone symmetry sites 'A','B','C'. The Image Potential contribution is plotted separately as the dashed line. Points which are either 1.95 or 2.08 Angstroms above one of the high symmetry points are marked.

Chapter VII: Figure Captions, continued

Fig. 7.6 a,b,c: Contour Maps of the Ion-Solid Interaction Potential $E_2(r)$ through planes at $z = .5\ a_o$, $2.0\ a_o$, $3.5\ a_o$.

Fig. 7.7a, b, c: Simulated ESD Ion Angular Distribution patterns for adsorption sites above high symmetry points 'A', 'B', and 'C' respectively. The W - O separation was taken to be 2.08 A.^{o} Desorption at 300^{o}K. was simulated. Note that scale marks appear each 5 degrees of colatitude on these and all subsequent computer generated ESDIAD plots.

Fig. 7.8: Simulated ESDIAD pattern for site 'P' of Fig. (7.1). The coordinates of the chosen site are $(-3a_o, 0, 3a_o)$. Note that the lobes are rotated from either the 'primary' or 'secondary' orientation.

Fig. 7.9: Cross Section view of the W(111) surface unit cell, drawn to scale. A slice of Fig.(7.1) through the y-z plane is shown. The positive sense for angles α, β, γ is counterclockwise from the 'A', 'C', 'B' axes shown. All dimensions are in Bohr radii. Curves 'S' ('T') mark the locii of adsorption sites 2.08 (1.95) Angstroms from the nearest tungsten atom, which were were covered by the scans described in the text. The upper and lower limits of α, β, γ were as follows:

	α_{max}	β_{min}	β_{max}	γ_{min}	γ_{max}	α_{min}
'T' :	89.4	-18.8	25.1	-64.0	25.1	-64.0
'S' :	84.7	-14.2	21.7	-60.6	21.7	-60.6

Chapter VII: Figure Captions, continued

Fig. 7.10a,b: Colatitudes of ESD emission lobe centers for O^+ desorption from W(111). The adsorption sites covered lie along curve 'T' of Fig.(7.9). Solid lines portray the lobe center colatitude $\langle\theta_v\rangle$ as a function of angle 'α', 'β', and 'γ'. Dashed lines depict $\langle\theta_a\rangle$, the mean acceleration colatitude. Lobe trios with the 'primary' orientation are found only for $0 < \alpha \leq \alpha_{max}$ and $-\beta_{min} \leq \beta < 0$, corresponding to adsorption along the unit cell symmetry axis of Fig.(7.1) between point 'A' (at the top of the figure) and point 'C'.

Fig. 7.10c: Mean desorption energies $\langle E\rangle$ and flight times $\langle t\rangle$ to the z = 50 A.° plane, for sites on curve 'T' of Fig.(7.9). These are 1.95 A.° from the nearest tungsten atom location. Data are plotted as functions of the angles 'α', 'β', and 'γ', with the solid line representing $\langle E\rangle$, the dashed line portraying $\langle t\rangle$. Energies are in multiples of .01 Hartrees. Times are in multiples of 10^4 atomic units, where 1 time atomic unit = 2.42×10^{-17} sec.

Fig. 7.11a,b: Colatitudes of ESD emission lobe trios, $\langle\theta_v\rangle$, and mean acceleration colatitudes $\langle\theta_a\rangle$ for 2.08 A.° W - O separation. Adsorption sites lie on curve 'S' of Fig.(7.9). (See caption for Fig. 7.10a,b.)

Fig. 7.11c: Mean Desorption energies $\langle E\rangle$ and flight times $\langle t\rangle$ to the z = 50 A.° plane, for adsorption sites covered in Fig. (7.11a,b). (See caption for Fig. 7.10c)

Chapter VII: Figure Captions, continued

Fig. 7.12a: Tabulation of simulated ESDIAD data for adsorption site candidates interpolated from Fig.(7.10a,b). The W-O separation is 1.95 A.^{o} Each site is identified by the angle 'α','β',or 'γ', or by 'A','B',or 'C' if it lies above a high symmetry point. For all sites, x = 0. The y,z coordinates are given. The ESD pattern type corresponding to desorption from each site is abbreviated 'PL' (primary lobes), 'SL', or 'CS' (central spot). The first three sites belong to the 'surface' group discussed in the text. The next four are in the 'interior' group. The results of ESD simulations for oxygen adsorbed at α_{max}, β_{max}, γ_{max} are displayed for comparison.

Fig. 7.12b: Tabulation of simulated ESDIAD data for sites interpolated from Fig.(7.11a,b). The W-O separation is 2.08 A.^{o} The first three sites are the 'surface' group, the next three are the 'interior' cluster.

Fig. 7.13: Comparison of simulated desorption energy spectra for a pair of oxygen adsorption sites producing 'primary' lobe patterns. From Fig.(7.12a) we selected those at $\alpha = 23^{o}$ and $\alpha = 85^{o}$. P(E) is normalized to 1.

Fig. 7.14a, b, c, d: Superposition of simulated ESD Ion Angular Distribution patterns displaying 'primary' and 'secondary' lobes, as discussed in the text.

Fig. 7.15a, b, c, d: Superpositions of ESDIAD patterns displaying a central spot in conjunction with 'primary' lobes. 'Surface'

Chapter VII: Figure Captions, continued

sites are portrayed in Figs. (7.15a,b). 'Interior' sites are superposed in Figs.(7.15c, d). For more complete identification, refer to Fig. (7.12a,b), where adsorption site data are tabulated.

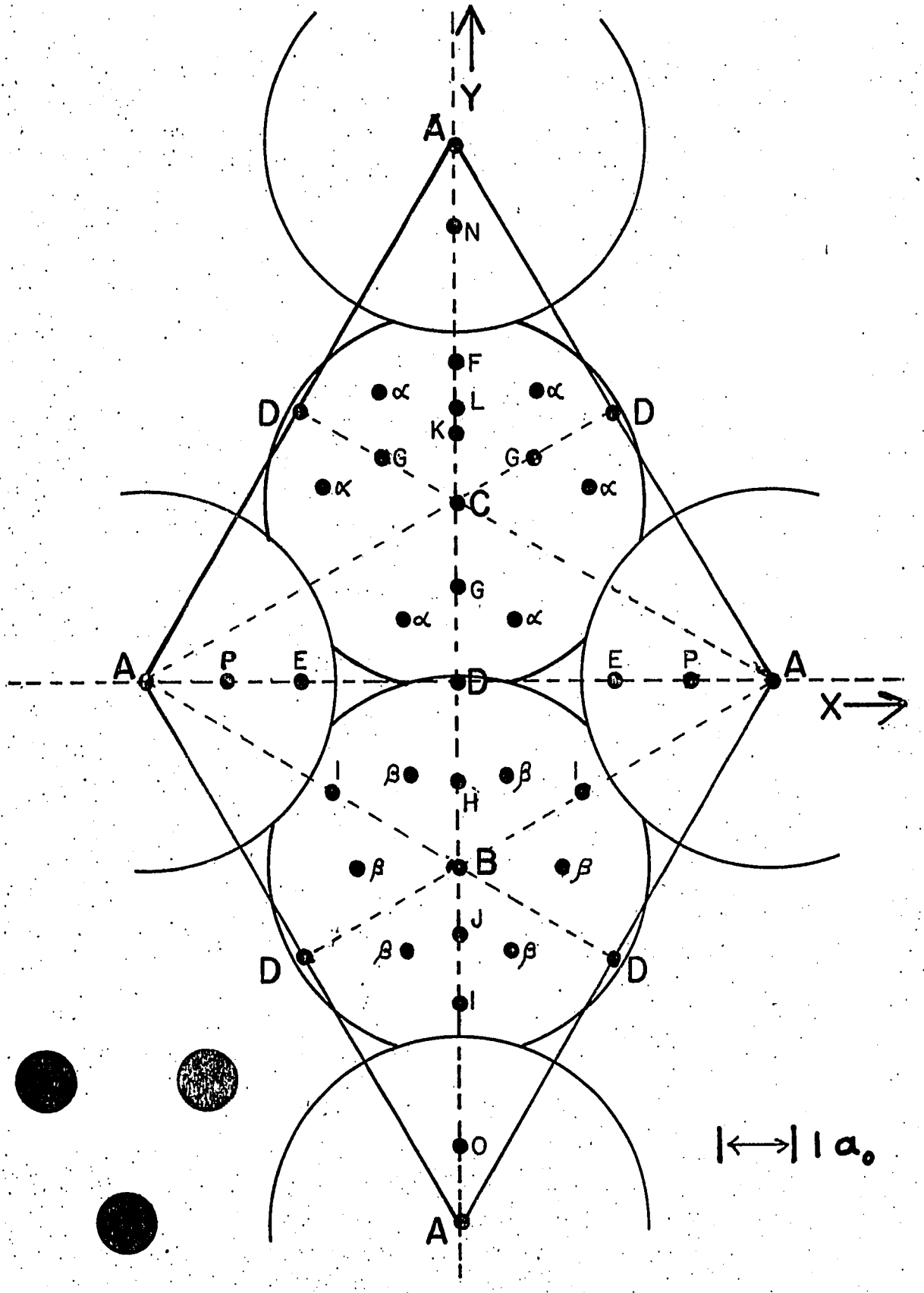

FIGURE 7.1

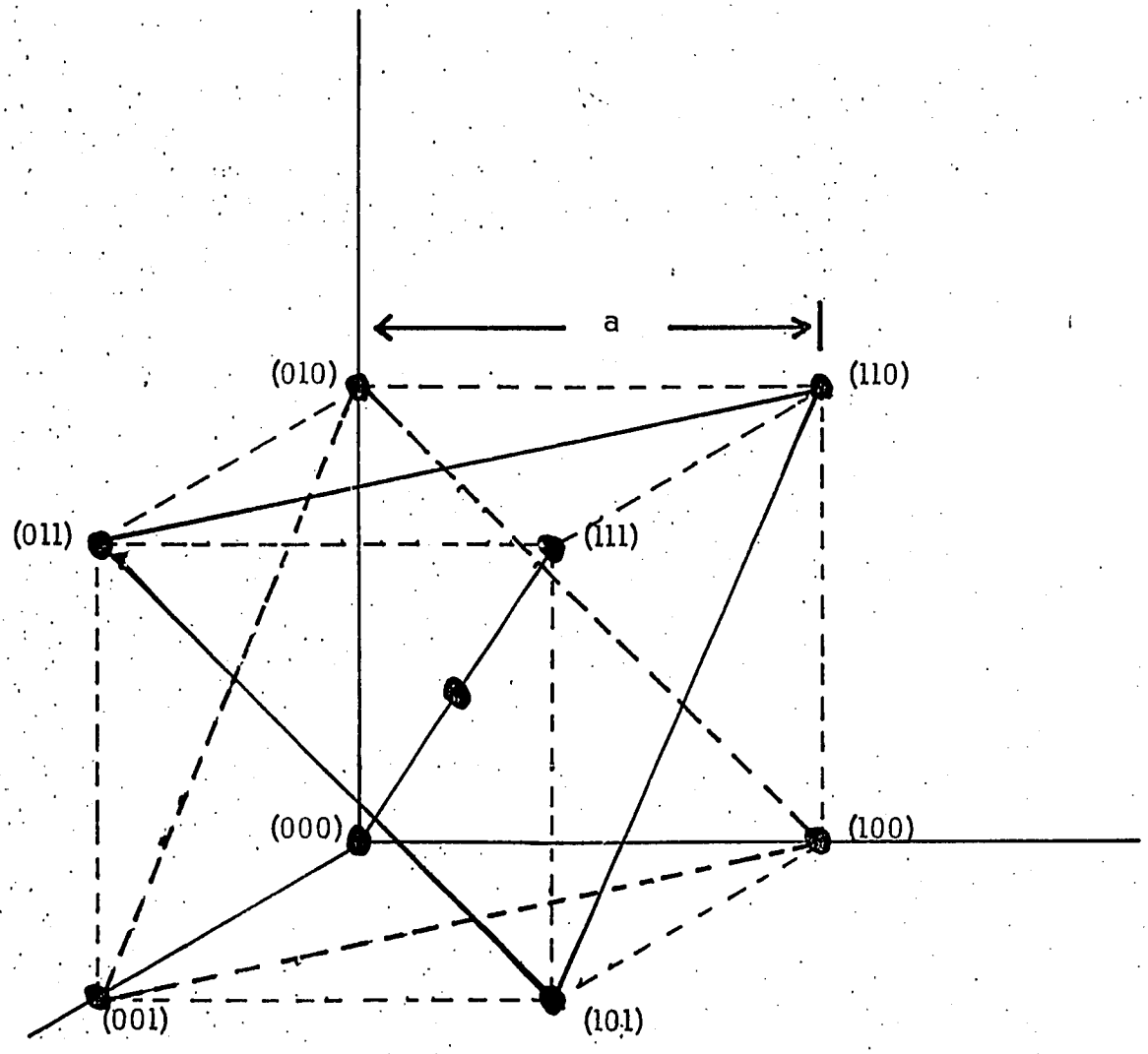

FIG. 7.2

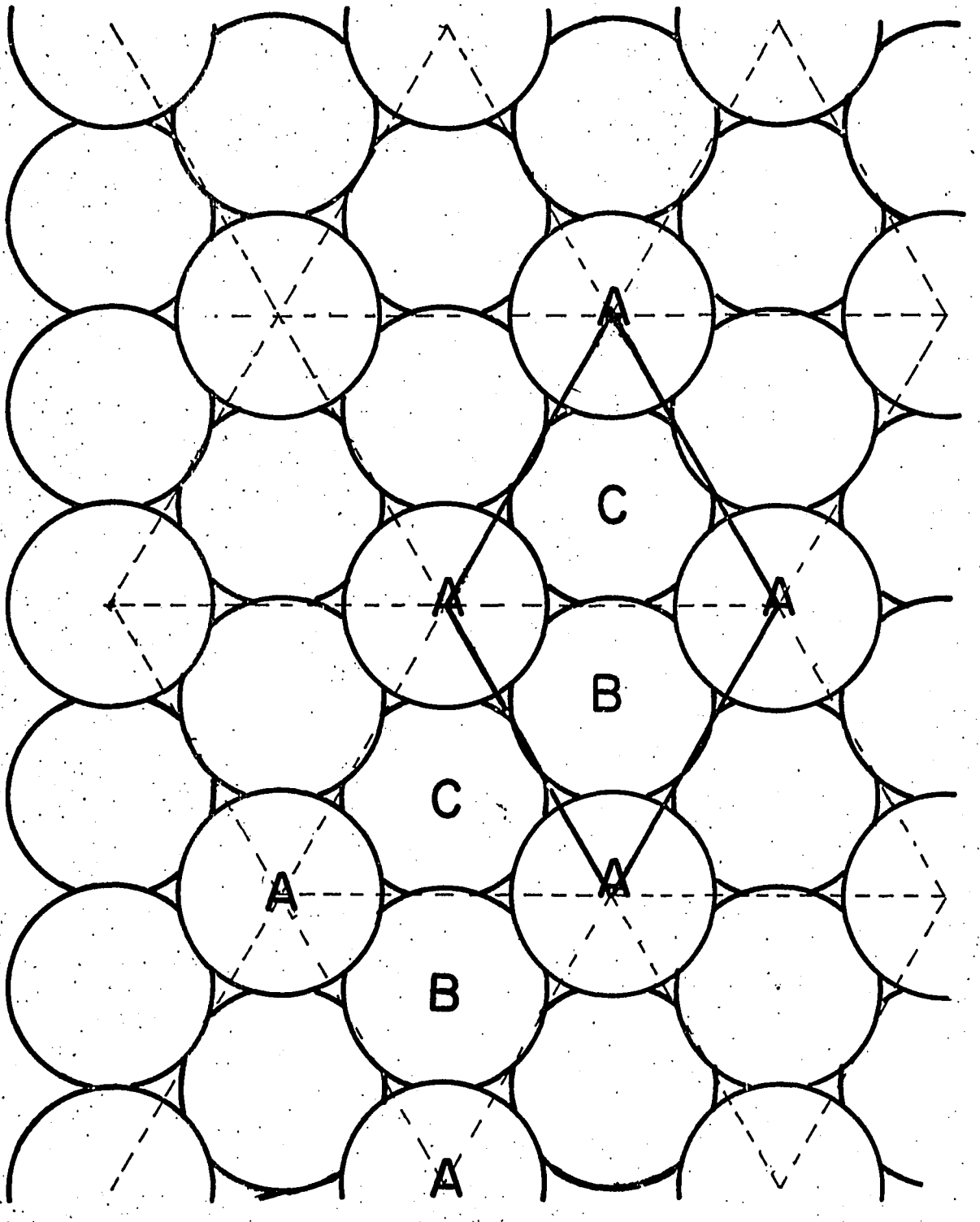

FIG. 7.3

FIGURE 7.4: Some Characteristic Lengths of the Tungsten-Oxygen System

Unless noted otherwise, lengths are taken from:
J. C. Slater, "Quantum Theory of Molecules and Solids", Vol. 2, McGraw-Hill (1965),
or from:
L. Pauling, "The Nature of the Chemical Bond", 3rd Ed., Cornell Univ. Press (1960)

Empirical Atomic Radii:		
Oxygen (Slater)	0.60 A.°	1.13 a_o
(Pauling, p.224)	0.66 "	1.25 "
Tungsten (Slater)	1.35 A.°	2.55 a_o
(Pauling, p. 256)	1.30 "	2.46 "
O - O Single Bond Radius (Pauling, p. 228)	0.74 "	1.40 "
Bulk Tungsten Lengths:		
Lattice Constant (B.C.C.) (= a)	3.16 A.°	5.97 a_o
W - W interatomic spacing	2.74 "	5.17 "
Tungsten Surface Lengths:		
a_s = Surface Lattice Constant		
d = Interplanar spacing along Surface Normal		
W(100) Face:		
a_s	3.16 A.°	5.97 a_o
d	1.58 "	2.98 "
W(111) Face:		
a_s	4.47 "	8.44 "
d	0.91 "	1.72 "
Bond Lengths:		
O_2 molecule	1.21 "	2.29 "
W - O bond lengths in solids	1.91-2.14 A.°	3.61 - 4.04 a_o
Sum of Empirical Atomic Radii (Slater)	1.95 A.°	3.68 a_o
(Pauling)	1.96 "	3.70 "
W - O Bond Length on W(110)	$2.08 \pm .07$ A.°	$3.93 \pm .13$ a_o
(Van Hove, S. Tong, PRL 36, 1092 (1975))		

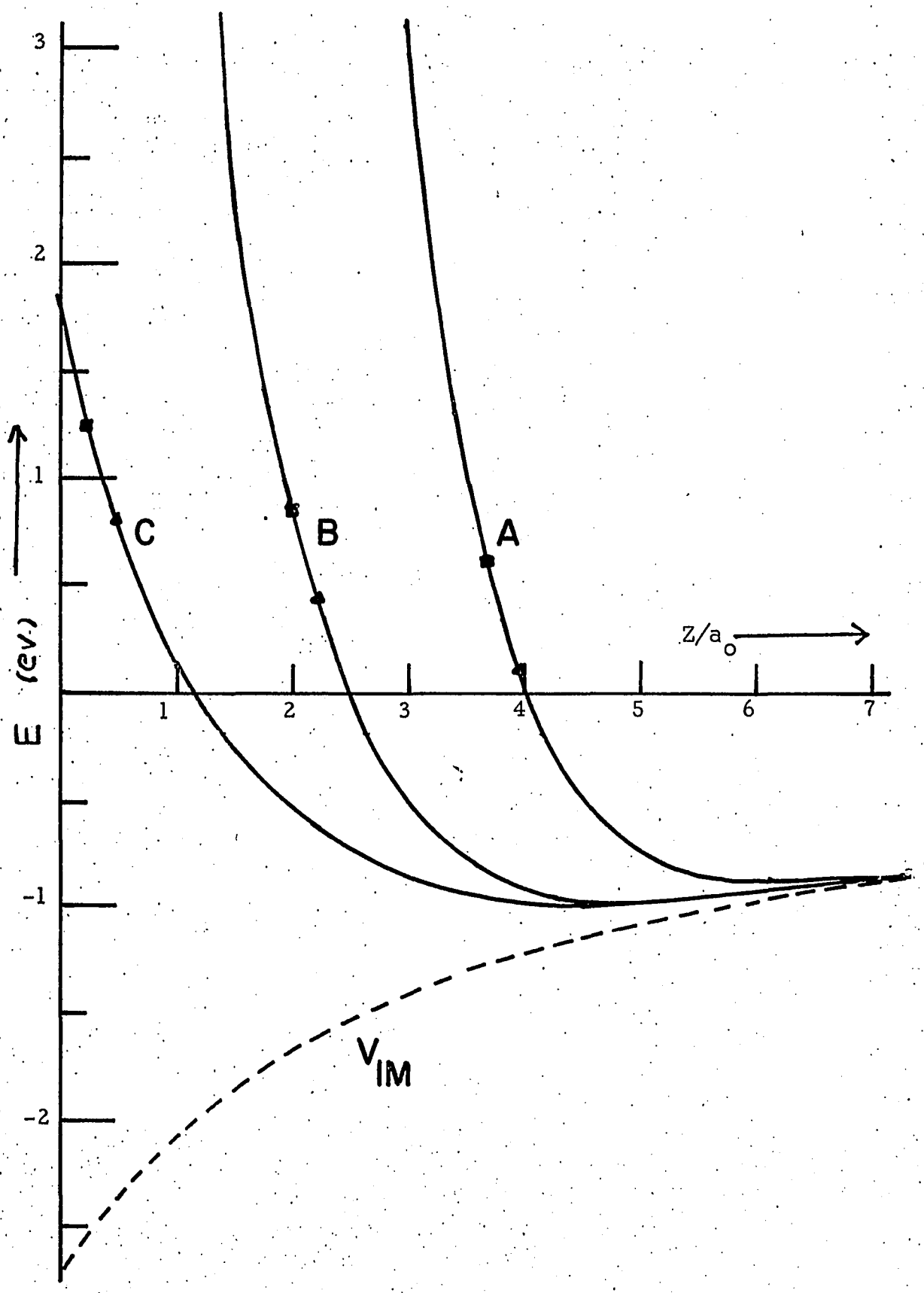

FIG. 7.5

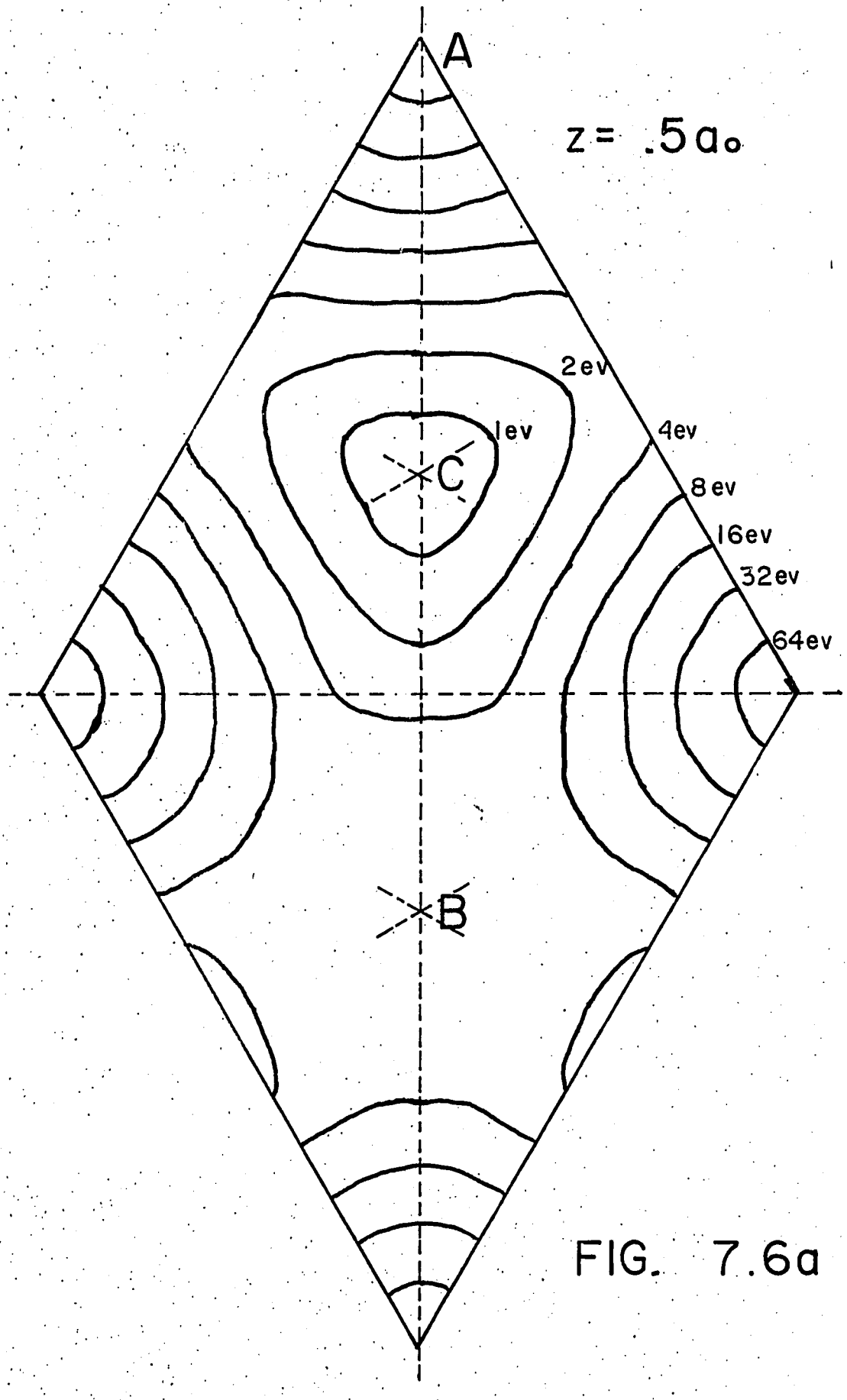

FIG. 7.6a

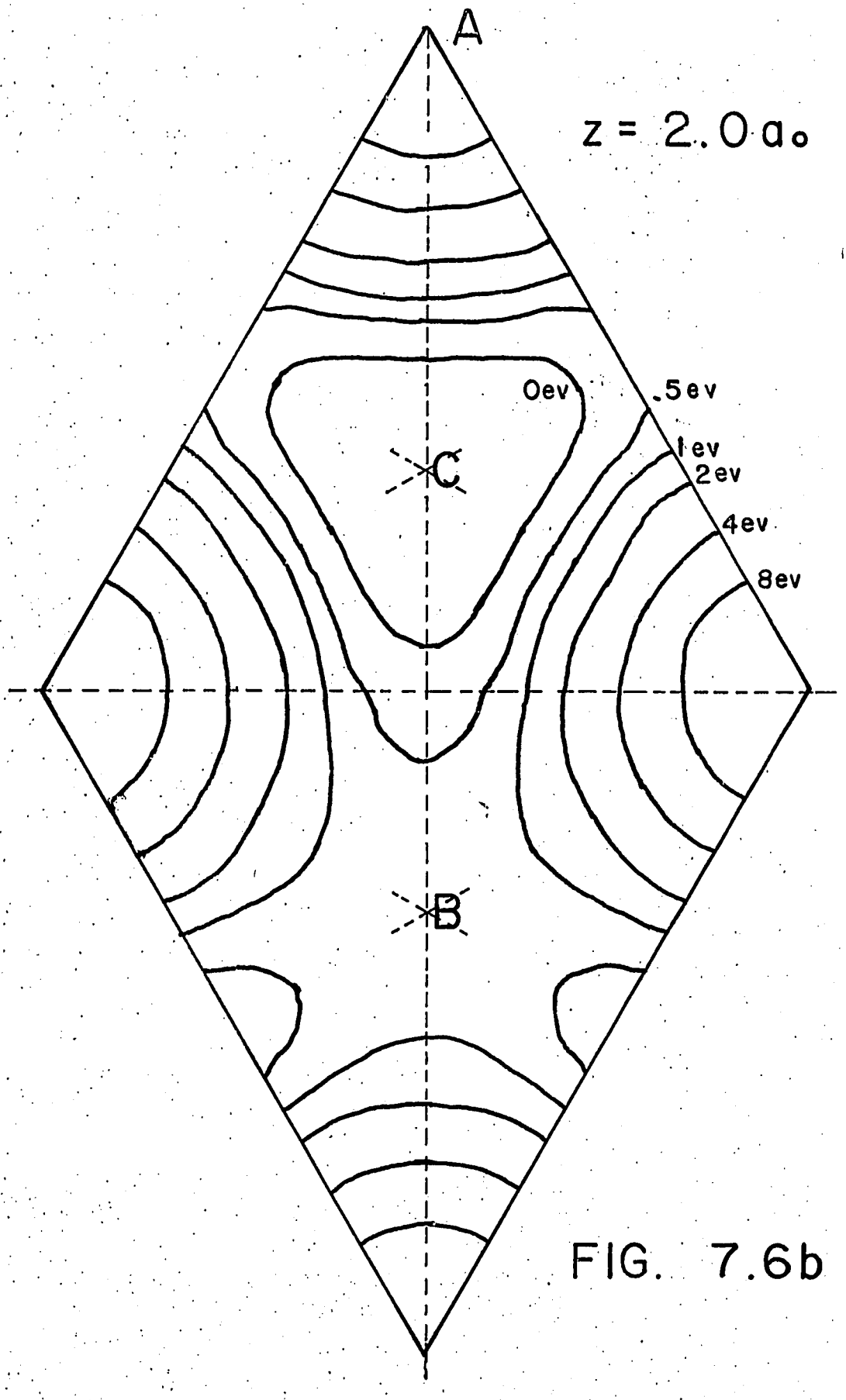

FIG. 7.6b

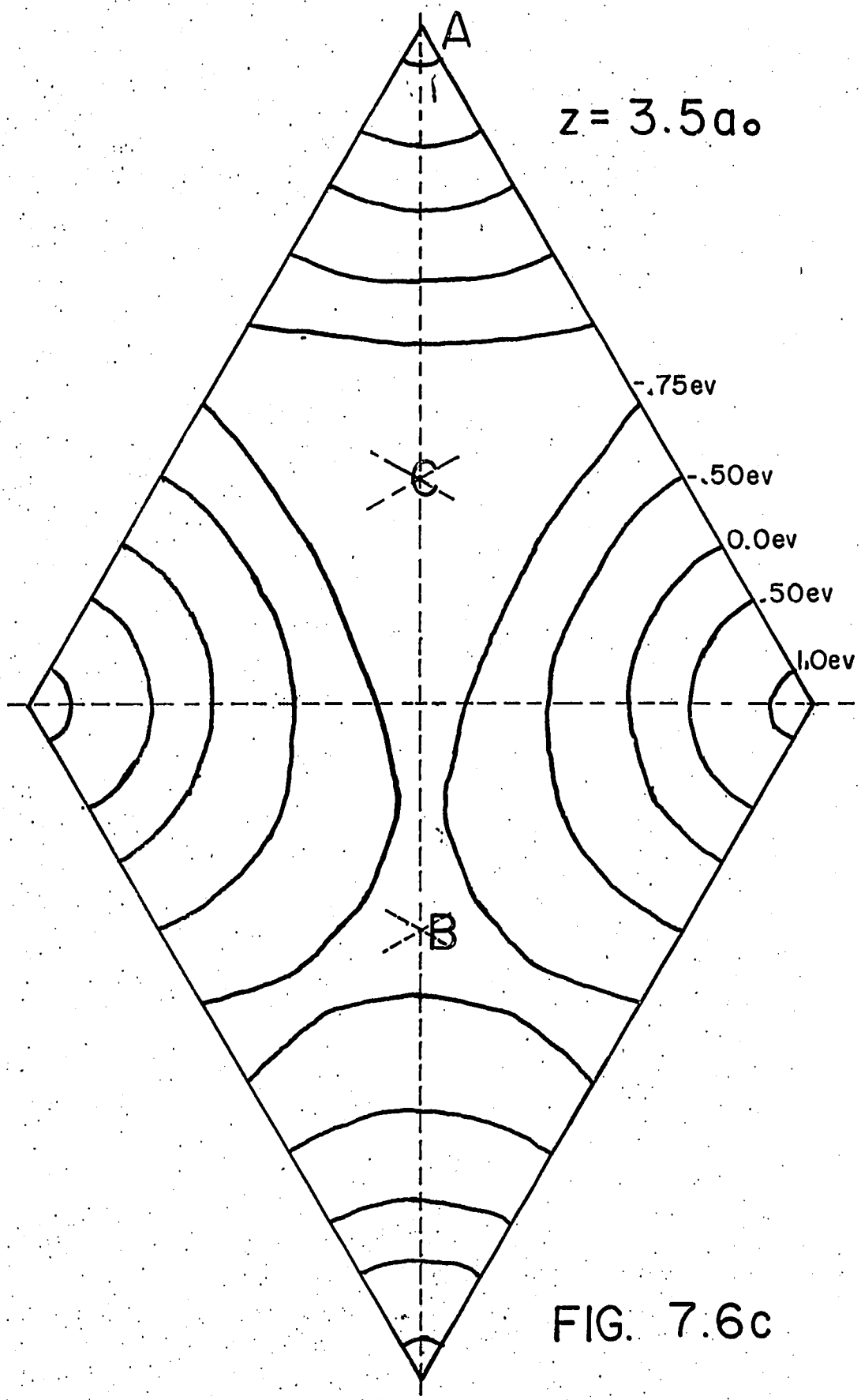

FIG. 7.6c

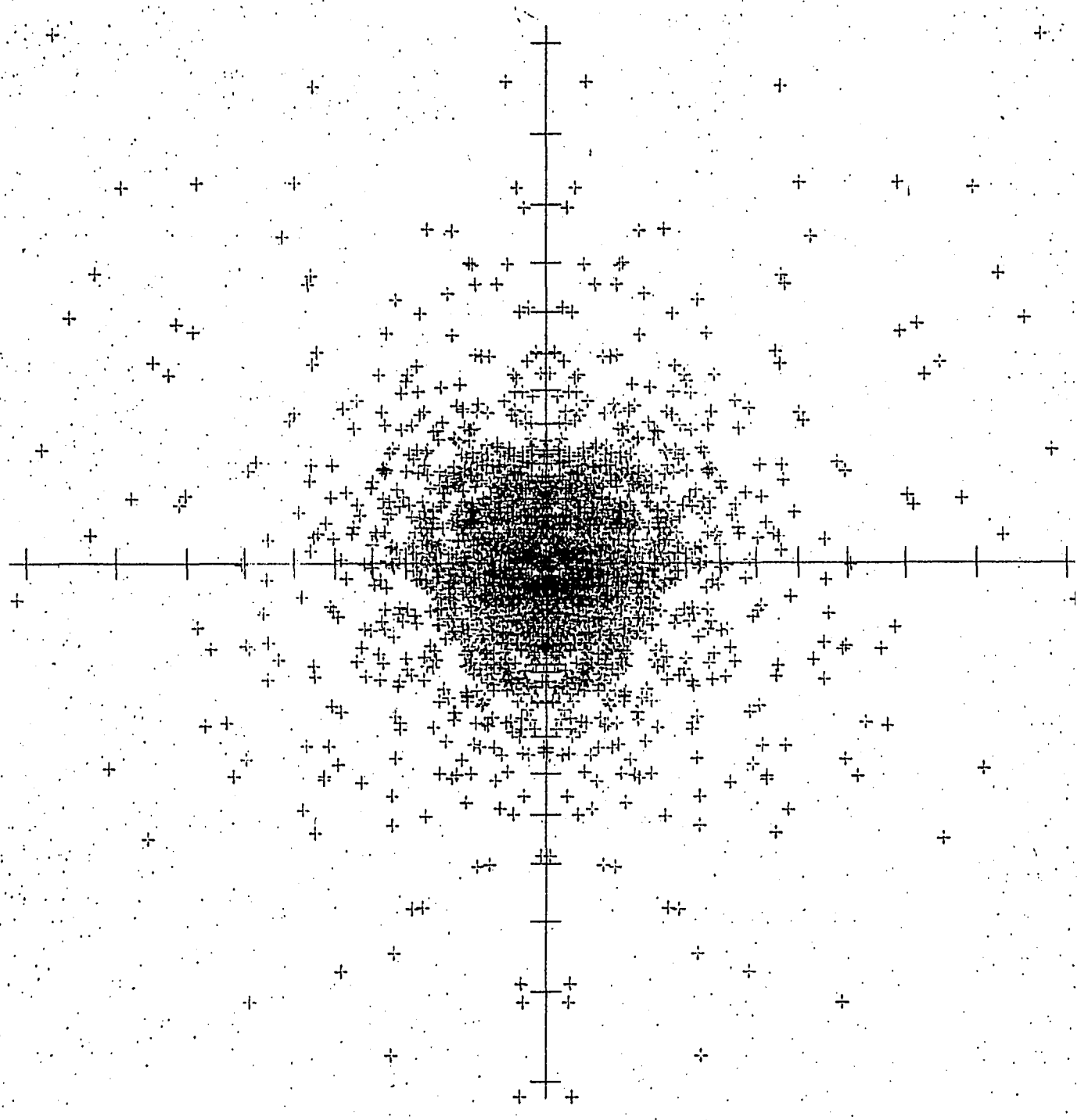
M1006
22-Jun-76
X = TAN(THETA) COS(PHI)
Y = TAN(THETA) SIN(PHI)
SIMULATED ESD PATTERN
3
SCALE FACTOR .230
5 DEGREE SCALE
2398 POINTS PLOTTED
38 POINTS OFF SCAL

FIGURE 7.7a

M1004
23-Jun-76

X = TAN(THETA) COS(PHI)
Y = TAN(THETA) SIN(PHI)

SIMULATED ESD PATTERN 3

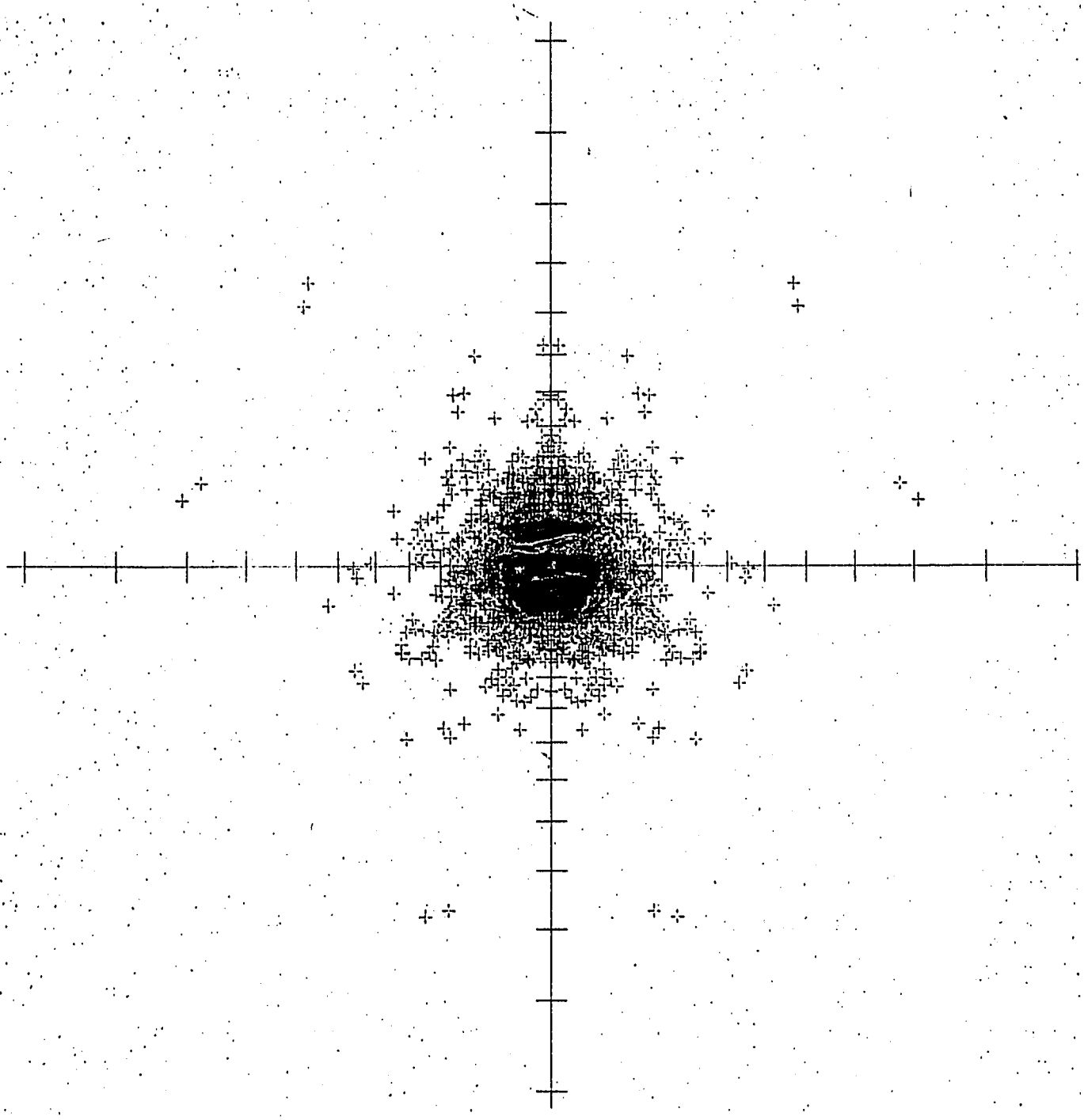

SCALE FACTOR .750
5 DEGREE SCALE

2000 POINTS PLOTTED
0 POINTS OFF SCAI

FIGURE 7.7b

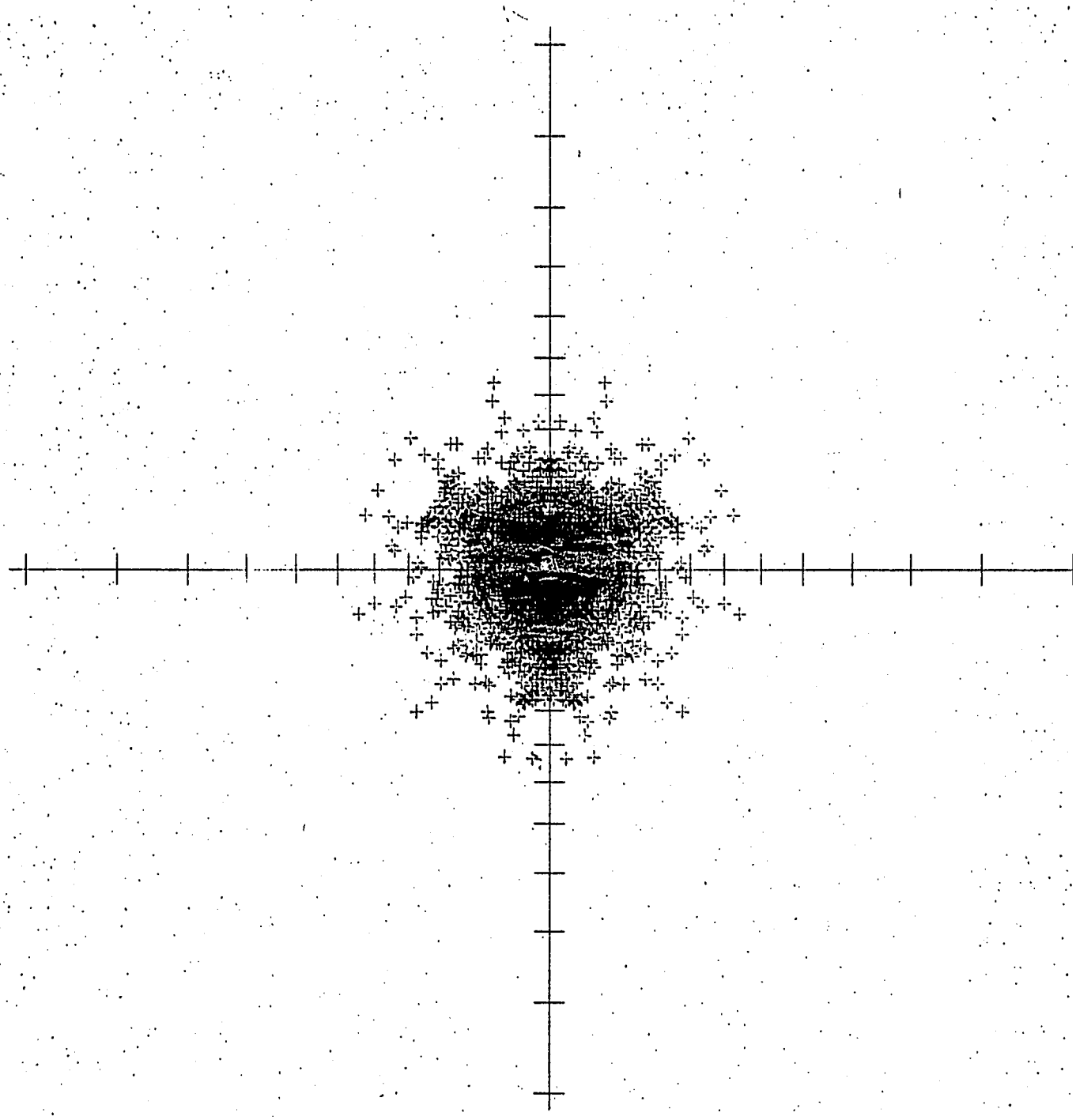
M1002
22-Jun-76
X = TAN(THETA) COS(PHI
Y = TAN(THETA) SIN(PHI
SIMULATED ESD PATTERN
3
SCALE FACTOR .700
5 DEGREE SCALE
3000 POINTS PLOTTED
0 POINTS OFF SCA

FIGURE 7.7c

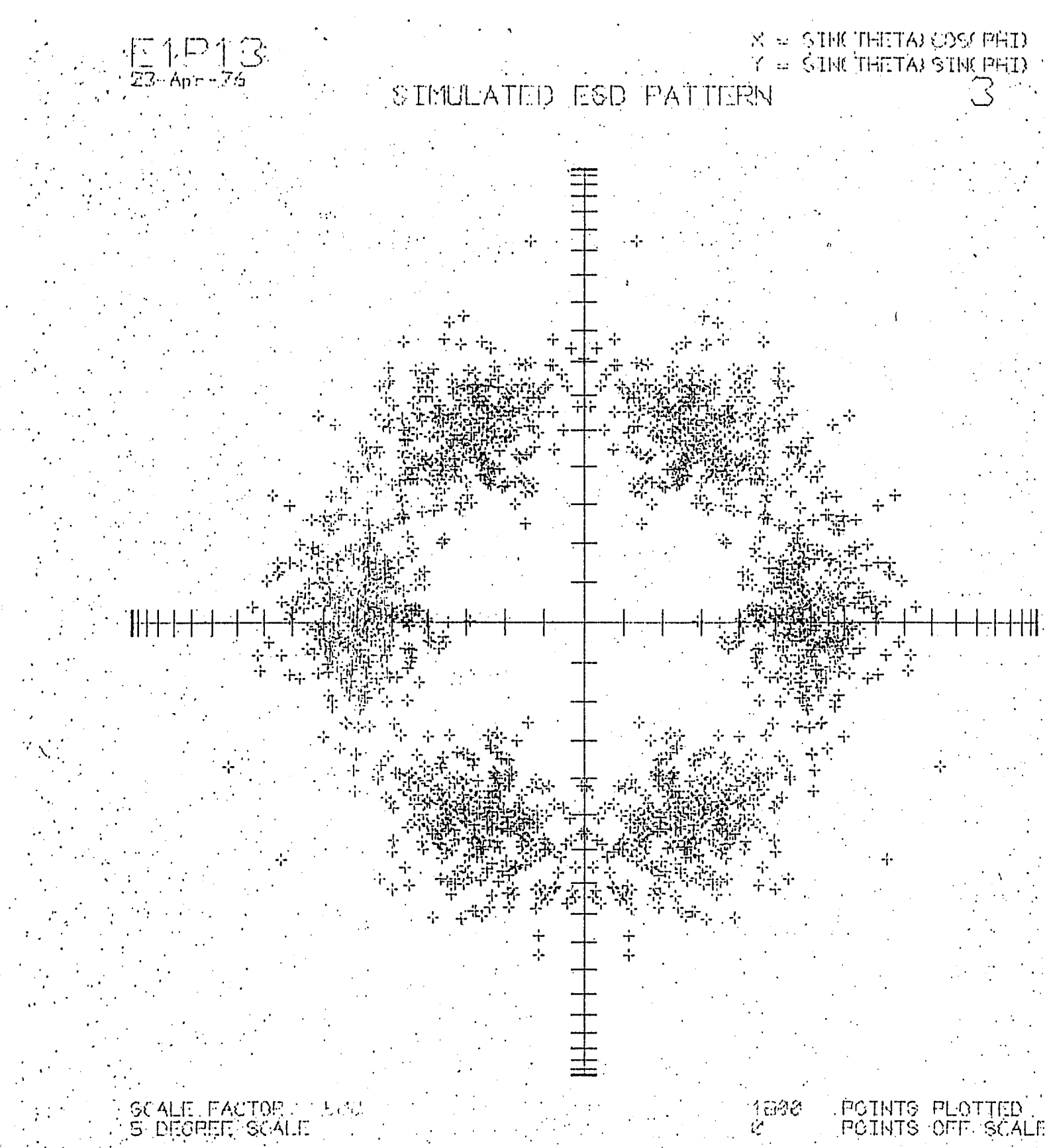
E1P13
23-Apr-76
X = SIN(THETA)COS(PHI)
Y = SIN(THETA)SIN(PHI)
SIMULATED ESD PATTERN
3
SCALE FACTOR
5 DEGREE SCALE
POINTS PLOTTED
POINTS OFF SCALE

FIGURE 7.8

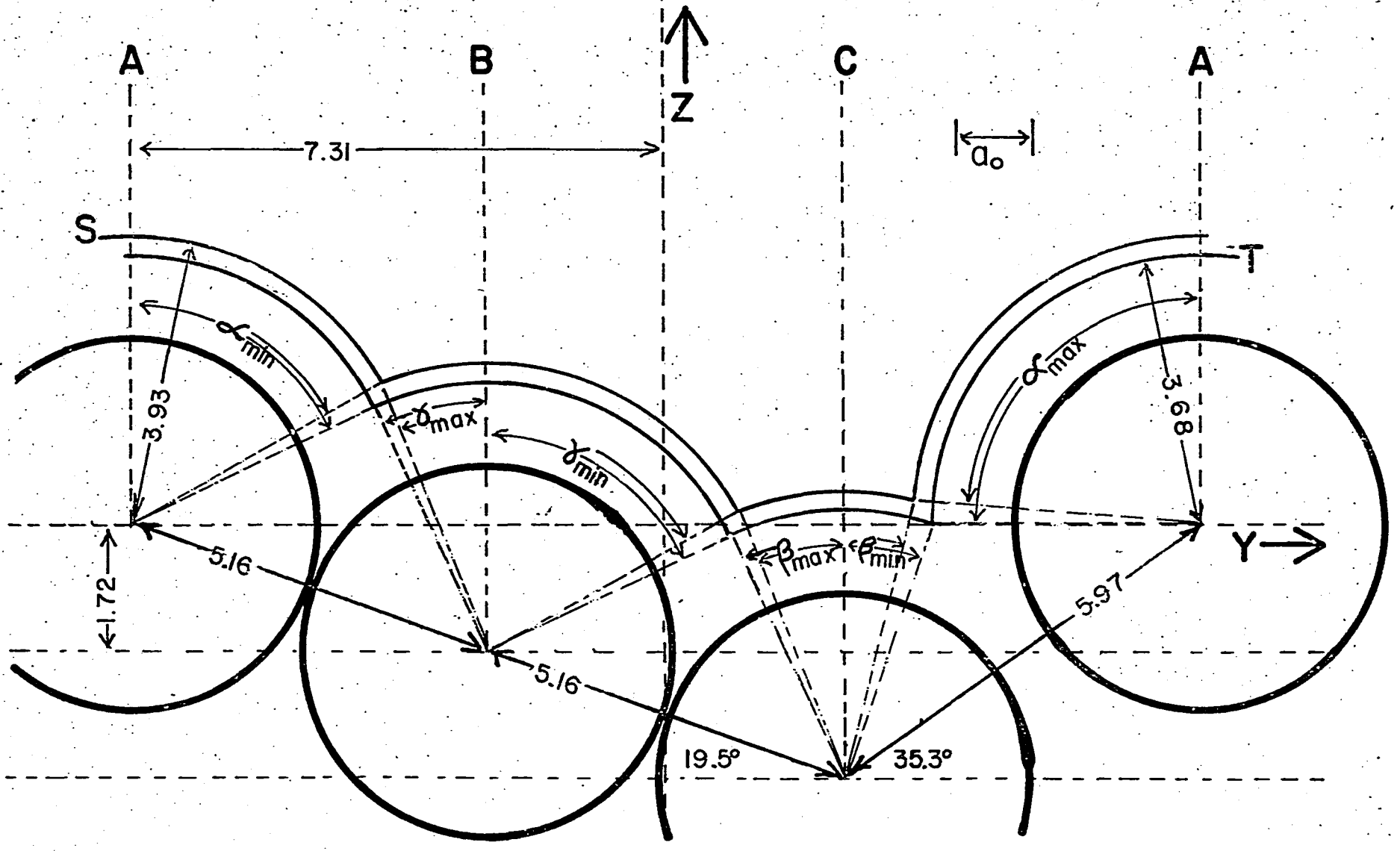
A
B
Z
C
A
7.31
a_o
S
T
α_{min}
α_{max}
3.93
3.68
γ_{max}
γ_{min}
β_{max}
β_{min}
Y
5.16
1.72
5.16
5.97
19.5°
35.3°

FIGURE 7.9

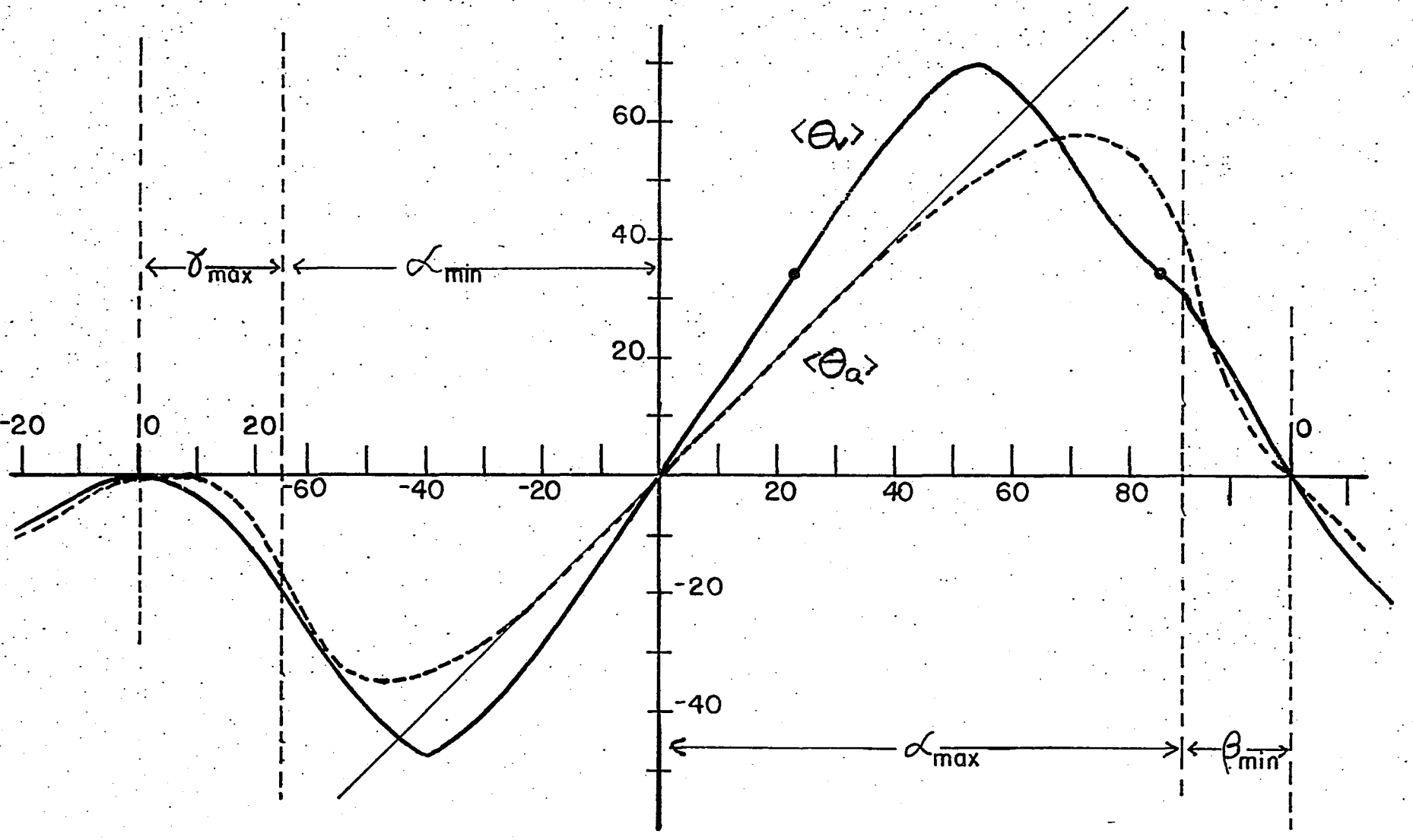
60
40
20
-20
-40
-20
0
20
-60
-40
-20
20
40
60
80
0
$\langle\theta_v\rangle$
$\langle\theta_a\rangle$
γ_{max}
α_{min}
α_{max}
β_{min}

FIG. 7.10a

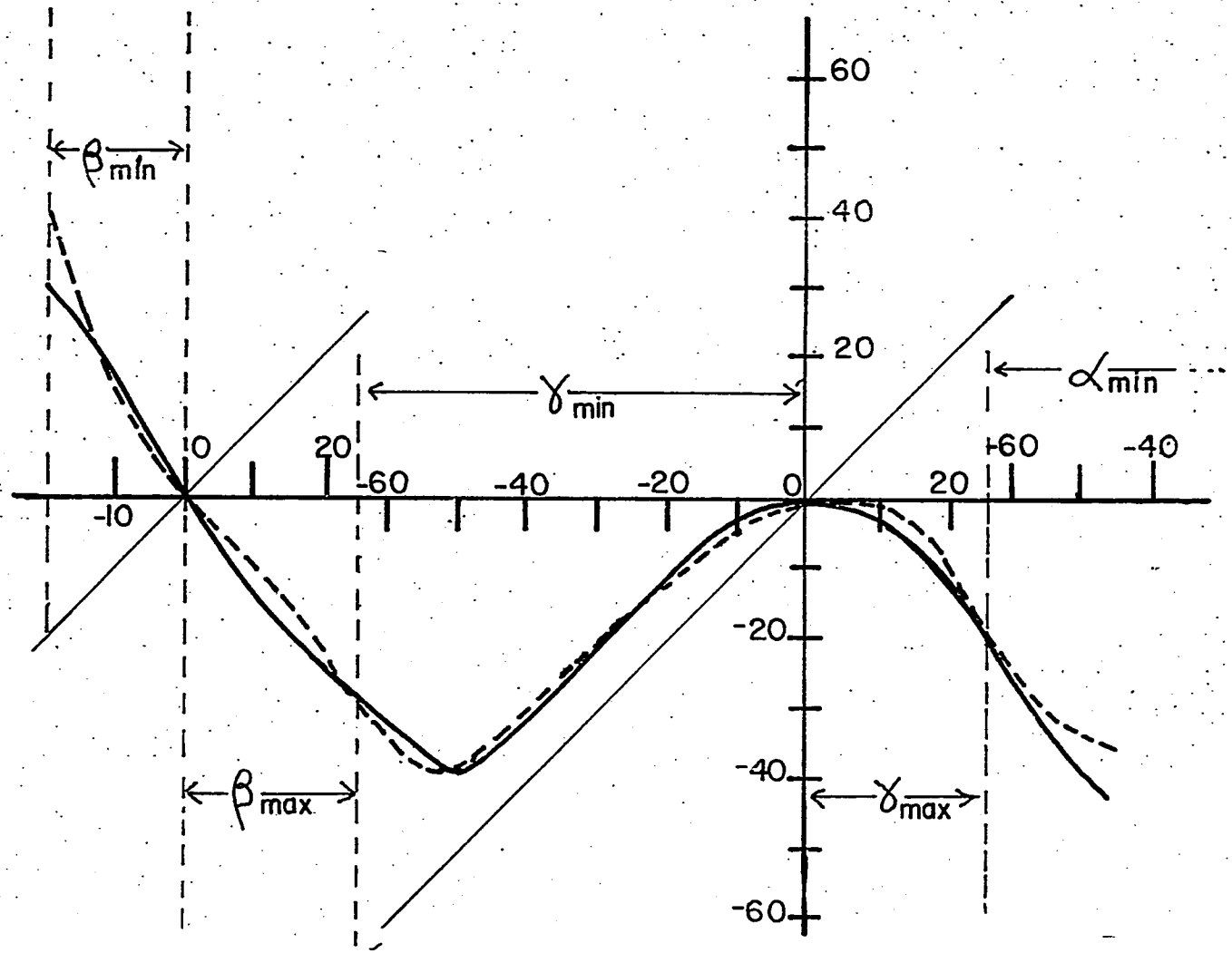
β min
γ min
α min
β max
γ max
60
40
20
-20
-40
-60
-10
0
20
-60
-40
-20
0
20
-60
-40

FIG. 7.10b

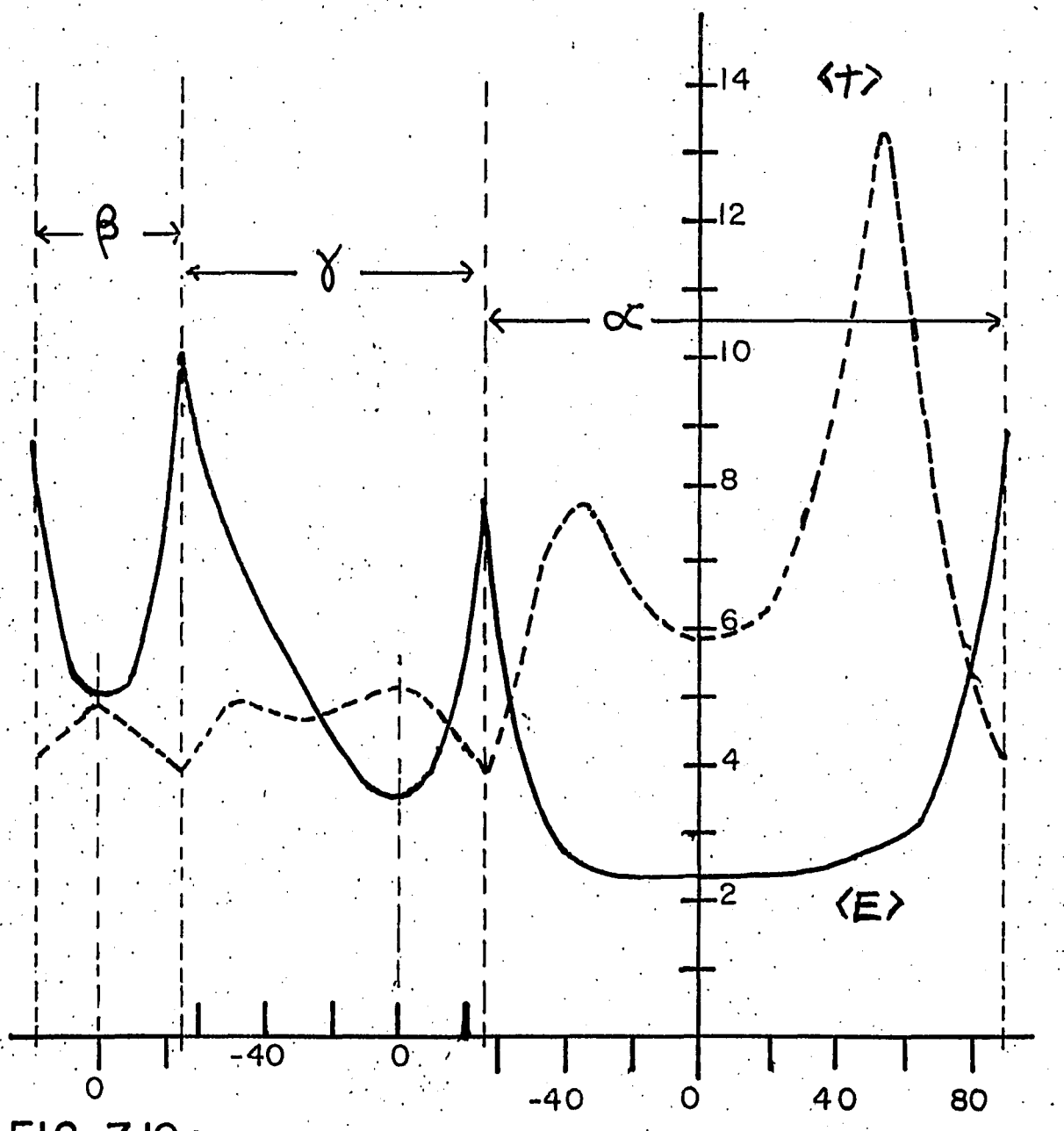

FIG. 7.10c

FIG. 7.11a

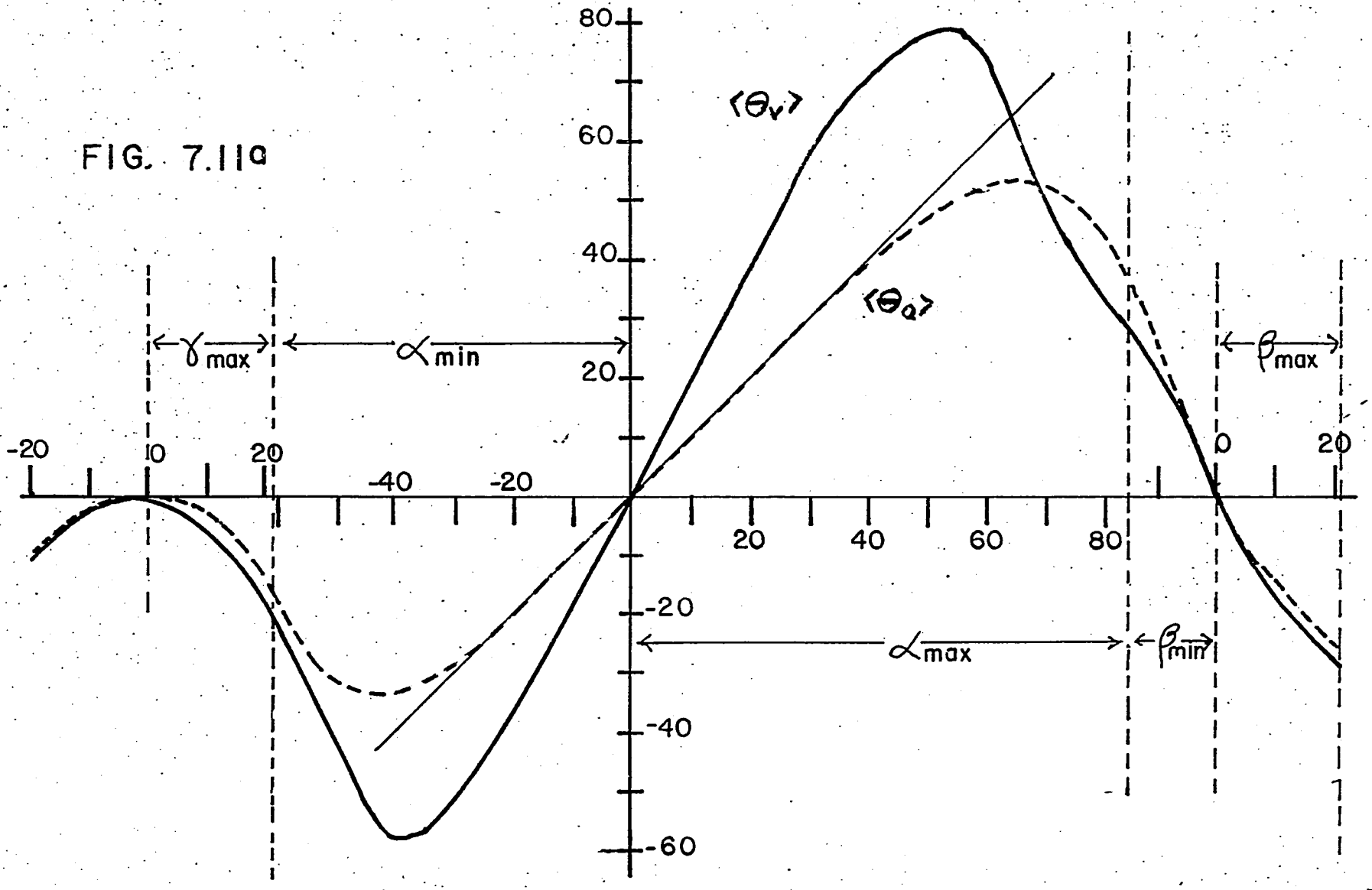
80
60
40
20
-20
-40
-60
-20
0
20
-40
-20
20
40
60
80
0
20
⟨θv⟩
⟨θq⟩
γmax
αmin
αmax
βmax
βmin

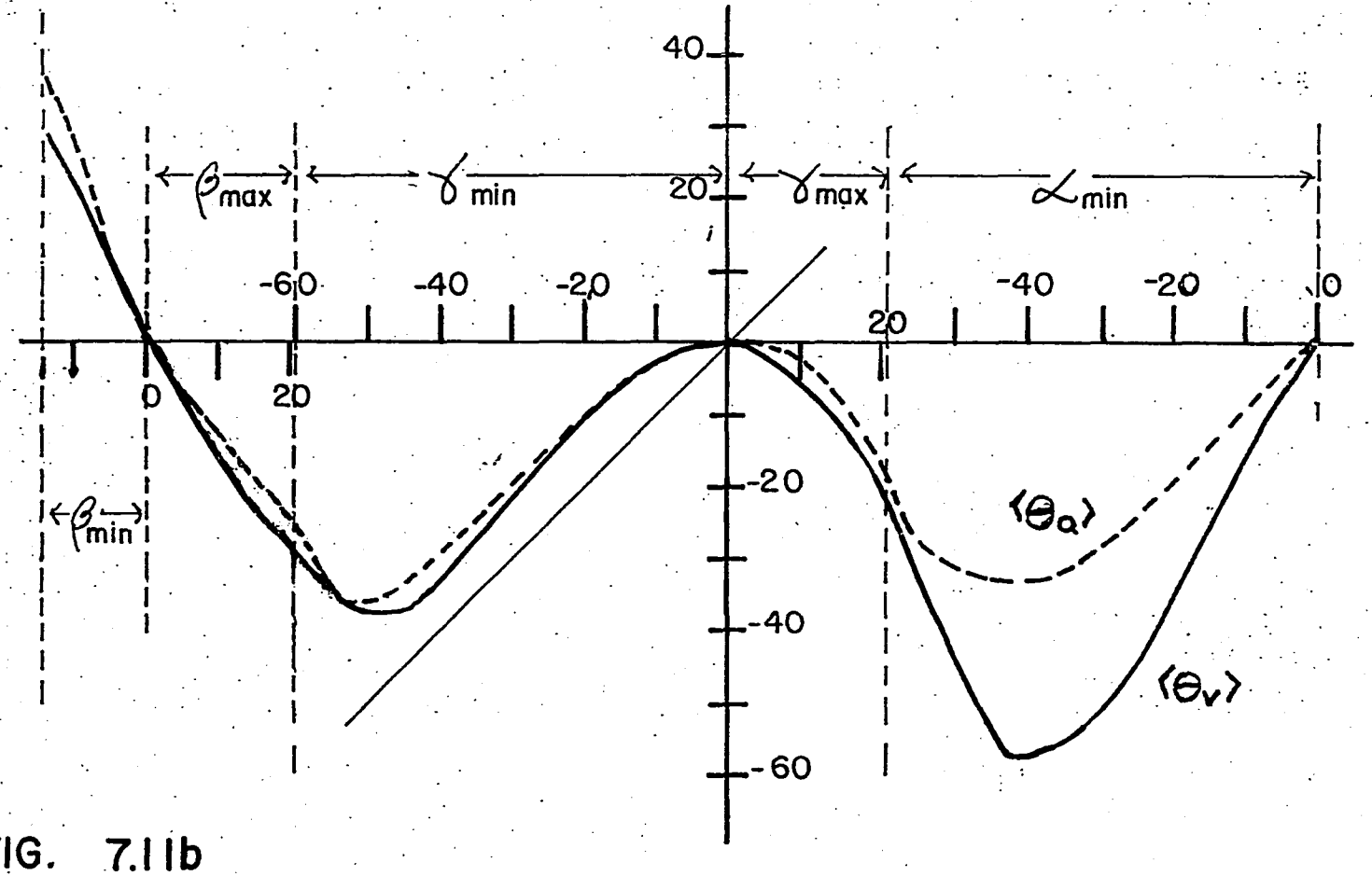
40
20
-20
-40
-60
-60
-40
-20
0
20
-40
-20
0
20
β_{max}
γ_{min}
γ_{max}
α_{min}
β_{min}
$\langle\theta_a\rangle$
$\langle\theta_v\rangle$

FIG. 7.11b

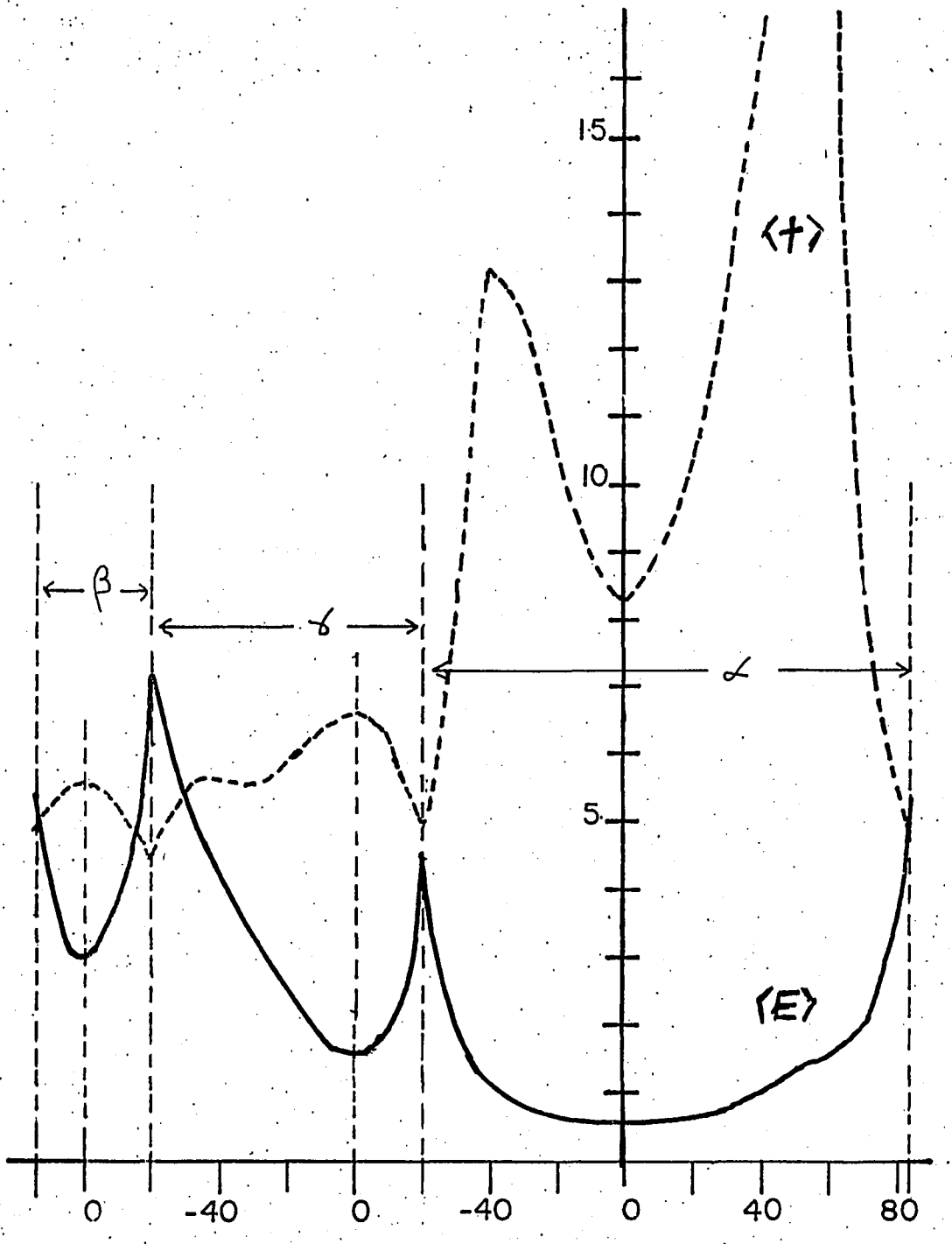

FIG. 7.11c

FIGURE 7.12a

SIMULATED ESDIAD DATA for TUNGSTEN-OXYGEN BOND LENGTH 1.95 A.^{o}

SITE	PATTERN TYPE	X (a_o)	Y (a_o)	$\langle\theta_i\rangle$	$\langle\theta_a\rangle$	$\langle E \rangle$ (ev.)	σ_E (ev.)	See Fig:
$\alpha = 23^{o}$	PL	5.87	3.39	33.5	22.8	0.69	.41	AIII.1, 7.14a, 7.15a
$\alpha = -27^{o}$	SL	-5.64	3.28	38.2	25.9	0.69	.44	AIII.2, 7.14a
'A'	CS	7.31	3.68	$<1^{o}$	$<1^{o}$	0.67	.41	AIII.3, 7.15a
$\alpha = 85^{o}$	PL	3.64	0.32	34.2	49.7	2.01	.49	AIII.4, 7.14c, 7.15c
$\gamma = -53^{o}$	SL	0.51	0.49	36.7	39.3	2.13	.51	AIII.5, 7.14c
$\gamma = -46^{o}$	SL	0.21	0.84	37.2	36.1	1.90	.50	AIII.6
'C'	CS	2.44	0.24	$<1^{o}$	$<1^{o}$	1.30	.42	AII.7, 7.15c
$\alpha = -52^{o}$	SL	-4.41	2.27	37.6	33.8	1.13	.50	AIII.8
'B'	CS	-2.44	1.96	$<1^{o}$	$<1^{o}$	1.00	.45	AIII.9
$\alpha_{max} = 89.4^{o}$	PL	3.63	0.41	30.4	41.2	2.48	.50	AIII.10
$\beta_{max} = 25.1^{o}$	SL	0.88	-0.11	28.0	29.6	2.82	.52	AIII.11
$\gamma_{max} = 25.1^{o}$	SL	-4.00	1.61	20.0	17.9	2.23	.59	AIII.12

FIGURE 7.12b

SIMULATED ESDIAD DATA for TUNGSTEN-OXYGEN BOND LENGTH 2.08 A.°

SITE	PATTERN TYPE	X (a_o)	Y (a_o)	$\langle\theta_v\rangle$	$\langle\theta_a\rangle$	$\langle E\rangle$ (ev.)	σ_E (ev.)	See Fig:
$\alpha = 17.5^\circ$	PL	6.13	3.75	30.8	17.5	0.25	.26	AIII.13, 7.14d, 7.15b
$\alpha = -20^\circ$	SL	-5.97	3.69	35.7	19.8	0.25	.36	AIII.14, 7.14d
'A'	CS	7.31	3.93	$<1^\circ$	$<1^\circ$	0.23	.27	AIII.15, 7.15b
$\alpha = 80^\circ$	PL	3.44	0.68	33.7	46.0	1.14	.37	AIII.16, 7.14b, 7.15d
$\gamma = -49^\circ$	SL	0.53	0.86	37.5	35.9	1.44	.40	AIII.17, 7.14b
'C'	CS	2.44	0.48	$<1^\circ$	$<1^\circ$	0.84	.28	AIII.18, 7.15d
$\alpha = -52^\circ$	SL	-4.21	2.42	37.5	29.8	0.62	.37	AIII.19
'B'	CS	-2.44	2.21	$<1^\circ$	$<1^\circ$	0.47	.32	AIII.20
$\alpha_{max} = 84.7^\circ$	PL	3.40	0.36	28.4	37.7	1.55	.39	AIII.21
$\beta_{max} = 21.7^\circ$	SL	0.99	0.21	28.9	30.0	2.01	.42	AIII.22
$\gamma_{max} = 21.7^\circ$	SL	-3.89	1.93	21.1	17.5	1.29	.45	AIII.23

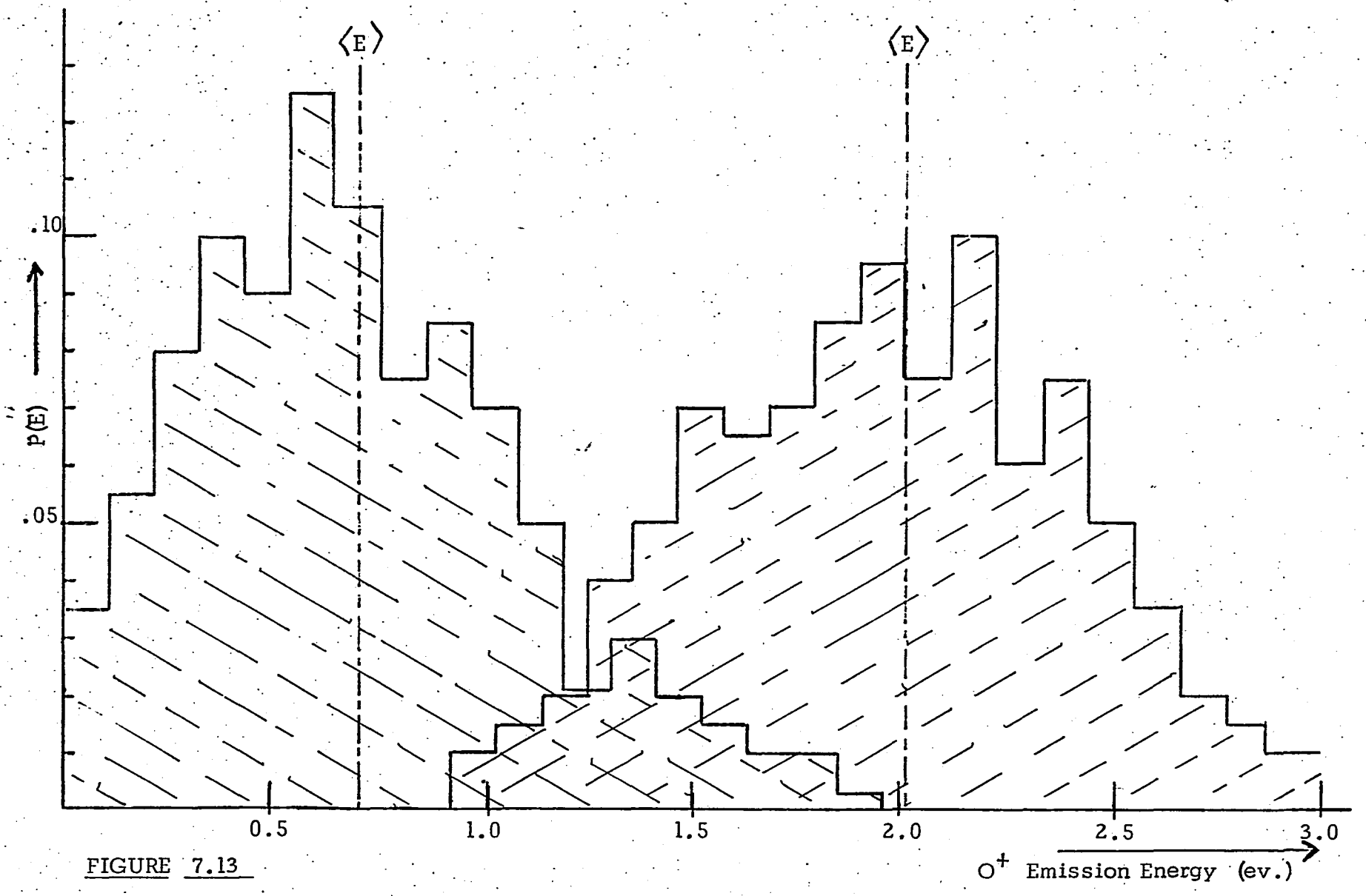

FIGURE 7.13

M1220
9-Jul-76

X = TAN(THETA) COS(PHI)
Y = TAN(THETA) SIN(PHI)

SIMULATED ESD PATTERN 3

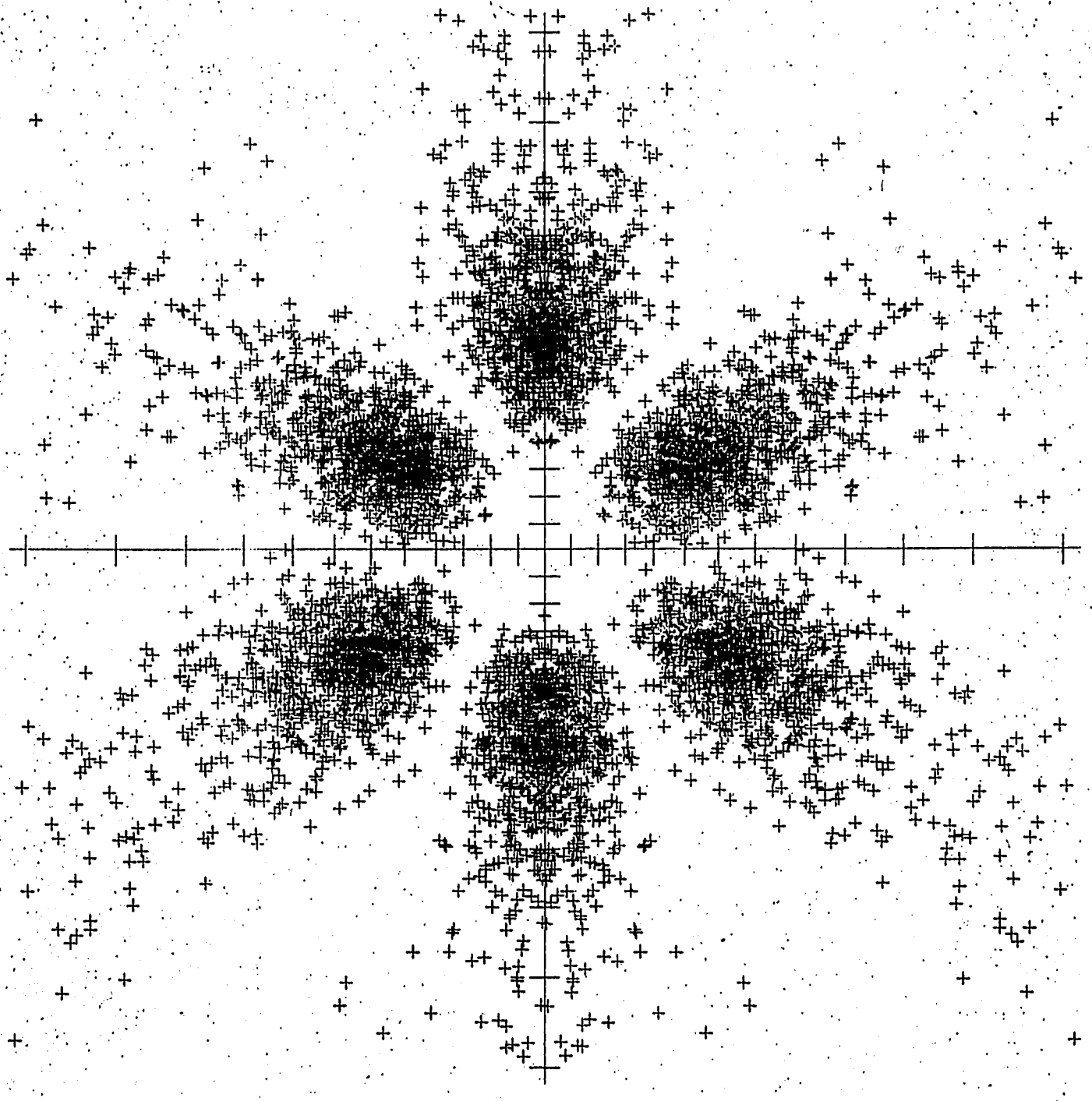

SCALE FACTOR 280
5 DEGREE SCALE

5708 POINTS PLOTTED
190 POINTS OFF SCALE

FIGURE 7.14a

M1224
10-Jul-76

X = TAN(THETA) COS(PHI)
Y = TAN(THETA) SIN(PHI)

SIMULATED ESD PATTERN 3

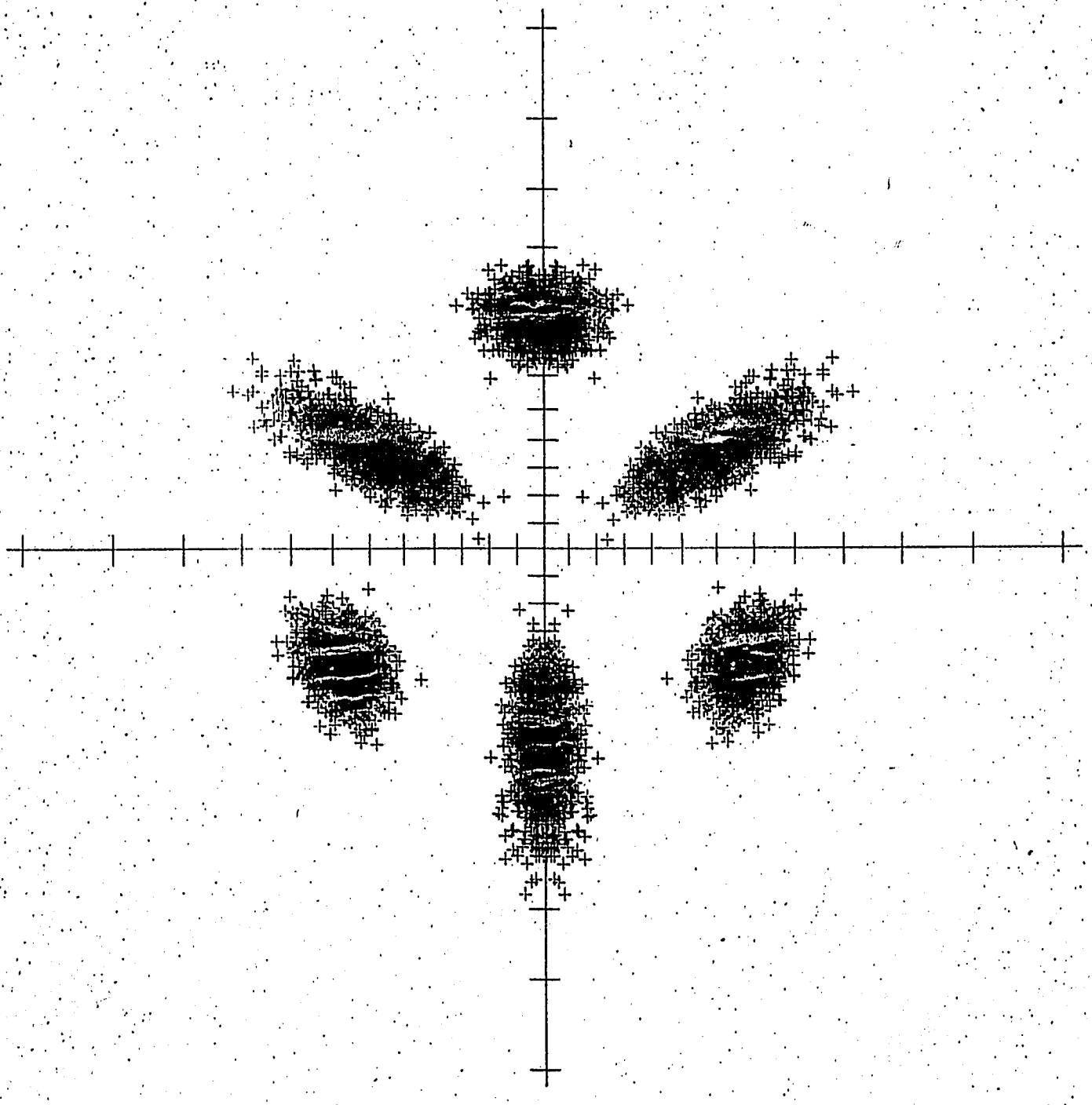

SCALE FACTOR .280
5 DEGREE SCALE

6000 POINTS PLOTTED
0 POINTS OFF SCALE

FIGURE 7.14b

M1223
10-Jul-76

X = TAN(THETA) COS(PHI)
Y = TAN(THETA) SIN(PHI)

SIMULATED ESD PATTERN 3

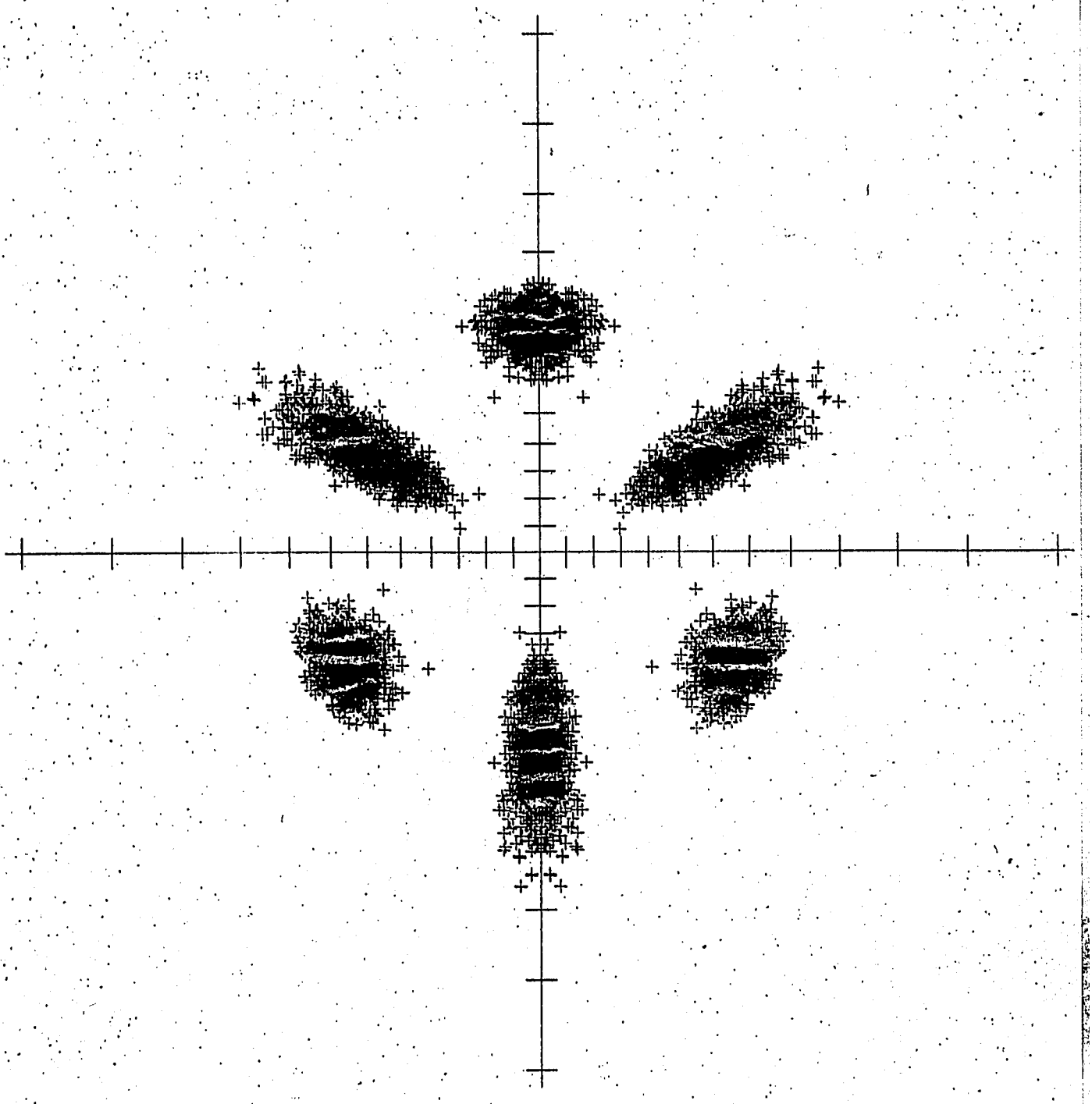

$CALE FACTOR .280
5 DEGREE SCALE

6000 POINTS PLOTTED
0 POINTS OFF SCALE

FIGURE 7.14c

M1222
9-Jul-76

X = TAN(THETA) COS(PHI)
Y = TAN(THETA) SIN(PHI)

SIMULATED ESD PATTERN 3

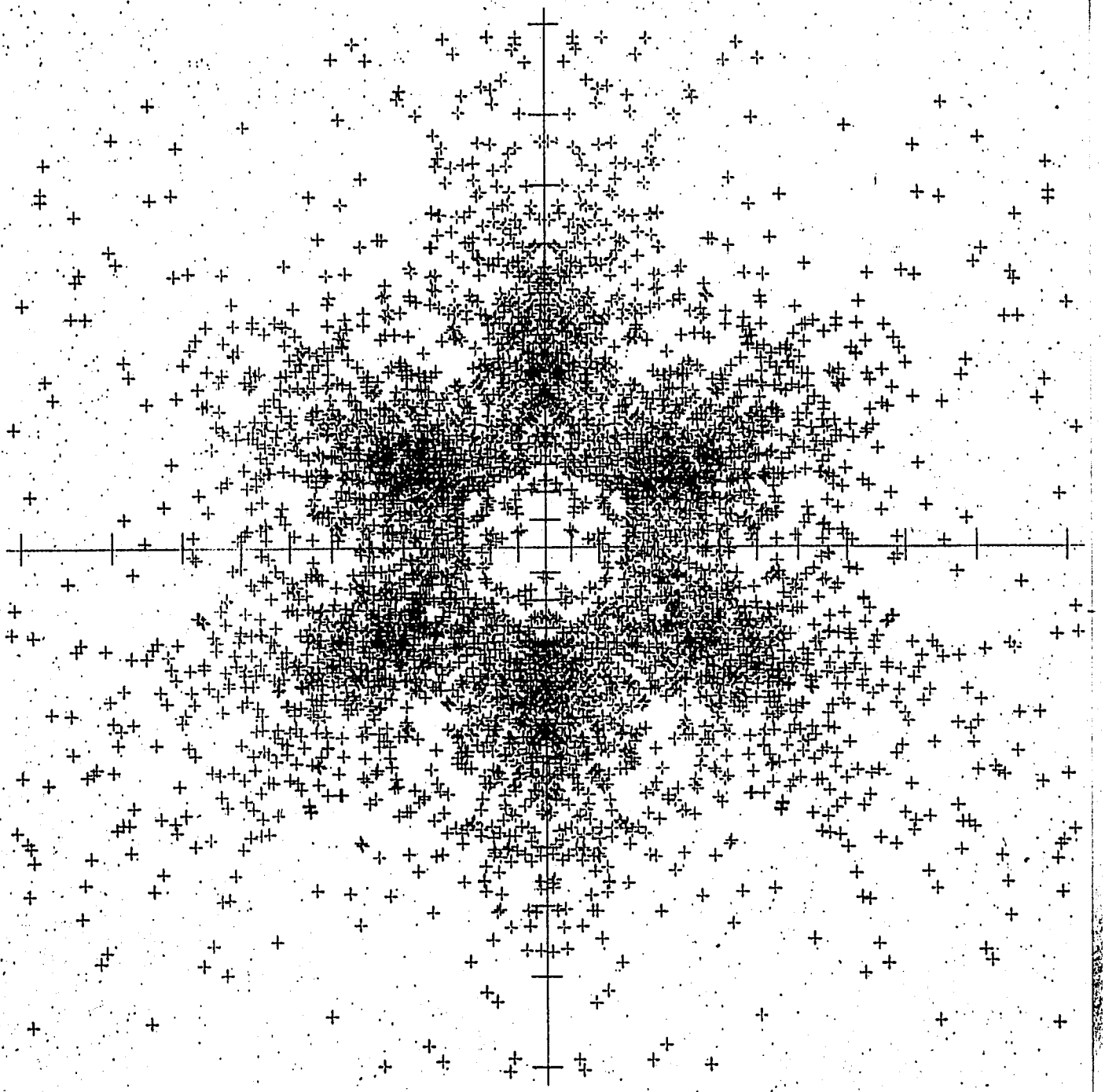

SCALE FACTOR .200
5 DEGREE SCALE

4852 POINTS PLOTTED
320 POINTS OFF SCALE

FIGURE 7.14d

M1221
9-Jul-76

X = TAN(THETA) COS(PHI)
Y = TAN(THETA) SIN(PHI)

SIMULATED ESD PATTERN 3

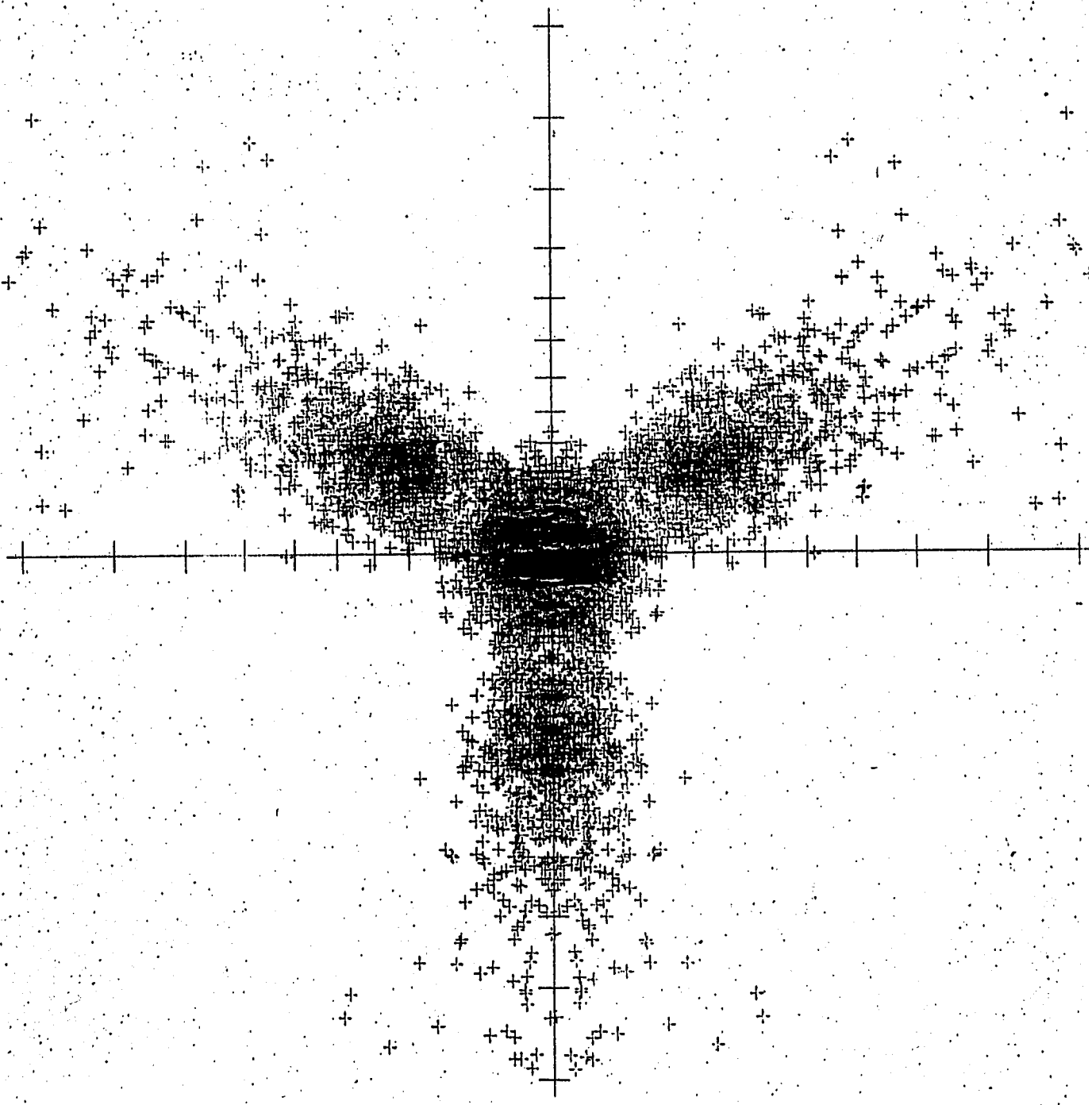

SCALE FACTOR 200
5 DEGREE SCALE

5994 POINTS PLOTTED
52 POINTS OFF SCAL

FIGURE 7.15a

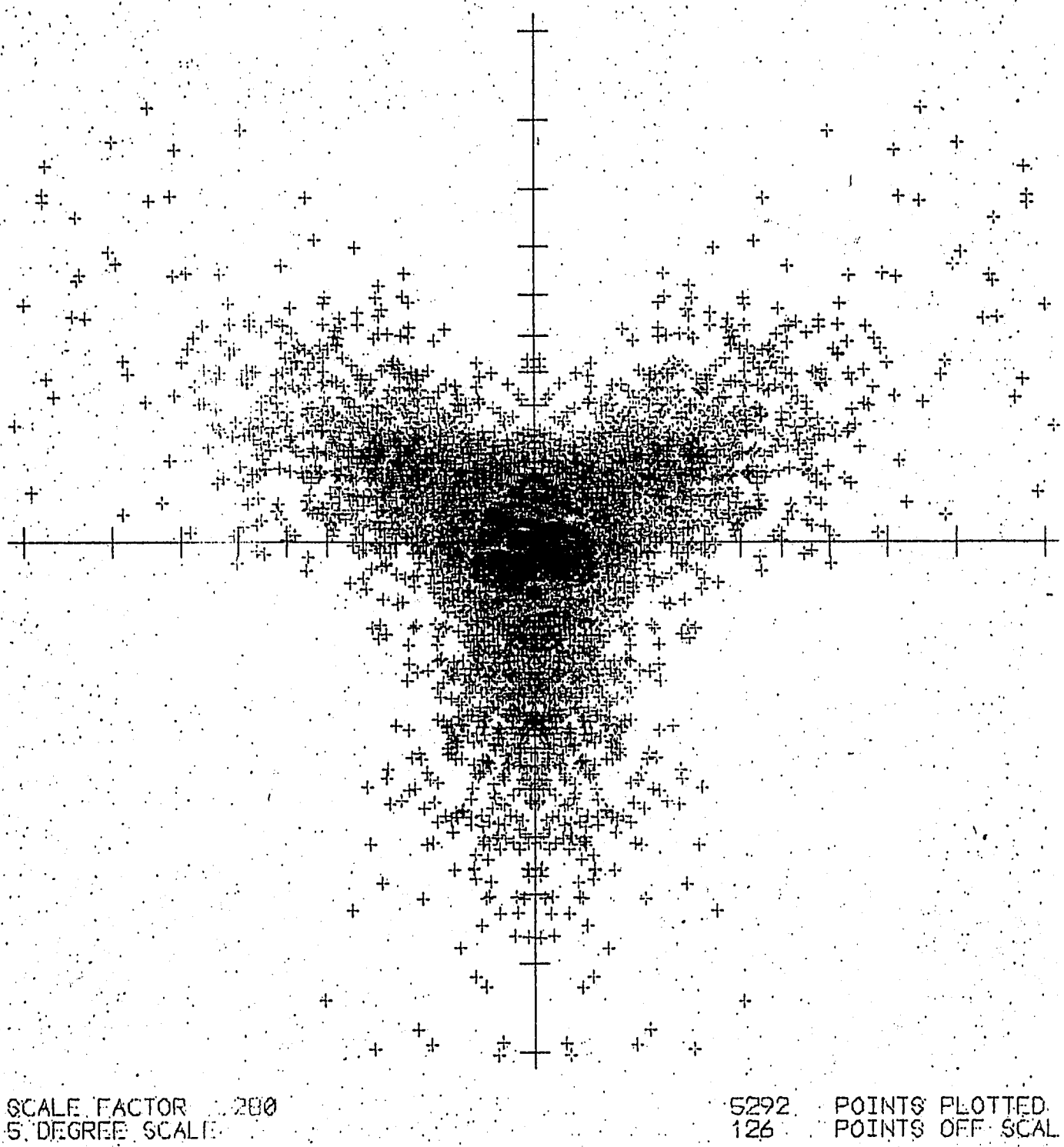
M1225
9-Jul-76
X = TAN(THETA) COS(PHI)
Y = TAN(THETA) SIN(PHI)
SIMULATED ESD PATTERN
3
SCALE FACTOR .200
5 DEGREE SCALE
5292 POINTS PLOTTED
126 POINTS OFF SCAL

FIGURE 7.15b

M1226
10-Jul-76

X = TAN(THETA) COS(PHI)
Y = TAN(THETA) SIN(PHI)

SIMULATED ESD PATTERN 3

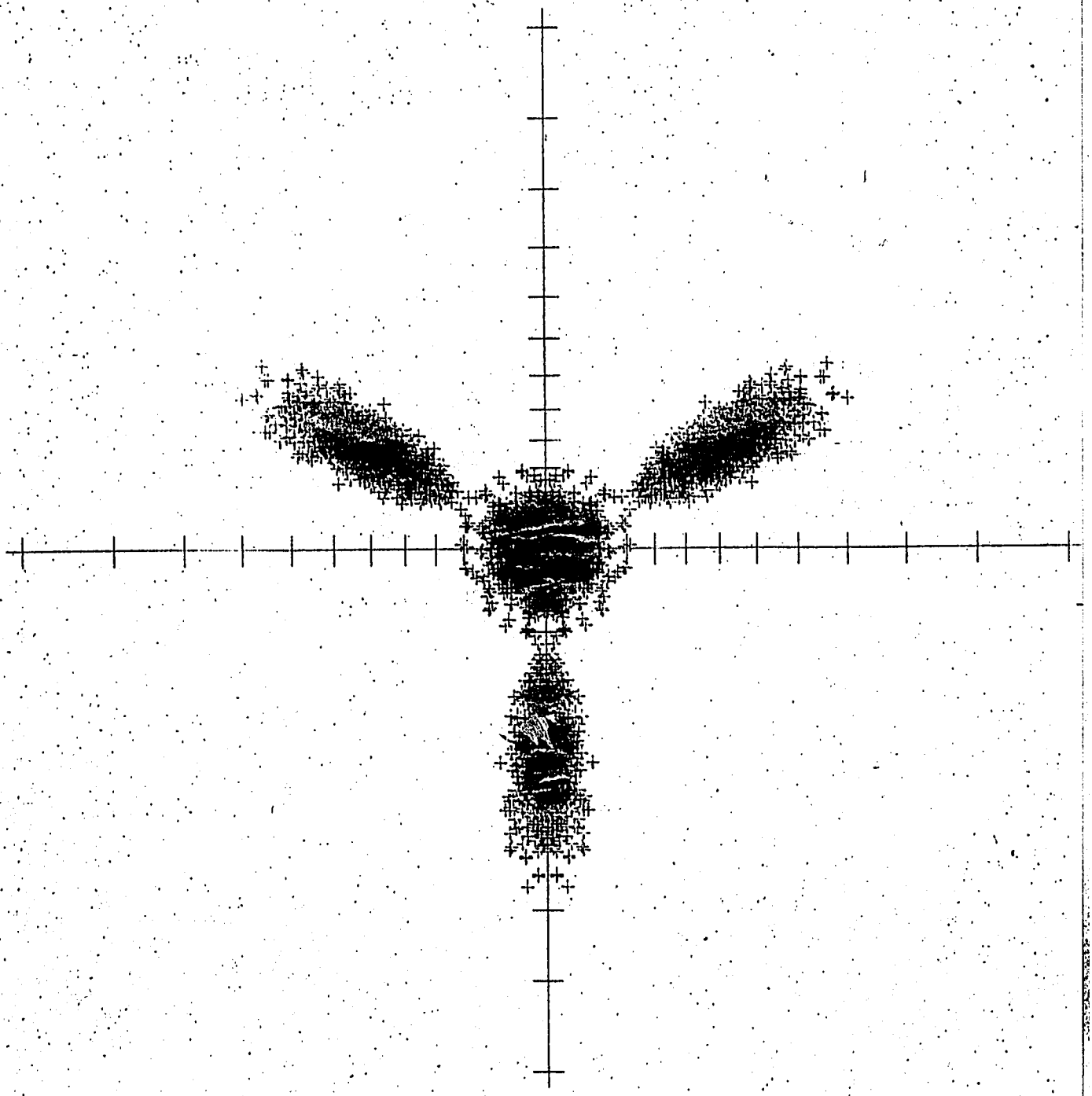

SCALE FACTOR 200
5. DEGREE SCALE

6000 POINTS PLOTTED
0 POINTS OFF SCALE

FIGURE 7.15c

M1227
10-Jul-76

X = TAN(THETA) COS(PHI)
Y = TAN(THETA) SIN(PHI)

SIMULATED ESD PATTERN 3

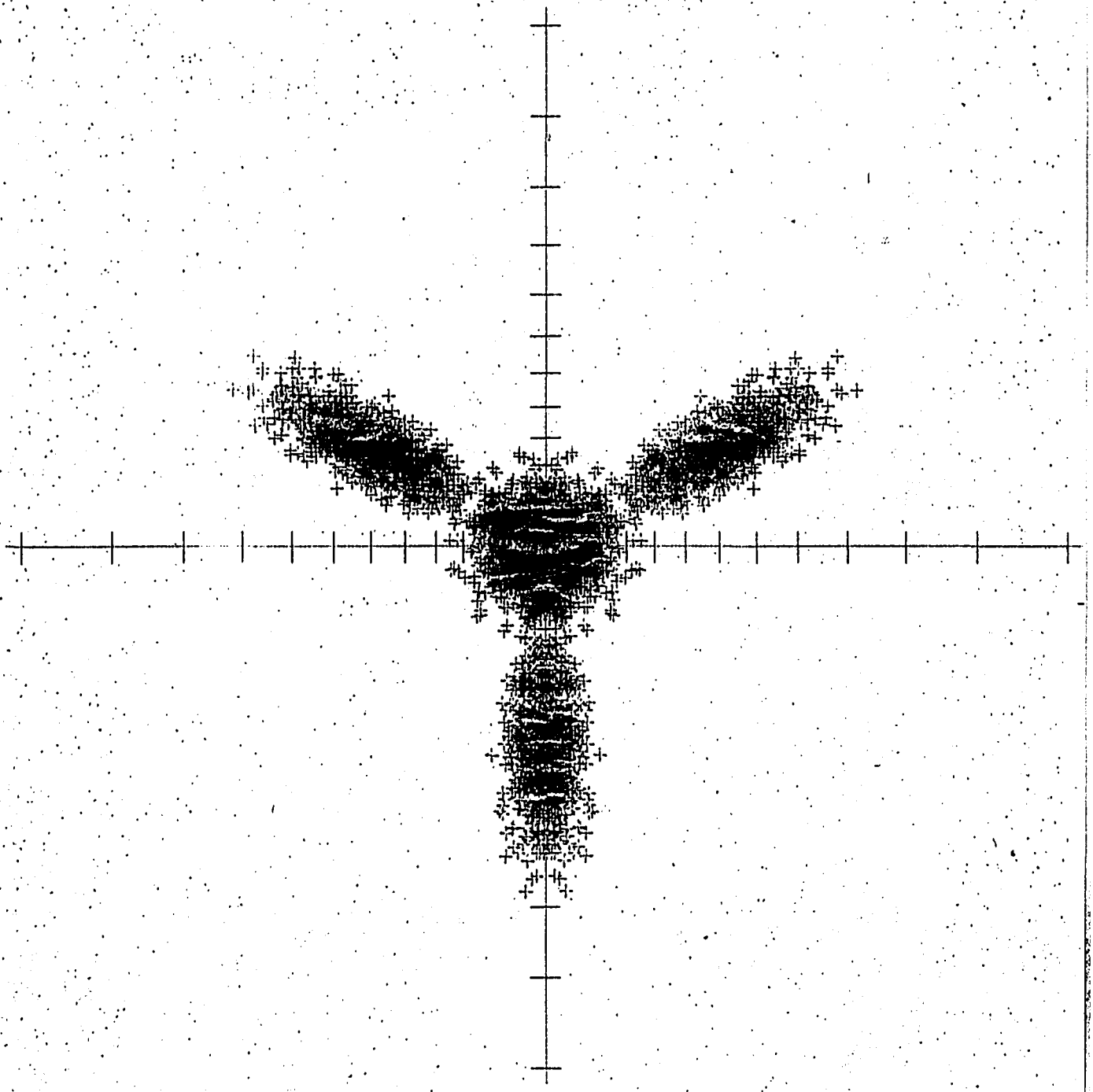

SCALE FACTOR .200
5 DEGREE SCALE

6000 POINTS PLOTTED
0 POINTS OFF SCAL

FIGURE 7.15d

Chapter VIII: ESD of O^+ from the (100) Surface of Tungsten

A detailed study of positive oxygen ion desorption from the (100) tungsten surface is now undertaken. The approach in this section closely parallels the method of Chapter VII, in which O^+ angular desorption from W(111) was examined. We simulated the Electron Stimulated Desorption Ion Angular Distributions (ESDIAD) patterns for oxygen chemisorbed at various sites on the W(100) surface mesh. Both isolated oxygen atoms and correlated groupings of adsorbed oxygen atoms in surface complexes were studied.

In a recent series of ESD experiments,[6,7] symmetrical patterns of O^+ emission spots from W(100) were found in orientational alignment with the host material tungsten atom rows. Sharp emission cones non-normal to the surface were observed, invariably accompanied by O^+ emission normal to the surface.

In this paper, we find that the number and orientation of the observed lobes may be predicted by studying ion propagation in the anisotropic interaction potential $E_2(\vec{r})$. This function possesses the same symmetry as the surface unit cell. We will place limitations on the adsorption site locations which can produce emission patterns with each observed symmetry. These qualitative conclusions are independent, within broad limits, of the model adopted for $E_2(\vec{r})$. A partial account of our findings has appeared recently in the literature.[80]

A plausible model of the β_1 oxygen adsorption phase at low temperatures is also presented. A number of atomic and molecular adsorption site geo-

metries are identified. These are consistent with the observed ESDIAD patterns for β_1 oxygen desorption from W(100). This work was conducted in tandem with our study of ESDIAD patterns for the (111) face. One should refer to Chapter VII for some of the detailed explanations which are omitted here.

A rich variety of experimental ion angular distributions has been revealed for O^+ desorbing from W(100). Here we summarize some of the pertinent experimental results found by Madey, Czyzewski, and Yates.[6,7]

The presence of two distinct adsorption phases for oxygen has been well established for some time.[3,15-17,87,88] An adsorbed state termed β_2 oxygen is associated with fractional monolayer coverages on W(100). The O^+ yield is in ESD experiments is low ($\leq 5 \times 10^{-9}$ ions/electron), corresponding to an ionic β_2 desorption cross section $< 3 \times 10^{-23}$ cm^2. For higher coverages, the O^+ yield is much higher ($> 10^{-6}$ ions/electron), corresponding to a β_1 ionic ESD cross section $> 3.4 \times 10^{-20}$ cm^2. This β_1 state is believed to constitute only a small fraction of the adsorbed oxygen on the surface at high coverages.[15-17] The surface concentration for β_1 has been estimated[3,17] to be $\sim 1.3 \times 10^{13}$ molecules/cm^2, when the total coverage is $\sim 4.9 \times 10^{14}$ molecules/cm^2. Madey[3,15] reports β_1 coverage of at most a few tenths of a monolayer, which desorbs partly as tungsten oxides upon heating. Hence, adsorbed O_2 molecules and surface tungsten oxides have been proposed for the β_1 state.[88]

Distinctly different classes of ESDIAD patterns are produced by the β_1 and β_2 phases. The β_2 phase produces a low yield pattern with diffuse

features, which has been described as a 'hazy cross'. Its arms are parallel to the tungsten atom rows in the substrate (see Fig. (2b) of Reference (7)). The β_1 state generates a diversity of sharply defined patterns, whose geometry depends on adsorption and annealing temperatures. For adsorption at $\sim 100^{\circ}K.$ the following sequence was seen. With annealing of the sample to $T \approx 300^{\circ}K.$ or below, the emission pattern displays a central spot accompanied by sharply defined lobes oriented at 45° to the substrate atom rows (see Fig. (3a, 3b) of Reference (7)). Annealing to temperatures $\sim 600^{\circ}K.$ produces only an emission spot normal to the surface (see Fig. (3c) of Reference(7)). With heat treatment to $T \approx 700\text{-}900^{\circ}K.$, lobes reappear centered on the 45° cell diagonal. However, each is now clearly resolved into two spots (see Figs. 3d, 3e) of Reference (7)). Above $T \approx 950^{\circ}K.$ only emission normal to the surface is seen. In each case, the desorption experiment was done at $100^{\circ}K.$ The changes are therefore irreversible ones produced by heat treating the sample.

At elevated adsorption temperatures, lobes aligned parallel to the substrate atom rows are observed. The mean ion kinetic energies for all of the ESD emission spots are estimated to be in excess of several electron volts. Previous studies have reported peak ion emission energies of $\sim$ 6.5 ev. and also $\sim$ 8 ev.[3,4,72] for β_1 oxygen.

We are principally concerned in this paper with explaining ion angular distributions for oxygen adsorbed in the β_1 phase. In particular, we focus interest on the low annealing and adsorption temperature ESD pattern sequence displaying single 45° lobes. The colatitude of these lobe centers is placed

by Madey, et al at $\langle\theta_v\rangle \approx 36^0$. In our calculations, $\langle\theta_v\rangle$ corresponds to the colatitude of the average ion emission velocity from a localized adsorption site. It has been shown that facetting and/or reconstruction of an oxygen covered W(100) surface is thermally activated at $T \approx 700^0K$.[26,27] Hence, we do not seek to explain features of ESDIAD patterns produced by annealing or adsorption in the high temperature range. At low temperatures, facetting of the surface is unlikely.

The W(100) Surface Cell

The W(100) surface unit cell is shown in Fig. (8.1) with several points labelled for reference. This structure covers the surface created by slicing the bulk B.C.C. tungsten lattice with a plane whose normal lies along the (100) direction of Fig. (7.2). Cartesian axes are picked as shown in Fig. (8.1), with $\hat{z}$ normal to the surface. The lengths used for cell dimensions are given in the table, Fig. (7.4). The lattice length, $a = 5.97\ a_0$, is the zone width, while the interplanar spacing, $d = a/2$, of the bulk solid was assumed. Tungsten atoms in the surface plane at $z = 0$ reside at the points labelled 'D'. Layers inside the solid at $z = -2nd$, $(n = 1, 2, 3.....)$ are also centered at 'D'. Axes normal to the surface through 'A' mark the B.C.C. tungsten locations, in planes at $z = -nd$ $(n = 1, 3, 5.....)$. Each tungsten atom is represented by a shaded circle whose radius, $2.55\ a_0$, is Slaters empirical tungsten atomic radius. This visualization is useful for determining reasonable tungsten-oxygen atom separations.

Recently, Van Hove and Tong[24] have identified a possible 6% con-

traction in the spacing between the two outermost tungsten layers on W(100), via LEED. This contraction affects our result only slightly, however, and was neglected in numerical calculations. A small increase in desorption energies of oxygen bound to the surface tungsten layer is implied, as well as a slight decrease in mean ejection energies for adsorption over site 'A'. Minor shifts in the ESDIAD patterns calculated are also implied.

For our purposes, the W(100) cell symmetry is classified as 8 fold degenerate in the following sense: a low symmetry point, such as 'α' in Fig. (8.1), is present in 8 orientations in the zone. Points 'A' and 'D' are four-fold rotation axes. Point 'E' is a two-fold axis. Any of the lines EAE, DAD, DED are reflection axes. Adsorption sites on any of them are replicated 4 times in the zone, rotated by 90°. Point 'E' is counted twice, while the symmetry sites 'A', 'D' replicate themselves only once under the symmetry operations of the cell.

Ion-Solid Interaction Energy

The focus in this investigation lies primarily on the propagation phase of ESD. As in our previous study, all spatial variation in the excitation cross section and in the reneutralization rate is neglected. As a result, relative intensities between spot patterns for different adsorption sites are not estimated in this model. We computed the ion-solid interaction energy E_2 via the prescription detailed in Chapters VI, VII, with the tungsten atom Hartree potentials now residing at points appropriate to the W(100) geometry. The dielectric surface was estimated to reside at $z = -a/4$.

We show, in Fig. (8.2), the ion-solid potential $E_2(\vec{r})$ as a function of z, over points 'A' through 'E' of Fig. (8.1). Contour maps of E_2 through the planes at $z = .5\ a_o$, $2.0\ a_o$, $3.5\ a_o$ are displayed in Fig. (8.3a, b, c). At large z, image attraction dominates and anisotropy in the transverse direction becomes negligible. Trapping occurs in the central portion of the zone at $z \simeq 3.5\ a_o$. Close to a tungsten atom, E_2 becomes strongly repulsive. At points 'A', 'D' the contours disclose near cylindrical symmetry for E_2. Point 'E' is a saddle point. For these sites, the normal force component will dominate over the transverse force components. Hence, we expect ion emission normal to the surface for atoms adsorbed over points 'A', 'D', or 'E'.

Away from the symmetry points, the transverse force component is non-zero. On the diagonal cell axes, it points toward the zone center, leading us to expect four emission lobes at 45^o to the substrate atom rows for adsorption along the unit cell diagonal. Similarly, four ion emission lobes oriented parallel to the tungsten atom rows are predicted for adsorption sites on the lines EAE, DED of Fig. (8.1). At points such as 'α', patterns with eight lobes are expected.

Adsorption Site Determinations

Both qualitative and quantitative ESDIAD simulations were performed, analogous to those described for W(111), except for modifications due to surface cell symmetry. The orientation and number of lobes were found to be as expected on the basis of the dynamical picture introduced in Chapter VI, and the contour maps of E_2. Lobed patterns were found for adsorption sites

away from the symmetry points. Quartets of lobes oriented as described above were found for atomic oxygen.

In order to ascertain the model independence of these conclusions, we studied a simple model potential of the following form:

$$E^{o}(\vec{r}) = \frac{A}{(1+aZ)^{6}}\left[1+\frac{C_x}{2}(1-\cos(k_x x))\right]\left[1+\frac{C_y}{2}(1-\cos(k_y y))\right]$$

This function has the desired properties, with the choice $k_x = k_y = 2\pi/a$. The assymetry parameters are C_x, C_y. There is a minimum of E^{o} in each plane at the x-y origin. The patterns generated, and their systematics of variation with this potential, correlated well with results using the ion-solid interaction potential as discussed above.

The 45^{o} diagonal lobe centers observed by Madey, et al (Fig. (3a, b) of Reference (7)) were estimated to lie $\sim 36^{o}$ off the normal emission direction. A set of adsorption site candidates consistent with emission lobes at this angle was obtained. We scanned sites along the unit cell diagonal which are a fixed distance from the nearest surface tungsten atom. The bond lengths 1.95 A^{o}. and 2.08 A^{o}. were used, as in Chapter VII, to bracket reasonable tungsten-oxygen separations, and as a check on the bond-length dependence of the results. In Fig. (8.4) we show a cross section of the W(100) cell in the plane formed by the cell diagonal and the z axis. The points at which computations were done are indicated. Adsorption sites with $\alpha > \alpha_{max}$ lie almost above the 'A' tungsten atom, and were not investigated, as they produce only low angle emission lobes. The desorption temperature $100^{o}K$. was assumed.

The presence of adsorbed O_2 molecules, or surface complexes involving

several oxygen atoms has been suspected on W(100).[7,88] Hence, we investigated both a 'bridge' and a 'surface' molecule, as well as isolated oxygenic locations. In Fig. (8.5a, b) we sketch the oxygen atom configurations connoted by these terms. For an oxygen atom adsorbed at $r \equiv (x, y, z)$, the 'bridge' partner is located symmetrically with respect to the zone center at (-x, -y, z). The 'surface' molecular partner is located symmetrically with respect to the nearest zone corner tungsten atom. We make no assumption about possible O-O bonding in the ground state, especially where the inter-oxygenic separations are large. The 'bridge' and 'surface' molecule structures were investigated only for adsorbed O-O separations larger than the O_2 bond length of 1.21 Angstroms.

We pictured the disruption of a surface complex by incoming electrons to occur as follows: one member of a pair of oxygen atoms is suddenly converted to an ion, while the other oxygen atom remains neutral. Both the asymmetry of the surface Hartree potential, and repulsion by the ions molecular partner govern the initial propagation phase. A repulsive Hartree potential was calculated and fitted to the form

$$V_{O\text{-}O} = 8.053 \exp[-2.292 r] \qquad (8.1)$$

in the manner described previously. We neglected the recoil of neutral oxygen atoms in computing ion trajectories. This may be a good approximation where directed bonding to the tungsten layer prevails.

The results of these scans are shown in Fig. (8.6a), for the 1.95 A^{O}.

length, where we plot $\langle\theta_v\rangle$ the lobe center colatitude, and $\langle\theta_a\rangle$, the mean acceleration colatitude at the point of ionization. The latter quantity, as discussed, is an indicator of the importance of image effects or repulsion on the in-flight ion dynamics. The analogous plot for W-O separation 2.08 A^o is given in Fig. (8.7a). We also plot average desorption energies and flight times to the $z = 50\ A^o$. plane in Figs. (8.6b) and (8.7b).

We note in Fig. (8.6a) and (8.7a) that for $\alpha \gtrsim 35^o$ the isolated atom and the 'surface' molecule branches are indistinguishable to this simulation. At the inter-oxygenic separations involved, the repulsion given by Eq. (8.1) is negligible. Similarly, when $\alpha \lesssim 20^o$, the components of the bridge molecule exert negligible repulsive impulse. Image effects dominate on the 'atom' and surface molecule branches for $\alpha \lesssim 50^o$, inasmuch as $\langle\theta_v\rangle >> \langle\theta_a\rangle$. Over the remainder of the α range, in-flight repulsion by neighboring tungsten atoms causes deflection of the lobe centers to smaller colatitudes. The single tungsten atom in the $z=0$ plane may be regarded as the sole source of the initial impulse for the 'atomic' and 'bridge' molecule branches of the $\langle\theta_v\rangle$ curves only for small α . The W(100) cell is much more closely spaced than the W(111) structure, and we find in this model that nearest neighbor tungsten interactions complicate the ion dynamics for adsorption sites close to the surface. The mean energy and flight time data portrayed in Fig. (8.6b) and (8.7b) show the expected trends.

We interpolated several sites which are possible sources of 36^o colatitude ESDIAD lobes, forming quartets of spots rotated 45^o to the tungsten rows. From Fig. (8.6a) either an isolated atom at $\alpha = 33^o$ or a surface molecule

at $\alpha = 30^{\circ}$ is plausible. At $\alpha = 51^{\circ}$, either the isolated atom or 'surface' molecule are possibilities as well. Compact lobes are to be expected here, as there is near cancellation of image and repulsion effects. It is interesting to note that the direction to the nearest vacant tungsten site is close to $\alpha = 51^{\circ}$. The 'bridge' is ruled out, for this bond length, as the 36° spot source. However, a 'bridge' molecule at $\alpha = 51^{\circ}$ produces a normal emission spot, via cancellation of the O^{+}-O repulsion with the transverse component of $\vec{\nabla} E_z$. This site was studied further despite its clear model dependence. The implied inter-oxygenic separation is 1.44 A°. which is close to the sum (1.49 A°.) of Paulings covalent oxygen single bond radii.[89]

From Fig. (8.7a) we found 36° lobes at $\alpha = 49^{\circ}$, for which atomic and 'surface' molecular occupation is indistinguishable. The 'atom' at $\alpha = 26^{\circ}$ and the 'bridge' at $\alpha = 27.5^{\circ}$ were also selected. Inter-oxygenic repulsion at small molecular bond lengths produces large angle lobes.

The results of extensive numerical computations are tabulated in Fig. (8.8). All calculations were done at $100^{\circ}K$. using 500 points selected by the Monte Carlo method. The spring constants were taken to be .01 atomic units. As noted in previous calculations for O^{+} on W(111), the widths of simulated ESDIAD patterns display some sensitivity to the spring constants, however, the lobe center locations have displayed insensitivity to the precise values chosen. Inasmuch as a large number of ion distribution plots were generated, we have relegated them to Appendix IV for examination. The locations of sites for oxygen adsorption included in our study, are fully identified in Fig. (8.8).

Discussion of Results

First we discuss O^+ emission cones normal to the surface. These are found for atomic oxygen desorption only over points 'A', 'D', 'E'. We observed mean desorption energies to quite generally decline for increased tungsten oxygen separations, which is to be expected, inasmuch as the atomic Hartree potentials vary rapidly with separation.

Sites A1 to A3 lie over the B.C.C. symmetry site 'A'. Multi-centered bonding equidistant from five tungsten atoms is assumed for site A1. Sites A2, A3 are directionally bonded. This geometry has been suggested for the β_2 adsorption mode responsible for the 'hazy cross' ESDIAD pattern. We find that spot patterns for sites A1-A3 display no tendency to form the 'hazy cross'. Spot widths tend to increase with z coordinate as expected but half widths remain in the range 12-15°.

Sites A1-A3 are the best candidates for the β_2 adsorption phase. One may attribute the low β_2 yield to efficient reneutralization of ions excited close to the surface. Rapid exponential weakening of the quenching rate has been proposed in one dimensional ESD models.[21, 32, 72] Several possible reasons for our failure to predict the 'hazy cross' may be found. One should expect lateral anisotropy of the quenching mechanism to be important where reneutralization is rapid. Madey, et al, suggest that quenching 'channels' may produce hazy patterns with ill defined boundaries, especially for adsorption at a multi-centered site such as A1, where adatom positions may not be highly localized in the transverse direction. Another possibility is anharmonicity of the ground state, which we neglect in this model calculation. Finally, lateral anisotropy

in the real W-O potential may be more pronounced than our model predicts, compressing the ion trajectories into a cross. If this is the case, however, one would expect sharply focussed patterns for the β_2 phase, which are not observed.

Normal emission spots are also found for adsorption over the surface tungsten atoms. Sites such as D1, D2 have been suggested for the β_1 oxygen site responsible for the normal ionic emission in ESDIAD patterns. This calculation predicts mean desorption energies for oxygen at sites D1, D2 which are an order of magnitude smaller than those observed,[7,72] We do not rule out the possibility that adsorption over site 'D' occurs as part of the β_1 phase. Our simulation suggests, however, that this geometry is at most a numerically small component of β_1 oxygen present on the surface.

The two-fold symmetric sites over 'E' provide the best candidates for the central spot producing β_1 adsorption phase. Site E1 is preferred, as its mean desorption energy in our calculation, 2.35 ev., is most consistent with experiment. The half width of the central spot we find to be $\sim 15^{\circ}$, which is consistent with the estimate made by Madey, et al, for Fig. 3c of Reference (7).

Normal emission spots were found for undissociated O_2 molecules at sites B1, C1. The inter-oxygenic separations in each case are close to Paulings single oxygen bond length (1.49 A°.).[89] Sites C1, B1 correspond to O_2 molecules bridge bonded across the unit cell with the molecular axes parallel to, and at 45° to the substrate atom rows respectively. Molecular adsorption for β_1 oxygen on tungsten has been suggested.[3,7,88] Single emission spots rather than four lobed patterns are found due to in-flight deflection of the de-

sorbing ions by O^+ - O repulsion.

These findings are highly model dependent; hence, sites C1, B1 are not regarded as plausible producers of the β_1 central spot. It is likely that the actual ion-solid potential is sufficiently different from our model for E_2 to produce cross shaped patterns for adsorption at C1 or B1. In the case of site C1, the oxygen centers lie at $z = 1.41\ a_o$, hence, one may expect rapid reneutralization if adsorption does in fact occur here. The distance to the surface is comparable to that for site A1, lying at $z = 1.49\ a_o$, which we associate with the heavily quenched β_2 phase. We do not assume, however, that molecular adsorption at C1 occurs, inasmuch as thermal desorption experiments produce atomic oxygen from the β_2 phase.[7]

Now we examine the evidence for sites B2-B7, obtained above by interpolation using Figs. (8.6a), (8.7a). Each site produces a quartet of lobes rotated to cover the unit cell diagonal and whose mean emission colatitude $\langle\theta_v\rangle \approx 36^o$ is close to that observed. Site B2, corresponding to $\alpha = 51^o$, has the mean desorption energy most consistent with experiment, namely $\langle E\rangle = 1.22$ ev. Hence, it is suggested as the possible β_1 adsorption site. For sites B3-B7 mean desorption energies are all <1 ev. Simulated ESDIAD patterns for sites B2-B7 (Figs. AIV.10 to AIV.15) reveal that compact emission spots closely resembling those observed are generated for site B2. We point out, however, that similarities between the observed lobes and simulated patterns, generated with quenching effects neglected, must not be considered conclusive evidence of adsorption site identity. The expected effects of reneutralization on the patterns we present here, were discussed in Chapter VII. In Fig. (8.9) we display a super-

position of ESDIAD patterns for sites E1 and B2.

Our simulation has adequately reproduced the angular dependent features of the low temperature ESDIAD sequence observed by Madey, et al. However, the mean desorption energies reported by those authors and by others [7, 72] are not reproduced. We note that the isotope effect in O^{16}, O^{18} desorption may be used to assign the value $S_2 \simeq 10^{-4}$ to the β_1 survival probability.[65] Some upward skewing of the desorption energy distribution is expected, as the result of preferential reneutralization of slower moving ions. We estimated in the last chapter, however, that the expected upward shift in $\langle E \rangle$ is insufficient to bring our energy estimates into agreement with experiment. The crudeness with which E_2 was modelled is suggested as the likely source of this deficiency.

As a check on the model dependence of our proposed site identification, the tungsten-oxygen ion Hartree potential was recalculated, using relativistic tungsten wave functions.[76] After fitting to an exponential, the following was found:

$$V_{W\text{-}O} = 23.92 \exp[-1.468 r]$$

Here, all quantities are in atomic units. E_2 was then constructed as described previously. ESDIAD patterns for sites E1, B1 were recalculated, with anisotropy introduced into the ground state via the choice .2 atomic units for the z component of the spring constant tensor. The superimposed ion distributions are shown in Fig. (8.10). Lobe centers for site B2 remained invariant at $\langle \theta_v \rangle = 35.4^\circ$, while a central emission spot is still found for site E1. Significant increases in the mean desorption energies were found, with $\langle E \rangle$

for the normal emission spot now given by 4.56 ev. , while the mean ion energies in the lobes is 2.52 ev. This result is taken as an indication that the adsorption site identification we propose will not suffer drastic modification when more quantitatively realistic models for E_2 are available.

The mean desorption energies calculated for site E1 are roughly twice those for the lobes of site B2. This finding is consistent with experiment. Madey, et al, report extinguishing the lobes at a lower stopping potential than that required to extinguish the central spot, taking care, however, to point out that comparable energies for the spot and the lobes are not ruled out. We note that mean desorption energies for an 'on top' position over point 'D' are smaller than those for sites such as B2, at comparable W-O bond length, almost independently of the model for E_2. Significantly smaller emission energies in the central spot appear to be inconsistent with experiment. Our rejection of adsorption sites over the surface tungsten atoms is therefore supported.

It is interesting to speculate why atoms would assume the B2 site bonded along the cell diagonal at $\alpha \approx 51^{\circ}$. A partial O-O bond may possibly exist in a surface WO_2 complex. One may also imagine one of the tungsten wave functions to have large amplitude in the direction $\alpha \approx 51^{\circ}$, forming a directed bond. We note that $\alpha = 54.7^{\circ}$ defines the direction to the site, over point 'A', which the next tungsten layer would occupy, lending some support to this interpretation.

Ordered structure on both β_2 and β_1 oxygen covered W(100) surfaces has been reported by a number of LEED investigators.[90,91] Madey, et al find evidence of (1x4) and (1x3) structures for β_1 oxygen at $T \approx 300^{\circ}K$. A

number of such structures involving occupation of E1 sites and surface WO_2 molecules may be visualized, coexisting with β_2 oxygen on the surface. We do not propose specific ordered structures, inasmuch as the technique we employ is fairly insensitive to long range surface order.

A number of adsorption sites which produce quartets of lobes aligned parallel to the substrate atom rows were studied. Several such patterns are displayed in Appendix IV, and listed in Fig. (8.8) for completeness. They are not, however, directly applicable to the problem at hand. Lobed patterns aligned parallel to the substrate are observed only at temperatures for which a planar W(100) surface may not be presumed to exist.

Conclusions, Summary

Our conclusions regarding O^+ adsorption at low temperatures on an unfacetted, unreconstructed W(100) surface are now summarized.

The picture of ESD proposed originally by Redhead and by Menzel and Gomer [20,21] was generalized in this paper to three dimensions. We found that a qualitatively correct description of ESDIAD patterns is obtained in this picture. We are able to explain the orientation and number of ESD emission spots with the use of an anisotropic model ion-solid potential, with simplified treatment accorded to excitation and reneutralization mechanisms.

The number of distinct ESD emission spots for each atomic oxygen adsorption site equals the number of points in the surface unit cell equivalent to the chosen site. On the flat W(100) surface, only normal emission spots, four lobed, or eight lobed ESD patterns, and their superpositions, should be observed.

Four lobed patterns aligned at 45^{o} to the substrate atom rows are evidence of adsorption along the unit cell diagonals. Quartets of lobes aligned parallel to the atom rows originate with adsorption between 'A' and 'E', or along the unit cell edge between 'D' and 'E' (Fig. 8.1). For atomic oxygen, normal O^{+} emission cones imply adsorption above point 'A', 'D' or 'E'. For molecular complexes the same rules apply, however, 'bridge' bonded O_2 molecules may possibly produce a central spot pattern as noted above.

ESDIAD patterns containing both a central emission spot and lobes are evidence of at least two coexisting adsorption geometries. Relative spot intensities in such superpositions depend on the partial coverage for each geometry and on the spacial variation of the excitation cross section and re-neutralization rate. Detailed intensity predictions are in principle possible with the simulation method we employ above, provided suitable model interactions are available.

It is assumed that the low ESD yield β_2 oxygen phase involves atomic oxygen adsorbed at a site over the zone center such as A1, A2 or A3. Mechanisms which can produce the observed 'hazy cross' ESD pattern were mentioned in the text, and by other authors.[7] It was speculatively suggested that adsorption geometries similar to sites C1, C2 or C3 may contribute to the β_2 phase.

The following picture of β_1 adsorption at low temperature emerged. Atomic oxygen adsorbed over site 'E' is the most plausible origin of O^{+}

emission normal to the surface. Surface WO_2 complexes oriented along the unit cell diagonal provide the most cogent explanation of 45^{o} rotated lobe quartets. The observed lobe center colatitude is best matched by taking the O-W-O angle to be $\approx 102^{o}$. Quantitative agreement between calculated and experimental desorption energies is inexact. However, the adsorption site identification is expected to remain substantially unchanged with improvements in modelling E_2. Adsorption directly over the surface tungsten atoms at 'D' is unlikely, except as a small fraction of the β_1 phase.

We decline to make adsorption site identifications for any of the high adsorption or annealing temperature sequences presented by Madey, et al, as the surface is assumed to facet. Our computational method may be readily extended to deal with non-planar surfaces at a later date.

The conclusions of this study are in substantial agreement with most features of the β_1 oxygen adsorption model proposed by Madey, Czyzewski, and Yates in their experimental paper.[7]

It is expected that joint experimental and theoretical studies of ESD angular distributions will provide a valuable spectroscopic tool for surface study. ESD samples principally short range order on the scale of the unit surface cell. Hence, information complementary to that revealed by established techniques may be obtained.

Chapter VIII: Figure Captions

Fig. 8.1: Unit Cell of the W(100) Surface. The cell outlines and features are superimposed on a billiard ball representation of tungsten atoms, drawn as circles with radius 2.55 a_o. Surface layer tungsten atoms reside at 'D', with cartesian coordinates ($\pm 2.98a_o, \pm 2.98a_o; 0$). The 'B.C.C' tungsten atom at 'A' is centered on the x-y origin, at $z = -a/2 = -2.98a_o$. All of the low symmetry sites 'a' are equivalent. All of the lines DAD, DED, EAE are bilateral symmetry axes of the surface mesh. Points such as 'B','C','I' are fourfold degenerate. Any of the triangular sectors ADEA is sufficient to generate the whole unit cell under eight covering operations. The high symmetry points are 'A','D','E'. Roman letters designate points of interest mentioned in the text, or for which computations were performed.

Fig. 8.2: The Ion-Solid Interaction Energy $E_2(r)$ as a function of z above points A - E of Fig.(8.1). Distances from the z = 0 plane are in Bohr radii. The contribution of V_{IM} alone is shown by the dashed line. E_2 was plotted neglecting an additive constant, essentially the oxygenic ionization energy. Hence, desorption kinetic energies may be inferred from Fig.(8.2).

Fig. 8.3a, b, c: Contour maps of $E_2(r)$ in the planes at $z = .5\ a_o$, $2.0\ a_o$, and $3.5\ a_o$.

Fig. 8.4: Cross Section of the W(100) unit cell in the plane defined

Chapter VIII: Figure Captions, continued

by a cell diagonal and the z axis (see inset, also Fig.8.1). Arcs from $\alpha = 0$ to α_{max} indicate adsorption sites which were scanned to match 36° colatitude lobe quartets. The left (right) half of the cell shows the locus of points scanned for tungsten-oxygen separations of 2.08 A.$^{\circ}$ (1.95 A.$^{\circ}$). The limit α_{max} of the scans for atomic oxygen is 76.4° (79.8°), and defines the point equidistant from the B.C.C. and Surface layer tungsten atoms. Note that the angle 35.3° suggests the production of 36° emission lobes for adsorption at α_{max}. This is not found to occur, as in-flight repulsion by neighboring tungsten atoms is strong in this region of the cell.

Fig. 8.5a: Geometry for a 'surface' WO_2 complex oriented at 45° to the substrate atom rows. Black circles represent oxygen atoms, white circles are tungstens. A top view and cross section along the unit cell diagonal are shown. The inter-oxygenic distance is a_{o-o}. Slaters empirical oxygen atomic radius is 1.13 a_o.

Fig. 8.5b: Views of the 'bridge' molecule similar to Fig.(8.5a).

Fig. 8.6a: Colatitudes of ESD emission lobe centers, as functions of the angle 'α'. Solid lines depict $\langle\Theta_v\rangle$ for quartets of ESD spots, while the dashed curves portray $\langle\Theta_a\rangle$, the mean acceleration colatitude at excitation. The main branch of each curve corresponds to lobes for an isolated oxygen atom. 'Surface' WO_2 and 'bridge' molecules produce lobes as indicated in the labelled branches of of the $\langle\Theta_v\rangle$, $\langle\Theta_a\rangle$

Chapter VIII: Figure Captions, continued

curves. The tungsten-oxygen separation was 1.95 A.^{o} The minimum plausible O-O separation, 1.21 A.^{o}, is obtained for the 'bridge' at $\alpha = 56.7^{o}$, and for the 'surface' WO_2 complex at $\alpha = 18.1^{o}$. Points interpolated for further study are marked by small circles.

Fig. 8.6b: Mean desorption energies $\langle E \rangle$ and flight times $\langle t \rangle$ to the z = 50 A.^{o} plane, as functions of the angle α. The sites covered in Fig.(8.6a), with tungsten-oxygen separation 1.95 A.^{o} are covered. Solid (dashed) lines and their branches refer to $\langle E \rangle$ ($\langle t \rangle$). Energies are in multiples of .01 Hartrees. Times are in units of 10^{4} atomic units, where 1 atomic unit of time = 2.42×10^{-17} sec.

Fig. 8.7a: Colatitudes of ESD emission lobe centers $\langle \theta_v \rangle$, and mean acceleration colatitudes $\langle \theta_a \rangle$ for 2.08 A.^{o} tungsten-oxygen separation. (See caption for Fig. 8.6a) The limit of plausible O-O separations is reached for the 'surface' molecule at $\alpha = 16.9^{o}$, and for the 'bridge' at $\alpha = 51.6^{o}$.

Fig. 8.7b: Average Desorption energies and flight times for the adsorption sites covered in Fig. (8.7a). The tungsten-oxygen separation is 2.08 A^{o}. (See caption for Fig. 8.6b).

Chapter VIII: Figure Captions, continued

Fig. 8.8: Tabulation of simulated ESDIAD data for the sites studied. The tungsten-oxygen atom separation is a_{W-O}. $\langle\Theta_v\rangle$, $\langle\Theta_a\rangle$ are the mean colatitudes for lobe centers and accelerations at excitation, before surface cell symmetry operations are carried out to produce ESDIAD patterns. $\langle E\rangle$ Is the mean desorption kinetic energy of O^+ ions. σ_E is the standard deviation of the calculated desorption energies, which gives a rough indication of the width of the desorption energy spectrum. Each site studied is described, and its coordinates (x,y,z) in Bohr radii given, relative to the scale drawings in Fig.(8.1) and Fig.(8.5).

Fig. 8.9: Superposition of simulated ESDIAD patterns for Sites E1, and B2 (see Fig. 8.8)

Fig. 8.10: Superposition of simulated ESDIAD patterns for Sites E1, and B2, with the atomic Hartree potentials recalculated as described in the text, using relativistic wave functions. A stiffer spring constant for the z direction was used. Little change in the ion angular distributions is evident.

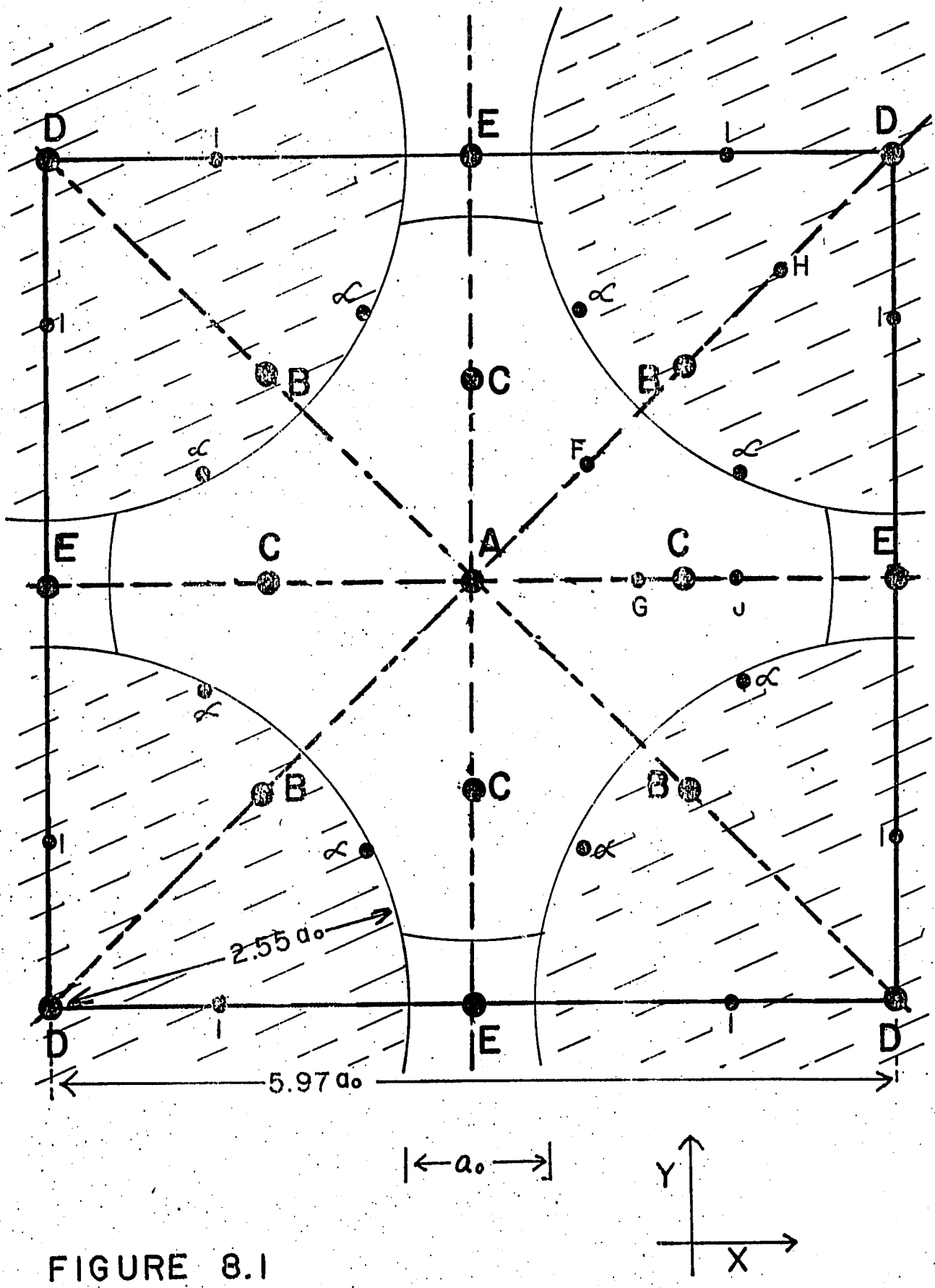

FIGURE 8.1

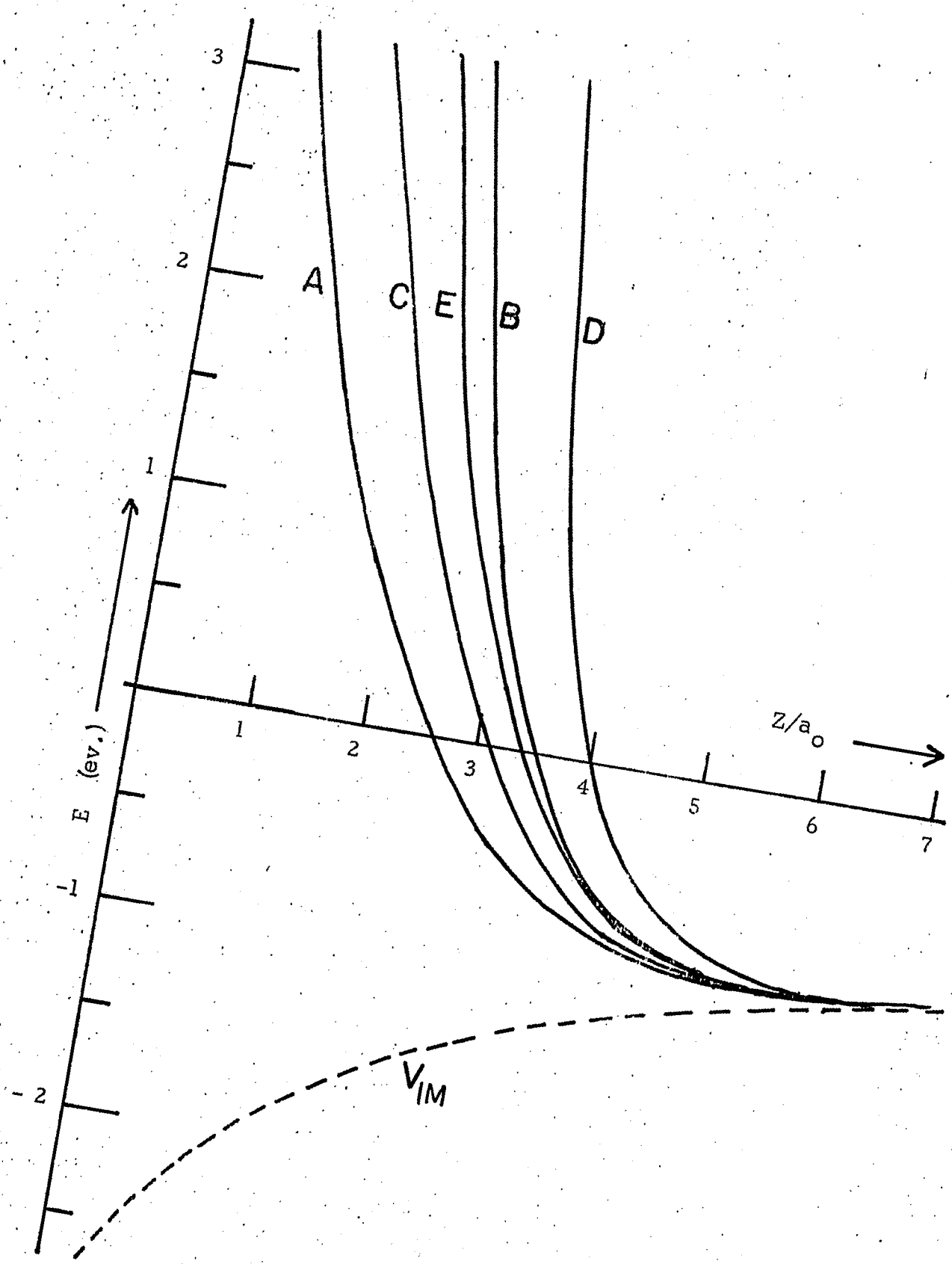

FIG. 8.2

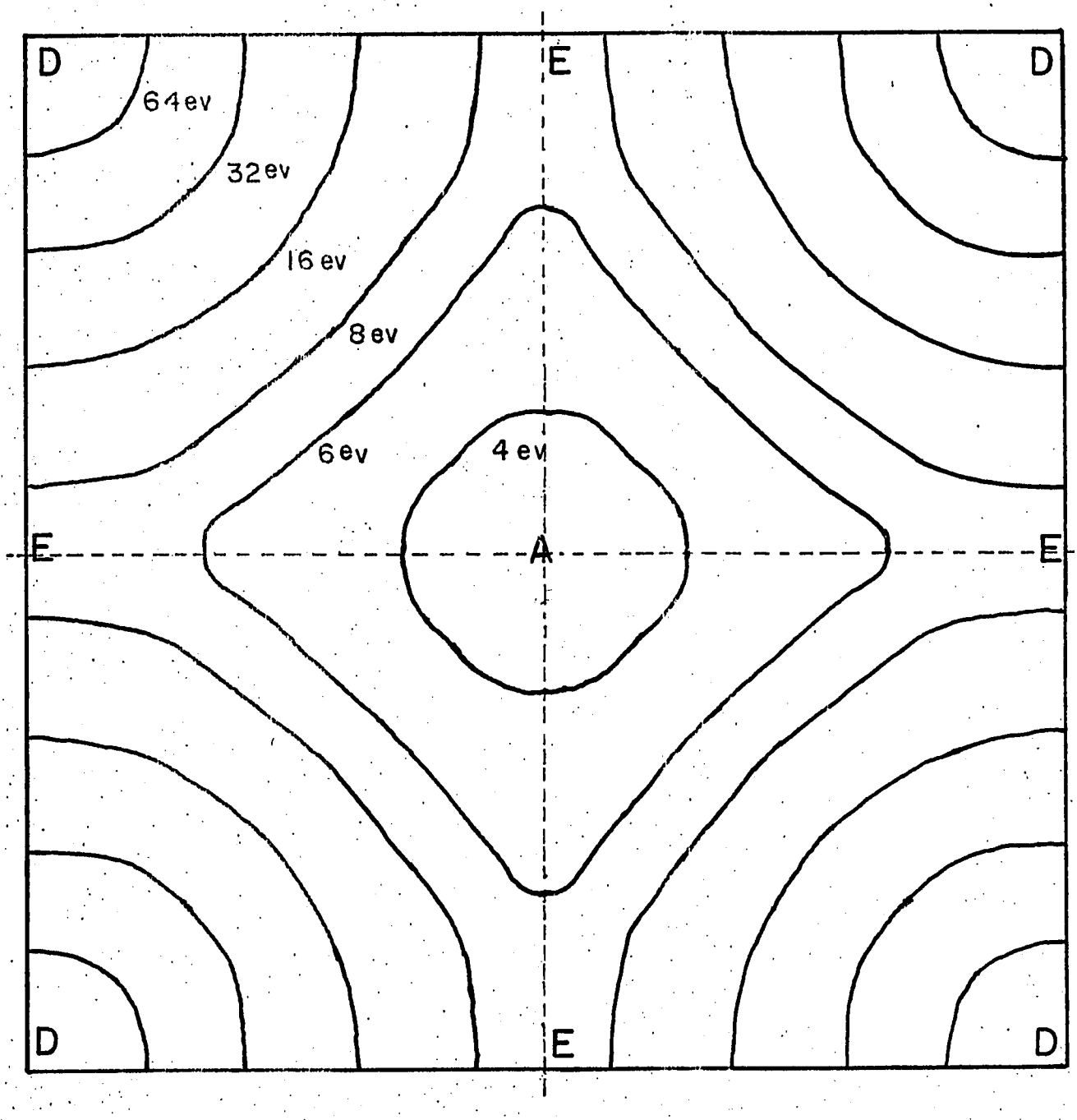

FIG. 8.3a $z = .5a_o$

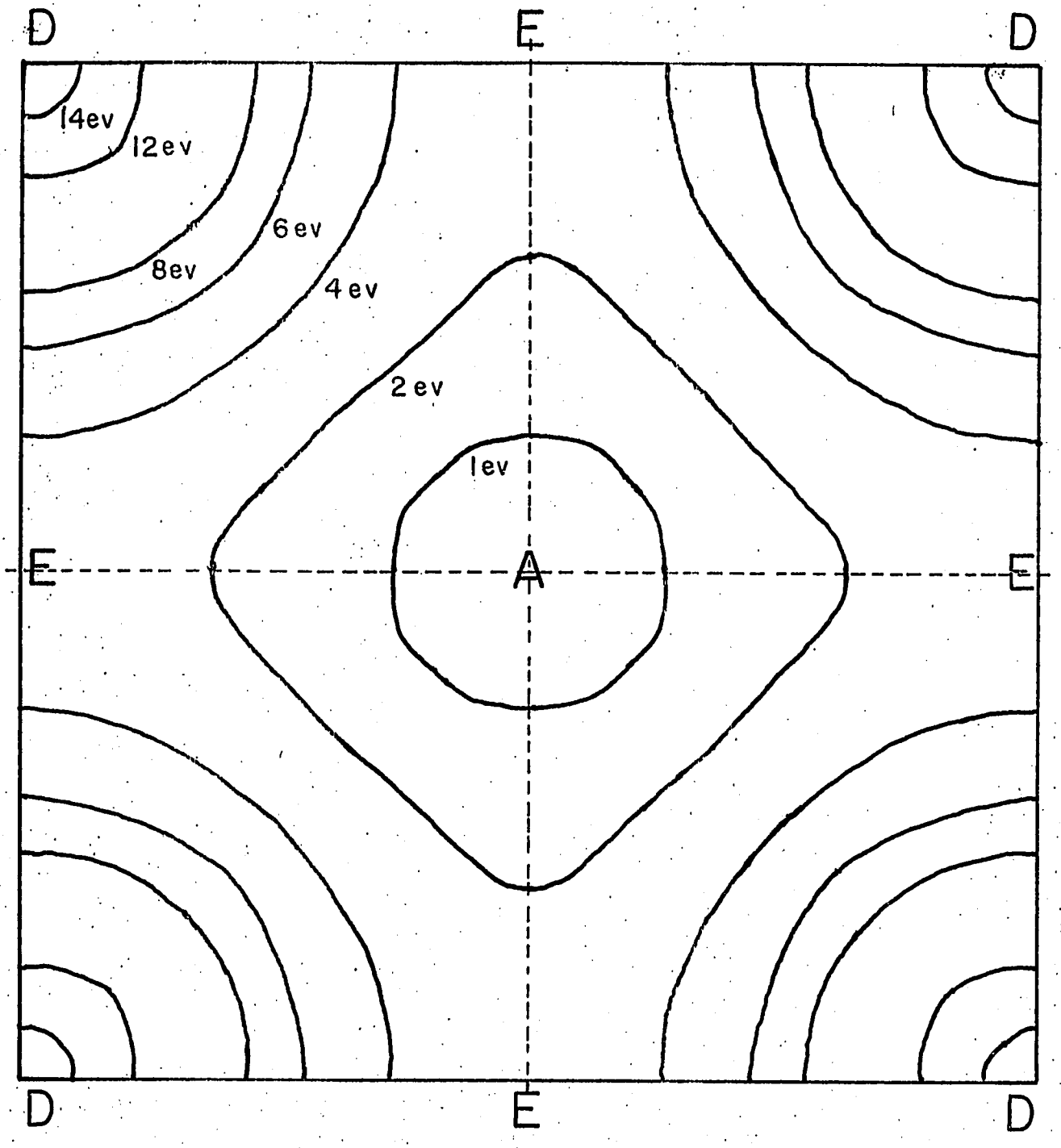

FIG. 8.3b $z = 2.0 a_o$

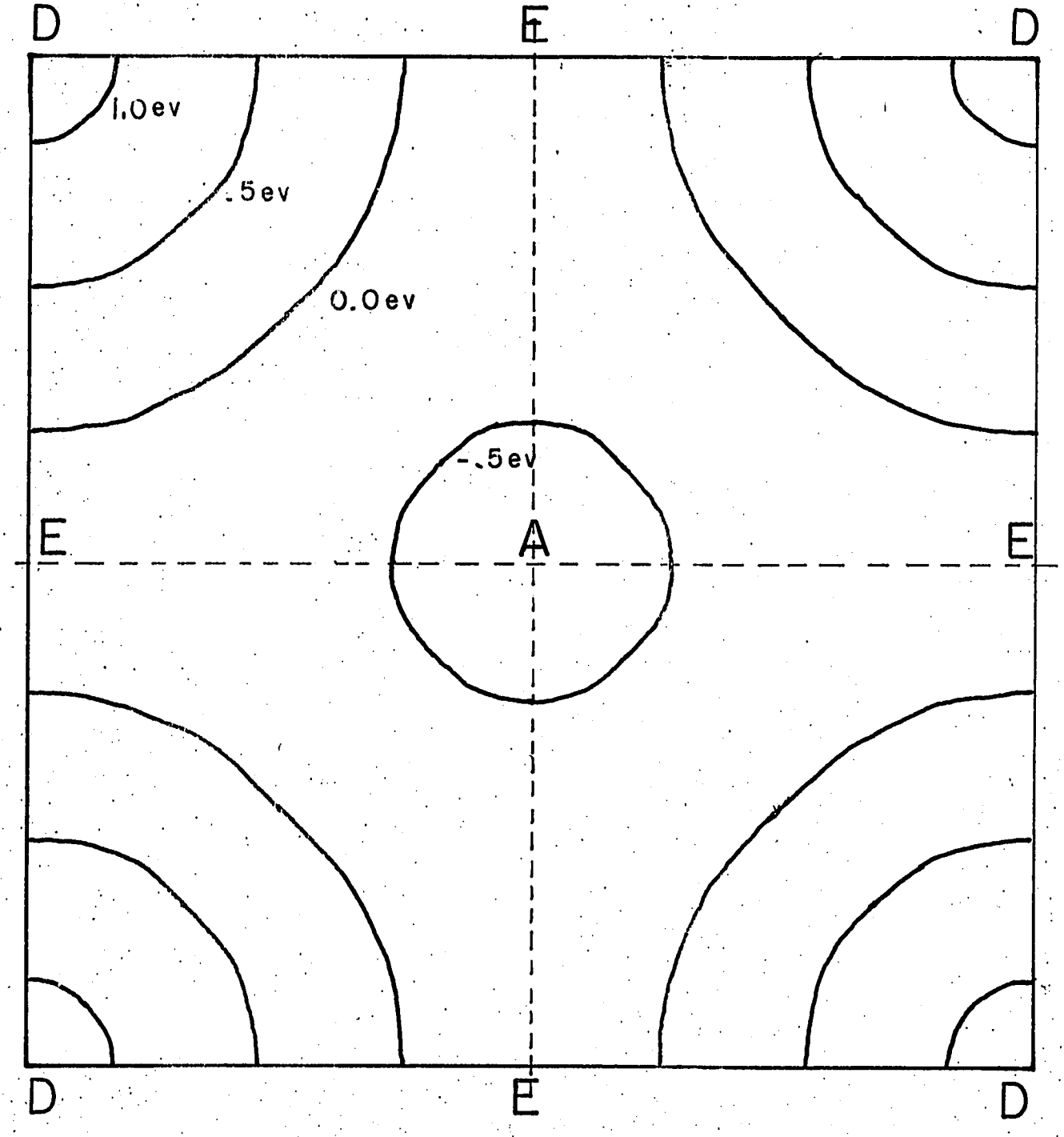

FIG. 8.3c $z = 3.5a_o$

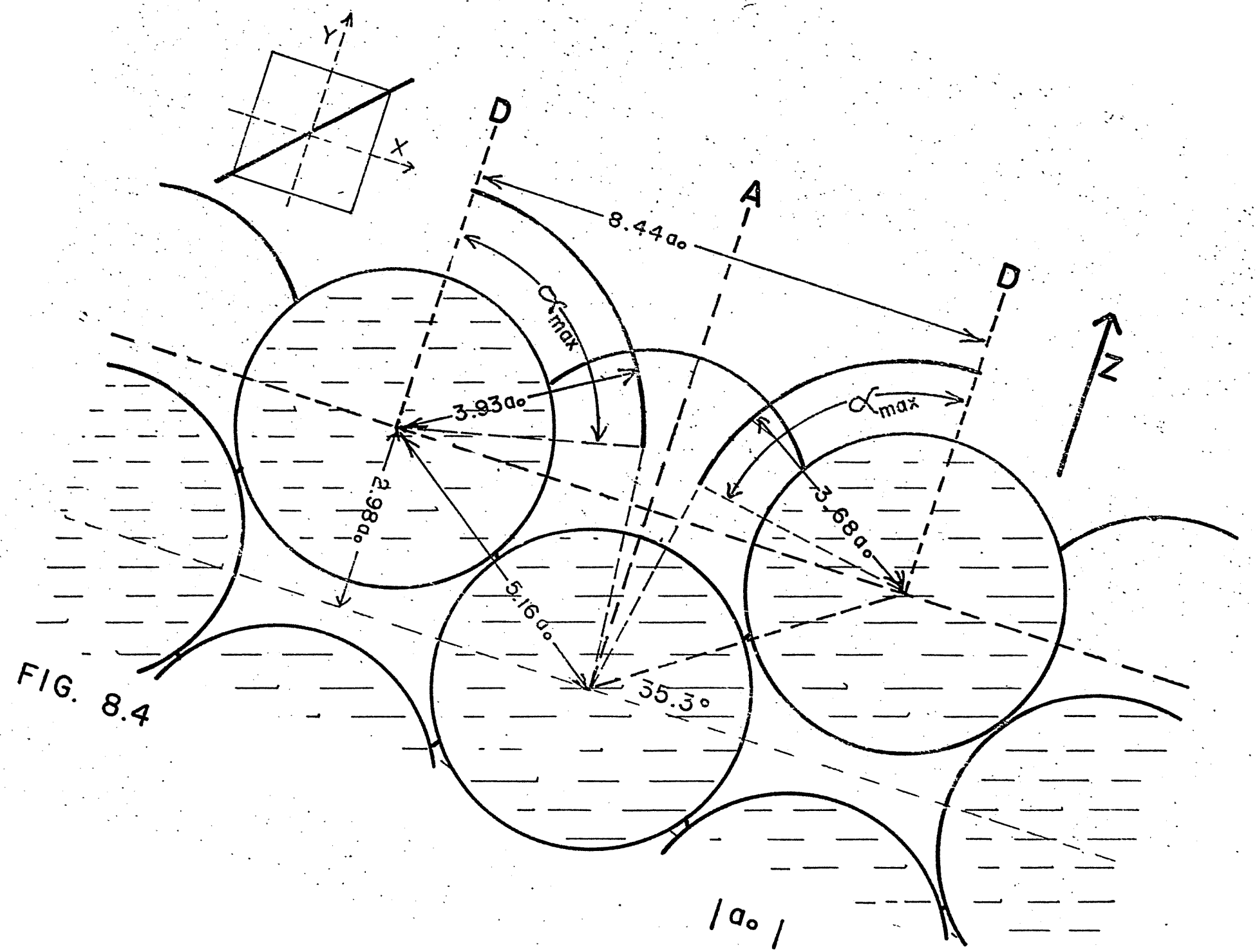

FIG. 8.4

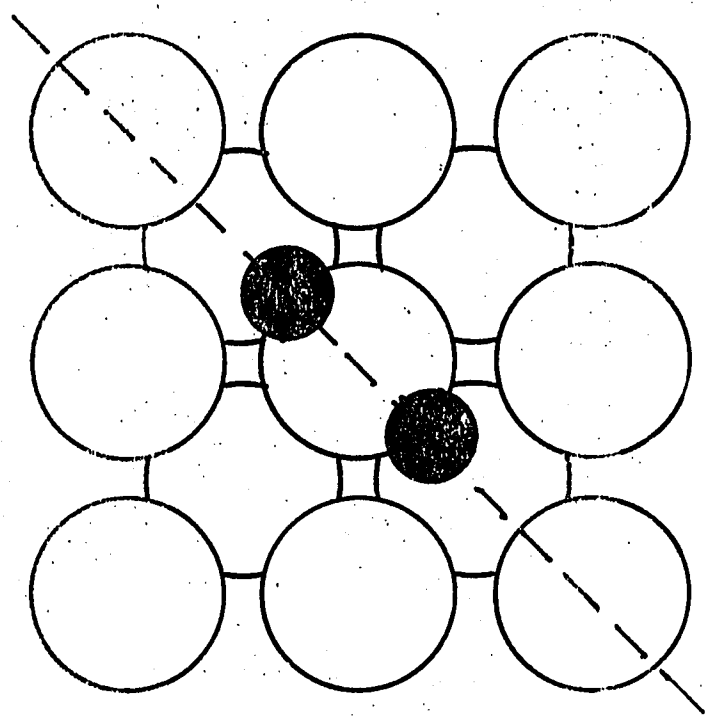

FIG. 8.5a 'Surface' Molecule

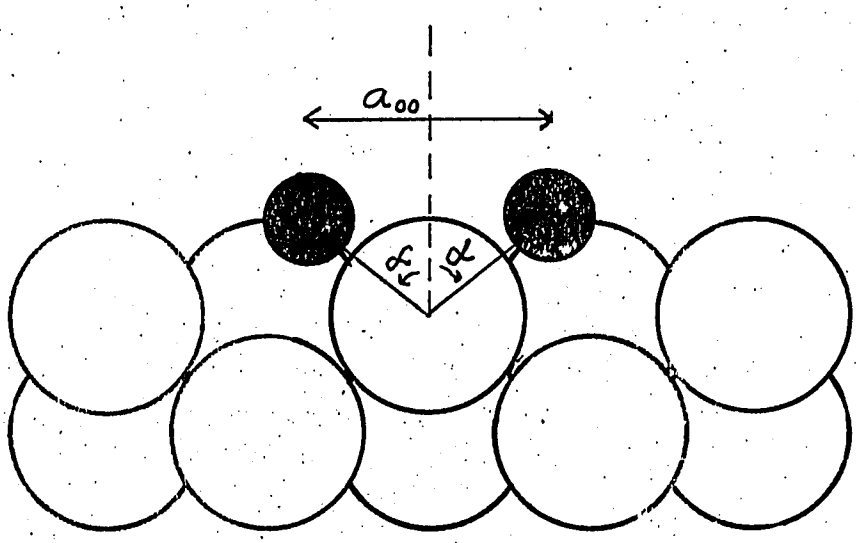

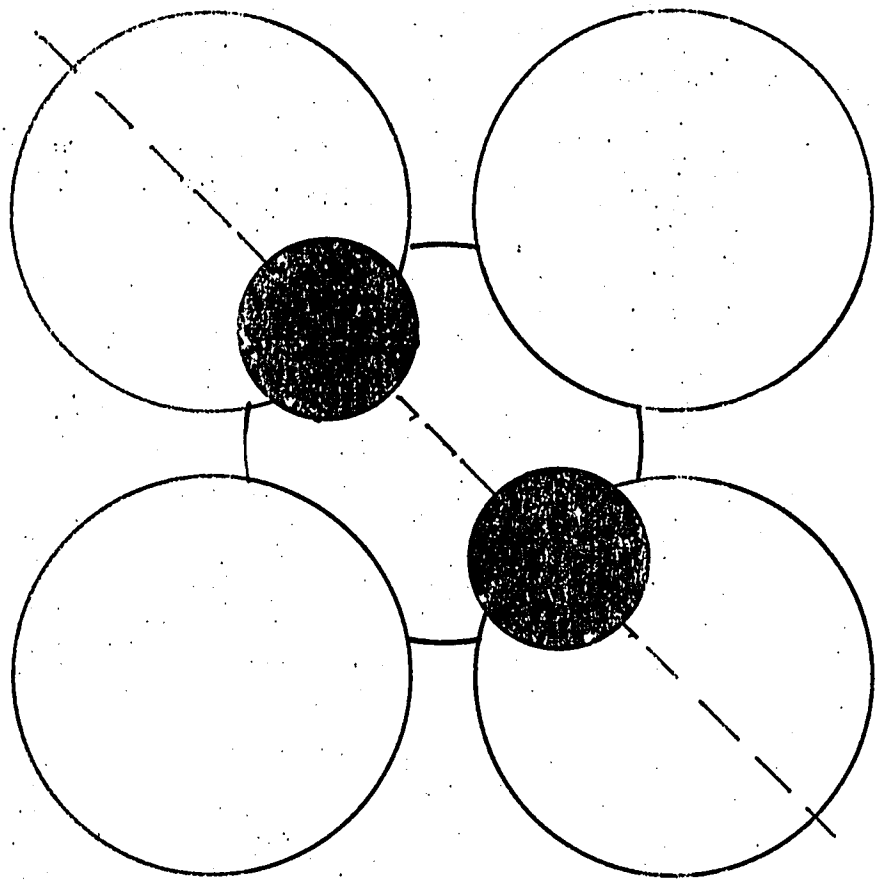

FIG. 8.5b 'Bridge' Molecule

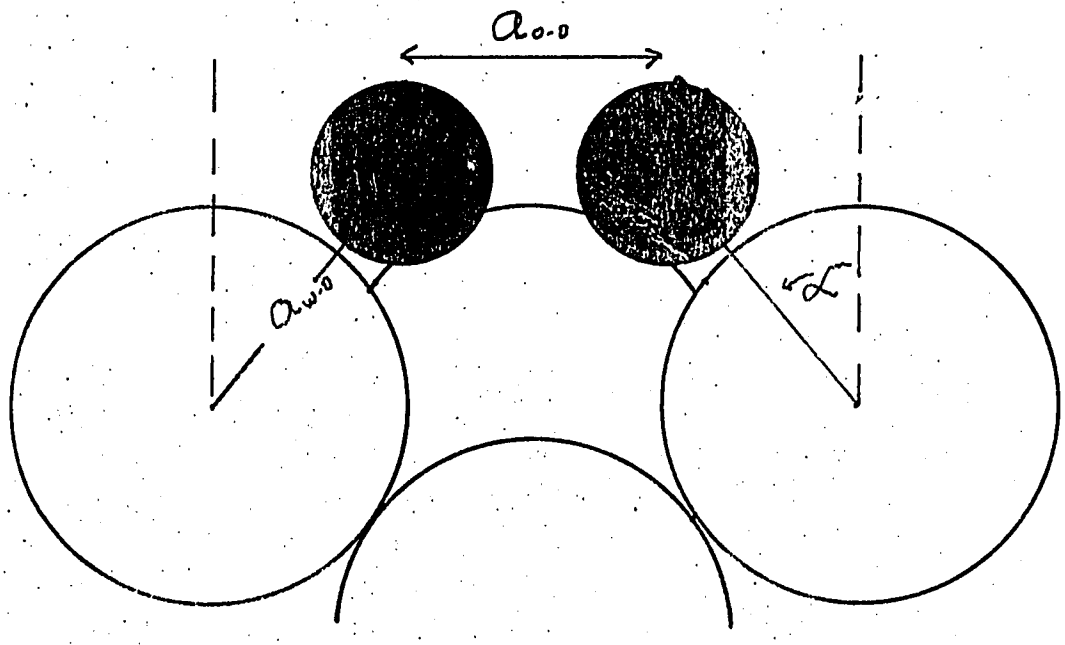

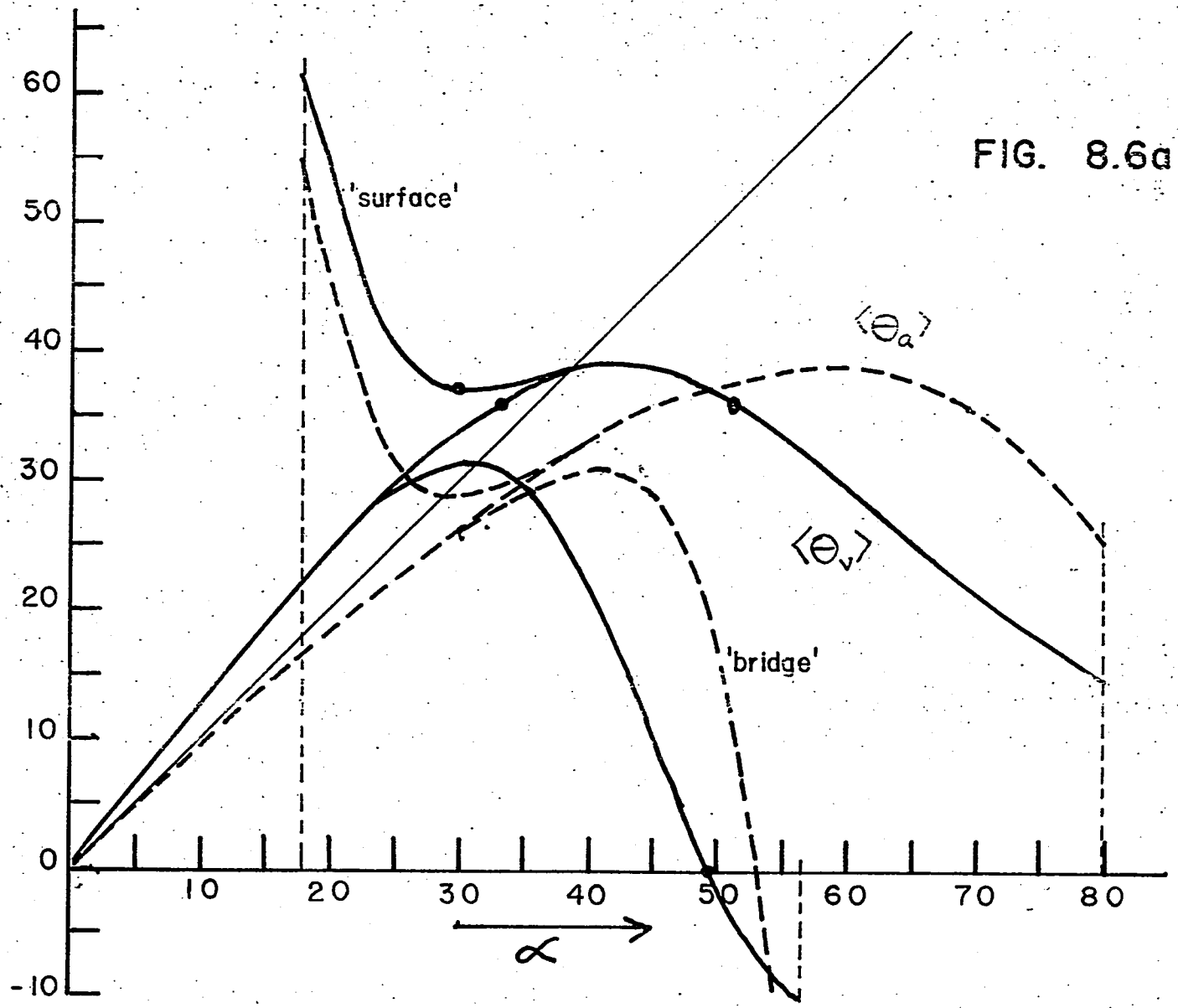

FIG. 8.6a

FIG. 8.6b

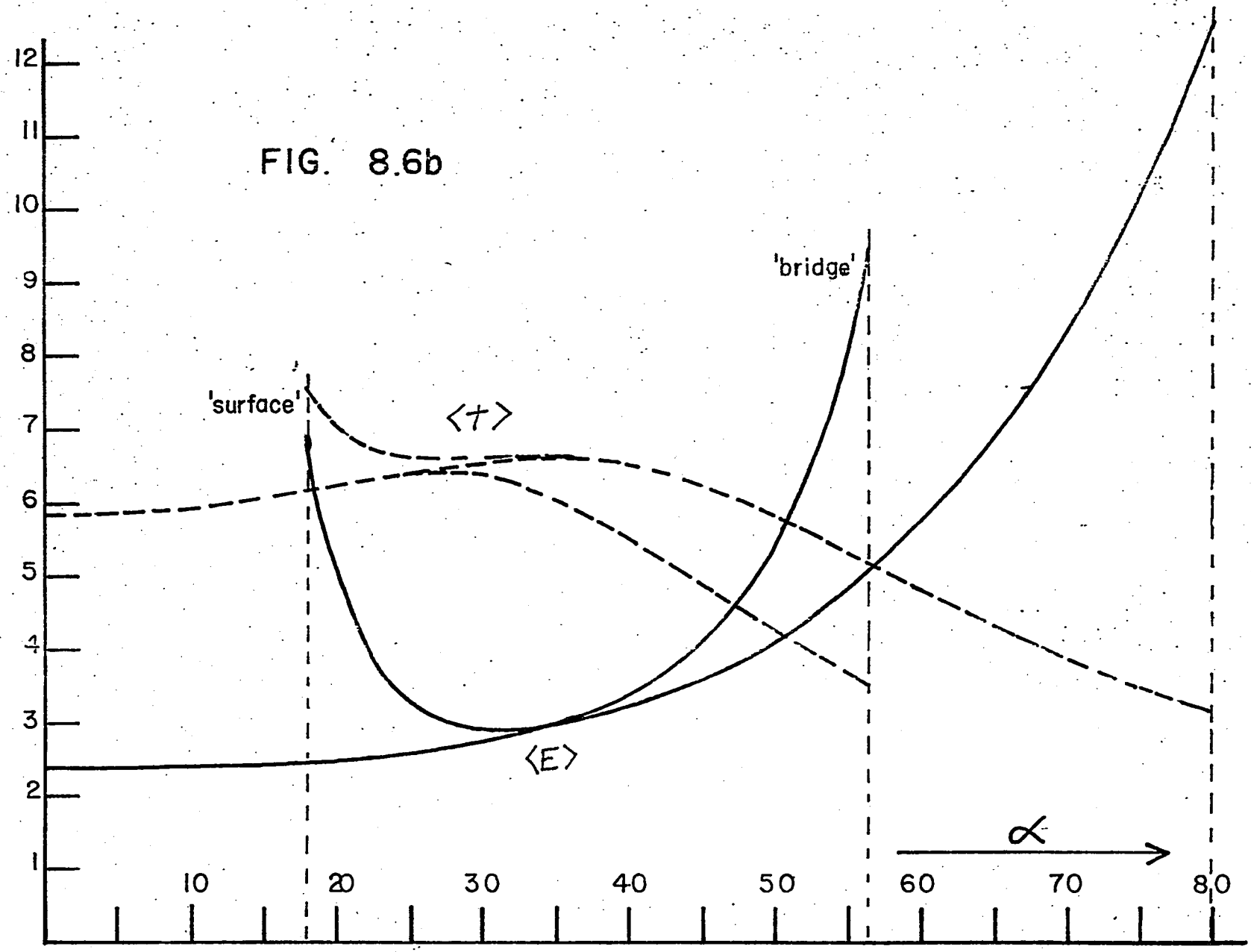

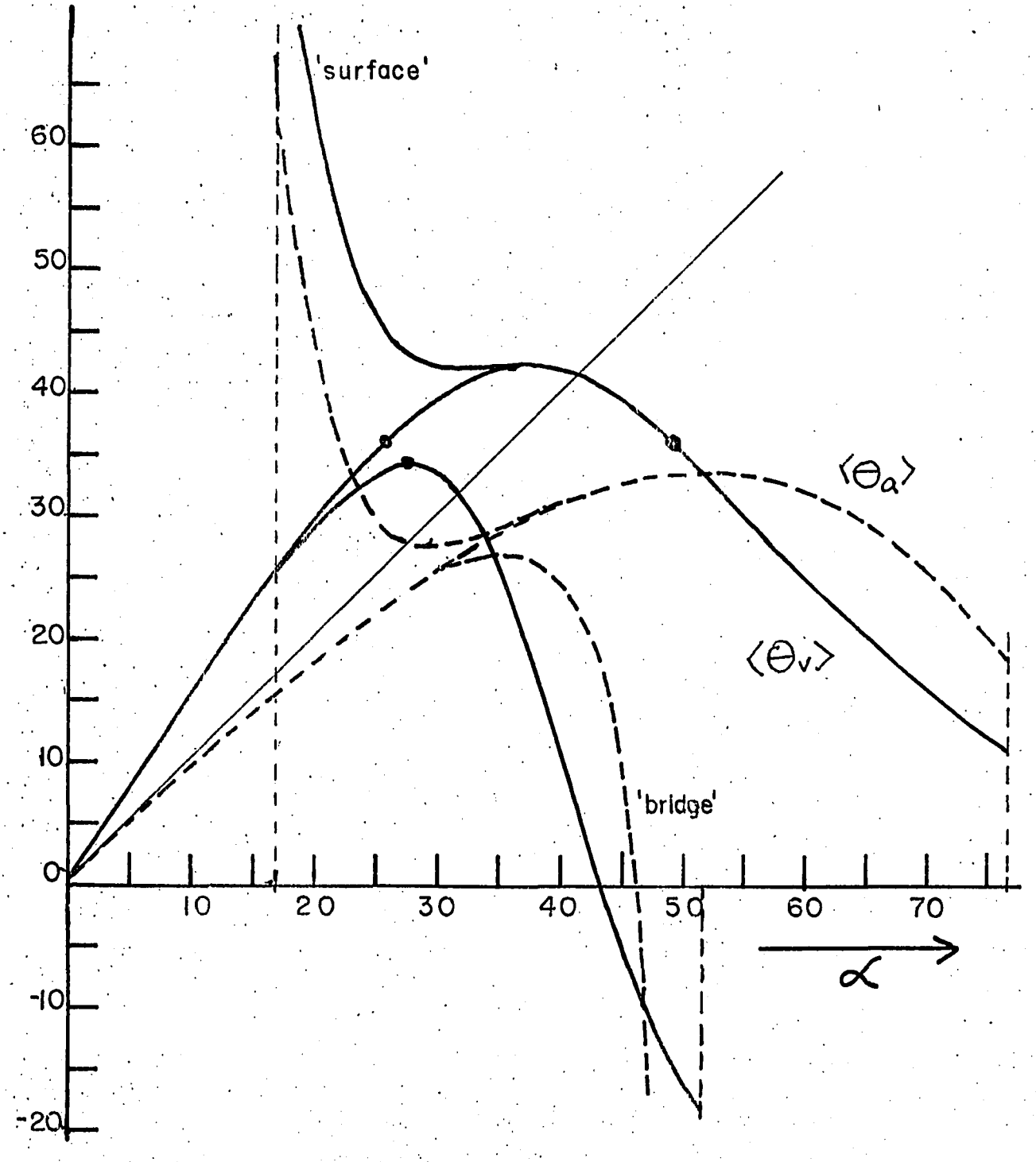

FIG. 8.7a

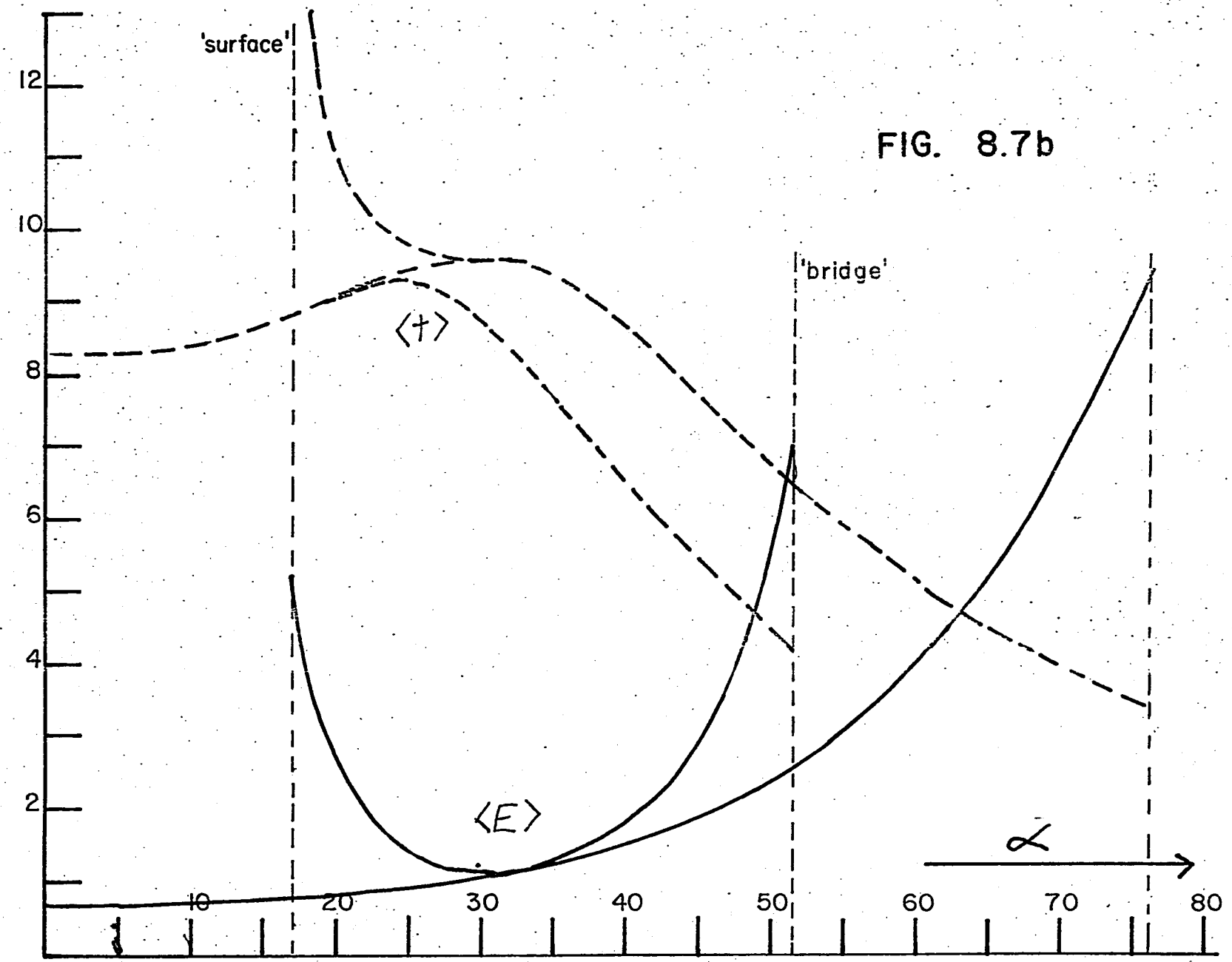

FIG. 8.7b

ESDIAD PATTERN	SITE No.	a_{w-g} (A.^{o})	$\langle\theta_e\rangle$	$\langle\theta_a\rangle$	$\langle E \rangle$ (ev.)	σ_E (ev.)	For ESDIAD Pattern see Fig.:
Central Spot	A1	2.37	$<1^{o}$	$<1^{o}$	1.47	.28	AIV.1
"	A2	2.08	$<1^{o}$	$<1^{o}$	2.48	.38	AIV.2
"	A3	1.95	$<1^{o}$	$<1^{o}$	3.05	.44	AIV.3
"	D1	1.95	$<1^{o}$	$<1^{o}$	0.70	.41	AIV.4
"	D2	2.08	$<1^{o}$	$<1^{o}$	0.24	.27	AIV.5
"	E1	1.95	$<1^{0}$	$<1^{o}$	2.35	.49	AIV.6, 8.9
"	E2	2.08	$<1^{o}$	$<1^{0}$	1.37	.39	AIV.7
"	B1	1.95	3.5^{o}	12.8^{o}	1.68	.35	AIV.8
"	C1	1.95	5.7^{o}	17.9^{o}	3.11	.43	AIV.9
45^{o} lobes	B2	1.95	35.8^{o}	37.7^{o}	1.22	.43	AIV.10, 8.9
"	B3	2.08	35.8^{o}	33.7^{o}	0.66	.32	AIV.11
"	B4	1.95	35.8^{o}	28.7^{o}	0.83	.42	AIV.12
"	B5	1.95	37.0^{o}	28.9^{o}	0.85	.42	AIV.13
"	B6	2.08	35.8^{o}	23.0^{o}	0.31	.28	AIV.14
"	B7	2.08	33.9^{o}	23.8^{o}	0.31	.28	AIV.15

FIGURE 8.8

FIGURE 8.8, continued

ESDIAD Pattern	SITE No.	a_{W-O} (A.°)	$\langle\theta_v\rangle$	$\langle\theta_a\rangle$	$\langle E \rangle$ (ev.)	σ_E (ev.)	For ESDIAD Pattern see Fig.:
90° lobes	C2	2.08	14.9°	22.9°	2.85	.44	AIV.16
"	C3	1.95	23.6°	33.9°	3.53	.49	AIV.17
"	C4	1.95	25.3°	24.2°	0.89	.43	AIV.18

ADSORPTION SITE DESCRIPTION:

Site A1: (0.0,0.0,1.49) Adsorption site over point 'A', equidistant from the four nearest tungsten atoms in the z = 0 plane, and the 'B.C.C.' tungsten atom at z = -a/2.

Site A2: (0.0,0.0,0.95) Adsorption over point 'A', with W-O separation 2.08 A.°

Site A3: (0.0,0.0,0.70) Same as site A2, W-O separation is 1.95 A.°

Site D1: (2.99,2.99,3.68) Single oxygen atom adsorbed over point 'D', 1.95 A.° from the nearest surface layer tungsten atom.

Site D2: (2.99,2.99,3.93) Same as site D1, W-O separation is 2.08 A.°

Site E1: (2.99,0.,2.16) Oxygen atom adsorbed over the saddle point 'E', equidistant at 1.95 A.° from the two adjacent tungsten atoms in the surface layer.

Site E2: (2.99;0.,2.56) Same as site E1, W- O separation is 2.08 A.°

FIGURE 8.8, ADSORPTION SITE DESCRIPTION, continued

Site B1: (.96,.96,2.32) O_2 molecule 'bridge' bonded diagonally across the unit cell, as in Fig.(8.5b). Interpolated from Fig. (8.6a). The O-O bond length 1.44 A.^{o} is close to the sum of Paulings oxygen single bond radii. Bonding to corner W atoms, with 1.95 A.^{o} separation is assumed.

Site C1: (1.41,0.,1.48) Bridge bonded O_2 molecule, with molecular axis parallel to subsrate atom rows. The O-O separation is 1.49 A.^{o}, which is twice Paulings oxygen single bond radius. Each O atom is equidistant from the nearest pair of zone corner tungsten atoms, with W- O separation 1.95 A.^{o}

Site B2: (.96,.96,2.32) Isolated oxygen atom or WO_2 'surface' molecular complex, bonded to a surface layer tungsten atom as in Fig.(8.5a). The angle $\alpha = 51^{o}$ was interpolated from Fig.(8.6a). The W-O separation is 1.95 A.^{o}, while the O - O separation for the WO_2 complex is 3.03 A.^{o} With this geometry, W-O or WO_2 are indistinguishable in the calculations.

Site B3: (.89,.89,2.58) Similar to site B2. $\alpha = 49^{o}$ as interpolated from Fig.(8.7a). W-O separation is 2.08 A.^{o} The O-O distance for a WO_2 complex is 3.14 A.^{o}

Site B4: (1.57,1.57,3.09) Isolated oxygen atom bonded at $\alpha = 33^{o}$, 1.95 A.^{o} from a surface layer tungsten atom

Site B5: (1.68.1.68,3.19) Surface WO_2 complex with half angle $\alpha = 30^{o}$. The W-O and O-O separations are both 1.95 A.^{o}

Site B6: (1.77,1.77,3.53) Single oxygen atom similar to site B4. $\alpha = 26^{o}$. W-O distace is 2.08 A.^{o}

Site B7: (1.70,1.70,3.49) O_2 molecule 'bridge' bonded diagonally across the cell, with $\alpha = 27.5^{o}$, and O-O separation 2.55 A.^{o}. The W-O bond distance is 2.08 A.^{o} The O-O repulsion is quite small at this separation.

FIGURE 8.8, ADSORPTION SITE DESCRIPTION, continued

Site C2: (0.,.59,.90) Site along the x axis equidistant from two surface layer tungsten atoms, and one at point 'A'. The z coordinate is comparable to those for sites A1 to A3, hence this site is a possible contributor to the β_2 adsorption phase.

Site C3: (1.0,0.,.84) O_2 molecule centered over point 'E', with its axis along the zone x axis, and O-O distance 2 A.^{o} Each oxygen atom is 1.95 A.^{o} from the zone corner tungsten atoms. This site is a possible contributor to the β_2 phase.

Site C4: (1.0,2.99,3.10) O_2 molecular adsorption site similar to C3, however, centered over point 'D', with molecular axis parallel to x axis of the zone.

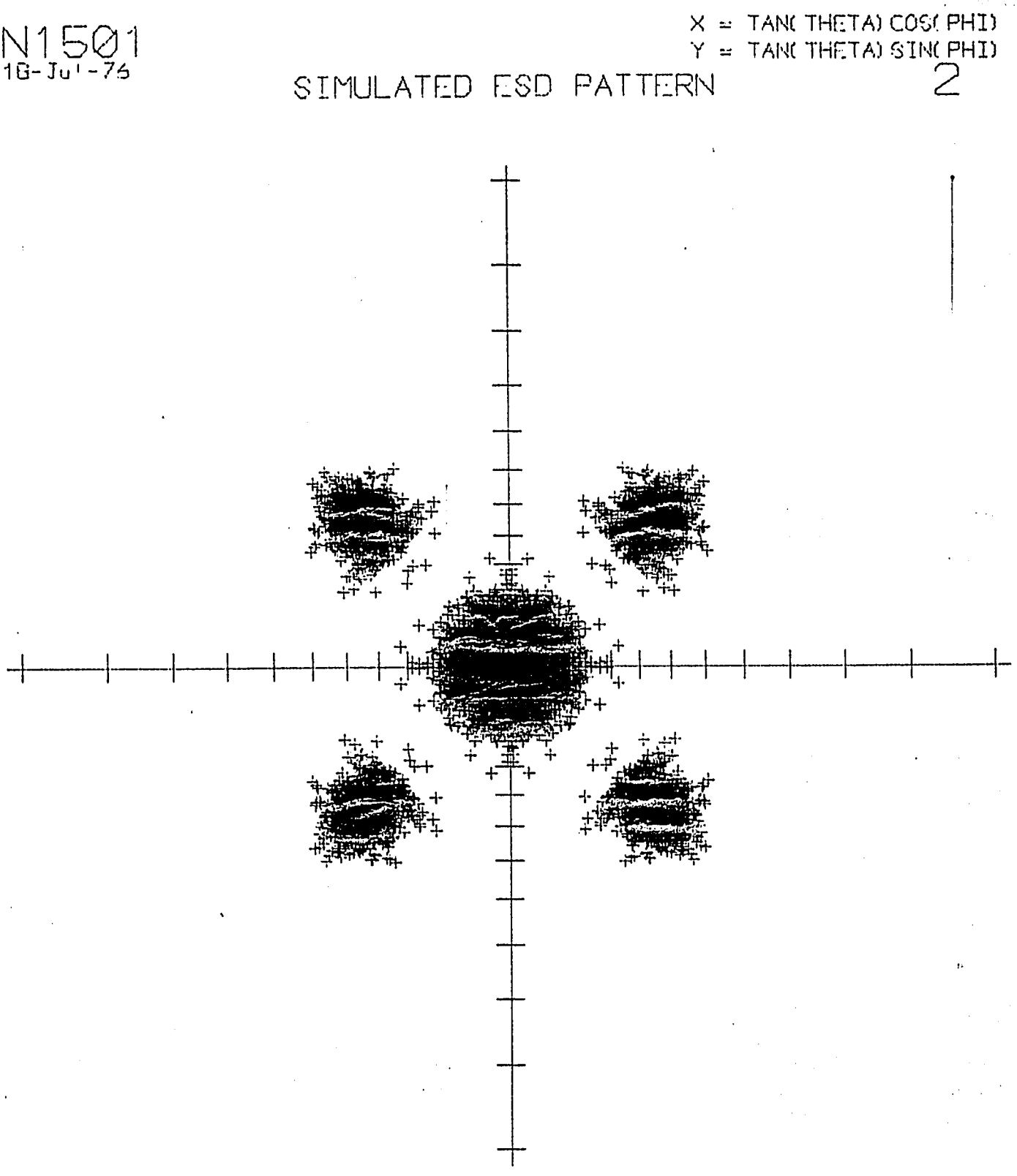
N1501
16-Jul-76
X = TAN(THETA) COS(PHI)
Y = TAN(THETA) SIN(PHI)
SIMULATED ESD PATTERN
2
SCALE FACTOR .200
5 DEGREE SCALE
8000 POINTS PLOTTED
0 POINTS OFF SCALE

FIGURE 8.9

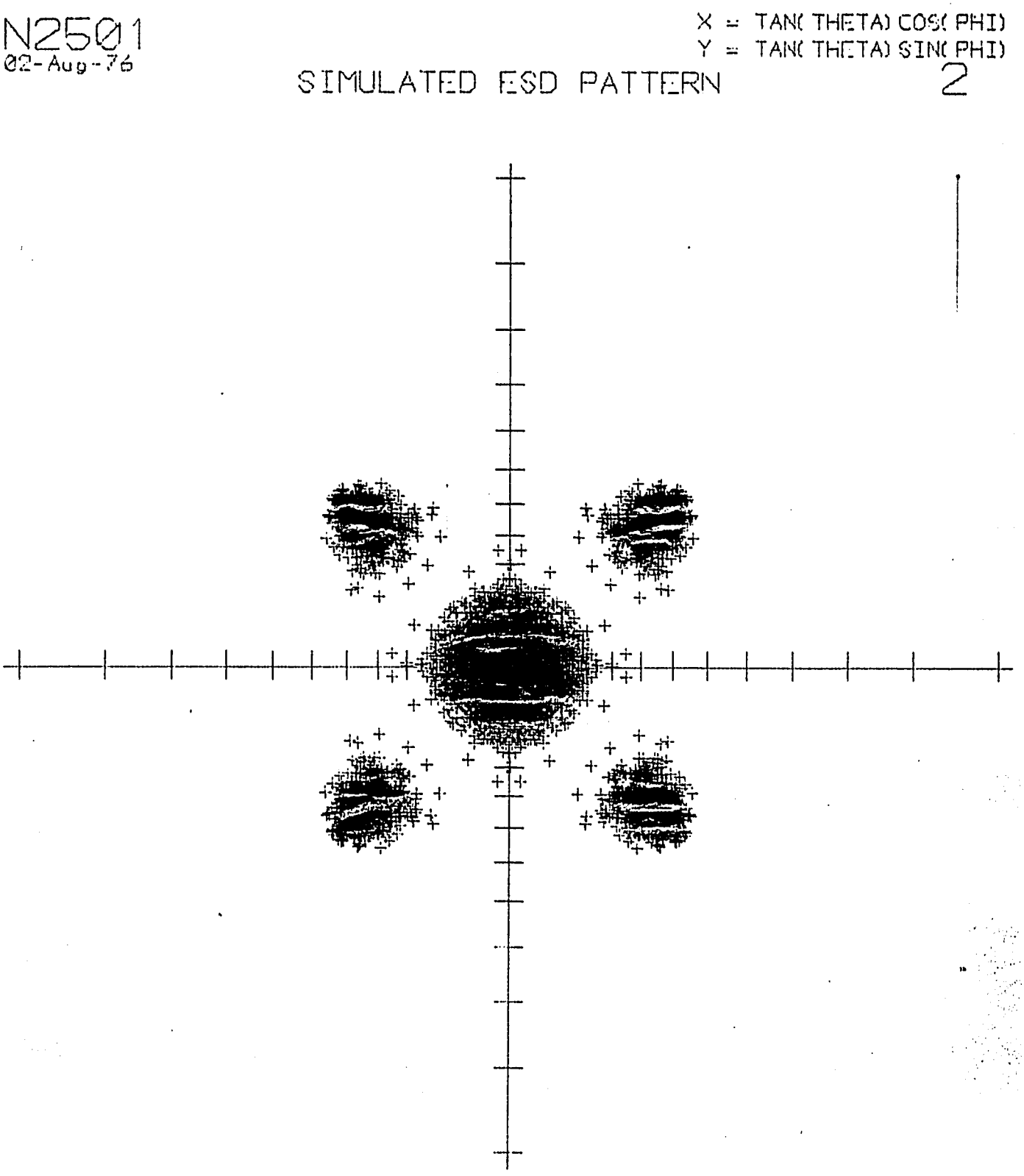
N2501
02-Aug-76
X = TAN(THETA) COS(PHI)
Y = TAN(THETA) SIN(PHI)
SIMULATED ESD PATTERN
2
SCALE FACTOR .280
5 DEGREE SCALE
8000 POINTS PLOTTED
0 POINTS OFF SCALE

FIGURE 8.10

Appendix I: The Ground State Photodesorption Cross Section - One Dimensional Solution

We now calculate the contribution to the Photodesorbed flux in the ground state. First, we solve transport equation (4.4b) for the non-thermal ground state distribution $P_1'(z,v)$. Then, we make use of Eq. (4.5), defining the cross section.

The solution method is similar to that employed in finding $P_2'(z,v)$. The speed of a particle in state 1, $u \equiv |v|$, is a function of z, where the trajectory is known. The total energy ϵ in the ground state is a constant of the motion, hence, the classical turning point z_L in the ground state trajectory satisfies

$$\begin{aligned} \epsilon &= E_1(z_L) \\ &= E_1(z) + \tfrac{1}{2} M u^2 \end{aligned} \qquad \text{(AI. 1)}$$

Taking α to be the kinetic energy of the ejected particle, we also represent ϵ as

$$\epsilon = \alpha + E_1(\infty) \qquad \text{(AI. 2)}$$

Our interest lies only in the part of P_1' which describes atoms actually able to desorb. These have $\alpha \geq 0$. They satisfy, therefore, the step function $\theta[\tfrac{1}{2}Mu^2 + E_1(z) - E_1(\infty)]$. The remainder of the flux rejoins the trapped ground state population after de-exciting, and is of no further interest. Also, we are neglecting the recoil upon non-radiative

decay. Hence, an atom which de-excites at z has the following relation between α and the thermal kinetic energy ξ :

$$\alpha = \xi + E_2(z_0) - E_2(z) + E_1(z) - E_1(\infty) \qquad \text{(AI.3)}$$

With these preliminary remarks in hand, we now proceed to solve the transport equation (4.4b). First we separate $P_1'(z, v)$ into incoming and outgoing components, viz:

$$P_1'(z,v) = \Theta(v)\, P_1^{+}(z,u) + \Theta(-v)\, P_1^{-}(z,u) \qquad \text{(AI.4)}$$

We make this substitution in Eq. (4.4b), separating P_2' similarly, as in Eq. (4.9). The set of equations satisfied for $u \neq 0$ is:

$$u \frac{\partial P_1^{\pm}}{\partial z} - \frac{1}{M} \frac{dE_1}{dz} \frac{\partial P_1^{\pm}}{\partial u} \mp Q(z)\, P_2^{\pm}(z,u) = 0 \qquad \text{(AI.5a)}$$

while at z_L, where $u=0$, the following boundary condition holds:

$$\lim_{u \to 0} P_1^{+}(z,u) = \lim_{u \to 0} P_1^{-}(z,u) \qquad \text{(AI.5b)}$$

There is a unique value of the turning point z_L for each atom which has enough energy to be ejected.

Next, we change variables to a set in which only a single integration remains. A suitable such choice is α , the desorption energy, and ϕ ,

which are defined by:

$$\phi \equiv z$$

$$\alpha \equiv \tfrac{1}{2} M u^2 + E_1(z) - E_1(\infty) \qquad \text{(AI. 6)}$$

Under this transformation:

$$P_1^{\pm}(z,u) \longrightarrow P_1^{\pm}(\phi,\alpha)$$

$$P_2^{\pm}(z,u) \longrightarrow P_2^{\pm}(\phi,\alpha)$$

The thermal energy ξ is necessarily positive, hence, we insert into $P_2^{\pm}(\phi,\alpha)$ the step function:

$$\Theta\left(\alpha + E_2(\phi) - E_1(\phi) + E_1(\infty) - E_2(z_0)\right) \qquad \text{(AI. 7)}$$

as well as the desorption requirement $\alpha > 0$, which is now written as:

$$\Theta\left(\xi + E_1(\phi) - E_2(\phi) + E_2(z_0) - E_1(\infty)\right) \qquad \text{(AI. 8)}$$

With the use of Eq. (AI. 6), the derivatives transform as follows:

$$\frac{\partial}{\partial z} \longrightarrow \frac{\partial}{\partial \phi} + \frac{dE_1}{dz}\frac{\partial}{\partial \alpha}$$

$$\frac{\partial}{\partial u} \longrightarrow Mu\frac{\partial}{\partial \alpha}$$

Only the ϕ integration survives in the resulting equation set, which is:

$$\frac{\partial}{\partial \phi} P_1^{\pm}(\phi,\alpha) = \frac{\pm Q(\phi)\, P_2^{\pm}(\phi,\alpha)}{u(\phi,\alpha)} \qquad \text{(AI. 9)}$$

The formal solution of the above may be immediately found by integrating on ϕ in the arbitrary interval $[z', z]$. The result is:

$$P_1^{\pm}(z,\alpha) = P_1^{\pm}(z',\alpha) \pm \int_{z'}^{z} \frac{d\phi\, Q(\phi) P_2^{\pm}(\phi,\alpha)}{u(\phi,\alpha)} \qquad \text{(AI. 10)}$$

The integral on the right just increments the probability of finding a particle desorbing in the ground state by its change over $[z', z]$. The expression for u is the speed at the point of de-excitation, which is the same for both states 1 and 2. Hence, u may be written in either of the alternative forms:

$$u(\phi,\alpha) = \left(\frac{2}{M}\right)^{\frac{1}{2}} [\alpha + E_1(\infty) - E_1(\phi)]^{\frac{1}{2}} \qquad \text{(AI. 11a)}$$

or

$$u(\phi,\alpha) = \left(\frac{2}{M}\right)^{\frac{1}{2}} [\xi + E_2(z_0) - E_2(\phi)]^{\frac{1}{2}} \qquad \text{(AI. 11b)}$$

The second form is convenient for use below.

We now simplify the solution for the case of low temperature: $1/\beta$ is small compared to typical potential energy differences. Following arguments presented previously (in Chapter IV) in the discussion of σ_2, only the dominant ξ dependence will be retained. We take $\xi \simeq 0$ judiciously in expression (AI. 10). First we approximate:

$$u(\phi,\alpha) = \left(\frac{2}{M}\right)^{\frac{1}{2}} \left[\frac{1}{\beta} + E_2(z_0) - E_2(\phi)\right]^{\frac{1}{2}} \qquad \text{(AI. 11c)}$$

Next, referring to Eq. (4.23) for the excited state solution, we observe that as $\xi \to 0$, the lower bound $z_{min} \longrightarrow z_o$. The source of incoming particles into the ground state at $\phi < z_o$ is cut off. The survival probability $S_2(z_o, \phi, \beta)$ was defined by:

$$S_2(z_0,\phi,\beta) = e^{-\left(\frac{M}{2}\right)^{\frac{1}{2}}\int_{z_0}^{\phi} \frac{d\phi' \, Q(\phi')}{[\beta + E_2(z_0) - E_2(\phi)]^{\frac{1}{2}}}} \tag{AI.12}$$

Note in Eq. (4.23) that $S_2(z_{min}, z_o) \longrightarrow 1$. Hence, we have:

$$P_2^+(\xi,\phi) = 2\,\theta(\phi - z_0)\,\theta(v)\,g(z_0)\left(\frac{M}{2\xi}\right)^{\frac{1}{2}} \times e^{-\beta\xi} S_2(z_0,\phi,\beta) \tag{AI.13}$$

There is no incoming particle flux in the excited state, therefore:

$$P_2^-(\phi,\alpha) = 0 \tag{AI.14a}$$

Next, we write P_2^+ in terms of the variable set ϕ, α. Equation (AI.3) is inverted to write ξ as a function of α, ϕ, namely:

$$\xi(\alpha,\phi) = \alpha + E_2(\phi) - E_1(\phi) + E_1(\infty) - E_2(z_0) \tag{AI.15}$$

The step function (AI.7) is inserted, which simply ensures that $\xi \geq 0$. We also insert the step function (AI.8), requiring the desorption kinetic energy α to be positive, after taking $\xi \approx 0$. This shifts the threshold only slightly. Hence, for the excited state:

$$P_2^+(\phi,\alpha) = 2\,\theta(\phi - z_0)\,\theta(v)\,\theta(E_1(\phi) - E_2(\phi) + E_2(z_0) - E_1(\infty)) \times g(z_0)\left(\frac{M}{2}\right)^{\frac{1}{2}} \frac{e^{-\beta[\xi(\phi,\alpha)]}}{[\xi(\phi,\alpha)]^{\frac{1}{2}}} S_2(z_0,\phi,\beta) \tag{AI.14b}$$

We first apply P_2^+, P_2^- to determine the incoming ground state distribution P_1^-. The integral on the right in our formal solution Eq. (AI.10) vanishes, since $P_2^- \simeq 0$. Hence, P_1^- is a constant for all z. There is no external source of ground state atoms bombarding the surface, thus the solution for negative velocities is:

$$P_1^-(z,\alpha) = 0 \qquad \text{all z, all } \alpha \geq 0$$

Next, we determine $P_1^+(z,\alpha)$. The boundary condition at the classical turning point z_L, specified in Eq. (AI.5b) and (AI.2), yields the following information:

$$P_1^+(z_L,\alpha) = P_1^-(z_L,\alpha) = 0$$

The solution has the form:

$$P_1^+(z,\alpha) = \int_{z_L}^{z} \frac{d\phi\, Q(\phi)\, P_2^+(\phi,\alpha)}{a(\phi,\alpha)}$$

The lower limit on this integration may be changed to z_o, inasmuch as P_2^+ vanishes for $\phi < z_o$. Note that $z_L \leq z_o$. The result above vanishes if $z < z_o$.

We now collect the results to write the distribution function describing ground state photodesorption:

$$P_1'(z,\alpha) = 2\Theta(z-z_0)\,\Theta(v)\,g(z_0)\int_{z_0}^{z} d\phi\,\frac{Q(\phi)\,S_2(z_0,\phi,\beta)}{u(\phi,1/\beta)} \times$$

$$\times \frac{e^{-\beta[\xi(\phi,\alpha)]}}{\left(\frac{2\xi(\phi,\alpha)}{M}\right)^{1/2}}\,\Theta[E_1(\phi)-E_2(\phi)+E_2(z_0)-E_1(\infty)]\,\Theta(\xi) \qquad \text{(AI.16)}$$

where

$$u(\phi,1/\beta) = \left(\frac{2}{M}\right)^{1/2}\left[\frac{1}{\beta}+E_2(z_0)-E_2(\phi)\right]^{1/2}$$

Now we find cross section for photodesorption in the ground state. As in the excited state case, we find that $P_1'(z, v)$ is approximately independent of z far from the surface, due to the rapid decay of Q(z). The detection plane lies at $z = L$, with the cross section given, as in Eq. (4.5) by the following prescription:

$$\sigma_1 = \frac{1}{F}\int_0^{\infty} dv\, v\, P_1'(z=L,v)$$

Clearly, it is appropriate to make the identification $\alpha = \frac{1}{2}M v_z^2$ which suggests the convenient variable change $v\,dv \rightarrow d\alpha/M$. Hence:

$$\sigma_1 = \frac{1}{MF}\int_0^{\infty} d\alpha\, P_1'(z=L,\alpha)$$

It is legitimate to interchange the α integration with the one on ϕ

contained in P_1' ($z = L$, α). Using Eq. (AI.16) for P_1', the following results:

$$\sigma_1 = 2\frac{g(z_0)}{F}\int_{z_0}^{\infty} d\phi \frac{Q(\phi) S_2(z_0, \phi, 1/\beta) J(\phi) \times}{\ell(\phi, 1/\beta)} \qquad \text{(AI. 17)}$$

$$\times \Theta[E_1(\phi) - E_2(\phi) + E_2(z_0) - E_1(\infty)]$$

Here the integral $J(\phi)$ contains all of the α dependence and is given by:

$$J(\phi) \equiv \left(\frac{M}{2}\right)^{\frac{1}{2}} \int_0^{\infty} \frac{d\alpha\, \Theta[\xi(\phi,\alpha)]\, e^{-\beta(\xi(\phi,\alpha))}}{[\xi(\phi,\alpha)]^{1/2}}$$

The integration above is performed easily after making the transformation defined by Eq. (AI.3) to convert the α integration to one on ξ, which is:

$$J(\phi) = \left(\frac{M}{2}\right)^{\frac{1}{2}} \int_{[E_2(\phi) - E_1(\phi) + E_1(\infty) - E_2(z_0)]}^{\infty} d\xi \frac{\Theta(\xi)\, e^{-\beta\xi}}{\xi^{1/2}}$$

The lower limit is guaranteed to be negative by the step function in Eq. (AI.17). The step cutoff on ξ therefore predominates. The well known integral which results is proportional to $\Gamma(\frac{1}{2})$:

$$J(\phi) = \left[\frac{\pi}{2}\frac{M}{\beta}\right]^{\frac{1}{2}}$$

The final expression for σ_1 is now written, after collecting results above. The definitions of $g(z_0)$ in Eq. (4.8) and the photon flux are substituted along with $J(\phi)$ into Eq. (AI.17). It is convenient to express the result in

terms of the excitation cross section $\sigma_{EX}(\beta, z_0)$ defined by:

$$\sigma_{EX}(\beta, z_0) = \frac{8\pi^2\omega}{c} \frac{e^{-\beta E_1(z_0)}}{\int_{-\infty}^{+\infty} dz' e^{-\beta E_1(z')}} \frac{|\langle 2|\mu_x|1\rangle|^2_{z_0}}{\left|\frac{d(E_2-E_1)}{dz}\right|_{z_0}} \quad (4.26a)$$

The ground state photodesorption cross section is:

$$\sigma_1(z_0,\beta) = \sigma_{EX}(z_0,\beta) \int_{z_0}^{\infty} \frac{dz\, Q(z)\, S_2(z_0,z,\beta) \times}{\left(\frac{2}{M}\right)^{\frac{1}{2}}\left[\frac{1}{\beta}+E_2(z_0)-E_2(\phi)\right]^{\frac{1}{2}}} \quad (4.27),\ (AI.18)$$

$$\times\, \Theta(E_1(\phi)-E_2(\phi)+E_2(z_0)-E_1(\infty))$$

The survival probability in the above is evaluated from the function:

$$S_2(z_0,z,\beta) = e^{-\left(\frac{M}{2}\right)^{\frac{1}{2}} \int_{z_0}^{z} \frac{dz' Q(z')}{\left[\frac{1}{\beta}+E_2(z_0)-E_2(z)\right]^{\frac{1}{2}}}} \quad (AI.19)$$

These results are discussed in the main text.

Appendix II: Cross Sections for Angle Resolved Desorption Studies

In this Appendix we present a derivation of Equations (6.7a, b) for the total desorption cross sections in three dimensions. The treatment below complements the heuristic derivation given in the text of Chapter VI.

We choose the transport equations (2.13a, b) as the starting point. These are not linearized, but possess the virtue of being symmetrical in the interchange of roles for quenching and excitation rates. Our strategy is as follows: we find the formal solutions of the non-linear transport problem, using Liouvilles Theorem. The classical trajectories in both the excited and the ground state are assumed to be known. The formal solutions generated for $P_n(t)$ are mappings which follow the occupants of an initial phase space region forward in time. A perturbation expansion is generated, and linearized in the excitation rate R. Depletion of the equilibrium ground state distribution is neglected. The resulting linearized single particle evolution functions are used to construct the cross sections.

First we make the following replacement in Equations (2.13a, b) using Liouvilles Theorem:

$$\frac{\partial}{\partial t} + \vec{V} \circ \vec{\nabla}_r + \vec{a} \circ \vec{\nabla}_v \rightarrow \frac{d}{dt}$$

All quantities in the transport equations depend parametrically on time via the particle trajectories. Hence, the new form of the transport equations is:

$$\frac{dP_2(t)}{dt} = R(t) P_1(t) - Q(t) P_2(t) \qquad \text{(AII. 1a)}$$

$$\frac{dP_1(t)}{dt} = Q(t) P_2(t) - R(t) P_1(t) \qquad \text{(AII. 1b)}$$

Next, we introduce the survival probabilities $S_2(t_o, t)$, whose significance was discussed in the main text (see Chapter VI):

$$S_2(t_0,t) \equiv e^{-\int_{t_0}^{t} dt' Q(t')} \tag{AII. 2a}$$

$$S_1(t_0,t) \equiv e^{-\int_{t_0}^{t} dt' R(t')} \tag{AII. 2b}$$

The path integrations implicit in S_n are governed by E_n. We note that

$$S_n(t_0,t) = S_n^{-1}(t,t_0)$$

$$S_n(t_0,t_1)\, S_n(t_1,t) = S_n(t_0,t)$$

The quantities $S_n(t_o, t)$ are interpreted as mappings which follow the evolution of a single atom or molecule from t_o to time t, in state n.

The following trial solutions of Eqs. (AII. 1a, b) are adopted:

$$P_2(t) \equiv g(t) S_2(t_0,t) \tag{AII. 3a}$$

$$P_1(t) \equiv h(t) S_1(t_0,t) \tag{AII. 3b}$$

These trial solutions are now formally differentiated and the result compared with Eqs. (AII. 1a, b). The following differential equations for the unknown functions h, g are the result:

$$\frac{dg(t')}{dt'} = R(t')\,P_1(t')\,S_2^{-1}(t_0,t') \tag{AII. 4a}$$

$$\frac{dh(t')}{dt'} = Q(t')\,P_2(t')\,S_1^{-1}(t_0,t') \tag{AII. 4b}$$

One integrates formally over the range $t_0 \leq t' \leq t$, and combines the result with Eqs. (AII. 3a, b), defining the trial solutions. Hence:

$$P_2(t) = g(t_0)S_2(t_0,t) + \int_{t_0}^{t} dt' P_1(t') R(t') S_2(t',t) \tag{AII. 5a}$$

$$P_1(t) = h(t_0)S_1(t_0,t) + \int_{t_0}^{t} dt' P_2(t') Q(t') S_1(t',t) \tag{AII. 5b}$$

We assume that all of the functions in the above are mathematically well behaved. The integration constants $g(t_0)$ and $h(t_0)$ may be identified by letting $t \to t_0$. In this limit,

$$\lim_{t \to t_0} S_n(t_0,t) = 1$$

while the integrations on the right in Eq. (AII. 5a, b) must vanish. Thus:

$$g(t_0) = P_2(t_0) \tag{AII. 6a}$$

$$h(t_0) = P_1(t_0) \tag{AII. 6b}$$

Here $P_n(t_o)$ represents the supposedly known initial distribution functions of the system.

Now we uncouple Equations (AII. 5a, b) simply, by substituting one member of this pair into the other. The following integral equations for P_n then follow:

$$P_2(t) = P_2(t_o)S_2(t_o,t) + P_1(t_o)\int_{t_o}^{t} dt' S_1(t_o,t')R(t')S_2(t',t) + \int_{t_o}^{t} dt' \int_{t_o}^{t'} dt'' P_2(t'')Q(t'')S_1(t'',t')R(t')S_2(t',t) \quad \text{(AII. 7a)}$$

$$P_1(t) = P_1(t_o)S_1(t_o,t) + P_2(t_o)\int_{t_o}^{t} dt' S_2(t_o,t')Q(t')S_1(t',t) + \int_{t_o}^{t} dt' \int_{t_o}^{t'} dt'' P_1(t'')R(t'')S_2(t'',t')Q(t') \times S_1(t',t) \quad \text{(AII. 7b)}$$

Fortunately, the exact solutions of the above are not of interest. They provide a realistic description of the desorption problem only when the ground state vibrational levels are well approximated by the classical approximation. Moreover, in the intermediate coupling regime discussed in Chapter II, a relaxation mechanism involving interaction with the surface should be included in the transport equations. We make use of Equations (AII. 7a, b) to generate a set of perturbation series in R, which we then linearize. After iterating in the above equations once, we display only a few leading terms:

$$P_2(t) = P_2(t_0) S_2(t_0,t) + P_1(t_0)\int_{t_0}^{t} dt' S_1(t_0,t') R(t') S_2(t',t) \tag{AII. 8a}$$

$$P_1(t) = P_1(t_0) S_1(t_0,t) + P_2(t_0)\int_{t_0}^{t} dt' S_2(t_0,t') Q(t') S_1(t',t)$$
$$+ P_1(t_0)\int_{t_0}^{t} dt' \int_{t_0}^{t'} dt'' S_1(t_0,t'') R(t'') S_2(t'',t') \times$$
$$\times Q(t') S_1(t',t) \tag{AII. 8b}$$

In writing the above, we neglected terms proportional to R^2 and higher powers. Also, the combination P_2R^1 is intrinsically higher order, so terms in which it appeared were dropped. Each remaining contribution may be interpreted by reading the time ordered propagators and interactions from left to right. We now also neglect depletion of the ground state. The survival probability S_1 against excitation is approximated by:

$$S_1(t_1,t_2) \simeq 1 \qquad \text{All } t_1, t_2$$

The distributions are now written:

$$P_2(t) = P_2(t_0) S_2(t_0,t) + P_1(t_0)\int_{t_0}^{t} dt' R(t') S_2(t',t) \tag{AII. 9a}$$

$$P_1(t) = P_1(t_0) + P_2(t_0)\int_{t_0}^{t} dt' S_2(t_0,t') Q(t')$$
$$+ P_1(t_0)\int_{t_0}^{t} dt' \int_{t_0}^{t'} dt'' R(t'') S_2(t'',t') Q(t') \tag{AII. 9b}$$

The quantities $P_n(t)$ are the evolved images in either state of the arbitrary initial density distributions $P_n(t_o)$. The implied freedom is utilized to construct two sets of mappings, each of which describes the evolution of a single particle started in the m th state at t_o to the n th state at time t.

First a unit source in the ground state at t_o is constructed. We choose $P_2(t_o) = 0$ in Eq. (AII. 9a, b). The conditional probability of finding the atom in the n th state at t is:

$$U_n(t_o, t) \equiv \frac{P_n(t)}{P_1(t_o)} \tag{AII. 10}$$

Here t_o implies a specific choice of $\vec{r}_o$, $\vec{v}_o$: hence, there is a set of such U_n for each initial phase space point. The explicit linearized forms for the U_n are:

$$U_2(t_o, t) = \int_{t_o}^{t} dt' R(t') S_2(t', t) \tag{AII. 11a}$$

$$U_1(t_o, t) = 1 + \int_{t_o}^{t} dt' Q(t') U_2(t_o, t') \tag{AII. 11b}$$

The '1' in Eq. (AII. 11b) indicates that a trajectory in the ground state is merely followed from $\vec{r}_o$, $\vec{v}_o$ to $\vec{r}(t)$, $\vec{v}(t)$, without interaction. The second term in Eq. (AII. 11b) is a higher order correction, which will be dropped at a later point.

Making the complementary choice, $P_1(t_o) = 0$, in Eq. (AII. 9a, b), we map the response to a unit source at t_o in the excited state. We define:

$$V_n(t_o, t) \equiv \frac{P_n(t)}{P_2(t_o)} \tag{AII. 12}$$

for which the explicit forms are:

$$V_2(t_0,t) = S_2(t_0,t) \tag{AII. 13a}$$

$$V_1(t_0,t) = \int_{t_0}^{t} dt' S_2(t_0,t') Q(t') \tag{AII. 13b}$$

Finally, let us map the system forward from a time $t = 0$ when it was in equilibrium, to the time t_0 when its state is examined, and mapping of the evolution begins. We let $t_0 \rightarrow 0$; $t \rightarrow t_0$ in Eq. (AII. 9a, b). The choice $P_1(t = 0) = P_1^0$; $P_2(t = 0) = 0$ conforms to the normalization assumed earlier for equilibrium. Making these changes:

$$P_2(t_0) = P_1^0 \int_0^{t_0} dt' R(t') S_2(t';t_0) \tag{AII. 14a}$$

$$P_1(t_0) = P_1^0 + P_1^0 \int_0^{t_0} dt' \int_0^{t'} dt'' R(t'') S_2(t;t'') Q(t') \tag{AII. 14b}$$

The first term in Eq. (AII. 14b) cannot contribute to desorption, by assumption. The second term is small in the weak coupling limit; however, it can include ground state desorption.

Desorption Cross Sections

We now construct the formal expressions for the total desorption cross sections given in the text in Eq. (6.7a, b). We imagine the state of the system to be known and given by $P_n(t_0)$ at an arbitrary initial time t_0. The response of the system to external excitation during a small finite time interval $[t_0, t_1]$

is traced. Then the evolution subsequent to t_1 is mapped for particles on desorbing trajectories. At the end of the calculation, we let $t_1 \rightarrow t_o$, obtaining finite limits.

First we trace the response of a single atom or ion whose coordinates are $\vec{r}_o = \vec{r}(t_o)$, $\vec{v}_o = \vec{v}(t_o)$. No particle can desorb unless it is excited at least once to state 2. We require R to act exactly once on an adsorbed particle during $[t_o, t_1]$ for us to count its history as part of the linear response during that interval. Terms containing additional excitations before t_o or subsequent to t_1 are non-linear, and we neglect them. Hence, it is sufficient to map only particles found in the ground state at t_o, as those in state 2 at t_o contribute to response during a previous interval.

The change in the occupation of state n over $[t_o, t_1]$ is given by:

$$\Delta \mathcal{U}_n(t_o, t_1) = \mathcal{U}_n(t_o, t_1) - \mathcal{U}_n(t_o, t_o) \qquad \text{(AII. 15)}$$

We note that $U_1(t_o, t_o) = 1$, and $U_2(t_o, t_o) = 0$. Hence:

$$\Delta \mathcal{U}_2(t_o, t_1) = \mathcal{U}_2(t_o, t_1) \qquad \text{(AII. 16a)}$$

$$\Delta \mathcal{U}_1(t_o, t_1) = \mathcal{U}_1(t_o, t_1) - 1 \qquad \text{(AII. 16b)}$$

The average transition rate per particle to the n th state over $[t_o, t_1]$ is identified as

$$\dot{\bar{n}}_n(t_o, t_1) \equiv \frac{\Delta \mathcal{U}_n(t_o, t_1)}{(t_1 - t_o)} \qquad \text{(AII. 17)}$$

while the average cross section for excitation the state n is analagously defined:

$$\bar{\chi}_n(t_0,t_1) \equiv \frac{\Delta U_n(t_0,t_1)}{F(t_1-t_0)} \qquad \text{(AII. 18)}$$

Here, F is the external electron or photon flux. In the case of $n=1$, these quantities involve both excitation and quenching during $[t_0, t_1]$. When the limit $t_1 \to t_0 + \epsilon$ is taken, $\bar{\chi}_2$ becomes identical to the excitation cross section at a given phase space point. The explicit forms for $\bar{\chi}_n$ are displayed, after referring to Eq. (AII. 11a, b):

$$\bar{\chi}_2(t_0,t_1) = \frac{1}{F(t_1-t_0)} \int_{t_0}^{t_1} dt' R(t') S_2(t';t_1) \qquad \text{(AII. 19a)}$$

$$\bar{\chi}_1(t_0,t_1) = \frac{1}{t_1-t_0} \int_{t_0}^{t_1} dt' (t'-t_0) Q(t') \bar{\chi}_2(t_0,t') \qquad \text{(AII. 19b)}$$

Subsequent to t_1, the evolution of a particle proceeds as follows. $\Delta U_1(t_0,t_1)$ occupies the ground state at t_1, hence, it maps to the detection plane via:

$$\Delta U_1(t_0,t_1) \longrightarrow \Delta U_1(t_0,t_1)[U_1(t_1,t) + U_2(t_1,t)]$$

while $\Delta U_2(t_0,t_1)$, the state 2 occupation probability at t_1, evolves as follows:

$$\Delta U_2(t_0,t_1) \longrightarrow \Delta U_2(t_0,t_1)[V_1(t_1,t) + V_2(t_1,t)]$$

Collecting the contributions to each state at time t, we define a new set of

mappings $\Pi_n(t_0,t_1,t)$ which assign to a single particle in the ground state at t_o the probability of finding it in the n th state at t anywhere in phase space:

$$\Pi_2(t_0,t_1,t) = [U_1(t_0,t_1)-1]U_2(t_1,t) + U_2(t_0,t_1)V_2(t_1,t) \tag{AII. 20a}$$

$$\Pi_1(t_0,t_1,t) = [U_1(t_0,t_1)-1]U_1(t_1,t) + U_2(t_0,t_1)V_1(t_1,t) \tag{AII. 20b}$$

Here we used Eq. (AII. 16a, b). It is evident after referring to Eqs. (AII. 11a, b) that the first term in Π_2 is of order R^2, hence we neglect it. The first term in Π_1 must be linearized by approximating $U_1(t_1, t) \approx 1$. The remaining terms are linear in R, as required.

We use Eq. (AII. 11a, b) and (AII. 12a, b) to write the explicit forms for Π_n :

$$\Pi_2(t_0,t_1,t) = \int_{t_0}^{t_1} dt' R(t') S_2(t',t) \tag{AII. 21a}$$

$$\Pi_1(t_0,t_1,t) = \int_{t_0}^{t_1} dt' \int_{t_0}^{t'} dt'' R(t'') S_2(t'',t') Q(t') + \left[\int_{t_0}^{t_1} dt' R(t') S_2(t',t_1)\right]\left[\int_{t_1}^{t} dt' S_2(t_1,t') Q(t')\right] \tag{AII. 21b}$$

We denote the response of the distribution functions at t, due to excitation during $[t_o, t_1]$, by $\Delta P_n(t_o, t_1, t)$. For $(t - t_1)$ large, a portion of ΔP_n lies far from the surface, representing desorbed particles. We define:

$$\Delta P_n(t_0,t_1,t) \equiv P_1(t_0)\Pi_n(t_0,t_1,t) \tag{AII. 22}$$

Referring to Eq. (AII.14b), we note that for linear response one must approximate $P_1(t_o) \approx P_1^{\,o}(\vec{r}_o, \vec{v}_o)$.

Now we identify the macroscopic quantities which become the desorption rates in the limit $t_1 \to t_o$. We define:

$$\dot{\bar{N}}_n(t_o, t_1, t) \equiv \frac{N(t_o)}{(t_1 - t_o)} \int d^3\vec{r}_o \, d^3\vec{v}_o \, \Delta P_n(t_o, t_1, t) \tag{AII.23}$$

The integral yields the total induced change in the state n probability at time t. $N(t_o)$ is the surface coverage. Prototypes for the state n total desorption cross sections are defined by:

$$\bar{\sigma}_n(t_o, t_1, t) \equiv \frac{\dot{\bar{N}}_n(t_o, t_1, t)}{N(t_o) F} \tag{AII.24}$$

With the aid of Eq. (AII.24), (AII.23), (AII.22), (AII.21a, b), and (AII.19a, b), we write explicit expressions for $\bar{\sigma}_n$:

$$\bar{\sigma}_2(t_o, t_1, t) = \int d^3\vec{r}_o \, d^3\vec{v}_o \, P_1^o(\vec{r}_o, \vec{v}_o) \, \bar{\chi}_2(t_o, t_1) \, S_2(t_1, t) \tag{AII.25a}$$

$$\bar{\sigma}_1(t_o, t_1, t) = \int d^3\vec{r}_o \, d^3\vec{v}_o \, P_1^o(\vec{r}_o, \vec{v}_o) \times \left\{ \bar{\chi}_1(t_o, t_1) + \bar{\chi}_2(t_o, t_1) \int_{t_1}^{t} dt' \, S_2(t_1, t') Q(t') \right\} \tag{AII.25b}$$

We now observe that $\bar{\chi}_1(t_o, t_1)$ produces no desorption when the limit $t_1 \to t_o + \epsilon$ is taken. Referring to Eq. (AII.19b), it becomes clear that the coordinates of a particle quenched at $t' < t_1 = t_o + \epsilon$ differ only infinitesimally

from its coordinates at t_o, which we assumed to define a bound state. Secondly, the integration in Eq. (AII. 19b) is squeezed to zero, when Q(t') is well behaved. When Q(t') contains a resonance, which might be the case for some quenching models, the integrand of $\bar{\chi}_1$ then contains the combination $(t'-t_o)\,\delta(t'-t_o) = 0$. We therefore drop $\bar{\chi}_1$ in Eq. (AII. 25b).

Passage to the limit $t_I \rightarrow t_o + \epsilon$ is non-trivial in the expressions for the cross sections only for the excitation cross section $\bar{\chi}_2(t_o, t_1)$, which we now denote $\chi(t_o, t_1)$, dropping the superfluous subscript. We facilitate integration of the final expressions for σ_1, σ_2 using a finite number of phase space points by introducing a small arbitrary width Γ into the spread of incoming particle energies. Hence, we average Eq. (AII. 25a, b) over the narrow energy range Γ, or equivalently, we replace $R(\omega_o, t')$, the upward transition rate, by its average. Here ω_o is the central energy of the incoming beam. We make the following replacement for Eq. (AII. 19a):

$$\chi(t_o, t_1) = \frac{1}{\Gamma(t_1 - t_o)} \int_{t_o}^{t_1} dt' S_2(t_1', t_1) \int_{\omega_o - \Gamma/2}^{\omega_o + \Gamma/2} d\omega\, R(\omega, t') \tag{AII. 26}$$

This step is important for the case of photodesorption, where the transition rate for a monochromatic photon beam may have the form:

$$R_\gamma(\omega, t) = M_{PD}(\omega)\, \delta(\omega - \Delta(t)) \tag{AII. 27}$$

Here, M_{PD} is the matrix element. $\Delta(t)$ is an energy difference evaluated

for a particle at time t in its trajectory. In the absence of a finite energy width in the photon flux, an infinite number of points are required to perform the numerical integration.

Evaluating Eq. (AII. 26) for the photodesorption case using R_γ as above, we find the excitation cross section becomes:

$$\chi_\gamma(\omega, t_0) = \frac{M_{PD}(\omega)\,\theta(\omega+\frac{\Gamma'}{2}-\Delta(t_0))\,\theta(\Delta(t_0)-\omega_0+\frac{\Gamma'}{2})}{\Gamma' F_\gamma} \qquad \text{(AII. 28)}$$

In effect, we approximate the transition rate by a constant over a narrow band of frequencies. It was assumed that the non-radiative decay rate is sufficiently well behaved to justify:

$$\lim_{t_1 \to t_0} \left\{ \frac{1}{t_1 - t_0} \int_{t_0}^{t_1} dt' \, e^{-\int_{t'}^{t_1} dt'' Q(t'')} \right\} = 1$$

This is certainly the case if Q is always finite.

As remarked in the text, the transition rate for ESD contains no delta function. Eq. (AII. 26) may be trivially evaluated for small Γ' with the result:

$$\chi_e(\omega, t_0) = \frac{R_e(\omega, t_0)}{F_e} \qquad \text{(AII. 29)}$$

The final expressions for the total desorption cross sections will now be presented. We insert the step functions $\theta(E_2(\vec{r}_0) + \frac{1}{2}MV_0^2 - E_2(\infty))$ and $\theta(\frac{1}{2}MV_0^2 + E_2(\vec{r}_0) - E_2(\vec{r}') + E_1(\vec{r}') - E_1(\infty))$. These ensure the energetic feasibility of desorption. The result is:

$$\sigma_2(\omega) = \int d^3\vec{r}_0\, d^3\vec{v}_0\, P_1^0(\vec{r}_0,\vec{v}_0)\, \chi(\omega,t_0)\, S_2(t_0,t) \times \times \Theta\left(\tfrac{1}{2}MV_0^2 + E_2(\vec{r}_0) - E_2(\infty)\right) \tag{AII.30a}$$

$$\sigma_1(\omega) = \int d^3\vec{r}_0\, d^3\vec{v}_0\, P_1^0(\vec{r}_0,\vec{v}_0)\, \chi(\omega,t_0) \times \times \int_{t_0}^{t} dt'\, Q(t')\, S_2(t_0,t')\, \Theta\left[\tfrac{1}{2}MV_0^2 + E_2(\vec{r}_0) - E_2(\vec{r}') + + E_1(\vec{r}') - E_1(\infty)\right] \tag{AII.30b}$$

The result above is identical with Equations (6.7a,b). The path integrals S_2 are defined in Eq.(AII.2a), and in the text, where the method of evaluation is discussed. One should compare the result expressed in Eq.(AII.30a,b) in the one dimensional limit, with the results of Chapter IV, to verify that the correct limit is obtained for a translationally invariant system.

Only trajectories which are unbound, and hence, quasi-classical for large mass particles, are present in the integration. It is clear that one may generalize the result to the case where Franck-Condon transition from a quantized ground state are considered, by making the appropriate replacement for the Boltzmann distribution and phase space integration.

Appendix III: Simulated ESDIAD Patterns for O^+ - W(111)

In this appendix we present simulated ESD Ion Angular Distribution plots for O^+ desorption from the (111) face of tungsten. The adsorption site candidate corresponding to each of the following polar projections is fully identified in Fig.(7.12a) or (7.12b) of Chapter VII. Axes in the following plots are parallel to those of Fig.(7.1). The same scale and projection scheme is used for each. Scale marks each 5 degrees of colatitude are provided.

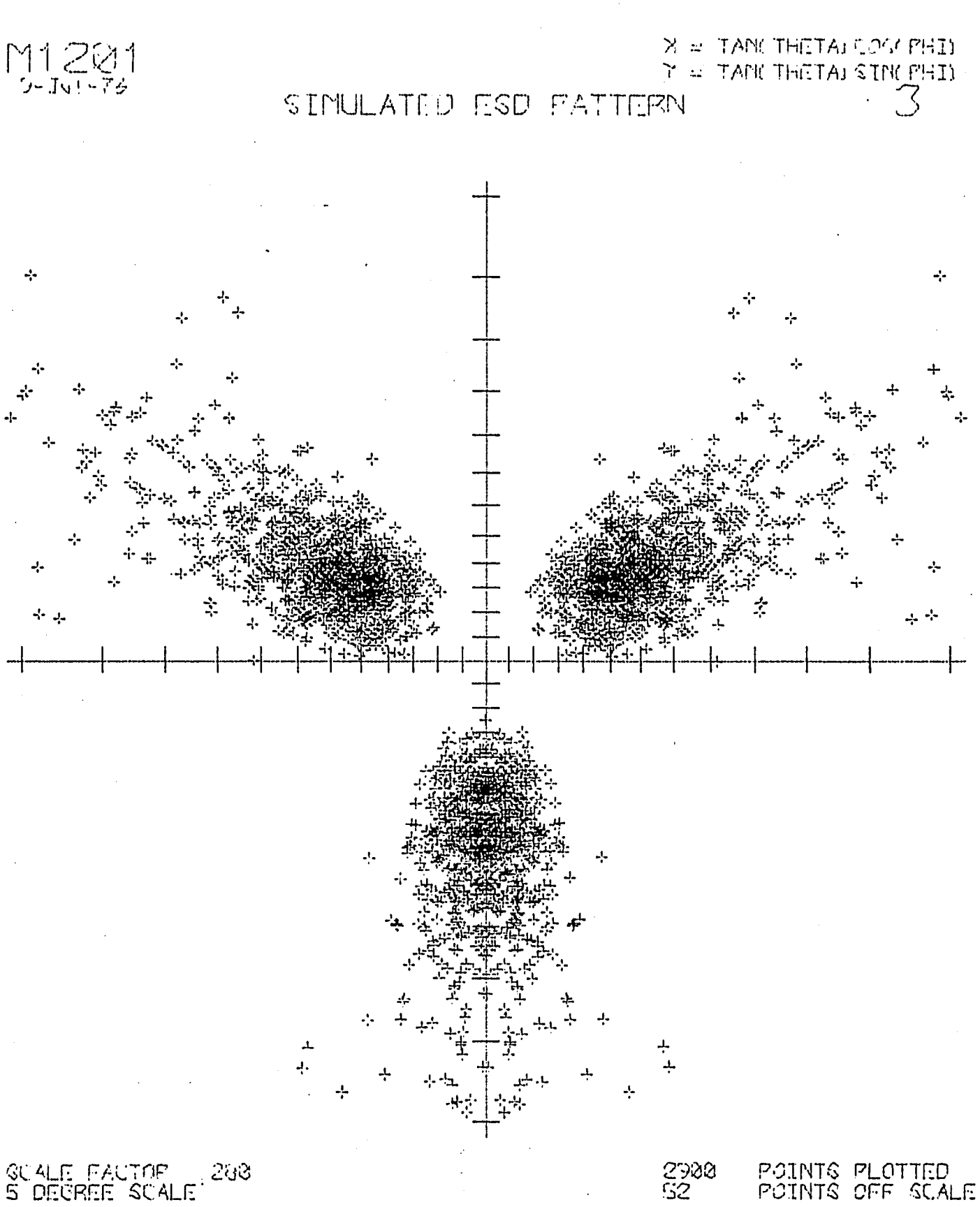

FIGURE AIII.1

M1203
10-JUL-76

X = TAN(THETA) COS(PHI)
Y = TAN(THETA) SIN(PHI)

SIMULATED ESD PATTERN 3

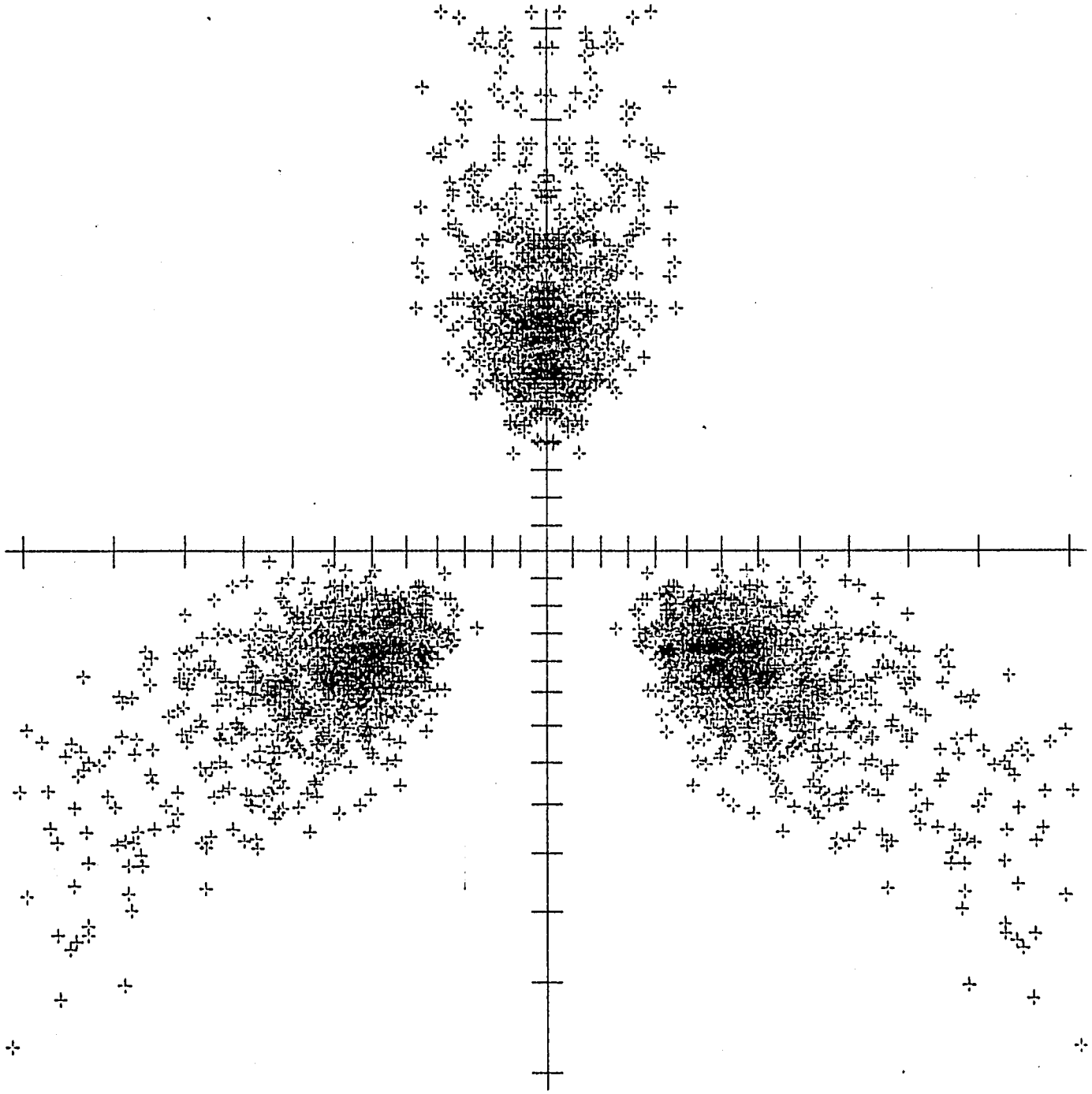

SCALE FACTOR .200
5 DEGREE SCALE

2003 POINTS PLOTTED
138 POINTS OFF SCALE

FIGURE AIII.2

M1018
24-Jul-76

X = TAN(THETA) COS(PHI)
Y = TAN(THETA) SIN(PHI)

SIMULATED ESD PATTERN 3

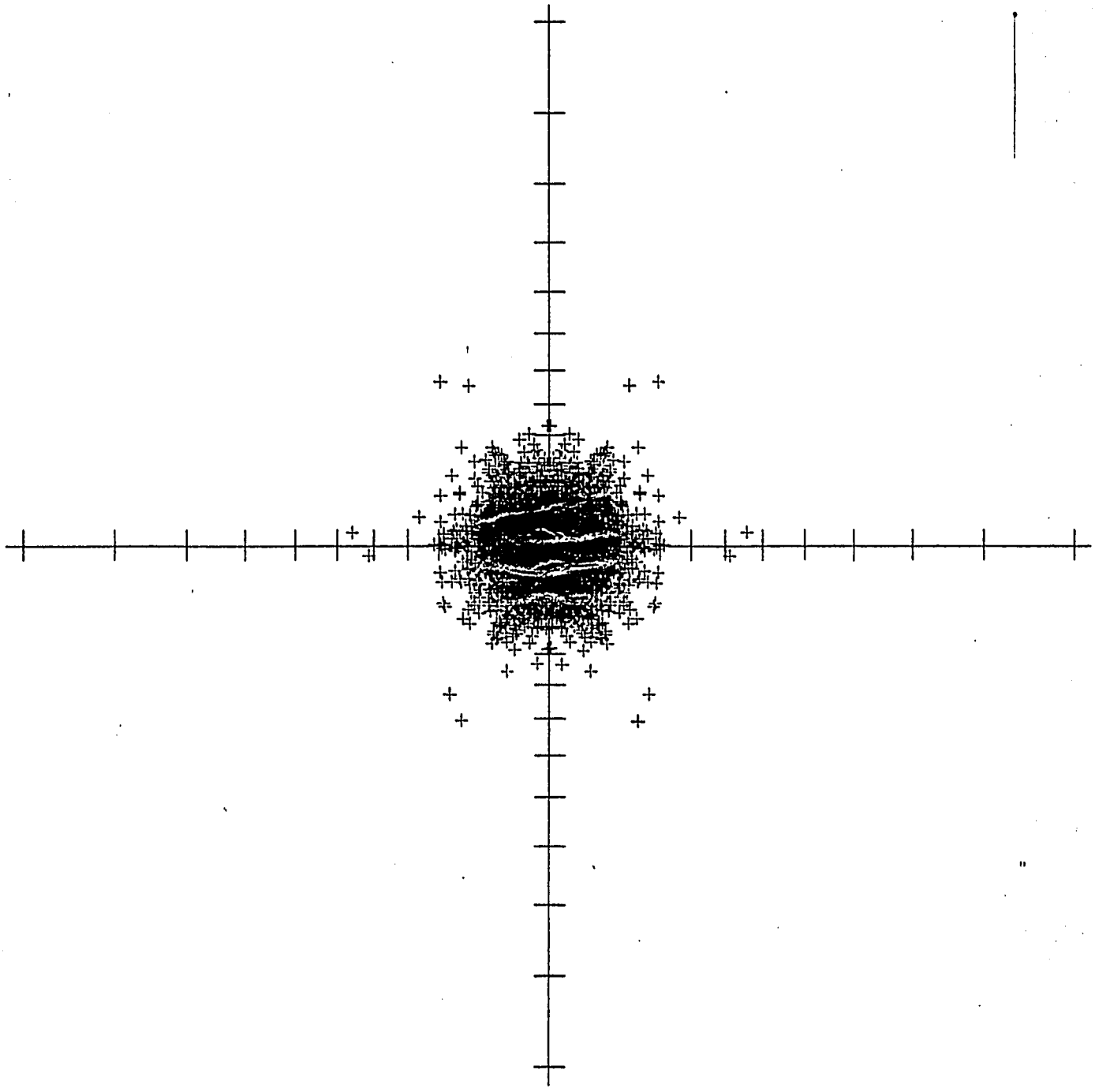

SCALE FACTOR .280
5 DEGREE SCALE

2994 POINTS PLOTTED
0 POINTS OFF SCALE

FIGURE AIII.3

M1202
10-JUL-76

X = TAN(THETA) COS(PHI)
Y = TAN(THETA) SIN(PHI)

SIMULATED ESD PATTERN 3

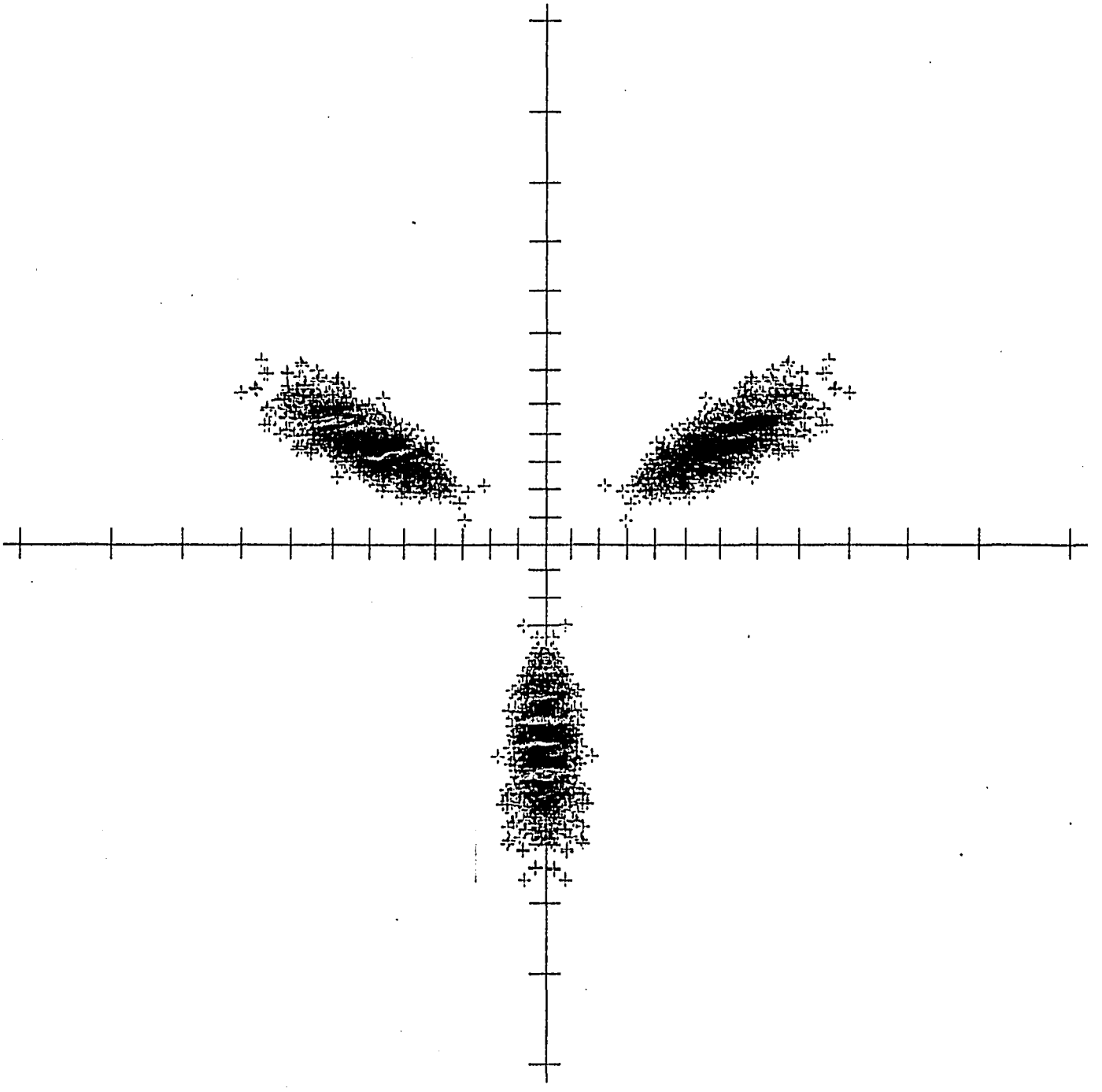

SCALE FACTOR .200
5 DEGREE SCALE

3000 POINTS PLOTTED
0 POINTS OFF SCALE

FIGURE AIII.4

M1205
10-Jul-76

X = TAN(THETA) COS(PHI)
Y = TAN(THETA) SIN(PHI)

SIMULATED ESD PATTERN 3

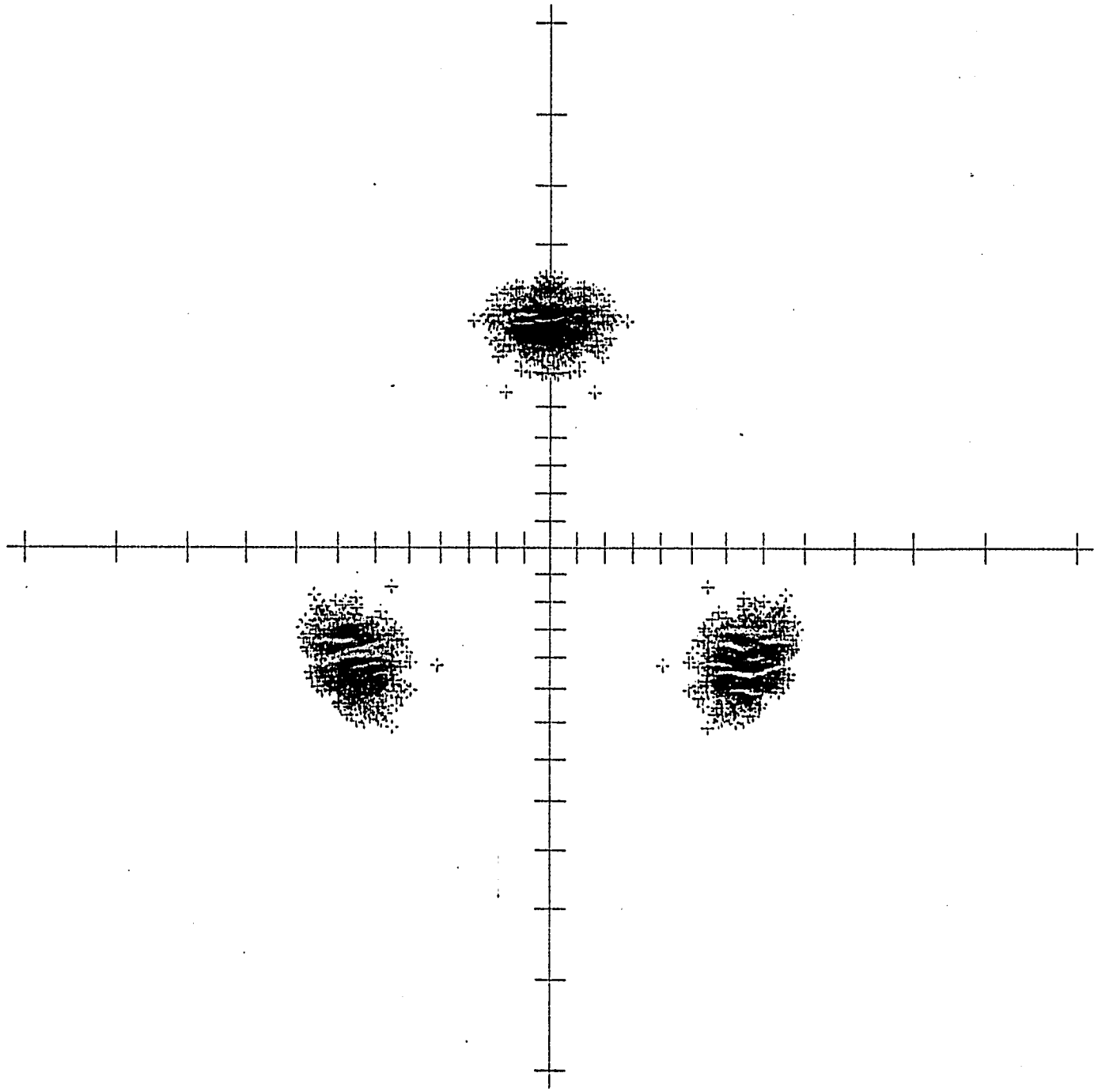

SCALE FACTOR .200
5 DEGREE SCALE

3000 POINTS PLOTTED
0 POINTS OFF SCALE

FIGURE AIII.5

M1206
11-Jul-76

X = TAN(THETA) COS(PHI)
Y = TAN(THETA) SIN(PHI)

SIMULATED ESD PATTERN 3

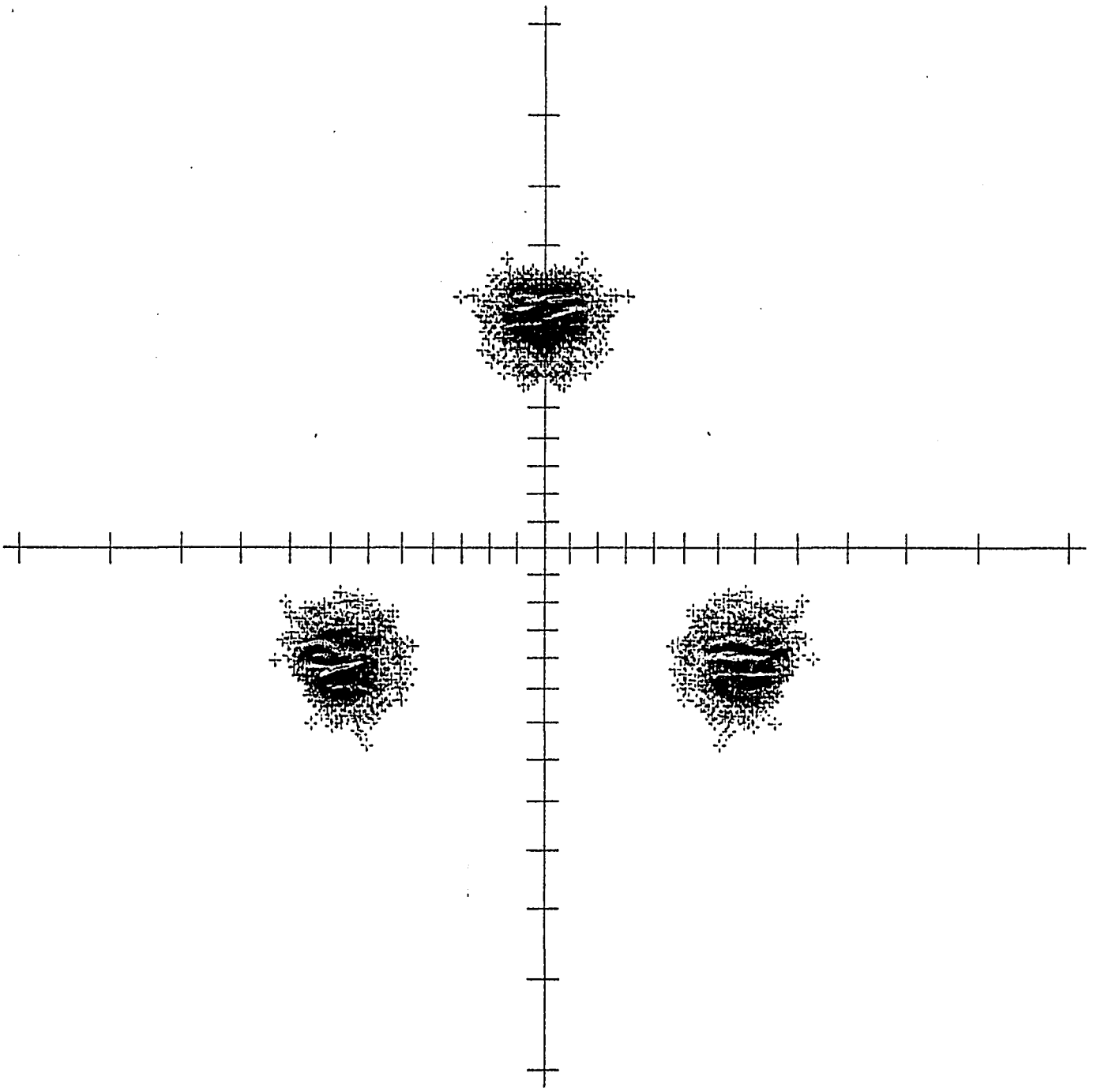

SCALE FACTOR .250
5 DEGREE SCALE

3000 POINTS PLOTTED
0 POINTS OFF SCALE

FIGURE AIII.6

M1016
23-Jul-76

X = TAN(THETA) COS(PHI)
Y = TAN(THETA) SIN(PHI)

SIMULATED ESD PATTERN 3

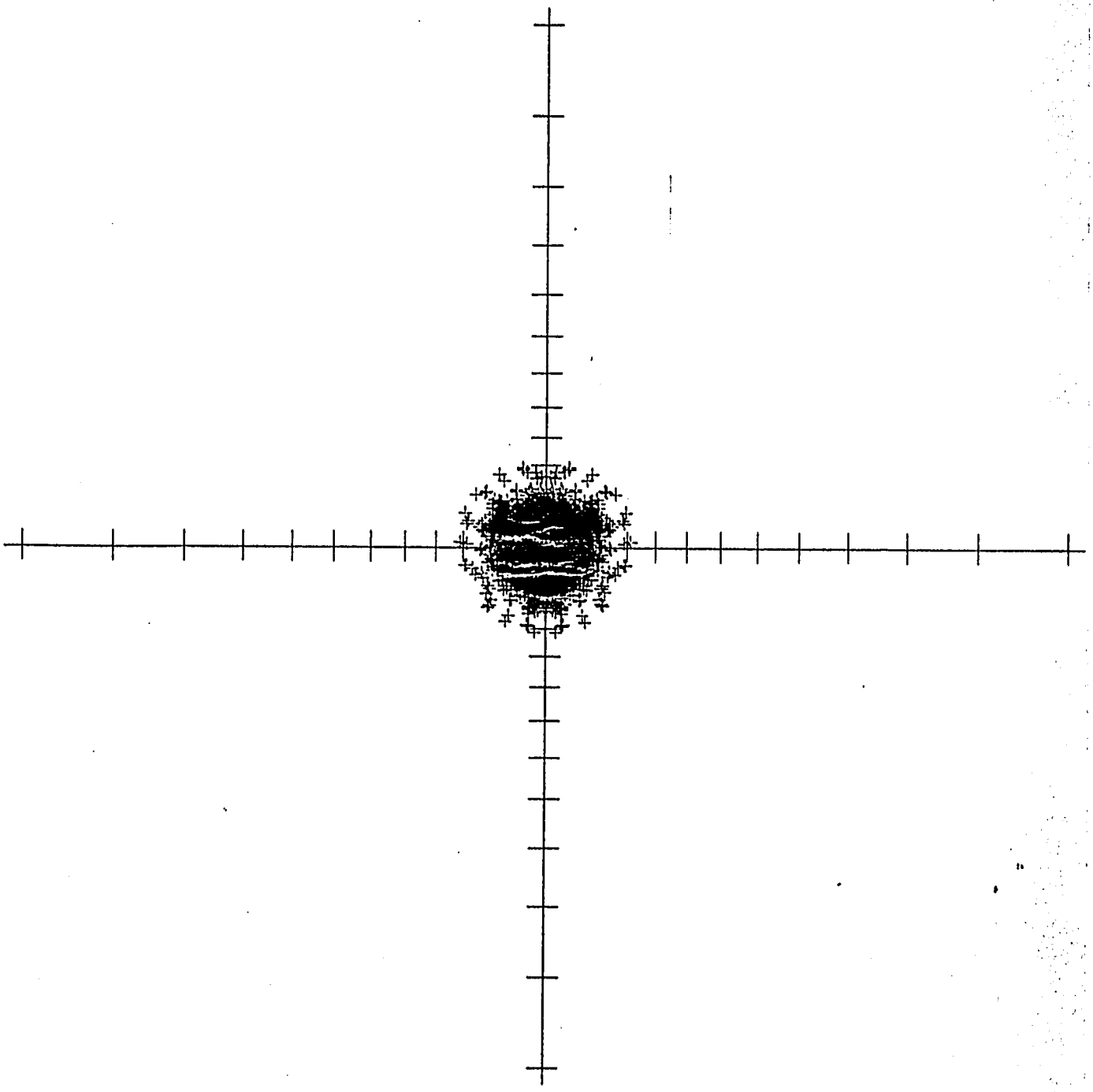

SCALE FACTOR .280
5 DEGREE SCALE

3000 POINTS PLOTTED
0 POINTS OFF SCALE

FIGURE AIII.7

M1204
11-Jul-76

X = TAN(THETA) COS(PHI
Y = TAN(THETA) SIN(PHI

SIMULATED ESD PATTERN 3

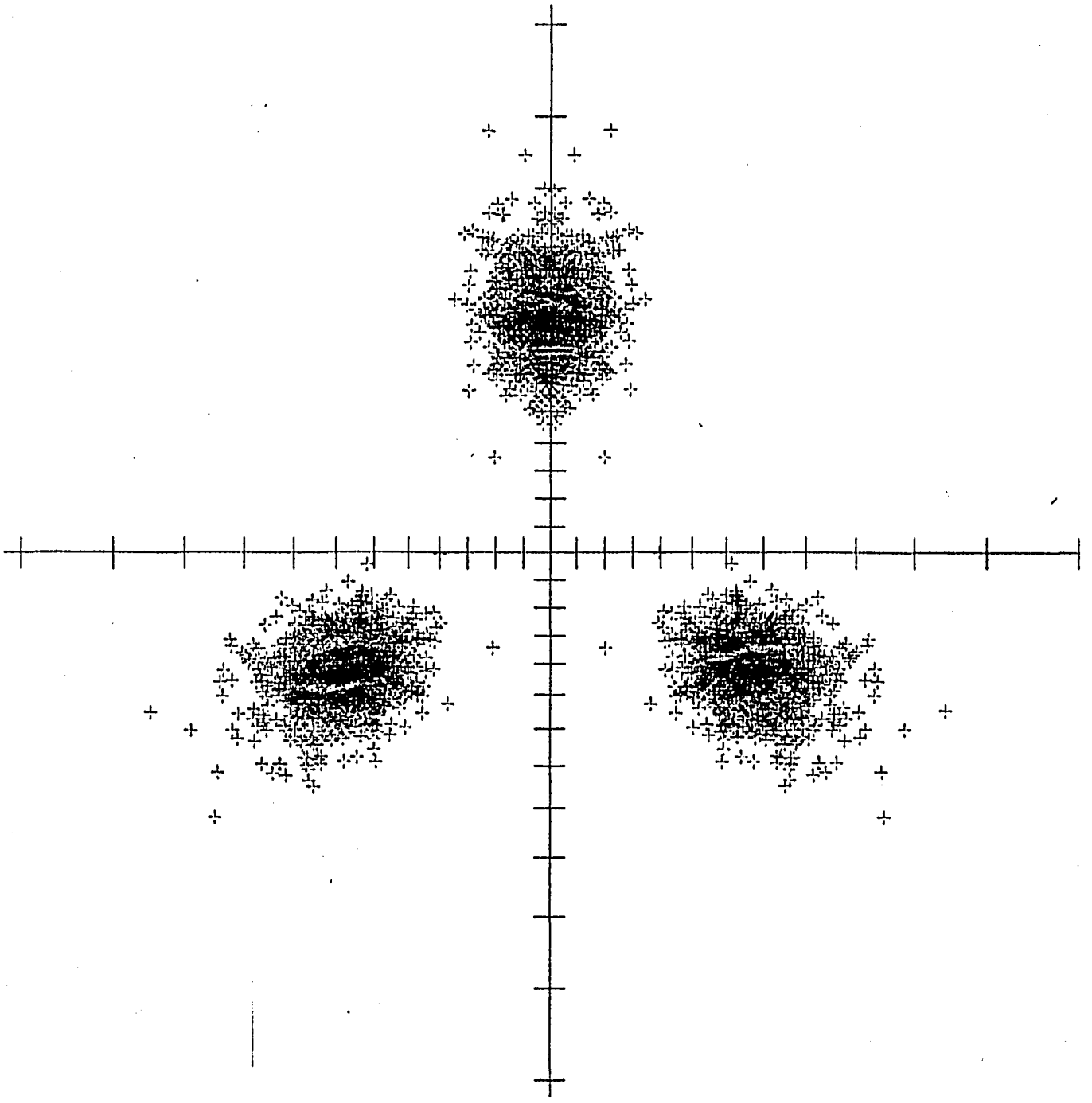

SCALE FACTOR .200
5 DEGREE SCALE

3000 POINTS PLOTTED
0 POINTS OFF SCAL

FIGURE AIII,8

M1017
24-Jul-76

X = TAN(THETA) COS(PHI)
Y = TAN(THETA) SIN(PHI)

SIMULATED ESD PATTERN 3

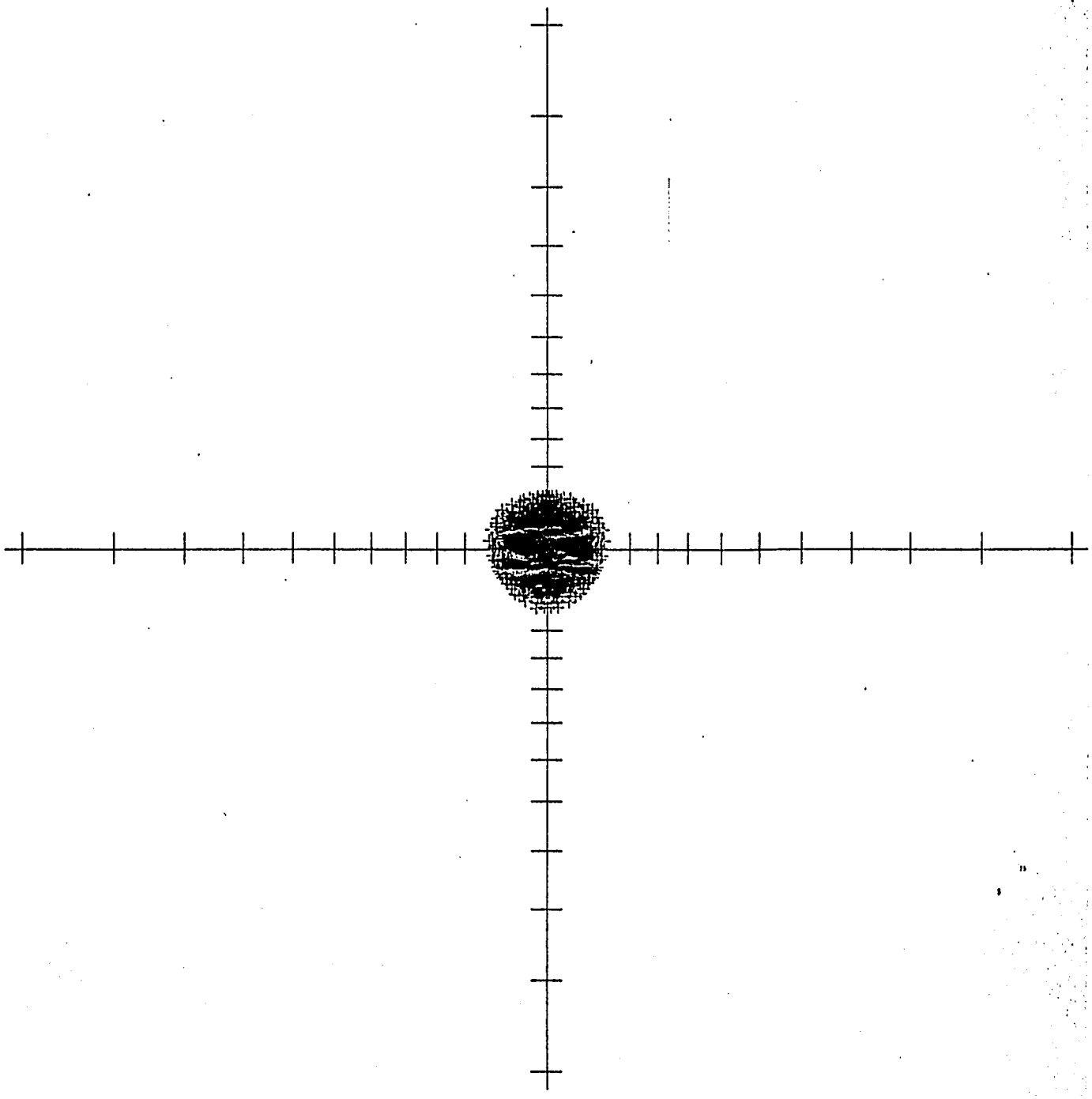

SCALE FACTOR .280
5 DEGREE SCALE

3000 POINTS PLOTTED
0 POINTS OFF SCAL

FIGURE AIII.9

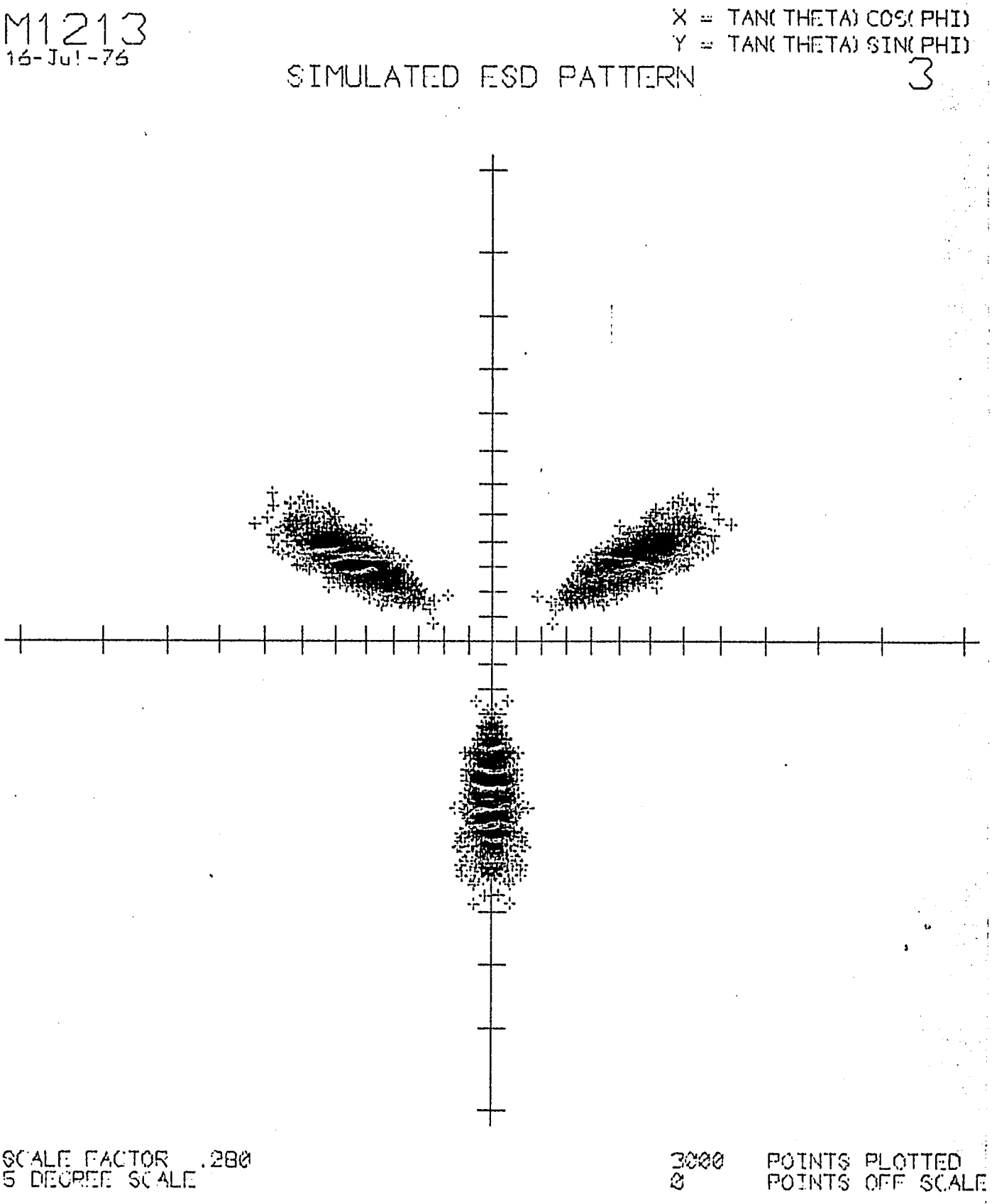

FIGURE AIII.10

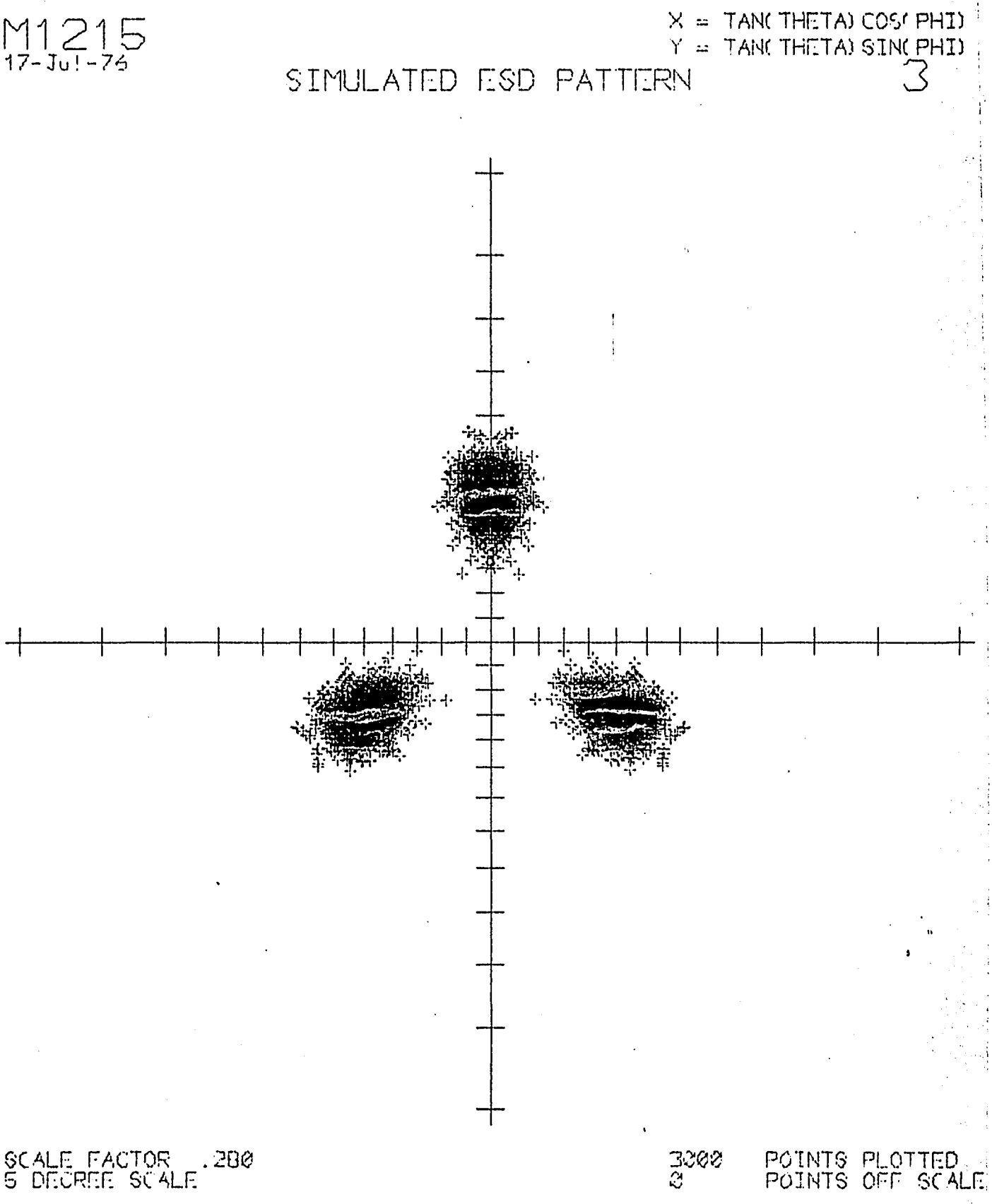

FIGURE AIII.11

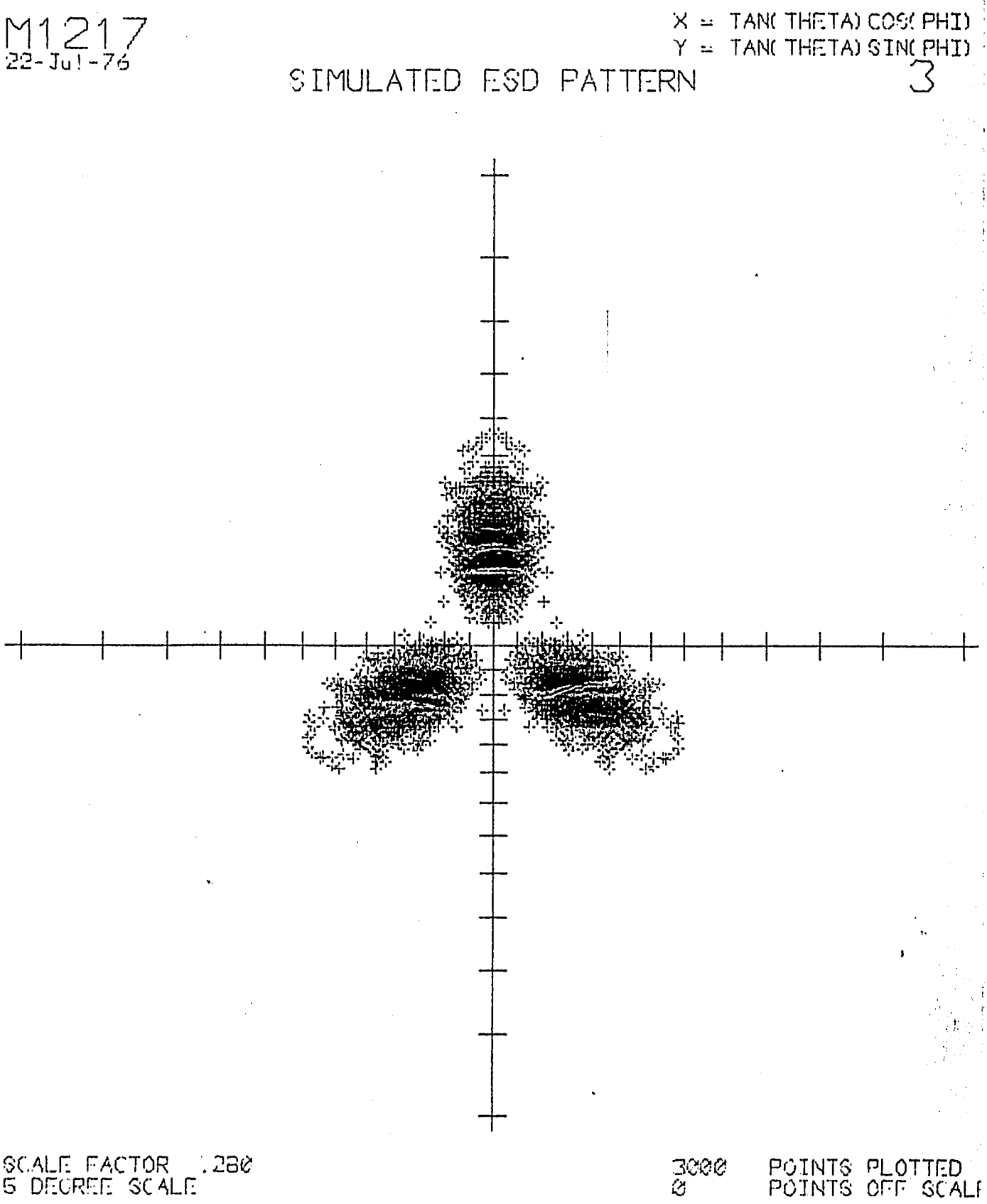

FIGURE AIII.12

M1207
9-Jul-76

X = TAN(THETA) COS(PHI)
Y = TAN(THETA) SIN(PHI)

SIMULATED ESD PATTERN 3

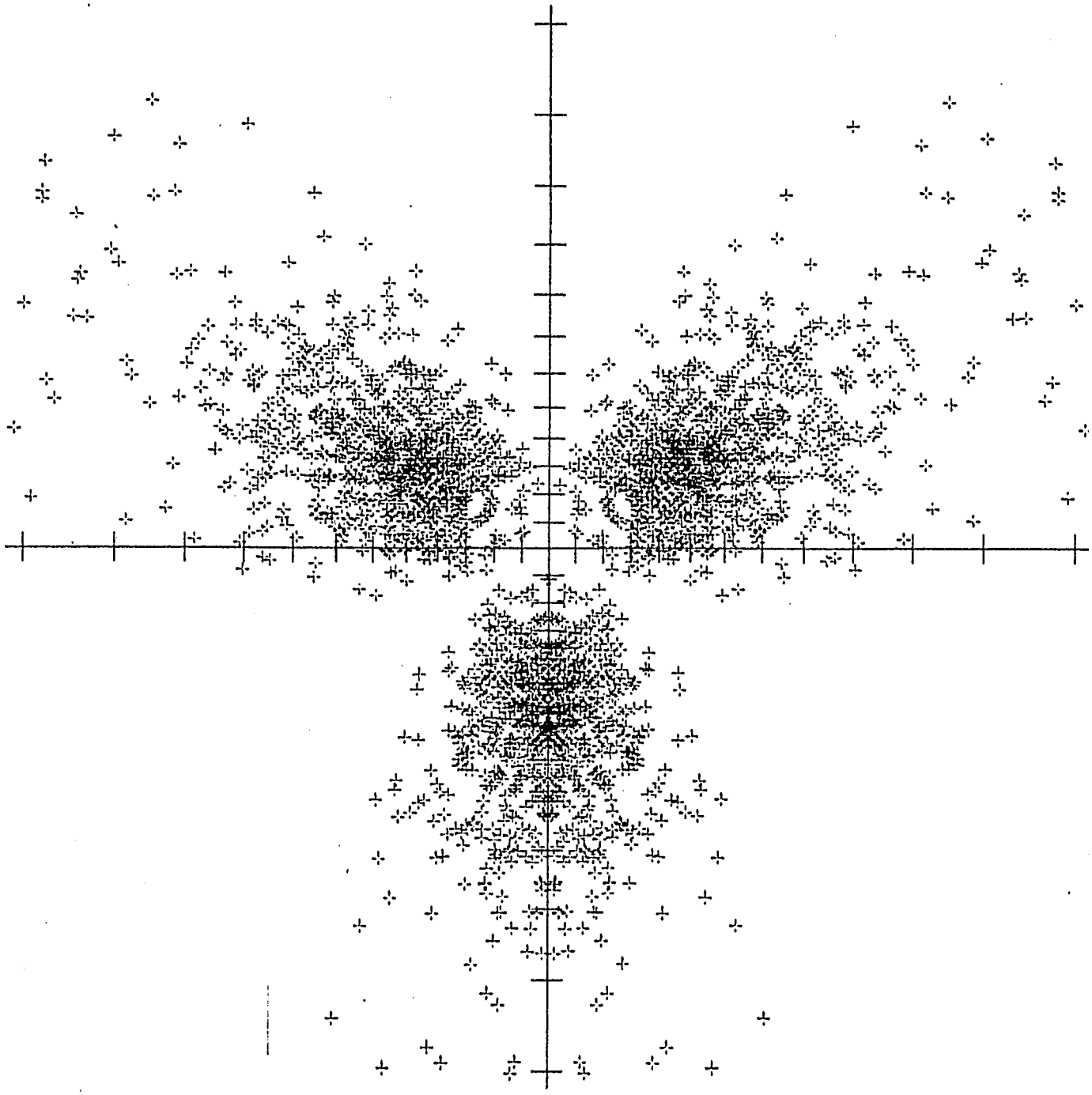

SCALE FACTOR .280
5 DEGREE SCALE

2520 POINTS PLOTTED
126 POINTS OFF SCALE

FIGURE AIII,13

M1209
10-Jul-76

X = TAN(THETA) COS(PHI)
Y = TAN(THETA) SIN(PHI)

SIMULATED ESD PATTERN 3

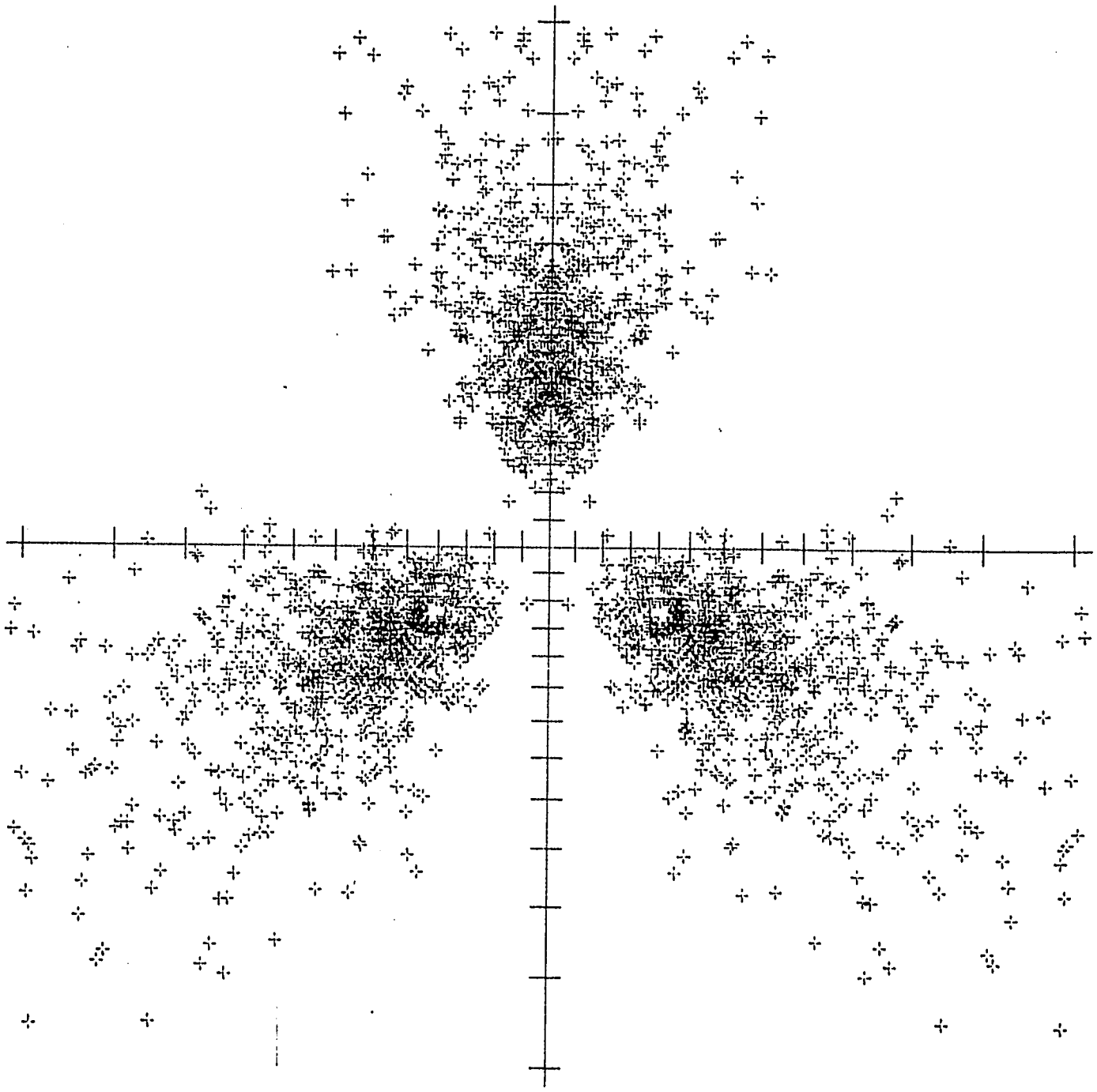

SCALE FACTOR .280
5 DEGREE SCALE

2332 POINTS PLOTTED
194 POINTS OFF SCALE

FIGURE AIII,14

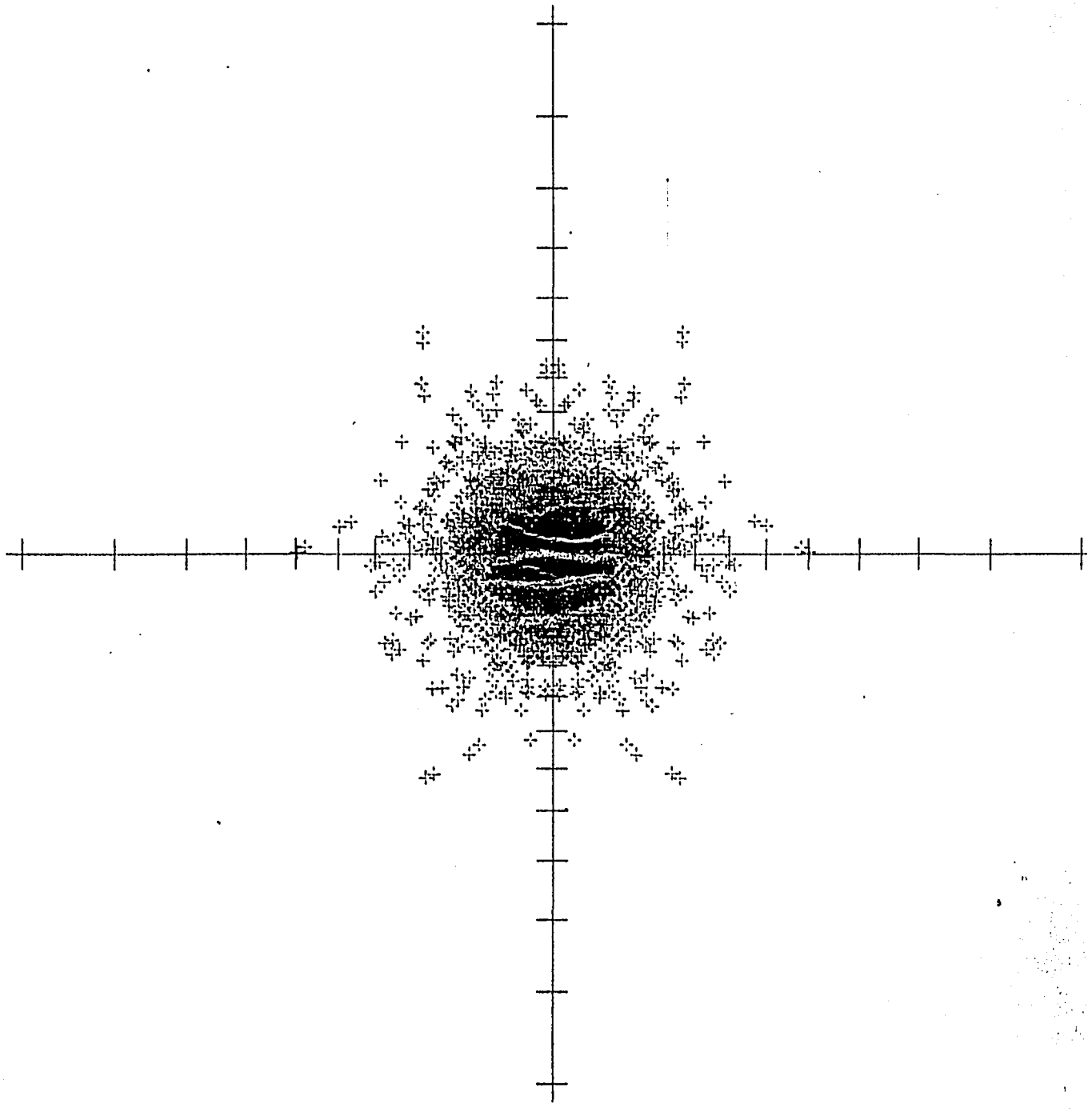

FIGURE AIII,15

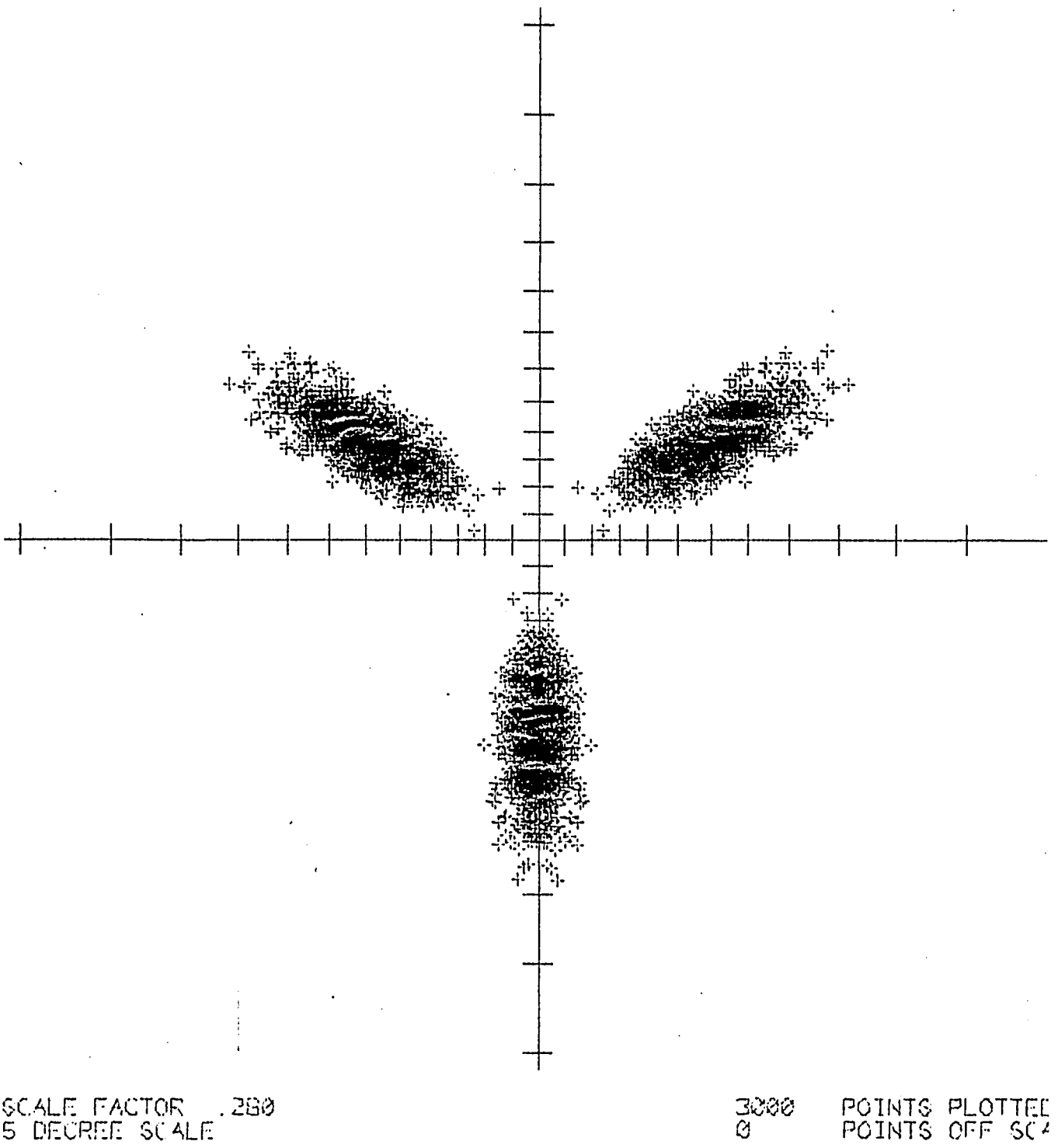

FIGURE AIII. 16

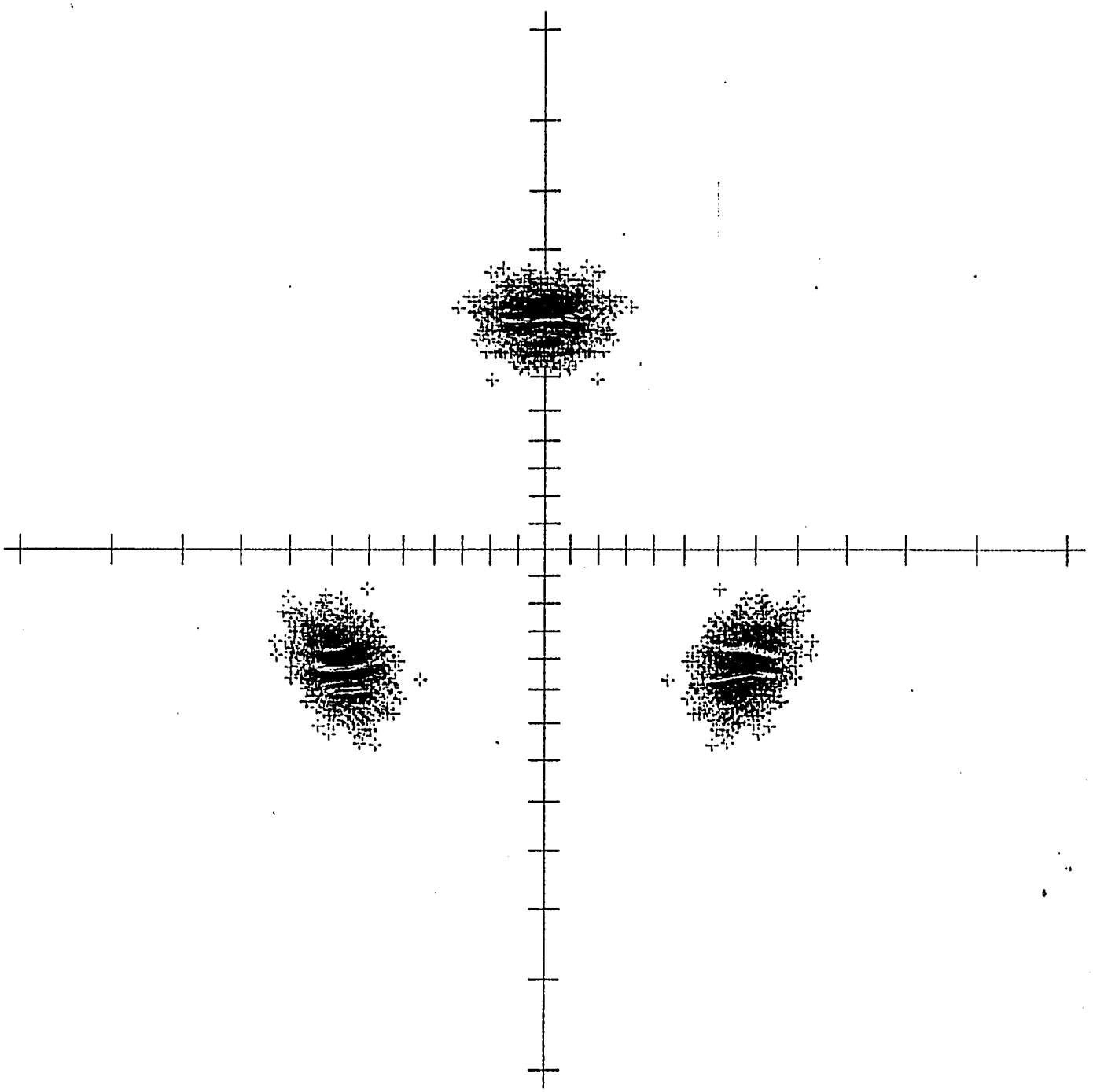

FIGURE AIII.17

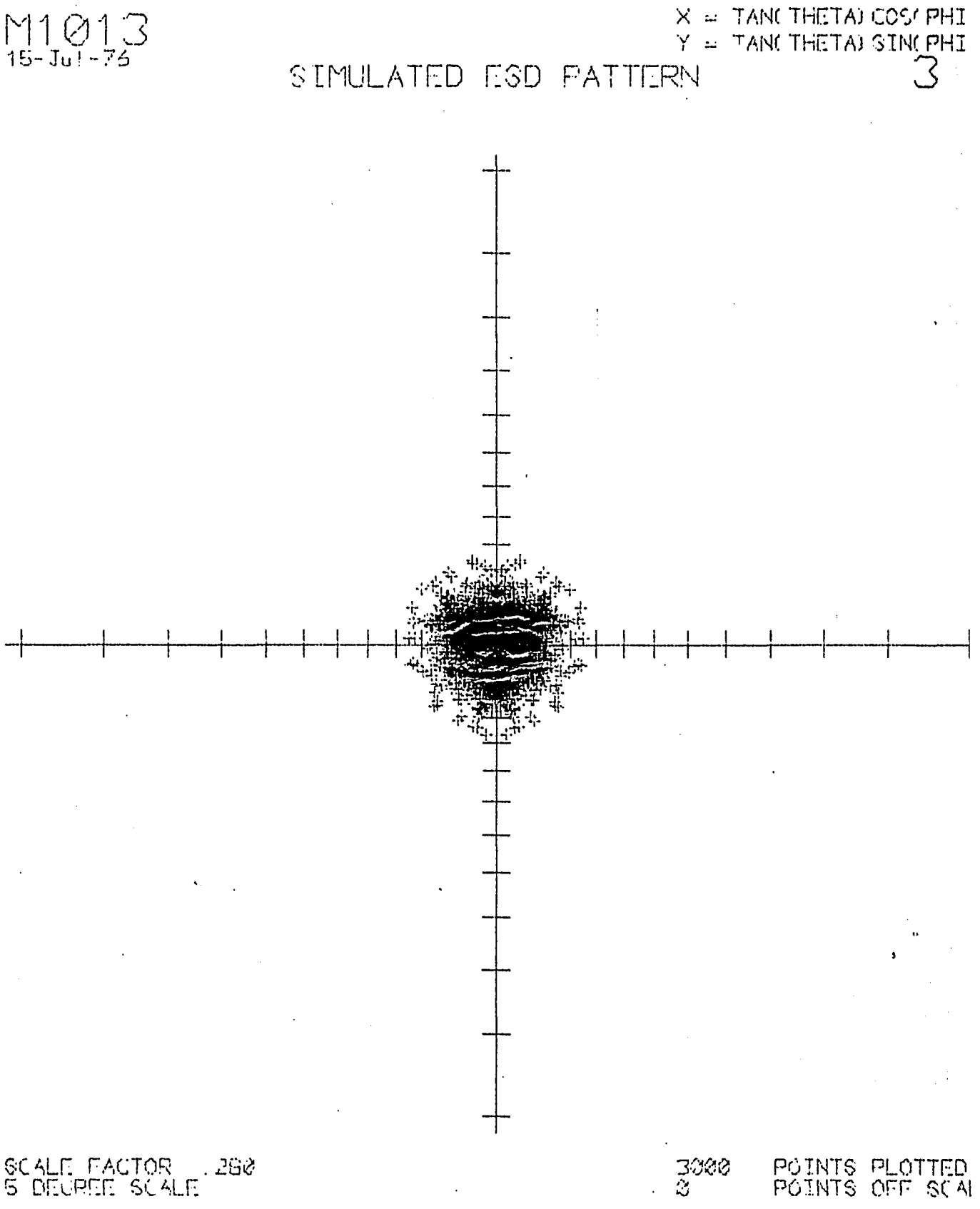

FIGURE AIII.18

M1210
11-Jul-76

X = TAN(THETA) COS(PH
Y = TAN(THETA) SIN(PH

SIMULATED ESD PATTERN 3

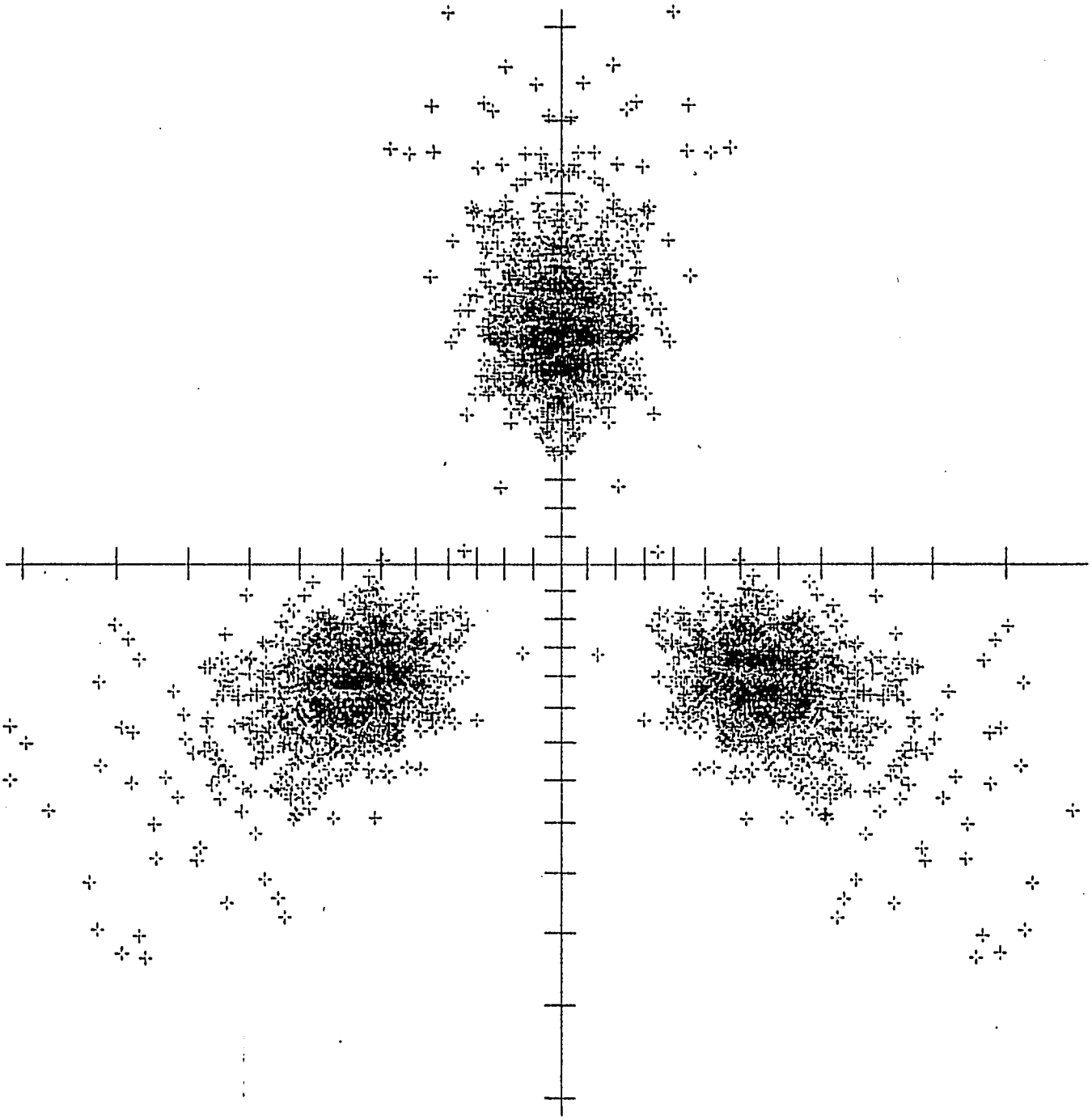

SCALE FACTOR .280
5 DEGREE SCALE

2966 POINTS PLOTTE
22 POINTS OFF SC

FIGURE AIII.19

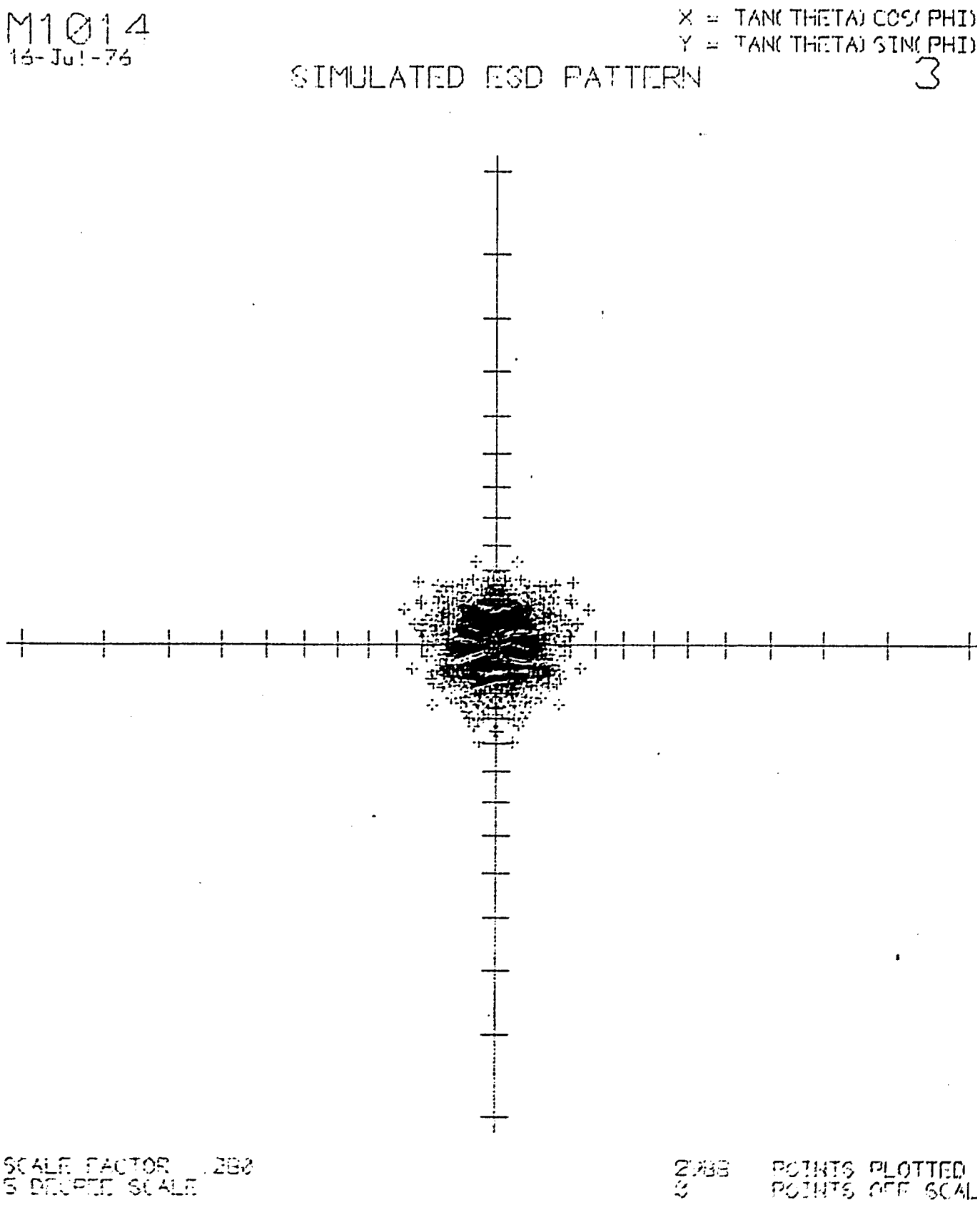

FIGURE AIII.20

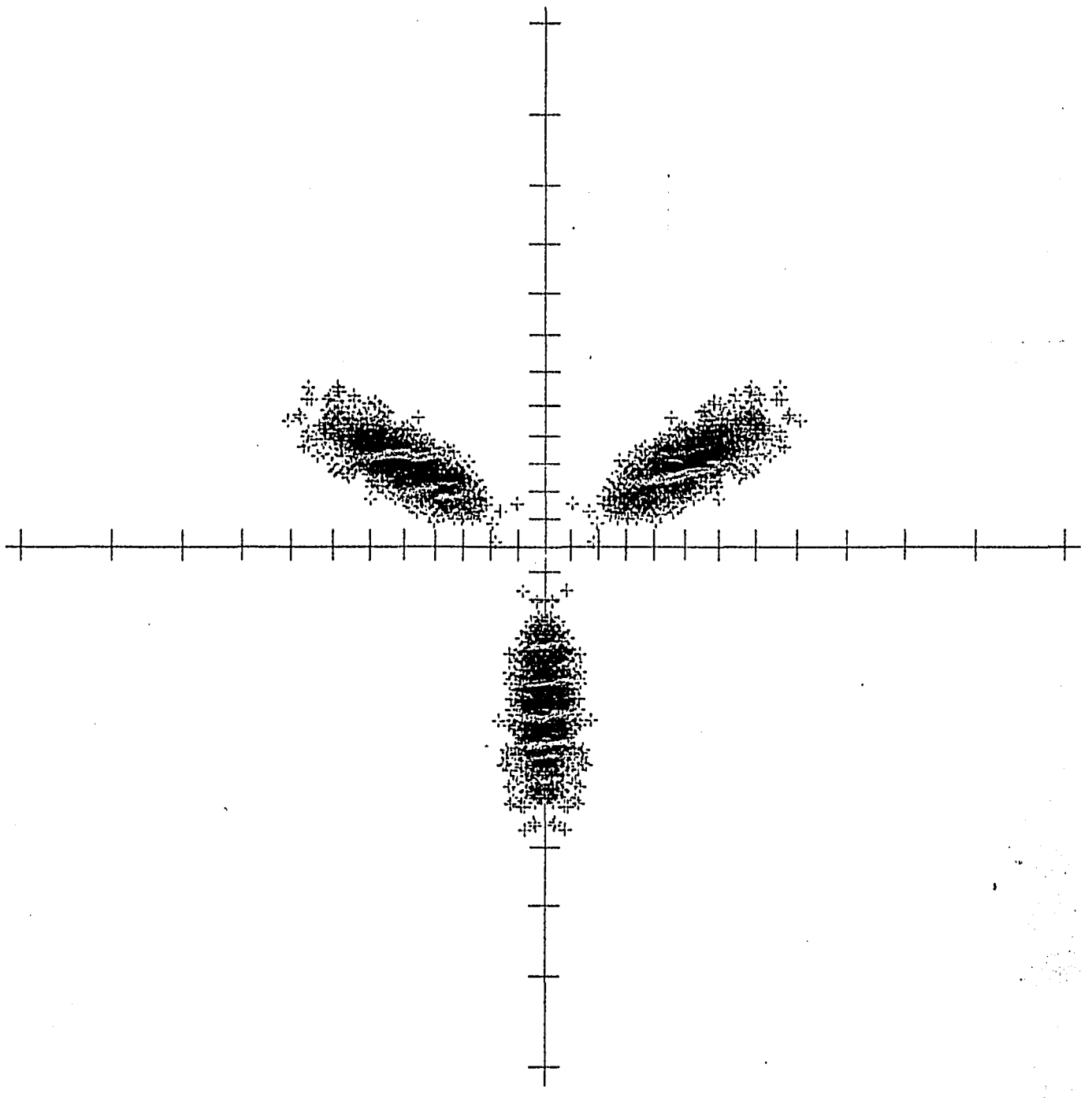

FIGURE AIII.21

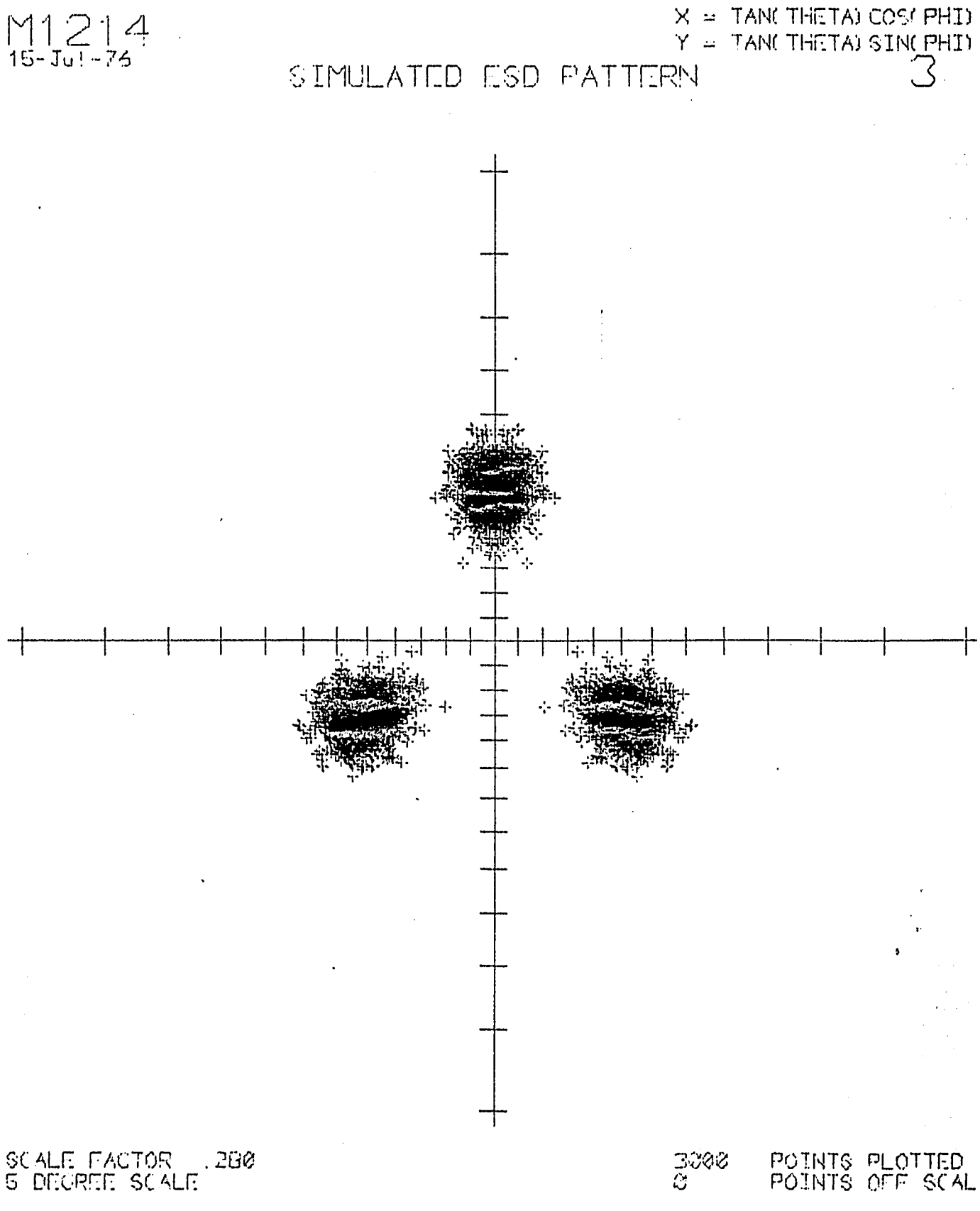

FIGURE AIII.22

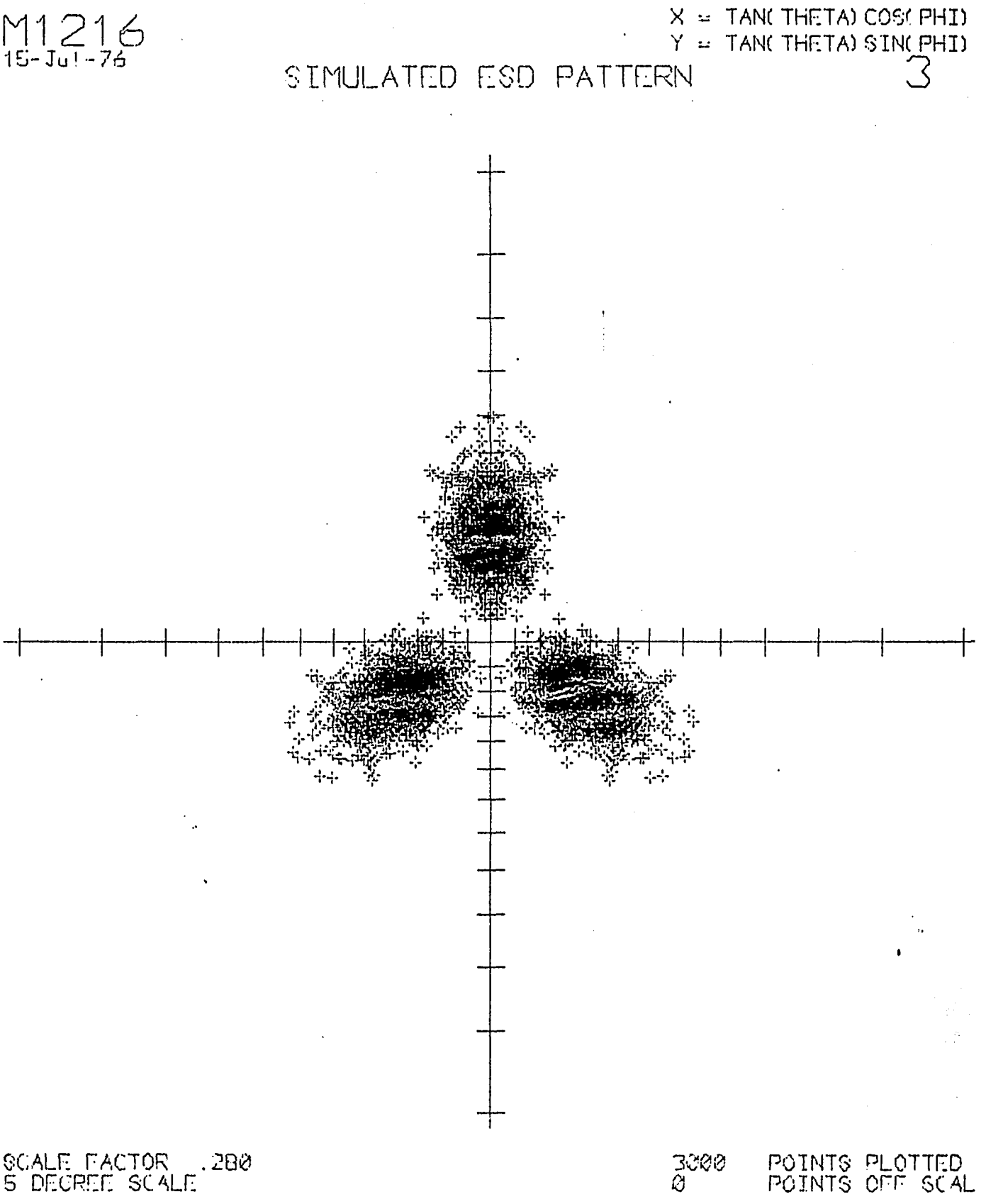

FIGURE AIII.23

Appendix IV: Simulated ESDIAD Patterns for O^+- W(100)

For completeness, we present here simulated ESD Ion Angular Distribution patterns for desorption of O^+ from the (100) face of tungsten. The adsorption site candidate to which each of the following ion distribution plots belongs is fully identified in Fig.(8.8), and in the text of Chapter VIII. All are polar plots, using the same scale and projection scheme. Axes are parallel to the substrate atom rows defined by the cartesian axes of Fig. (8.1). Scale marks are provided each 5 degrees of colatitude.

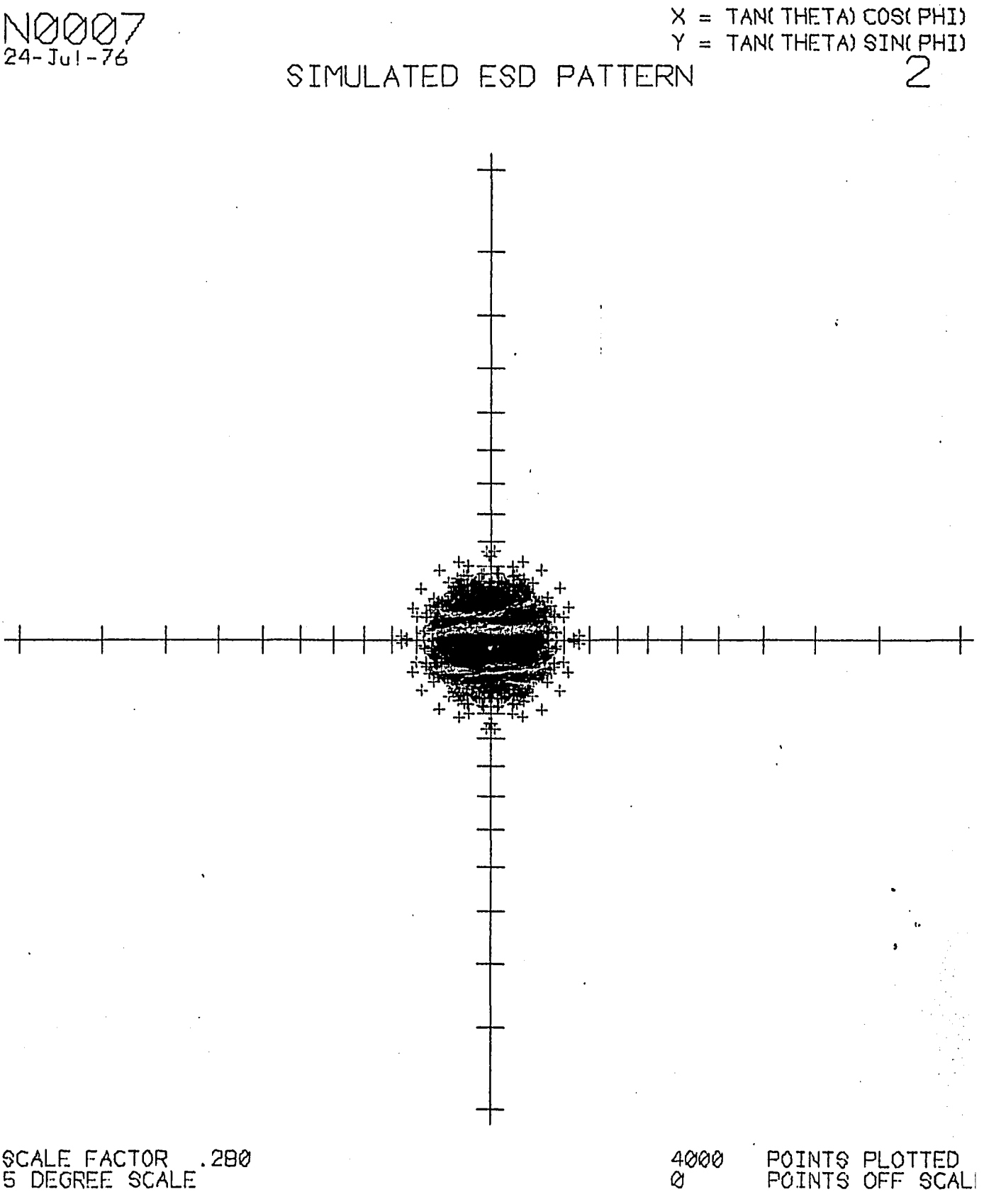

Figure AIV.1 ESDIAD Pattern for Site A1

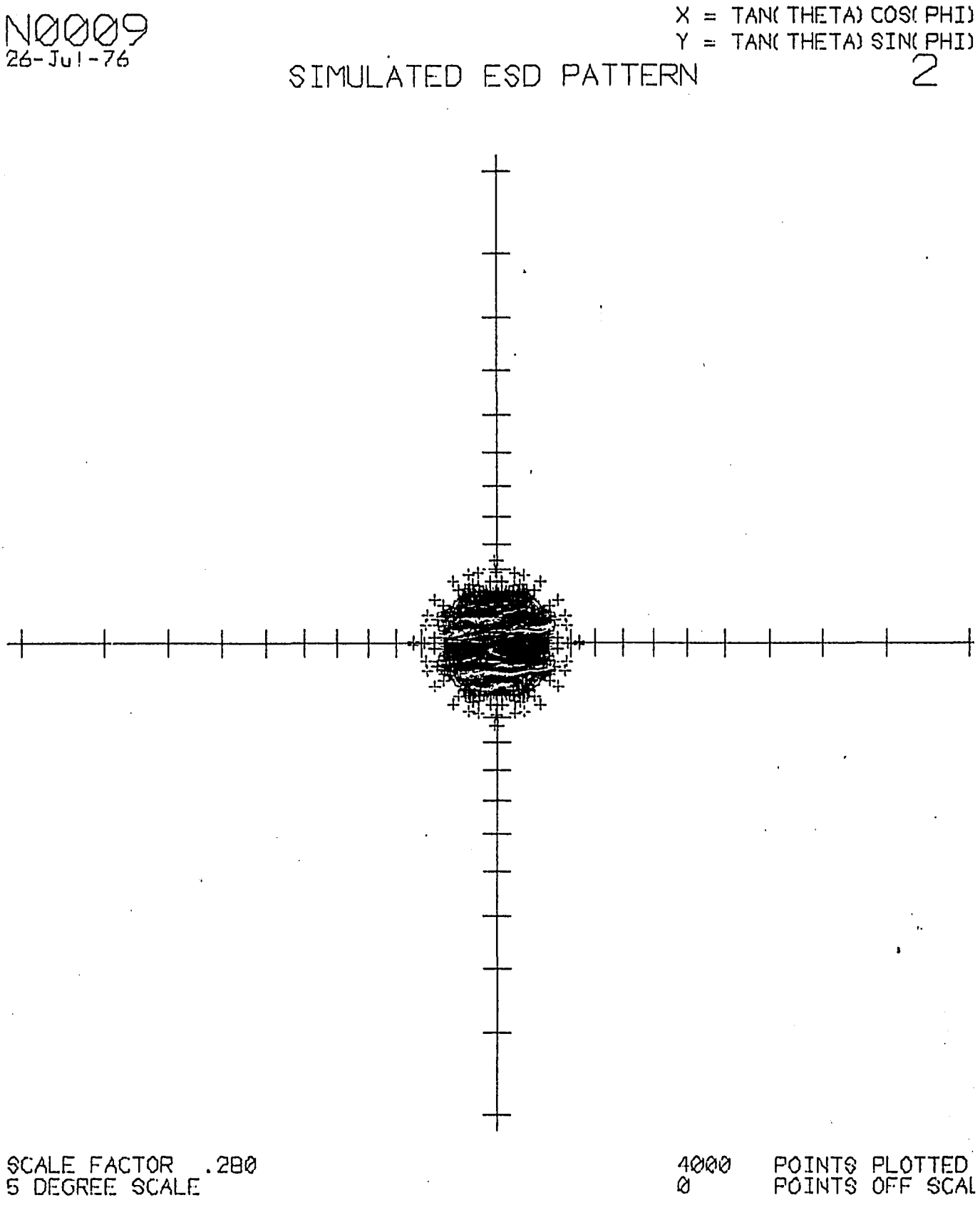

Figure AIV.2 ESDIAD Pattern for Site A2

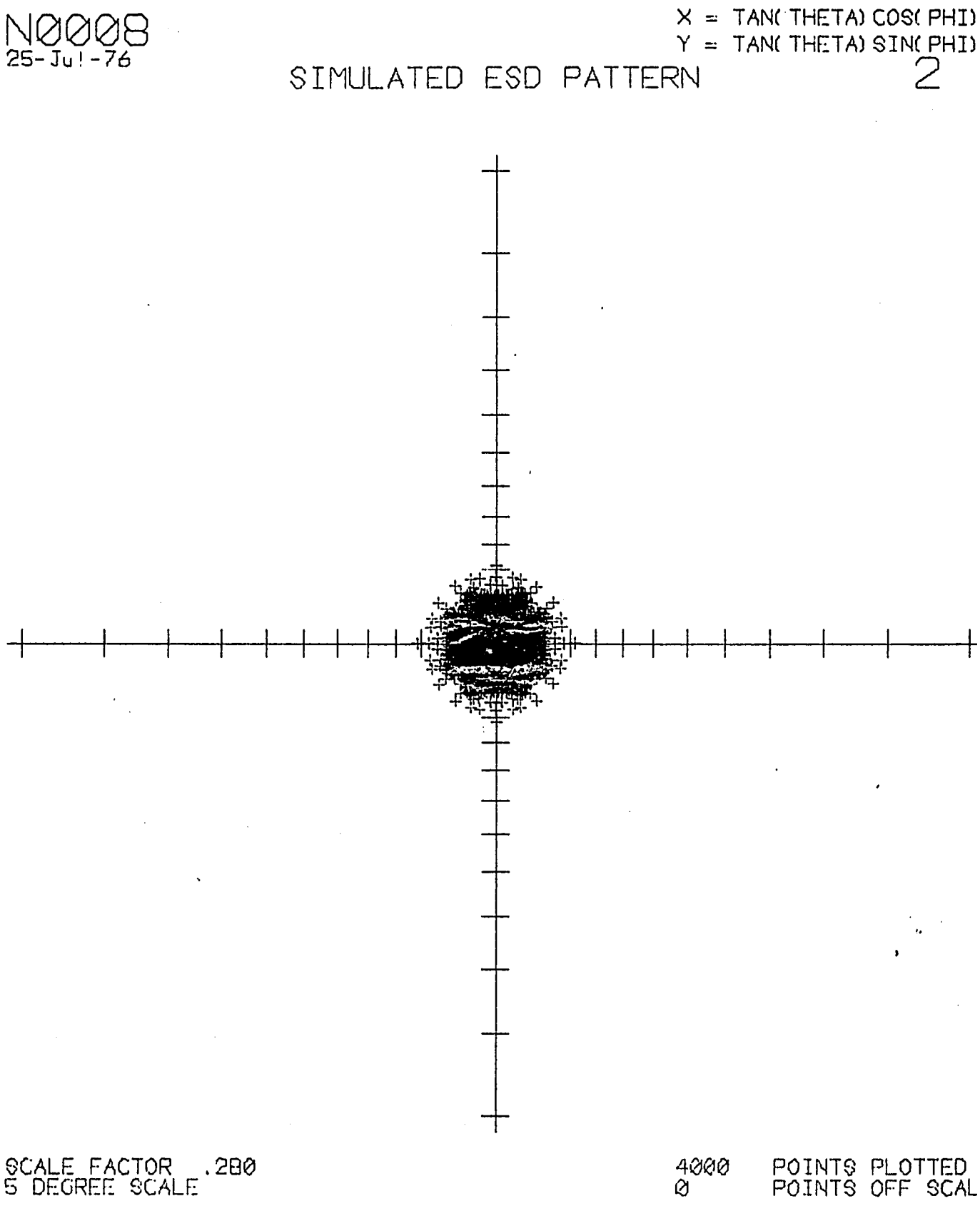

Figure AIV.3 ESDIAD Pattern for Site A3

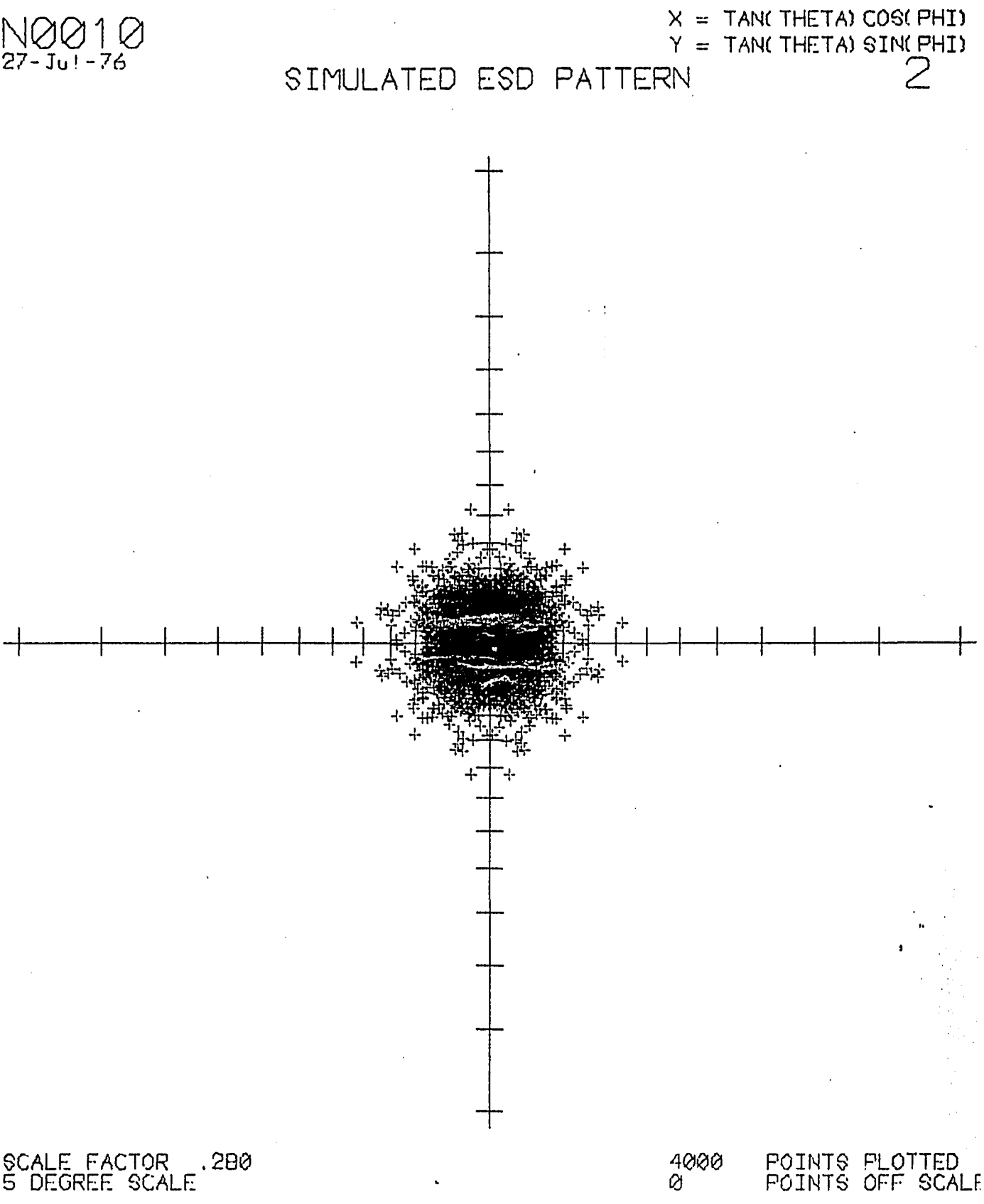

Figure AIV.4 ESDIAD Pattern for Site D1

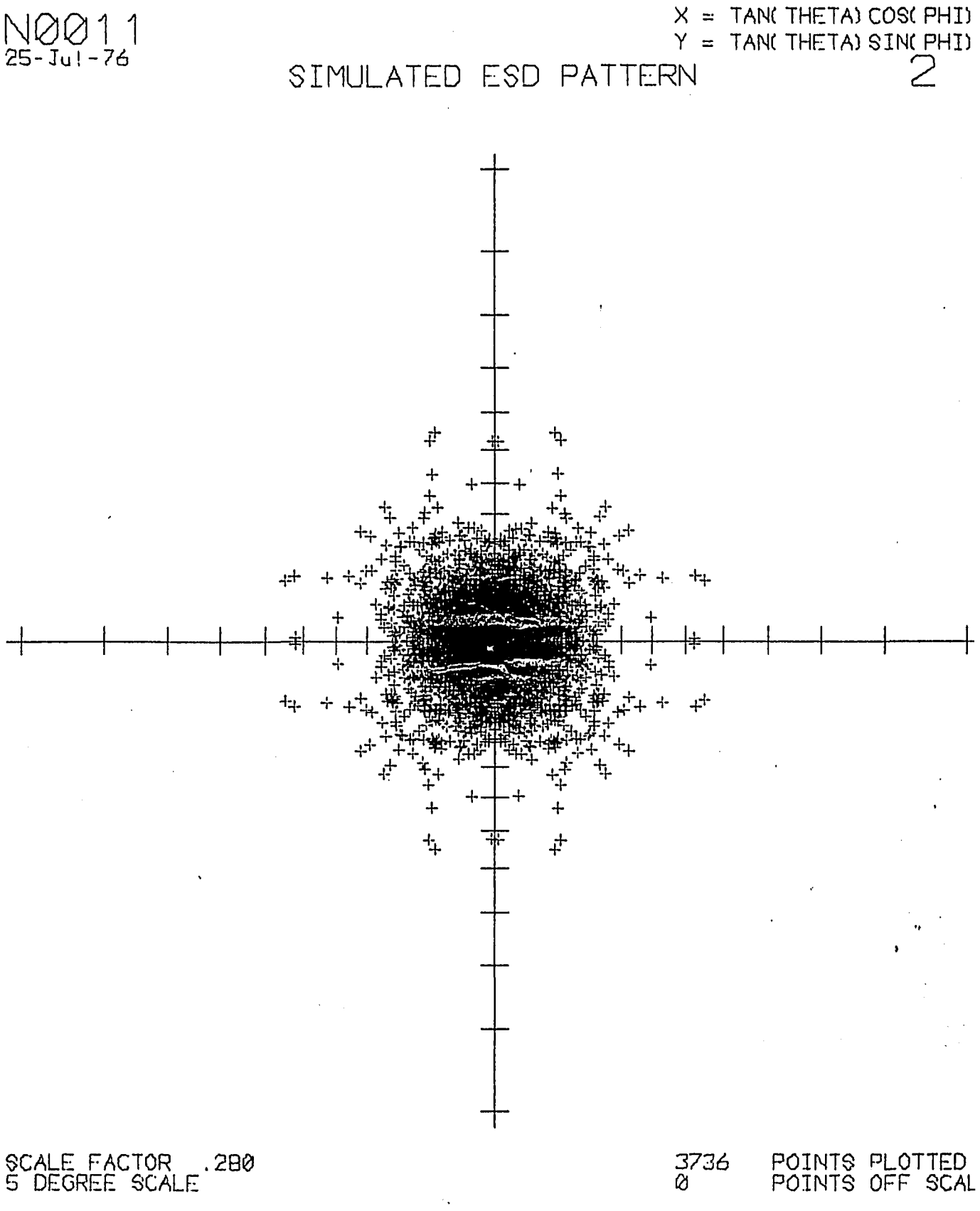

Figure AIV.5 ESDIAD Pattern for Site D2

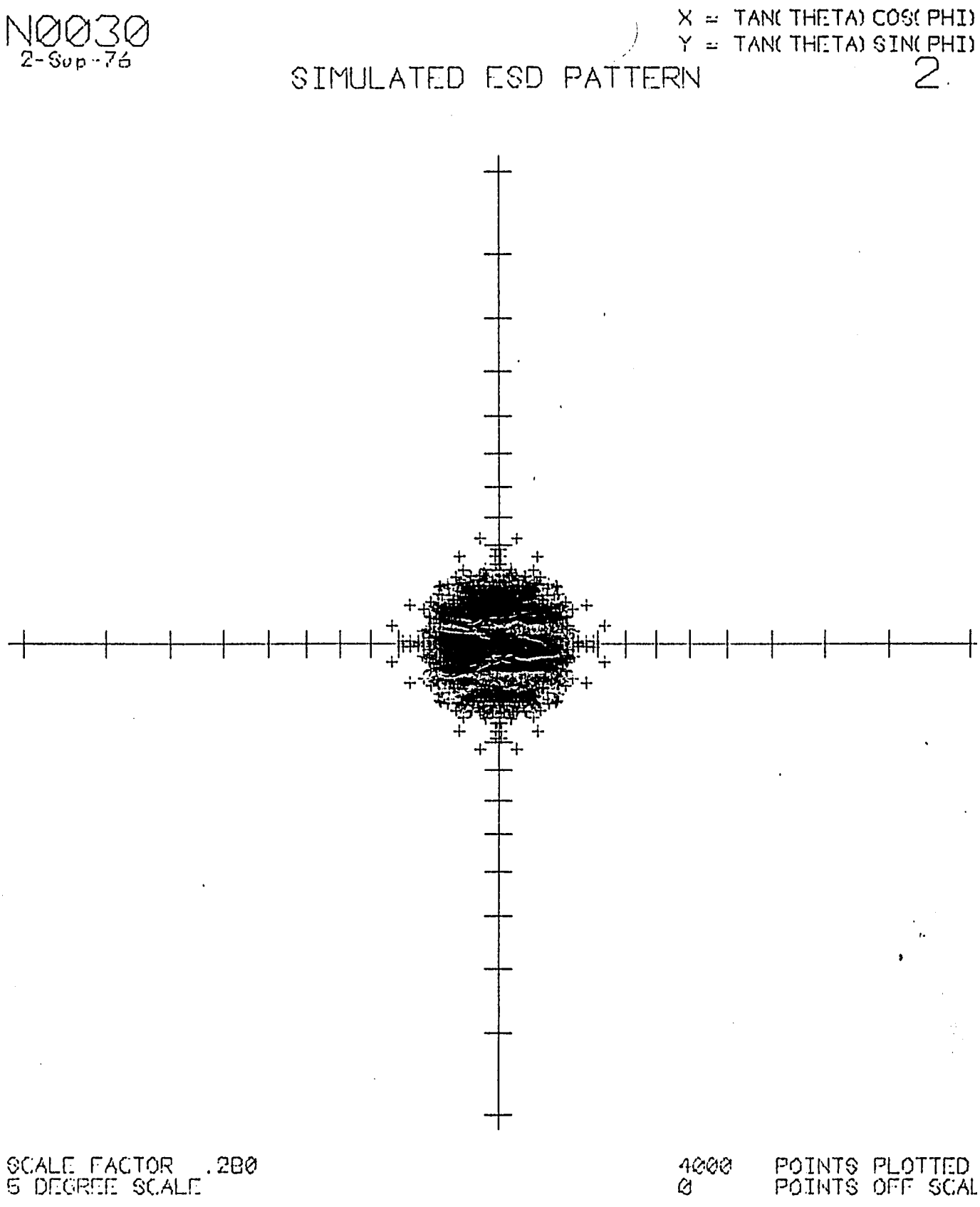

Figure AIV.6 ESDIAD Pattern for Site E1

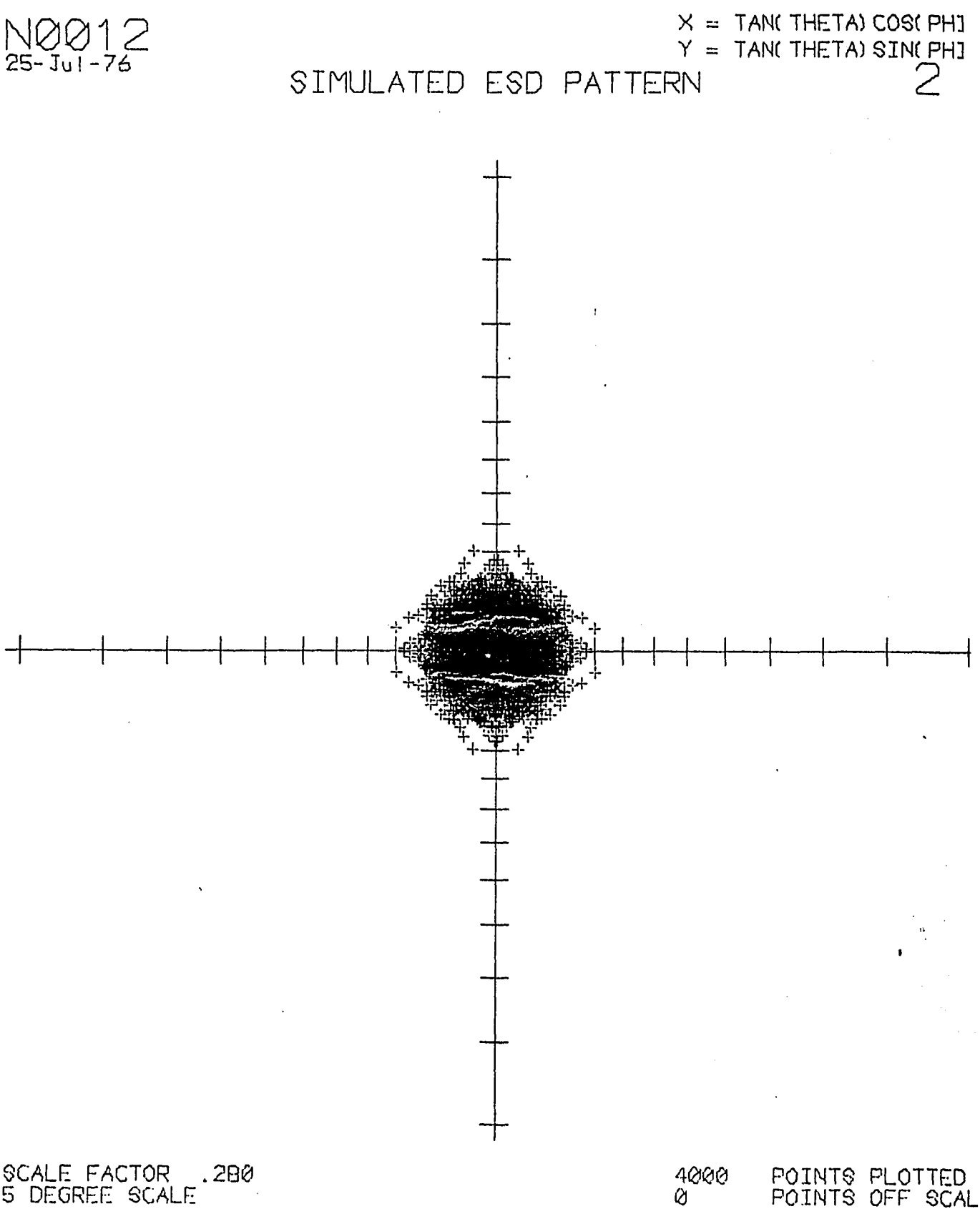

Figure AIV.7 ESDIAD Pattern for Site E2

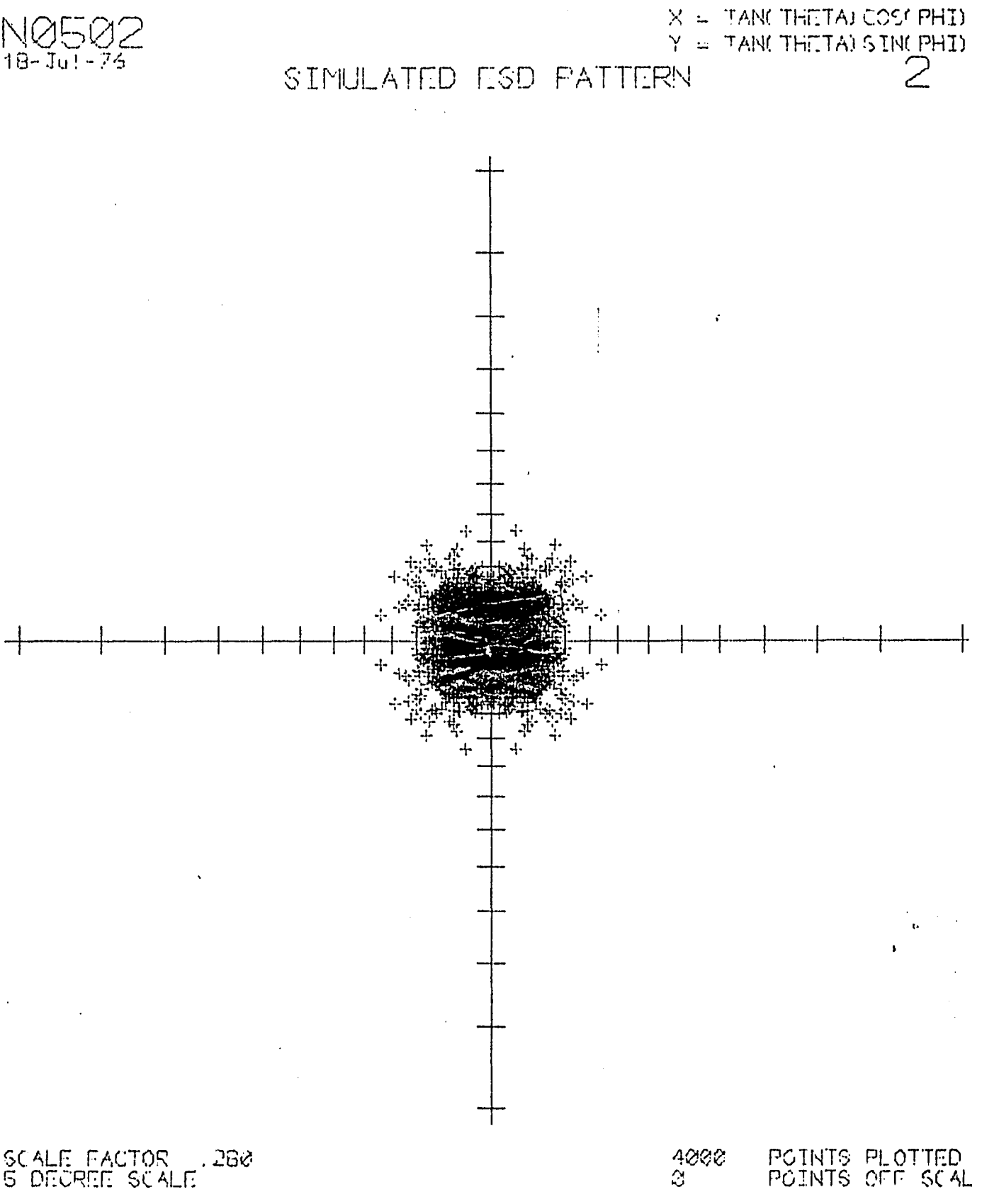

Figure AIV.8 ESDIAD Pattern for Site B1

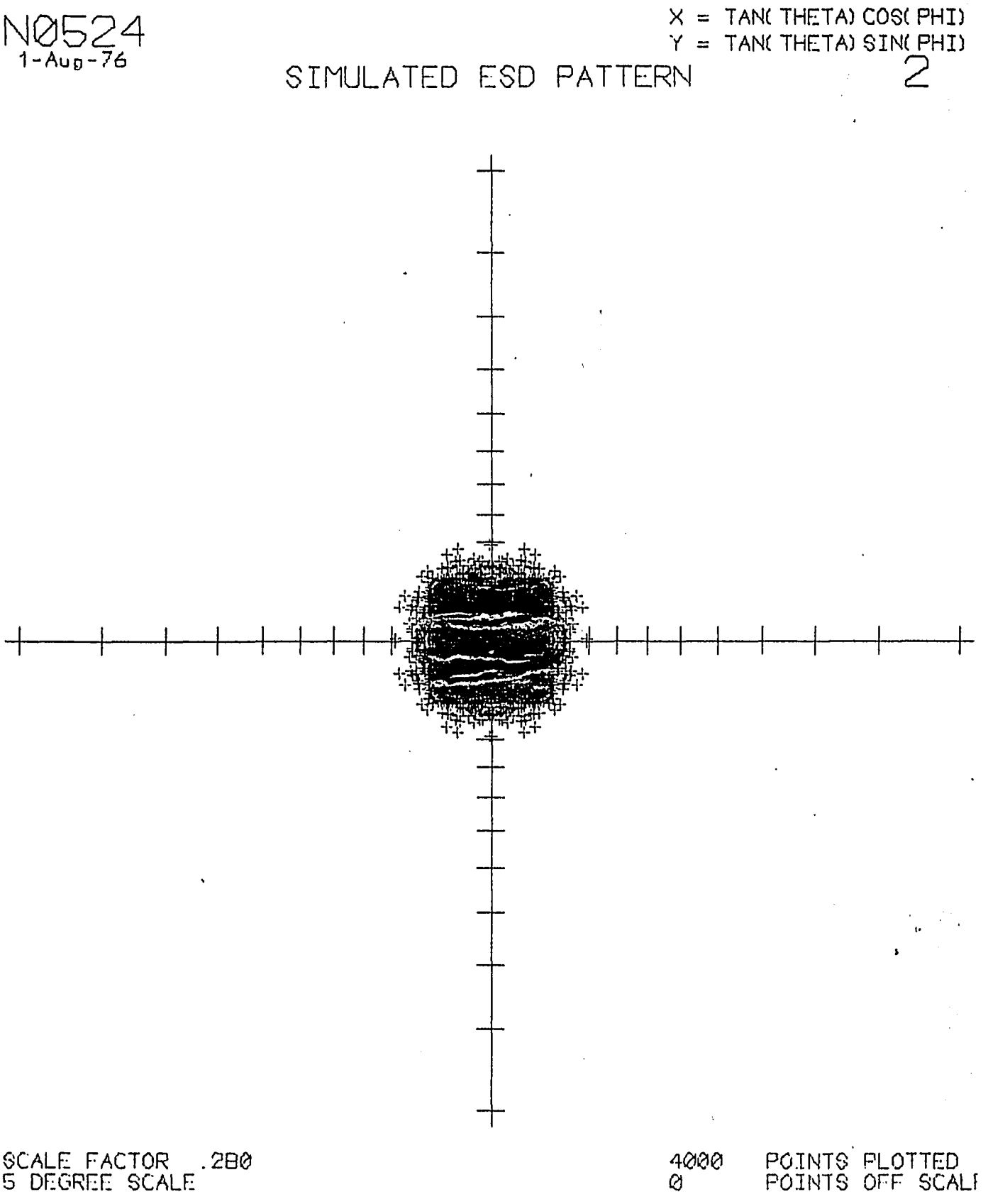

Figure AIV.9 ESDIAD Pattern for Site C1

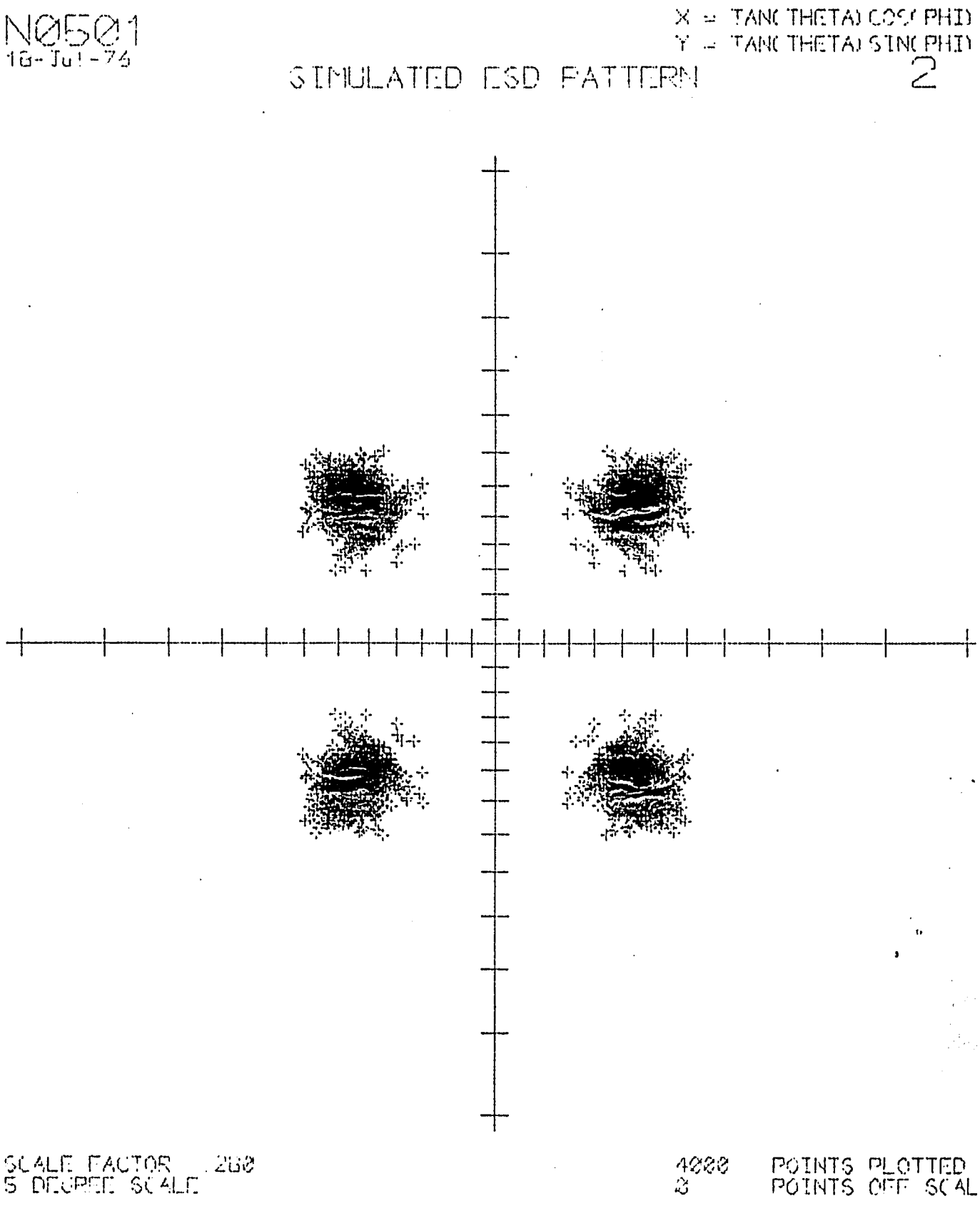

Figure AIV.10 ESDIAD Pattern for Site B2

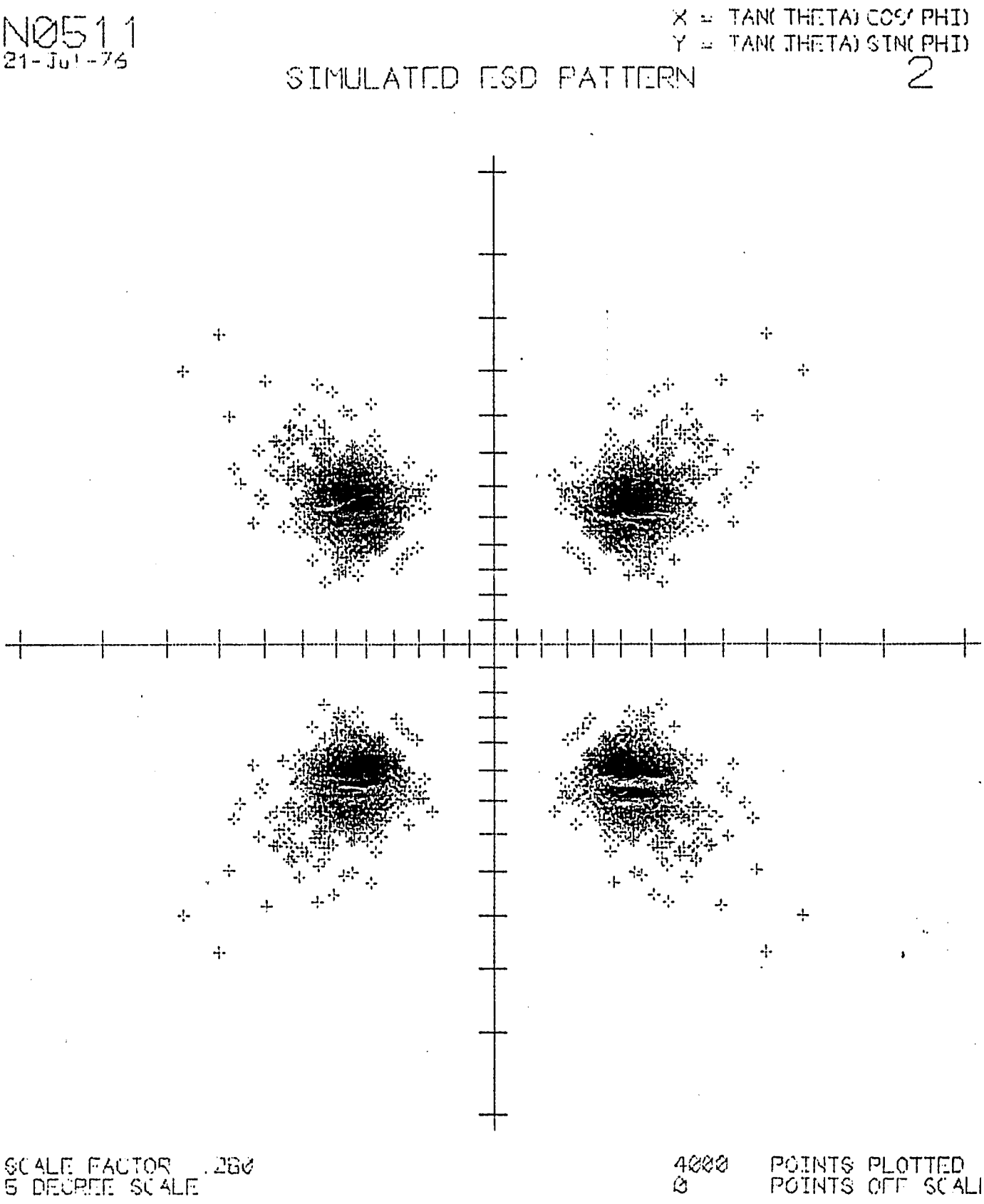

Figure AIV.11 ESDIAD Pattern for Site B3

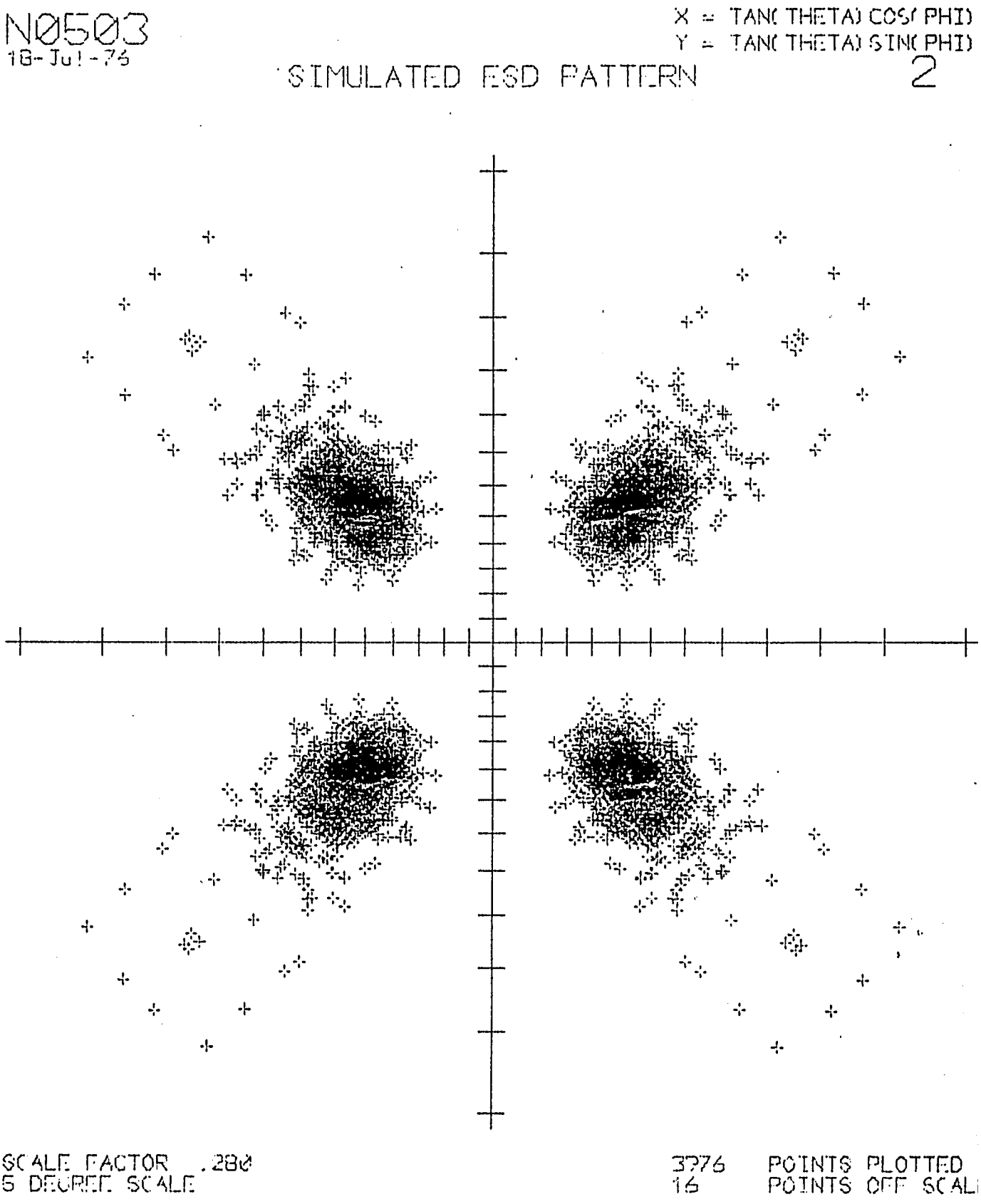

Figure AIV.12 ESDIAD Pattern for Site B4

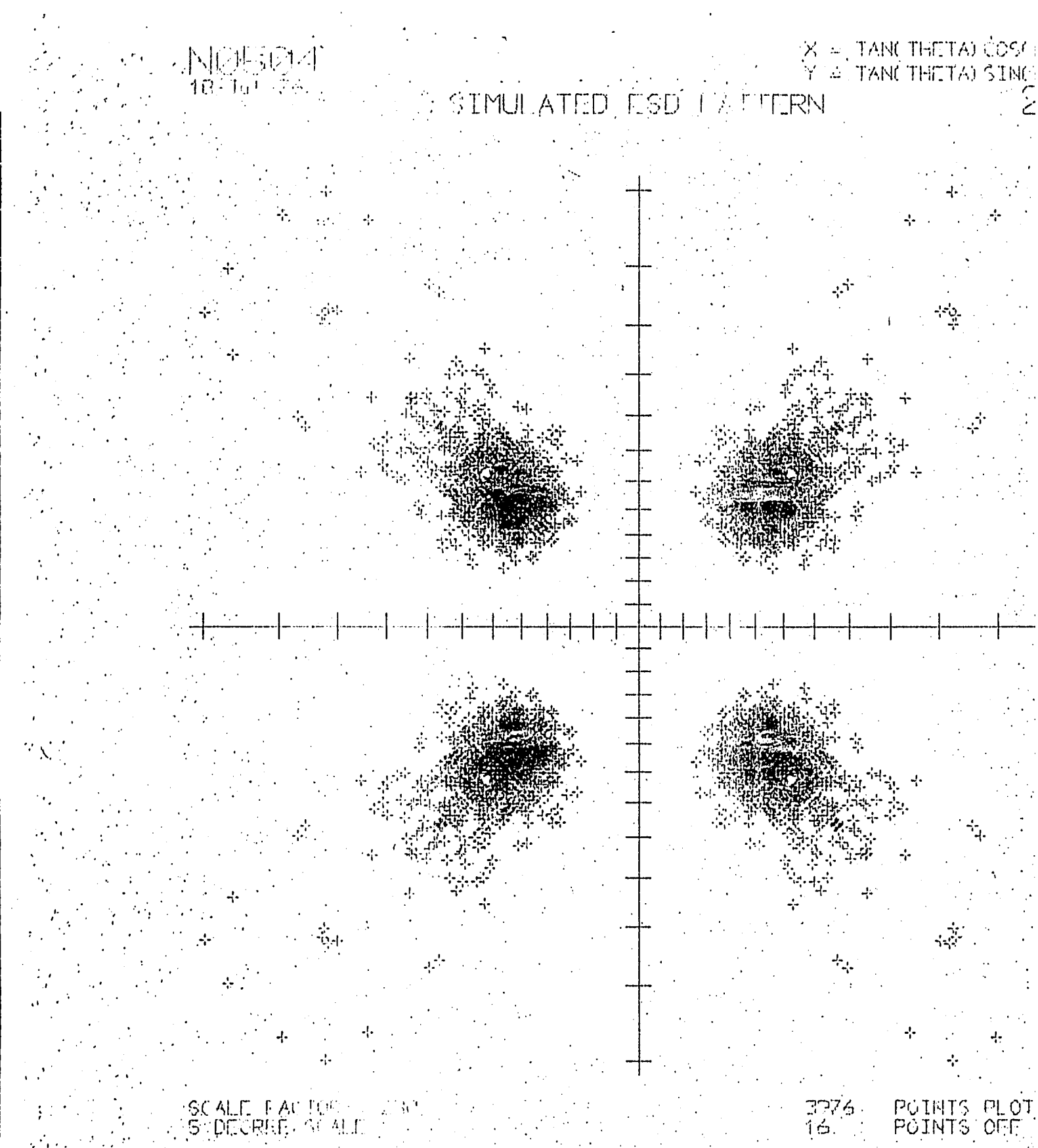

Figure AIV.13 ESDIAD Pattern for Site B5

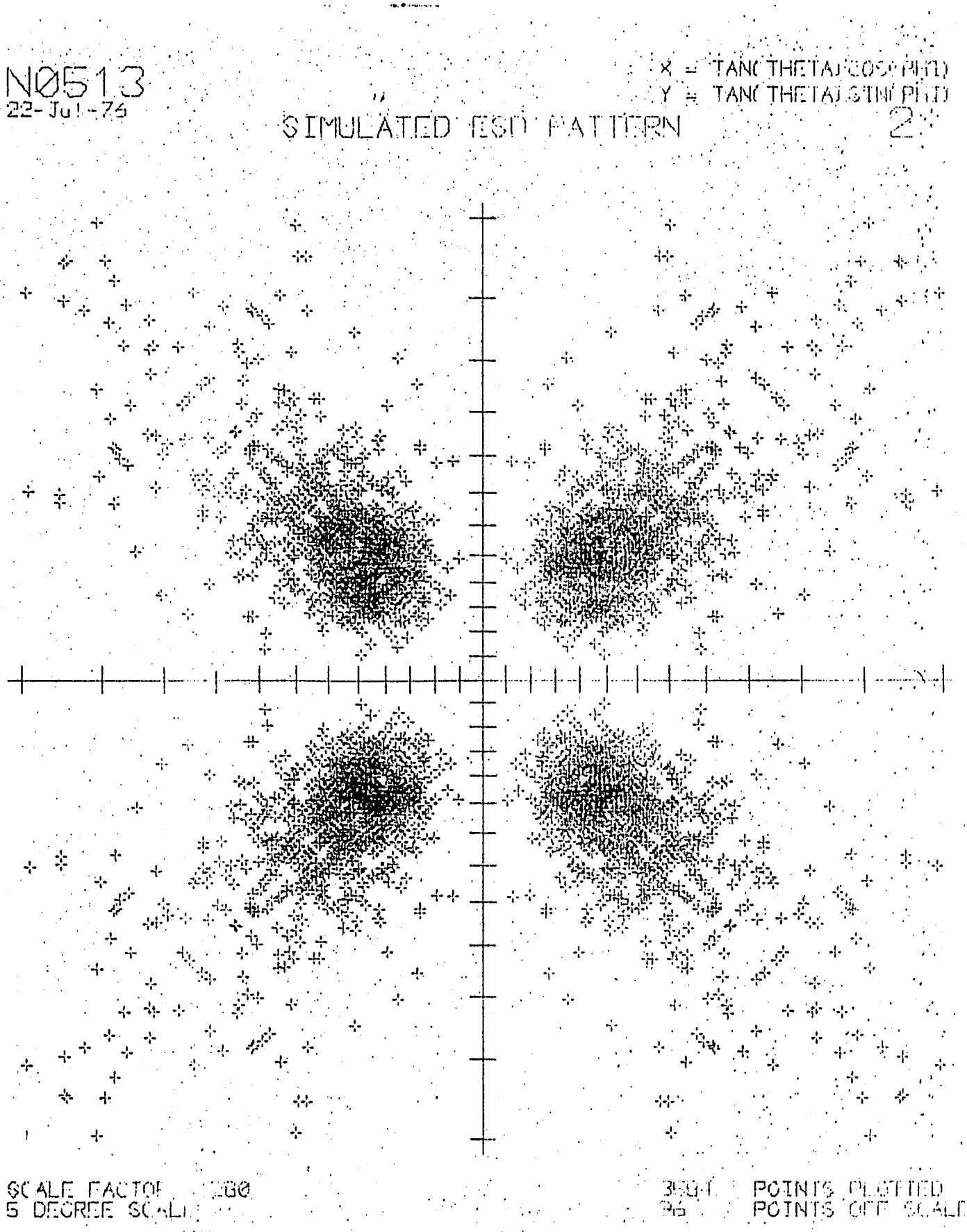

Figure AIV.14 ESDIAD Pattern for Site B6

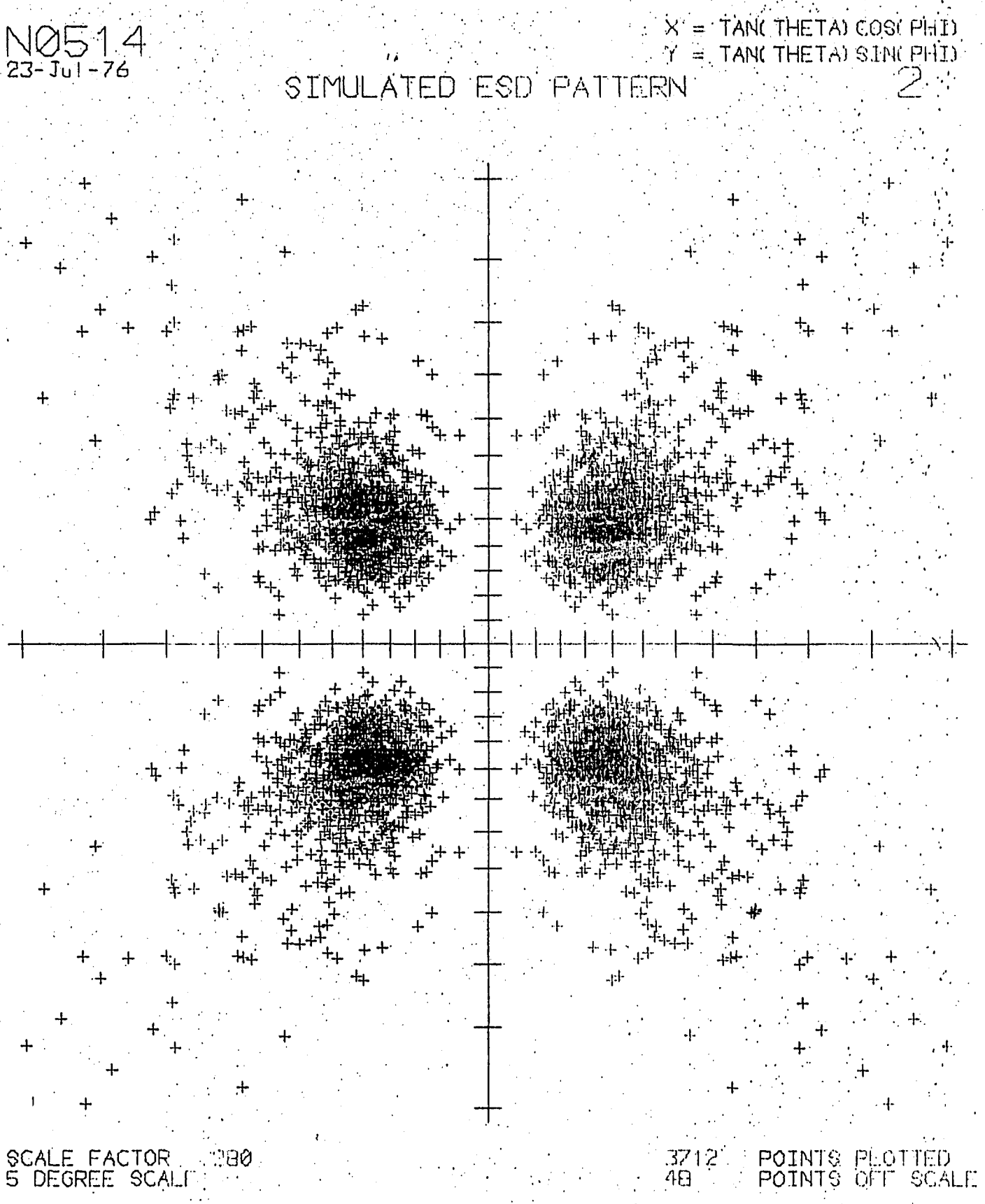

Figure AIV.15. ESDIAD Pattern for Site B7

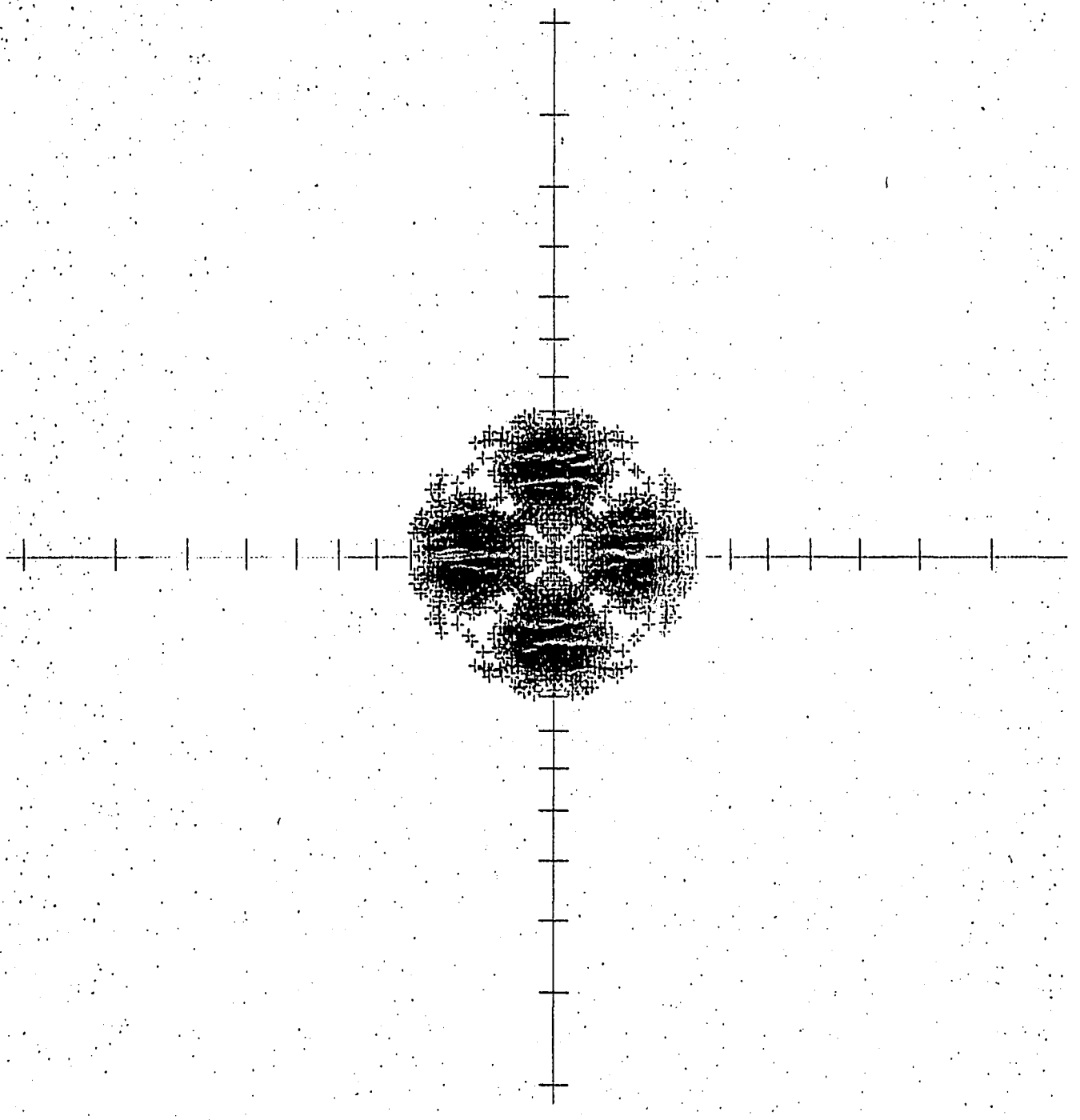

Figure AIV.16 ESDIAD Pattern for Site C2

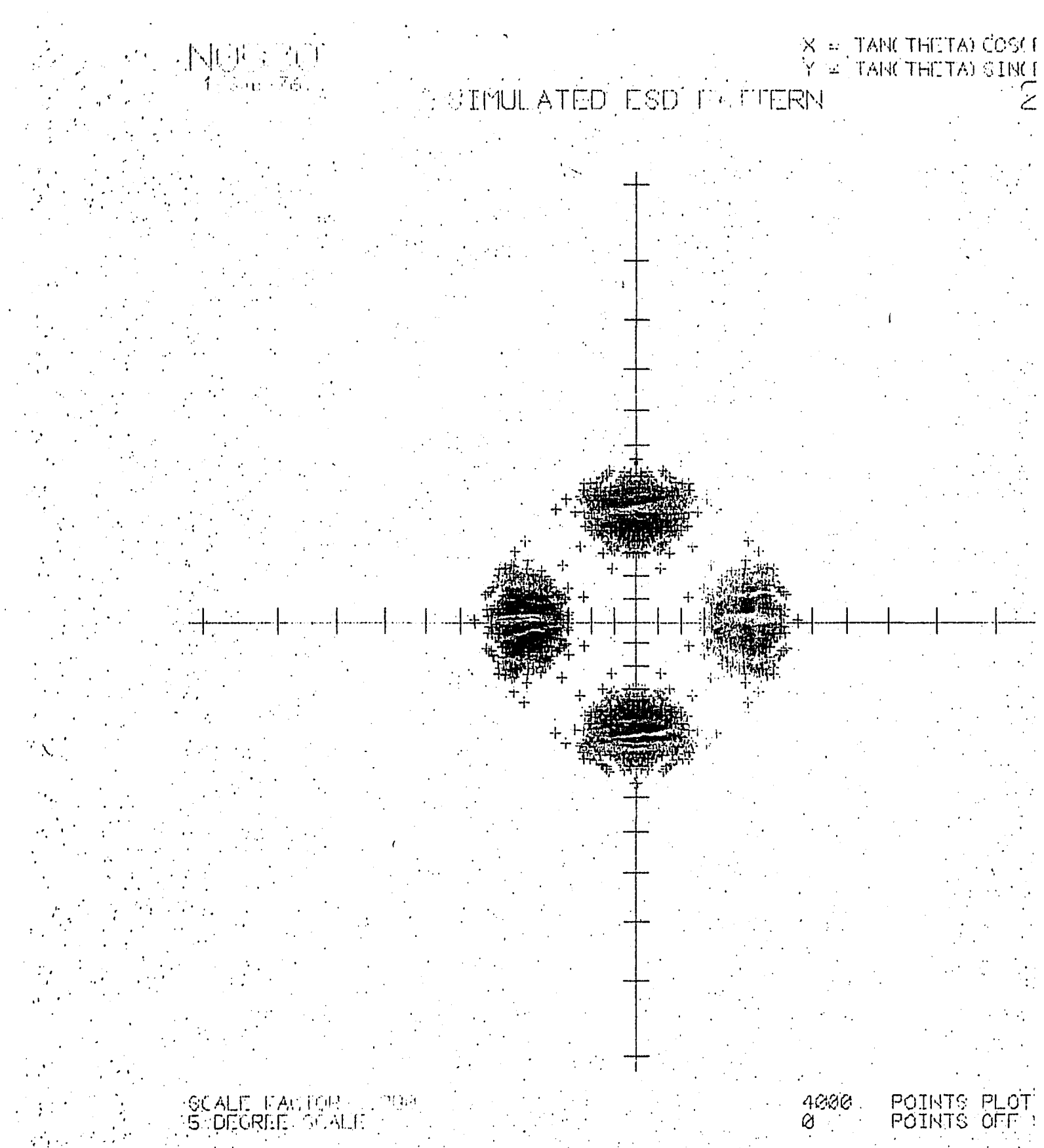

Figure AIV.17 ESDIAD Pattern for Site C3

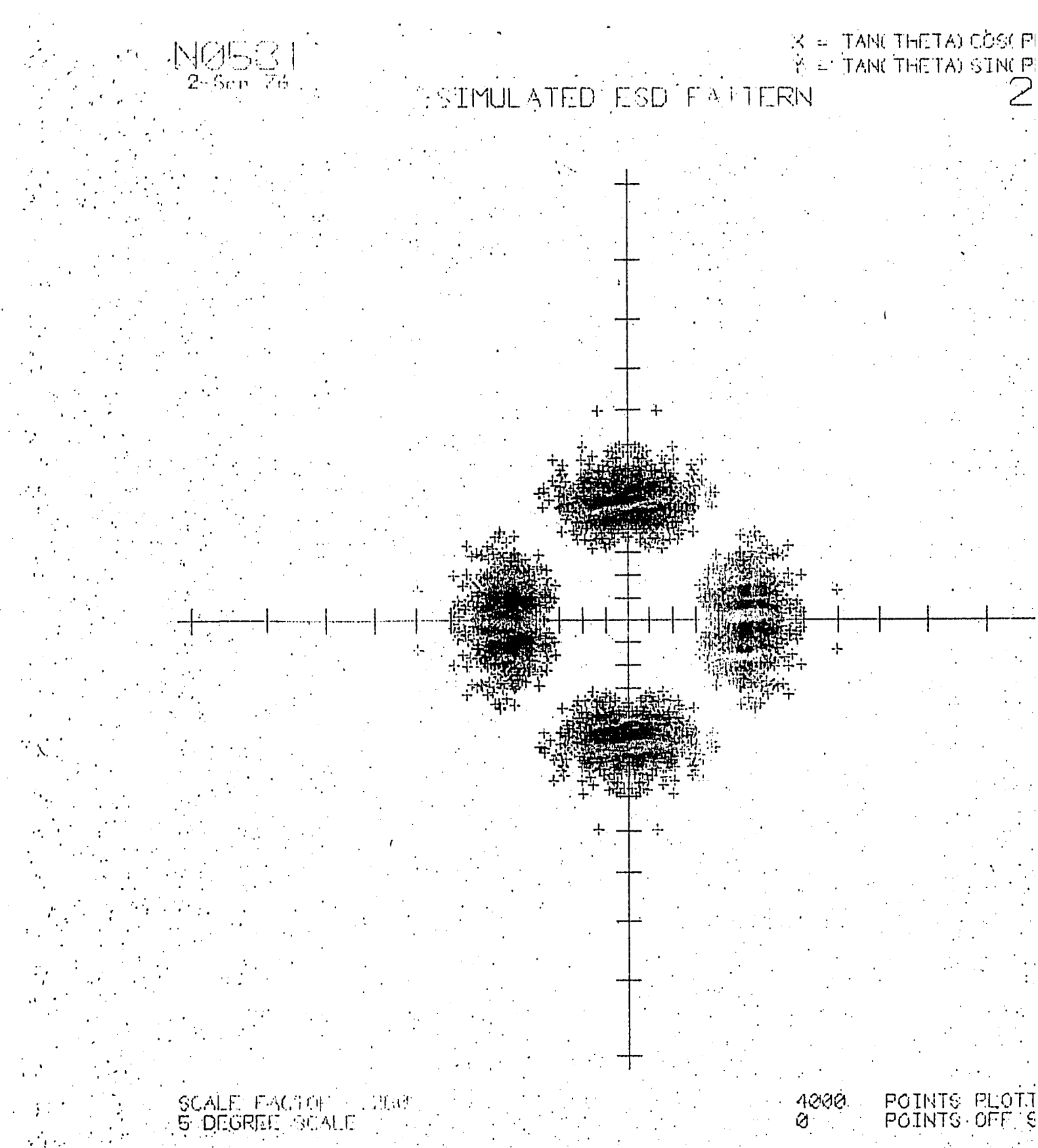

Figure AIV.18 ESDIAD Pattern for Site C4

References:

1. Gomer, R.,'Chemisorption on Metals' Solid State Physics 30, 94-226 (1975) Review of several areas of surface research.

2. Menzel,D.,Surface Science,47,370 (1975) Review of Electron Stimulated Desorption.

3. Madey,T. E., J. T. Yates, Jr., J. Vac. Sci. and Technol. 8, 525 (1971). Review of ESD to 1970.

4. Leck,J. H., B. P. Stimpson, J. Vac. Sci. Tech.,9,273 (1972). Review of ESD to 1971.

5. Menzel, D., Angew. Chem. Intern. Ed.,9,255 (1970)

6. Czyzewski,J. J., T. E. Madey, J. T. Yates Jr., Phys. Rev. Lett.,32, 777 (1974). 'Angular Distribution of Electron Stimulated Desorption Ions: Oxygen on W(100)'.

7. Madey, T. E., J. Czyzewski, J. T. Yates Jr., Surf. Sci. 49, 465 (1975). ESDIAD of Oxygen from W(100).

8. Madey, T. E.,J. Czyzewski, J. T. Yates Jr., Technical Report, Office of Naval Research (12/75). 'Ion Angular Distributions in Electron Stimulated Desorption: Oxygen and Carbon Monoxide on W(111).

9. Madey, T. E., J. T. Yates Jr., Bull. A.P.S. Ser. II,21,935 (9/76). ESDIAD study of SF_6, O^+ on W(110).

10. Duke,C. B., N. O. Lipari, G. E. Laramore, J. Vac. Sci. Tech. 11, 180 (1974)

11. Gadzuk,J. W., Surf. Sci.,53,132 (1975).

12. Physics Today, April 1975. This issue is devoted to review articles on Surface Physics, introducing various spectroscopies.

13. Fabel,G. W., S. M. Cox, D. Lichtman, Surf. Sci. 40,571 (1973).

14. Schwartz, Robert, Private communication (1975).

15. Madey, T. E., Surf. Sci. 33, 355 (1972).

16. King, D. A., T. E. Madey, J. T. Yates, J. Chem. Phys. 55, 3236, 3247 (1971).

References: continued

17. Madey, T. E., J. T. Yates, Surf. Sci. 11, 327 (1968)

18. Demuth, J. E., D. W. Jepsen, P. M. Marcus, Phys. Rev. B11, 1460 (1975).

19. Estrup, P. 'The Geometry of Surface Layers', Physics Today (4/75). Review of LEED.
Rhodin, T., S. Y. Tong,'Structure and Analysis of Solid Surfaces', Physics Today (10/75). Discussion of LEED.

20. Menzel,D., R. Gomer, J. Chem. Phys. 41, 3311, 3329 (1964) One Dimensional Theory of ESD.

21. Redhead, P. A., Can. J. Phys. 42, 886 (1964). One Dimensional Theory of ESD.

22. Slater, J. C., 'Quantum Theory of Molecules and Solids', Vol.I, Electronic Structure of Molecules, McGraw-Hill (1963).

23. Herzberg, G., 'Molecular Spectra and Molecular Structure', 2nd Ed., Vol. I, Spectra of Diatomic Molecules, Van Nostrand (1951).

24. Van Hove, M. A., S. Y. Tong, Surf. Sci. 54,91 (1976)

25. Van Hove, M. A., S. Y. Tong, Phys. Rev. Lett.35,1092 (1975).

26. Tracy, J. C., J. M. Blakely, Surf. Sci. 13, 313 (1968).

27. Taylor, N. J., Surf. Sci. 2, 544 (1964).

28. Schrieffer, J. R., J. Vac. Sci. Tech. 9, 561 (1971).

29. Appelbaum, J. A., D. R. Hamann, Phys. Rev. Lett. 32,255 (1974); Phys. Rev. Lett. 31, 106 (1973).

30. Newns, D. M., Phys. Rev. 178, 1123 (1969).

31. Gadzuk, J. W., Surf. Sci. 43, 44 (1974).
Recent issues of Phys. Rev.,Surface Science contain numerous attempts to solve the chemisorption problem.

32. Hagstrum, H. D., Phys. Rev. 96,336 (1954).

33. White, C. W., D. L. Simms, N. H. Tolk,D. V. McCaughan, Surf. Sci. 49, 657 (1975).

34. Bendow, B., S. C. Ying, J. Vac. Sci. Tech. 9, 804 (1972).

References: continued

35. Harris, S., 'Introduction to the Theory of the Boltzmann Equation', Holt-Rinehart and Winston (1971).

36. Platzman, P. M., P. A. Wolff, 'Waves and Interactions in Solid State Plasmas', Academic Press (1973).

37. Pines,D., P. Nozieres, 'The Theory of Quantum Liquids', Vol. I, Benjamin (1966).

38. Pines, D., 'Elementary Excitations in Solids', Benjamin (1963).

39. Ritchie, R. H., Phys. Rev. 106, 874 (1957).

40. Ritchie, R. H., Surf. Sci. 34, 1 (1973).

41. Flodstrom, S. A., G. V. Hansson, S. B. M. Hagstrom, J. G. Endriz, Surf. Sci. 53, 156 (1975).

42. Tzoar, N., J. I. Gersten, Phys. Rev. B8, 5671 (1973). Gersten, J. I., N. Tzoar, Phys. Rev. B8, 5684 (1973).

43. Gersten, J. I., N. Tzoar, Phys. Rev. B9, 4038 (1974).

44. Langer, J., S. Vosko, J. Phys. Chem. of Solids 12,196 (1960).

45. Duke, C. B., U. Landman, Phys. Rev. B8, 505 (1973). see also C. B. Duke, U. Landman, J. O. Porteus, J. Vac. Sci. Tech. 10, 183 (1973).

46. Feibelman, P., Phys. Rev. Lett. 30, 975 (1973).

47. Ritchie, R., Marusak, Surf. Sci. 4, 234 (1966).

48. Sowell, R. R., R. E. Cuthrell, D. M. Mattox, R. D. Bland, J. Vac. Sci. Tech. 11, 474 (1974).

49. Menzel, D., P. Kronauer, Proc. Second Int. Symp. on Adsorption/Desorption Phenomena, Ed. Ricca, Academic Press (1972).

50. Genequand, P., Surf. Sci. 25, 643 (1971).

51. Lange, W. J., J. Vac. Sci. Tech. 2, 74 (1965).

52. Adams, R. O., E. E. Donaldson, J. Chem. Phys. 42,770 (1965).

53. Lange, W. J., H. Riersma, 'Desorption of Gas by Photons' in Trans. Am. Vacuum Soc., Pergamon (1962).

References: continued

54. Cox,S. M., D. Lichtman, Surf. Sci. 54, 675 (1976).

55. Shapira,Y., S. M. Cox, D. Lichtman, Surf. Sci.54, 43 (1976).

56. Shapira,Y.,S. M. Cox, D. Lichtman, Surf. Sci. 50,503 (1975).

57. Schubert, R., K. W. Boer, J. Phys. Chem. of Solids 32, 77 (1971).

58. Kohl,D., M. Henzler, G. Heiland, Surf. Sci. 41,403 (1974).

59. Gersten, J., R. Janow, N. Tzoar, Phys. Rev. B11,1267 (1975).

60. Lennard-Jones,J. E., A. E. Ingham, Proc. Roy. Soc.(london), A107,636 (1925).

61. Born, M., J. E. Mayer, Z. fur Physik 75,1 (1932).

62. Lichtman, D., Crit. Rev. Sol. St. Sci. 4,395 (1974).

63. Condon, E. U., Phys. Rev. 32, 858 (1928).

64. Jelend,W., D. Menzel, Chem. Phys. Lett. 21, 178 (1973).

65. Madey, T. E., J. T. Yates Jr., D. A. King, C. J. Uhlaner, J. Chem. Phys. 52, 5215 (1970).

66. King, D. A., D. Menzel, Surf. Sci. 40, 399 (1973).

67. Madey, T. E., Surf. Sci. 36, 281 (1973).

68. Scheibner, E. J., L. N. Tharp, Surf. Sci. 8, 247 (1967).
Glicksman, M., 'Plasmas in Solids', Solid State Physics Vol. 26, p.275 (1971).
Powell, C. J., J. L. Robins, J. B. Swan, Phys. Rev. 110, 657 (1958).

69. Landau,L. D., L. M. Lifshitz,'Statistical Physics', Addison-Wesley (1958).

70. Hildebrand,F. B.,'Introduction to Numerical Analysis', McGraw-Hill (1956).
Ralston,A.,'First Course in Numerical Analysis', McGraw - Hill (1965).

71. Wharton,L., Private communication.

72. Nishijima,M., F. M. Propst, Phys. Rev. B2,2368 (1970).
Nishijima,M.,F. M. Propst, J. Vac. Sci. Tech. 7, 410, 420, (1970).

References: continued

73. Appelbaum, J., G. A. Baraff, D. R. Hamann, Phys. Rev. B14, 588 (1976): Phys. Rev. B12, 5749 (1975): Phys. Rev. B11, 3822 (1975).

74. Slater, J. C., 'Quantum Theory of Molecules and Solids', Vol. IV, The Self-Consistent Field for Molecules and Solids, McGraw-Hill (1974).

75. Herman, F., S. Skillman, 'Atomic Structure Calculations', Prentice-Hall (1963).

76. Liberman, D., J. Waber, D. Cromer, Phys Rev. 137, A27 (1965).

77. Dimmock, J. O., Solid State Physics 26, 103-274 (1971). See pp. 192-194.
Adler, D., Solid State Physics, 21, 1 (1968).

78. Matheiss, L. F., Phys. Rev. 139, A1893 (1965).

79. Loucks, T. L., Phys Rev. 143, 506 (1966).

80. Gersten, J, R. Janow, N. Tzoar, Phys. Rev. Lett. 36, 610 (1976).

81. Nicolas, J., 'Atlas of Models of Crystal Surfaces', Gordon and Breach (1965).

82. Slater, J. C., 'Quantum Theory of Molecules and Solids', Vol. II, Symmetry and Energy Bands in Solids, McGraw-Hill (1965).

83. Plummer, E. W., A. E. Bell, J. Vac. Sci. Tech. 9, 583 (1972).

84. Propst, F. M., T. C. Piper, J. Vac. Sci. Tech. 4, 53 (1967).

85. Zingerman, Ta. P., V. A. Ishchuk, Sov. Phys.-Solid State 9, 1992 (1968).

86. Madey, T. E., Private communication.

87. Madey, T. E., J. T. Yates, J. Chem. Phys. 51, 1264 (1969).

88. King, D. A., T. E. Madey, J. T. Yates, J. Chem. Soc. Faraday Trans. I68, 1347 (1972).

89. Pauling, L., 'The Nature of the Chemical Bond', 3rd. Ed., Cornell Univ. Press (1960).

90. Papageorgopoulos, C., J. Chen, Surf. Sci. 39, 313 (1973).

91. Estrup, P. J., J. Anderson, Proc. 27th Annual Physical Electronics Conf., MIT (1967).